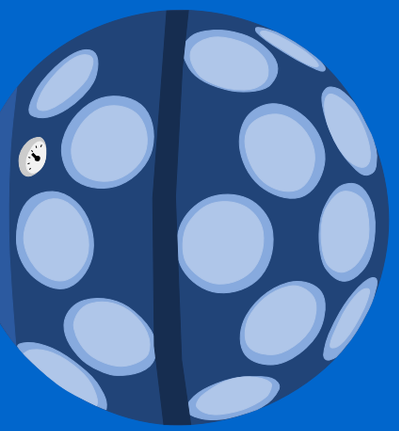

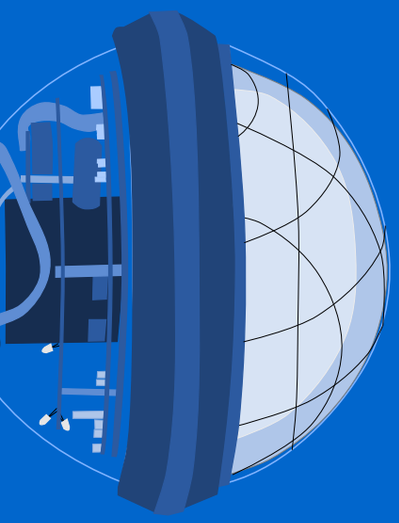

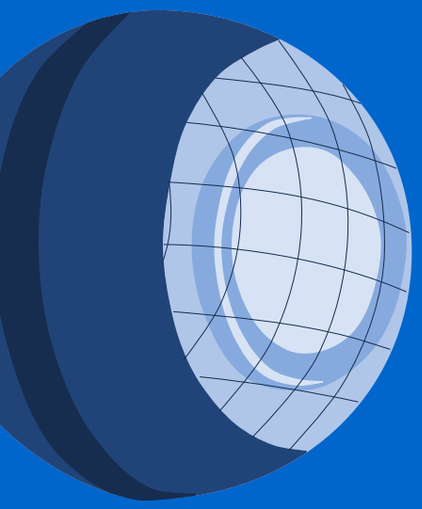

2018

Javier Barrios Martí

Tesis doctoral

VNIVERSITAT DE VALÈNCIA

Departament de Física Atòmica Molecular i Nuclear
Institut de Física Corpuscular

DOCTORAT EN FÍSICA

Search for cosmic sources in neutrino telescopes and time calibration in the ANTARES neutrino telescope

PhD thesis dissertation by:
Javier Barrios Martí

Under the supervision of:
Juan Zúñiga Román
Juan de Dios Zornoza Gómez

Valencia, April 2018

VNIVERSITAT DE VALÈNCIA

DOCTORAT EN FÍSICA
Departament de Física Atòmica, Molecular i Nuclear
Institut de Física Corpuscular (CSIC-UV)

Search for cosmic sources in neutrino telescopes and time calibration in the ANTARES neutrino telescope

Javier Barrios Martí

Supervisors Dr. Juan Zúñiga Román and Dr. Juan de Dios Zornoza Gómez

Valencia, April, 2018

Javier Barrios Martí

Search for cosmic sources in neutrino telescopes and time calibration in the ANTARES neutrino telescope

April, 2018

Supervisors: Dr. Juan Zúñiga Román and Dr. Juan de Dios Zornoza Gómez

Universitat de València

Astroparticle physics group

Institut de Física Corpuscular (CSIC-UV)

Departament de Física Atòmica, Molecular i Nuclear

Dr. JUAN ZÚÑIGA ROMÁN, profesor titular de la Universitat de València al Departament de Física Atòmica, Molecular i Nuclear de la Facultat de Física, i Dr. JUAN DE DIOS ZORNOZA GÓMEZ, investigador científic Ramón y Cajal al Departament de Física Atòmica, Molecular i Nuclear de la Facultat de Física,

CERTIFIQUEN,

Que la present memòria, Search for cosmic sources in neutrino telescopes and time calibration in the ANTARES neutrino telescope, ha sigut realitzada baix la seua direcció al Institut de Física Corpuscular (centre mixte Universitat de València - CSIC) per D. Javier Barrios Martí i constitueix la seua Tesi Doctoral al Departament de Física Atòmica, Molecular i Nuclear de la Universitat de València per a optar al grau de Doctor en Física.

I per a que conste, en compliment de la legislació vigent, signem el present certificat a Paterna, a 25 d'abril de 2018.

Dr. Juan Zúñiga Román

Dr. Juan de Dios Zornoza Gómez

A mis padres

Acknowledgements

> *Glen: Well, you know what it's like when you first sleep with someone you don't know?*
> *Russell: Yes.*
> *Glen: It's... you, like, become this blank canvas and it gives you an opportunity to project onto that canvas who you want to be. That's what's interesting because everybody does that.*
> *Russell: So do you think that I did it?*
> *Glen: Course you did. Well, what happens is while you're projecting who you want to be... this gap opens up between who you want to be and who you really are. And in that gap, it shows you what's stopping you becoming who you want to be.*
>
> — **Andrew High**
> Weekend (2011)

Some of the people who know me may find this shocking but, above all, the writing of this Thesis is the completion of one of my life goals. I believe I was 15 when I first decided I wanted to become a physicist, even after some of the patronising comments that I got when I said it. As it is often said, there is little knowledge about what Physics really is at those ages (though what I liked the most was the *way of thinking* of the physicists). But I had

very clear that, even if little, I wanted to contribute to push knowledge in some specific topic[1].

This PhD has been a culmination of a life goal, but definitely not without effort. A PhD is a *process* with many ups-and-downs, some rewards, headaches, moments of joy and of anxiety. Sometimes you feel extremely efficient and you're working non-stop, some other times you feel like quitting and sending everything to hell. Despite all, if I had to summarise what this PhD has meant to me, I would honestly say that this has been the period of my life in which I have learnt the most (and not just academically).

The figure of the PhD student is sometimes portrayed to be of a person who works on their own. However, in order to reach this point, I should thank a whole bunch of people for making this document a reality, either because of scientific, academic or personal reasons. These acknowledgements are written in the three languages that define me, so I am sorry if you, the reader, cannot understand everything which is written here.

First of all, I would like to thank my two supervisors. From Juan Zúñiga, I would like to outline his patience, his willingness to help, his passion of statistics, and especially, for being the first person who introduced me in the exotic world of neutrino astronomy. From Juande, I can mainly say that many of the topics presented here would have not ended in this Thesis without his support and his insistence to have the best results possible. I should also thank Juanjo, the former PI of the ANTARES group at IFIC, not only for accepting me in this group, but also because of his very concise comments and inputs.

Inside the ANTARES group at IFIC I have met quite some coworkers, some of whom have been crucial for the work presented here. I cannot help thanking Juan Pablo for introducing me, with patience, into the world of point-source analyses, and Agustín for all the discussions and his deep knowledge in everything regarding the time calibration. I must thank also Christoph for his always kind spirit and Giulia for being the most dedicated and hard-working coworker that I could ever had. I cannot forget mentioning the company and help of Rebecca, Alexis, Marta, Tarak, Moritz, Nafis, Liam, Tom, Faye, Judith, Jordan...

[1] Yep, I was a nerd as a teenager!

The ANTARES and KM3NeT Collaborations are, fortunately, large collaborations, and I have had the pleasure to be part of them. During these years I have had the opportunity to meet plenty of great people from many different places. In this sense, I would first like to thank Aart not only for accepting me at NIKHEF for my stay, but also because of your always accurate inputs. During my stay at NIKHEF I felt like at home, and this could not have been possible without the great ambiance of the group. Especially, I would like to thank Robert for being always the one who tried to make everyone in. I must also thank Rosa for inviting me to make a short stay in Catania, where I also felt very much welcomed. In this respect, my special thanks also go to Agata, for always making sure I was not feeling alone and for even bringing me to the hospital due to an anomalous sty. Finally, I must mention Marco Circella for his dedication and his altruistic corrections, Dorothea for helping to have all the required clarifications, Clancy for all the useful inputs and Luigi for always giving fast and accurate answers to any issue with the Monte Carlo (or really, any issue). I am sure I have missed some names here, so my apologies for those I forgot.

During my PhD I have had the privilege to make the first analysis which combined data from ANTARES and IceCube detectors, and I must thank both collaborations for this. With respect to this analysis, I would especially like to thank Chad for making the most accurate and detailed insights possible.

Al principio de estos agradecimientos he mencionado que decidí dedicarme *a esto de la física* cuando tenía 15 años. Parte de la culpa las tienen dos de mis profesores de ciencias durante la adolescencia. Principalmente, esto se lo debo al contagioso gusto por la física de Guillermo Martínez, i a totes les *xerraes* i respostes (no necessàriament de física) de qui després es convertiria en una de les meues millors amigues, Amparo Piquer.

Me temo que durante la carrera en física tuve un trato bastante más *formal* hacia mis profesores, pero aparte del ya mencionado Juan Zúñiga, guardo muy buen recuerdo de las clases de óptica de Eugenio Roldán y de las de José Antonio Manzanares, quien hacía ver toda la física que había detrás de la frecuentemente denostada termodinámica. De mis compañeros y amigos de carrera, no puedo olvidarme de Héctor, quien fuera casi siempre mi compañero de laboratorio, y de una capacidad bastante particular para

entender la física; de Mire, una de las personas más brillantes que he conocido en todos los sentidos; de Yolanda, con quien he perdido bastante el contacto, pero de quien guardo muy buenos recuerdos; de Celia, con quien compartí las primeras experiencias dentro de ANTARES; de Sergio C., con quien ya antes de la carrera compartí buenos momentos dentro y fuera de la física; y de Sergio G. y Adrián, buenos compañeros de frikadas varias.

A big thanks should also go here to the IAYC (International Astronomical Youth Camp), and to all the people I have met there. I knew about this camp after one of my friends, Mire, found it in a random search in Google, and it is one of the best random coincidences that could have happened in my life. This is not just because of all the great time I had spent there, both in the camps before and after I began my PhD. This is basically the place where I first did a project on my own, and a place where very particular kind of people gather every summer to learn and have fun because of astronomy. The names I could mention from this camp would be simply too long, but I cannot skip saying *mila esker* to Aitor for one of the closests friendships I've ever had.

En el IFIC no sólo he tenido a buenos colegas de trabajo, también he conocido a otros *doctorandoms* de otros experimentos que han hecho de estos años algo más que un lugar de trabajo. Aquí uno no se va a olvidar de las excursiones y grandes planes de Ana, dels partidets de l'IFIC que sempre organitzava Nuria, de las tarjetas amarillas de Víctor, de las discusiones de viernes noche con Damián, de los juegos de mesa con Miguel Ángel, Jonathan, Ander y Pablo R., de las muy agradecidas visitas de estudiantes organizadas por Alberto, de todas las anécdotas y curiosidades de Álvaro, o de las discusiones de cine con André, Dominik y Pablo.

No quiero terminar estos agradecimientos sin mencionar a algunos de mis más viejos amigos, quienes también me han acompañado en este viaje, aunque sólo fuera para escuchar mis idas y venidas. Creo que a Bea nunca le he reconocido su enorme paciencia. De Fran, creo que nos conocemos desde demasiado tiempo como para decirnos nada nuevo, pero nunca es mala ocasión para agradecer, de nuevo, su compañía. De Juanjo G., toda

su sinceridad ante cualquier tema. Y de Máriam, su gran capacidad para resolver los problemas en tan pocas palabras.

A Josep, no puc més que agraïr-li la companyia dels quasi dos anys que estiguérem junts, i la seua confidència de tots el assumptes relacionats o no amb la tesi durant eixe temps. Més recentment, no puc ni vull saltar-me la gran e inestimable companyia de Ricardo en els últims mesos, transformant el que pensava que serien moments de gran ansietat en tot el contrari.

Ya para acabar, y desde luego no menos importante, querría dar las gracias a mis cuatro sobrinos (Ariadna, Isaac, Marc y Lara), a mis hermanos y mis cuñadas, y sobre todo a mis padres, quienes han dado todo lo posible para que esta (y cualquier otra) hazaña que he hecho en la vida, hayan sido posibles.

Contents

Preface

Neutrino astronomy is a relatively newborn field. It has been almost one century since the neutrino was proposed by Pauli, and more than 50 years since Markov proposed the initial idea on which high energy neutrino telescopes are based on. Despite the first astronomical observation of neutrinos from the Sun in the 1960s, it has not been until the 2010s when the first evidences of cosmic high energy neutrinos have been obtained. These first evidences constitute a revolution inside the field, but even after their observation, there are still many open questions regarding their exact origin.

The main goal of the work performed in this Thesis is related to the searches of point and extended source searches of cosmic neutrinos. It has been long known that these sources must also be the acceleration sites of cosmic rays, and places where a γ-ray emission could be expected. Indeed, evidences of hadronic acceleration regions have been shown in the last decade. The observation of specific neutrino sources would help to answer the long standing question of the origin of cosmic rays.

Currently, there are three neutrino telescopes in full operation: ANTARES, Baikal and IceCube. Furthermore, the KM3NeT Collaboration is building what will become the largest network of neutrino telescopes. In this respect, the results presented in this thesis have been obtained by using data taken by the ANTARES and IceCube neutrino telescopes, and with simulations of the KM3NeT Collaboration.

The first two chapters of this Thesis give an overview of the field. A summary of the current status of high energy neutrino astronomy, the physics behind it and its links with other types of astronomy are given in Chapter 1. A

description of all the currently operating neutrino telescopes, and the future KM3NeT network, is given in Chapter 2.

The third and the fourth chapters explain more technical details which are needed for the understanding and reconstruction of the data. A description of the official simulation chains and the event reconstruction algorithms of ANTARES, IceCube and KM3NeT which are relevant for the results presented in this work are presented in Chapter 3. The time calibration procedures in the ANTARES telescope are presented in Chapter 4, including the last update performed for most of the ANTARES data taking period.

The last two chapters are focused on the point and extended source searches. Chapter 5 includes an overview of the main statistical tools and procedures used for these type of searches. The results of the searches performed are presented in Chapter 6.

1 Neutrino astronomy: a new window to observe the Universe

> *Neutrinos they are very small.*
> *They have no charge and have no mass*
> *And do not interact at all.*
> *The Earth is just a silly ball*
> *To them, through which they simply pass,*
> *Like dustmaids down a drafty hall*
> *Or photons through a sheet of glass.*
> *...*
>
> **— John Updike**
> Collected Poems, 1953

In the 20th century, the observation of the Universe with the use of wavelengths other than visible light led to a set of important discoveries in astronomy. Examples of these discoveries are the first observations of pulsars in the radiowave spectrum, the cosmic microwave background, or the gamma-ray bursts.

In a similar manner, the use of other messengers different to photons has recently opened new windows to study the cosmos. On the one hand, the detection of gravitational waves by LIGO [1] started the detection of massive objects at distances which cannot be reached with the use of photons. On the other hand, the high energy neutrino flux reported by the IceCube neutrino observatory [2, 3, 4, 5] has proven the feasibility of using high energy neutrinos as cosmic messengers. In parallel, the successful operation of the ANTARES neutrino telescope has shown the possibility of building and operating a neutrino telescope in the Mediterranean Sea. This experience has led to the ongoing construction of KM3NeT, which will help

to understand the high energy flux reported by the IceCube Collaboration (and go beyond) with the largest neutrino telescope network ever built.

High energy neutrino astronomy has traditionally been linked to the physics behind cosmic rays and γ-ray astronomy. Because of this, a review on cosmic rays and on γ-ray astronomy is presented in Sections 1.1 and 1.2. The high-energy neutrino flux observed by IceCube is not the first time neutrinos have been successfully used in astronomy. A description of these first results is given in Section 1.3. The physics behind high energy neutrino astronomy is briefly explained in Section 1.4. Finally, the high energy flux observed by IceCube is explained in detail in Section 1.5, along with a review of some hypotheses on their origin.

1.1 Cosmic Rays

The discovery of a flux of charged particles coming from outside the Earth (cosmic rays) is attributed to Victor Hess, who performed a set of observations of the dischargement of an electroscope at different altitudes with manned balloon flights [6]. Before these experiments, the dischargement observed at sea level was mainly thought to be produced due to the natural radioactivity, but the increasing values up to altitudes of 4 km could only be explained due to cosmic origins. These measurements were replicated up to higher altitudes ($\sim$8 km) by Kolhörster [7].

This discovery had an immediate impact on particle physics: the use of cosmic rays as a source of high energy particles became standard and led to the discovery of a large number of particles, such as positrons [8], muons [9] (although originally thought to be the pions predicted by the Yukawa potential [10, 11]), kaons [12] and pions [13].

The development in the 1950s of the first particle accelerators enabled more control into the source of high energy particles. Because of this, the research topics about cosmic rays shifted from fundamental particle physics to the composition, energy spectrum, origin and acceleration processes of cosmic rays.

1.1.1 Composition and energy spectrum of cosmic rays

A first hint of their composition was available after the observation of the East-West effect [14, 15, 16, 17], in which a preference direction of cosmic rays coming from the West was observed. This effect, which is due to the Earth's magnetic field, showed that most of the cosmic rays have a positive charge.

Indeed, cosmic rays are mostly composed by protons ($\sim$80%), followed by Helium nuclei ($\sim$15%), other heavier nuclei and electrons ($\sim$1 %) [18, 19]. The hadronic component of cosmic rays has a similar abundance compared to the chemical abundances in the Solar System, although with a significantly larger amount of Li, Be and B nuclei, and also a larger abundance of nuclei between calcium and iron [20]. This is due to the fragmentation of heavier nuclei after the interaction with interstellar matter (*spallation*). Figure 1.1 shows the chemical abundance of cosmic rays as observed by different satellite based experiments.

The energy spectrum of cosmic rays above a few GeV can be described by a power law,

$$\frac{dN}{dE} \propto E^{-\alpha}, \tag{1.1}$$

where α is the spectral index. Depending on the energy range of the cosmic ray flux, this index presents different values. This variability is expected to be due to different origins of the cosmic rays. Cosmic rays of less than a few GeV are either originated at the Sun or are largely affected by its magnetic field. Cosmic rays between a few GeV up to the *knee* ($\sim 10^6$ GeV) are expected to be initially accelerated at shock waves in supernova remnants (diffuse shock wave acceleration model) and later by galactic magnetic fields (leaky box model). In this energy range, the slope presents a value of $\alpha \sim$ 2.6-2.7. A steepening is observed at energies between 10^6 to 10^9 GeV (*ankle*), in which the spectral index changes to $\alpha \sim$ 3.1. A spectral index of $\sim$ 2.6 is observed at energies beyond the ankle, which corresponds to cosmic rays that are accelerated by extragalactic sources. Figure 1.2 shows the energy spectrum of cosmic rays as observed by multiple experiments.

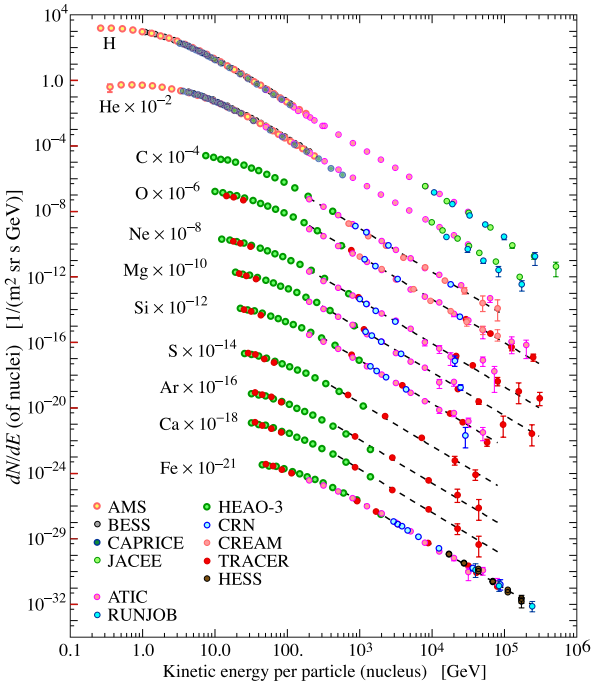

Fig. 1.1.: Abundances of nuclei in cosmic rays as a function of the energy. Figure taken from [18].

1.1.2 Cosmic rays until the GeV scale: the effects of the Sun

Solar flares (large energy releases correlated with sudden bright flashes of the Sun) eject particles up to a few GeV which can be detected on Earth [19, 20]. These particles mainly consist of protons, although electrons and heavier nuclei are also present.

The solar magnetic field and the solar winds, made of a continuous flux of charged particles of energies up to the order of $\sim$ 10 keV, limit the incoming flux of galactic cosmic rays. The solar wind is modulated by the 11 year solar magnetic cycle, which affects the amount of detected cosmic rays on Earth. As a consequence, experiments based on neutron-monitors have observed an anticorrelation between the strength of the solar magnetic field and the amount of cosmic rays of $\sim$ GeV detected on Earth [21].

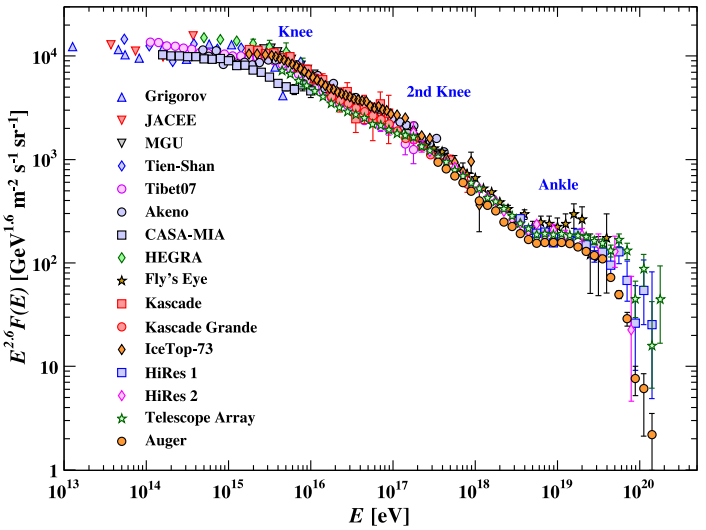

Fig. 1.2.: Energy spectrum for cosmic rays. Figure taken from [18].

1.1.3 Galactic cosmic rays up to the knee

Cosmic rays up to energies of $\sim 10^{15}$ eV are expected to be of galactic origin. The most accepted explanation for their acceleration is a mixture of the diffuse shock model in supernova remnants (SNRs) with the subsequent propagation in the Galaxy. The cosmic ray particles would gain energy by a set of collisions with irregularities on the magnetic field, called *magnetic mirrors*.

A simple explanation of the cosmic ray propagation in the Galaxy is given by the leaky box model [22]. This simple model suggests that cosmic ray particles remain confined within the Galaxy due to the magnetic fields (~ 3 μG) during a given livetime, τ_{esc} or escape time. In this sense, the probability for a particle to escape from the magnetic confinement depends on its energy (the higher the energy, the higher the probability). In other words, the escape time is energy dependent. By considering the density of cosmic ray particles per energy unit emitted by galactic sources, $Q(E)$, and the interaction of the particles with the interstellar medium (ISM), the

variation over time of the density of cosmic ray particles per energy unit in the Galaxy, $\mathcal{N}$, can be described as [19, 20, 23]

$$\frac{d\mathcal{N}(E)}{dt} = -\frac{\mathcal{N}(E)}{\tau_{esc}(E)} + Q(E) - \frac{\mathcal{N}(E)c}{\lambda}, \tag{1.2}$$

where λ is the mean free path for protons in the ISM ($\lambda \sim 55$ g·cm^{-2}). By assuming a stationary case, $\frac{d\mathcal{N}(E)}{dt} = 0$, this equation can be transformed in

$$\mathcal{N}(E) = \frac{Q(E)\tau_{esc}(E)}{1 + \frac{c\tau_{esc}(E)}{\lambda}}. \tag{1.3}$$

Since $\lambda >> c\tau_{esc}$, and the differential flux of cosmic rays, $\Phi(E)$, is proportional to $\mathcal{N}(E)$, the following relationship can be obtained:

$$\Phi(E) \propto Q(E)\tau_{esc}(E). \tag{1.4}$$

The energy dependence of τ_{esc}(E) can be obtained from experimental data by looking at the secondary-to-primary ratios of different cosmic ray elements as a function of the energy [24, 25]. From these experiments, an energy dependence of $\tau_{esc} \propto E^{-0.6}$ is obtained, which leads to a source flux spectral index of ∼2.0–2.1.

The diffuse shock wave model at SNRs can explain an ∼E^{-2} dependence on the emitted source flux. In this model, particles gain energy by collisions with magnetic irregularities present at the shock front, so that particles would stay crossing back and forth the boundary of the shock wave for a given period of time. At each collision, a particle has a probability P to escape and gains an amount of energy β. Therefore, the average amount of particles present and the energy gained per each particle after n collisions can be written as

$$N_n = (P)^n N_0, \tag{1.5}$$

$$E_n = (1+\beta)^n E_0, \tag{1.6}$$

where N_0 is the initial number of particles, and E_0 is the initial energy of the particle. From these two formulas, we can obtain the flux emitted by the source:

$$\frac{dN}{dE} = K\left(\frac{E}{E_0}\right)^{-1+\frac{logP}{log\beta}}. \tag{1.7}$$

It can be shown [19, 20] that in these shock waves, log(P) $\simeq (1 - \frac{v_s}{c})$ and log(β) $\simeq (1 + \frac{v_s}{c})$, where v_s is the speed of the shock wave. Since $v_s << c$ and $\log(1+x) \approx x$ for $x << 1$, a source spectrum of $\sim E^{-2}$ is obtained.

1.1.4 Cosmic rays with energies above the knee

The standard diffuse shock-wave model on SNRs can only explain the acceleration of cosmic rays up to energies of $\sim 10^{14}$ eV, since particles with larger energies cannot be contained in the region. By considering the Larmour radius to be smaller than the acceleration region size, R, the following relation can be obtained:

$$E_{max} \sim ZeRBU, \tag{1.8}$$

where Z stands for the charge of the cosmic ray particle, e is the charge of an electron, B is the magnetic field of the acceleration region, and U the speed of the magnetic scattering centres. Typical values for SNRs would be B $\sim 4{\cdot}10^{-10}$ T, U $\sim 2 \cdot 10^4$ km/s, and R $\sim$ 5 pc = $1.4 \cdot 10^{17}$ m, leading to a maximum energy of $E_{max} \approx 10^{14}$ Z eV.

This criterion was first introduced by Hillas [26], and can be applied to different types of sources. Figure 1.3 shows the relationship between the magnetic field and the acceleration region sizes for different astrophysical sources. The diagonal lines show the relationship between B and R required to accelerate a particle with a given maximum energy.

The change in the slope above the knee is consistent with the maximum energy obtained for SNRs. For energies up to the ankle, different galactic sources such as pulsars or binary sistems of a massive object (black holes or neutron stars) and a star have been proposed [19]. Also, some hints suggest that SNRs may be able to accelerate particles up to $\sim 10^{18}$ eV with the use

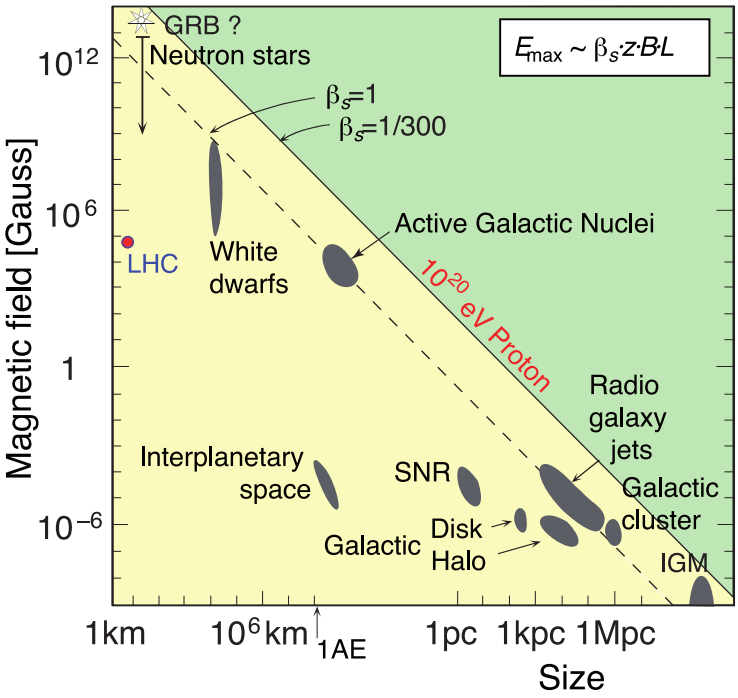

Fig. 1.3.: Hillas diagram for candidate cosmic ray acceleration sources. Figure taken from [27].

of nonlinear diffuse shock acceleration mechanisms [20], and because some observations infer the presence of stronger magnetic fields in the shock wave regions [28]. However, cosmic rays with energies above the ankle are for sure expected to be extragalactic. The magnetic field of the Galaxy is not strong enough to confine them inside (their Larmour radius is larger than the size of the Galaxy). The dipolar anisotropy observed by the Pierre Auger Observatory for cosmic rays over 10^{18} eV confirms the extragalactic origin of these particles [29]. A later study from the same experiment shows a significant correlation with bright extragalactic sources and the anisotropies found for cosmic rays above 20 EeV [30].

1.1.5 Energies above 10^{20} eV: The GZK cutoff

For ultra high energy cosmic rays (UHECR), the interaction of protons and nuclei with the photons of the comic microwave background (CMB) produces a cutoff on the energy spectrum, known as the Greisen-Kuzmin-

Zatsepin (GZK) cutoff [31, 32]. Due to the large energies of the cosmic rays, the photons of the CMB present energies in the rest frame which allow the production of pions and photons through the Δ^+ resonance:

$$p + \gamma_{CMB} \rightarrow \begin{cases} \pi^0 + p \\ \pi^+ + n \end{cases} . \tag{1.9}$$

The effects of the GZK begin to become important for proton energies above $\sim 5{\cdot}10^{19}$ eV [19, 18, 20]. The energy loss of a proton per interaction is approximately the ratio between the pion and proton masses, $\Delta E/E \sim m_\pi/m_p \sim 0.1$. By knowing the cross section of the interaction, $\sigma_{p\pi} \sim 250$ nb, and the density of CMB photons, $n \sim 5{\cdot}10^8$ m^{-3}, the mean free path for the total energy loss of a proton can be calculated, giving a value of ~ 30 Mpc. In other words, protons of energies above $\sim 5{\cdot}10^{19}$ eV detected on Earth must come from distances of $d \lesssim 30$ Mpc.

1.2 Gamma-ray astronomy

Gamma-ray (γ-ray) astronomy is the field inside astronomy which deals with photons detected above 0.1 MeV [33]. Until now, the highest energy photons detected surpass 100 TeV. γ-ray photons are produced after the interaction of high energy charged particles (electrons, positrons or nuclei) with electromagnetic fields or interstellar matter [34]. Due to its link to the neutrino production, this is further explained in Section 1.4.

γ-ray photons interact with the nuclei in the atmosphere when they reach the Earth, producing an electromagnetic cascade of particles. Because of this, their direct detection is not possible for ground-based experiments and as such, the first γ-ray telescopes were set in orbit in artificial satellites.

The first observation of a γ-ray source was done by the OSO-3 satellite in 1967-1968 [33, 35], which showed the bright emission of the Milky way. One year later, the US Vela satellites detected the first observed Gamma Ray Bursts (GRBs) [36], although this discovery was not announced to the scientific community until 1973, since the aim of these satellites were

for military purposes. Later experiments showed the first catalogues of γ-ray sources (such as COS-B [37] or EGRET [38]). Currently, the Fermi-LAT observatory monitors the γ-ray sky between the 20 MeV and 300 GeV energy range. The last published catalogue, the 3FGL, contains more than 3000 detected sources [39] (see Figure 1.4). Furthermore, it has led to intriguing discoveries such as the so-called Fermi-bubbles, a gamma-ray emission of $\sim 50^\circ$ above and below the Galactic Centre, with a likely origin from the Galactic Centre, but with a physical emission mechanism not fully understood [40, 41].

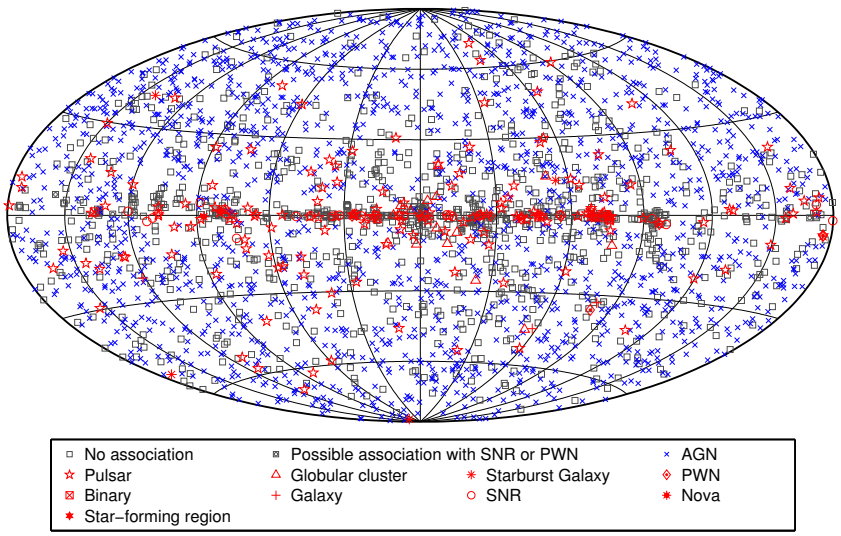

Fig. 1.4.: Location of 3FGL sources in equatorial coordinates. Figure taken from [39].

Satellite-based γ-ray experiments rely on the direct detection of the photons. In the case of Fermi-LAT, the photons are detected after the ionisation of the silicon layers due to the production of e^+e^- pairs, which are produced in the passing of the γ-ray through tungsten converter foils [42]. In order to avoid charged-particle background due to cosmic rays, the detector is surrounded by an anticoincidence detector. The size of satellite-based detectors are limited because of the launcher size, and always fall into effective areas smaller than ~ 1 m^2 [33]. Because of this, and due to the small fluxes expected, ground-based detectors are operated to detect photons with energies above ~ 100 GeV.

Ground-based experiments rely on the detection of the showers produced by the interaction of a γ-ray in the atmosphere. Imaging atmospheric Cherenkov telescopes (IACTs) detect the Cherenkov radiation induced by the charged particles produced in these showers. For this purpose, IACTs experiments use two or more telescopes with large mirrors which include a fast camera on the focal plane. Since the Cherenkov radiation produced is very dim, these telescopes can only operate at moonless nights. Examples of currently operating IACTs are HESS (in Namibia, South Africa) [43], MAGIC (La Palma, Spain) [44] or VERITAS (Southern Arizona, USA) [45]. These telescopes will be superseded by the future Cherenkov Telescope Array (CTA), which will be the largest array of IACT telescopes[46], and will operate in two different sites (one in La Palma, Spain, and another one in Paranal, Chile) [46].

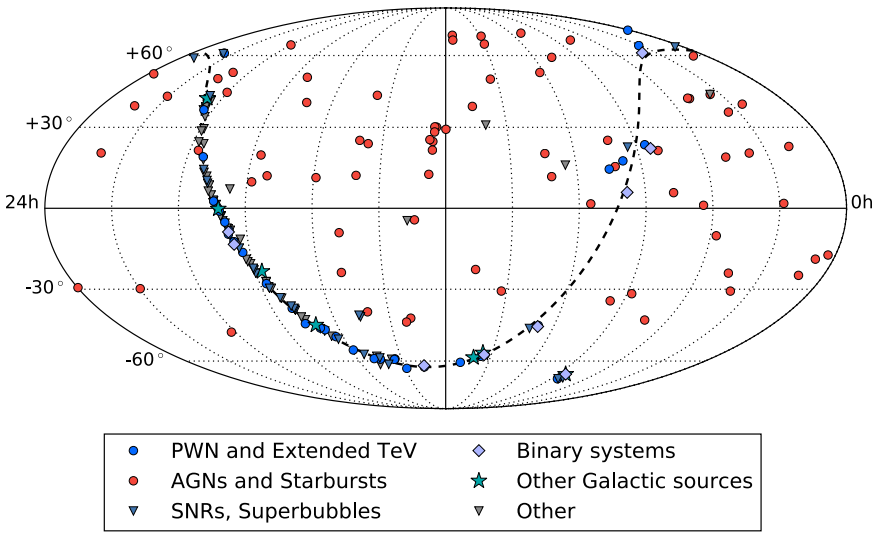

Fig. 1.5.: Currently confirmed sources with photon energies above 0.1 TeV according to the TeVCat in equatorial coordinates.

An alternative to IACTs are the Water Cherenkov Extensive Air Shower arrays (EAS), which directly detect the shower particles by the Cherenkov light they produce inside the detector. They present lower sensitivities and higher energy thresholds compared to IACTs, but in contrast, they

continuously observe the sky above the detector. An example of a currently operating EAS is HAWC, located at a height of 4100 m in Sierra Negra (Mexico) [47]. This detector consists of an array of $\sim$ 300 water tanks of 4 m $\times$ 7.3 m which contain 4 PMTs each so to detect the Cherenkov light of the particles.

Ground-based experiments have produced several discoveries, which are summarised in the TeV catalogue (or TeVCaT) [48]. Figure 1.5 shows the confirmed sources with photon energies above 0.1 TeV, as appeared on TeVCaT on 27/02/2018.

1.3 The neutrino. First results on neutrino astronomy.

Neutrinos are fundamental, neutral and fermionic particles included in the Standard Model of particle physics. Unlike charged leptons or quarks, they can only interact through the weak or gravitational interactions. There are three types (often called *flavours*) of neutrinos, each one corresponding to a charged lepton: electron, muon and tau neutrinos (ν_e, ν_μ, ν_τ).

Neutrinos were first proposed by Pauli in 1930 in order to explain the missing energy observed after the β^- decay of nuclei [49]. In these decays, the kinetic energy spectrum of the outgoing electron present a continuous distribution, which is unexpected for a decay into two bodies.A more formal theory of the β decay was introduced by Enrico Fermi four years later [50], which used similar principles to those of quantum electrodynamics to explain the interaction involved in this decay.

Even if the properties of neutrinos make them almost undetectable, a first unambiguous detection was achieved by Cowan and Reines in the 1950s [51]. In this experiment, tanks filled with water and Cadmium chloride were built to detect the antineutrinos emitted by the Savanah River nuclear reactor. These antineutrinos interact with the hydrogen nuclei of the water molecules, producing a neutron which is afterwards absorbed by the Cadmium nuclei, and a positron which is detected with liquid scintillator detectors after the photon production due to its annihilation with an elec-

tron. After a Cadmium nuclei absorbs the neutron, it decays and produces a gamma ray, which is detected by a set of photomultipliers.

The first experimental result of the existence of more than one neutrino flavour was obtained at the Brookhaven experiment in 1962 [52], in which antineutrinos from π^- decay collided with protons. This interaction always produced antimuons ($\bar{\nu}_\mu + p \rightarrow \mu^+ + n$), but never positrons ($\bar{\nu}_\mu + p \rightarrow e^+ + n$). Tau neutrinos were finally observed by the DONUT Collaboration in 2000 [53].

The unique properties of neutrinos make them ideal messengers to be used for astronomy: since they cannot interact via the electromagnetic or strong interactions, they can cross large distances and large amounts of matter without interacting. This property is, however, its main drawback for their detection. Because of this, only a few detections of neutrinos from outside the Earth have been achieved. The first one corresponds to the solar neutrinos produced in the nuclear reactions inside the Sun (Section 1.3.1). The first detection of neutrinos coming beyond the Solar System occurred in 1987 due to the burst of a supernova in the Large Magellanic Cloud (Section 1.3.2). Indirect measurements of the cosmic neutrino background have been confirmed in the cosmic microwave background, yet individual detection of these neutrinos has not been achieved (Section 1.3.3). The last observation of extraterrestrial neutrinos corresponds to the detection of a high energy cosmic neutrino flux of unknown origin by the IceCube Collaboration, which is further explained with more detail in Section 1.5.

1.3.1 Solar neutrinos and neutrino oscillations

The discovery of nuclear and particle reactions and the development of special relativity permitted to explain the origin of sunlight. The first hints were developed by Eddington in the 1920s [54], who realised that the Sun could release energy after the fusion of hydrogen nuclei into He. The actual mechanism, known as the Standard Solar Model and described by Hans Bethe [55], consists of a chain of nuclear reactions produced after the initial

reaction of protons (the *proton-proton* or *pp* chain). The whole chain can be roughly summarised as [18]:

$$4p \rightarrow {}^{4}He + 2e^{+} + 2\nu_e. \tag{1.10}$$

The neutrinos produced in this equation come from different reactions of the chain. Figure 1.6 shows the neutrino fluxes on Earth due to these reactions.

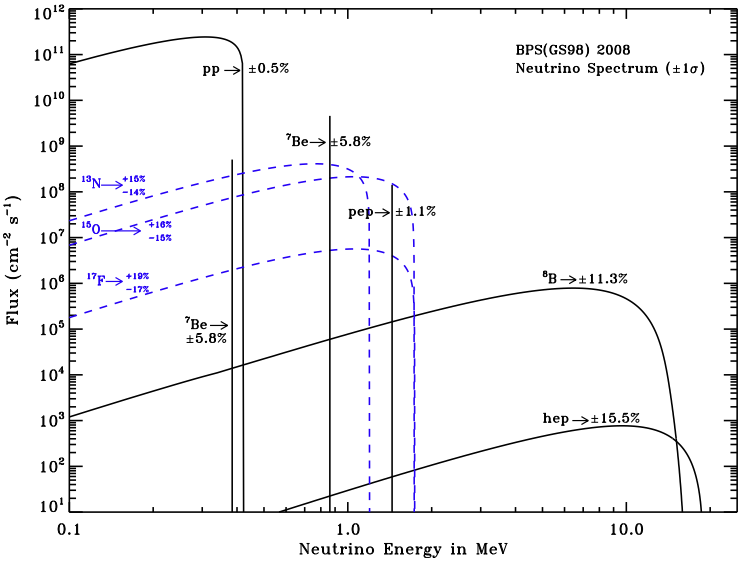

Fig. 1.6.: Flux of neutrinos detected on Earth as a function of the neutrino energy for the different reactions of the pp chain. Figure taken from [18].

The first confirmation of the existence of nuclear reactions in the Sun came from the Homestake experiment [56], in which electron neutrinos coming from the disintegration of ^{8}B produced in the Sun were detected. This underground experiment used tanks of tetrachloroethylene to detect neutrinos via inverse β decay. The ^{37}Cl nuclei present in the tanks could interact with the solar neutrinos, which produced radioactive Argon nuclei (^{37}Ar) and an electron. The detected flux, however, corresponded to ∼34% of the predicted flux. Since these results were replicated by other experiments, either the Standard Solar Model was incomplete, or there was another mechanism involved to explain the lower flux. This disagreement was called “the solar neutrino problem”.

Pontecorvo and Maki, Nakagawa and Sakata (PMNS) [57, 58, 59] developed the theoretical background of the mechanism which would end up explaining the phenomenon. According to this model, the eigenstates of the weak interaction for neutrinos (the *flavour eigenstates*) are different to the ones of the free-particle Hamiltonian (the *mass eigenstates*). In other words, neutrinos are produced as ν_e, ν_μ and ν_τ, but they propagate as the mass eigenstates ν_1, ν_2, ν_3. The flavoured neutrino field can be expressed as a linear combination of the mass fields of the ν_1, ν_2, ν_3 neutrinos as [18],

$$|\nu_l\rangle = \sum_j U_{lj}^{PMNS} |\nu_j\rangle \,, \tag{1.11}$$

where ν_l stands for the eigenstates of the weak interaction, ν_j represents the neutrino mass eigenstates, and U_{lj} corresponds to the matrix elements of the unitary PMNS matrix. The matrix elements can be expressed as a function of the mixing angles, θ_{ij}, the Dirac CP violation phase, δ_{CP} and the Majorana CP violation phases, α_{21} and α_{31}, as

$$U^{PMNS} = \begin{pmatrix} c_{12}c_{23} & s_{12}c_{13} & s_{13}e^{-i\delta} \\ -s_{12}c_{23} - c_{12}s_{23}s_{13}e^{i\delta} & c_{12}c_{23} - s_{12}s_{23}s_{13}e^{i\delta} & s_{23}c_{13} \\ -s_{12}s_{23} - c_{12}c_{23}s_{13}e^{i\delta} & -c_{12}s_{23} - s_{12}c_{23}s_{13}e^{i\delta} & c_{23}c_{13} \end{pmatrix} \times \begin{pmatrix} 1 & 0 & 0 \\ 0 & e^{\frac{i\alpha_{21}}{2}} & 0 \\ 0 & 0 & e^{\frac{i\alpha_{31}}{2}} \end{pmatrix}, \tag{1.12}$$

where $\mathrm{c}_{ij} = \cos\theta_{ij}$, $\mathrm{s}_{ij} = \sin\theta_{ij}$. From this matrix, the probability to detect a given neutrino flavour can be obtained. In vacuum, this probability depends on the neutrino energy, the squared neutrino mass differences, the travelled length and the mixing angles.

The first experimental confirmation of neutrino oscillations came from SuperKamiokande by the detection of atmospheric neutrinos produced after the interaction of cosmic rays with nuclei from the atmosphere [60]. This was later confirmed with further observations of solar neutrinos at SuperKamiokande and SNO [61, 62, 63]. In SuperKamiokande, neutrinos

are detected due to the Cherenkov light produced after the interaction of neutrinos with the hydrogen nuclei present in water. This detection principle allows also the observation of events produced after the interaction of ν_τ and ν_μ, although with a lower probability. As such, the rate between the detected and the predicted flux, assuming all detected neutrinos were ν_e, was of 45.1 $\pm$ 0.5%. The increase compared to the $\sim$35% observed by other experiments only sensitive to ν_e indicated the presence of ν_μ and ν_τ. The SNO experiment used heavy water instead, which could detect the solar neutrinos mainly through two different reactions, $\nu_e + d \rightarrow e^- + p + p$ and $\nu_x + d \rightarrow \nu_x + p + n$. A third possible channel was also possible, $\nu_x + e \rightarrow \nu_x + e$, although with reduced sensitivity for ν_τ and ν_μ. The first reaction showed a similar ratio as observed by experiments which could only measure the ν_e flux, whereas the second one detected the expected amount of neutrinos coming from the Sun.

Several measurements have been performed to obtain the squared neutrino mass differences and the mixing angles, yet there are still unanswered questions regarding neutrino oscillations. The value of the CP violating phase, the possibility of the neutrino to be a Majorana particle (i.e., being its own antiparticle) or the neutrino mass hierarchy are some of them [18]. In this sense, the ORCA detector from KM3NeT and PINGU in IceCube aim to answer whether the neutrino mass hierarchy is *normal* ($m_1 < m_2 < m_3$) or *inverted* ($m_3 < m_1 < m_2$).

1.3.2 Extrasolar neutrinos: SN1987A

On February 23.443 UT [64, 65], the brightest supernova since SN1604 was observed, which resulted in one of the most studied supernovae in human history: SN1987A. This core-collapse supernova was the result of the last stage of the stellar evolution of Sk -69 202, a blue giant star located in the Large Magellanic Cloud (distance of $\sim$ 51 kiloparsecs from Earth). In the same day, although $\approx$3h before the photons from this supernova arrived, a total of 29 neutrino events were observed in three detectors within a time frame of 30s [66]: 16 in Kamiokande II [67, 68], 8 in IMB [69, 70] and 5 in Baksan [71]. Even if the counts of the detected events is small, the background mean rates in each experiment were significantly smaller

(for instance, the significance detection at Kamiokande II was larger than 10σ).

The detection of these neutrinos played a crucial role to give insight on how core collapse supernovae are produced, which corresponds to the final stage of the evolution of stars with masses above $8M_{\odot}$ [65, 72]. According to these models, $\sim$99% of the total energy emitted in the supernova is ejected with neutrinos and antineutrinos in a burst lasting a few tens of seconds. These neutrinos are emitted in different stages due to partial photodisintegration of Fe nuclei, electron capture with free protons in the shock front and neutrino-pair production during the cooling of the proto-neutron star [73].

1.3.3 Cosmic Neutrino Background

Similar reasons to those concluding with the existence of the cosmic microwave background (CMB) predict the cosmic neutrino background (CNB). In the first second after the Big Bang, the reaction $e^+ + e^- \rightarrow \nu_x + \bar{\nu}_x$ was in equilibrium ($T_0 \approx 10^{10}$ K $\approx$ 1 MeV). After that moment, neutrinos decoupled from other particles. These neutrinos are the ones which form the CNB (sometimes also referred as *relic* neutrinos). Currently, the temperature of the neutrinos in the CNB is expected to be of $\approx$ 1.945 K [74], and therefore, their kinetic energy is of the order of meV.

Indirect detection of the CNB has been performed by studying its effects on the CMB using Planck data [75]. The effects on the acoustic oscillations on the CMB due to the gravitational potential of relic neutrinos were inspected, and compared to the situation in absence of this potential. Other indirect evidences of the CNB rely on the primordial abundance of He nuclei [76] and other effects on the CMB [77]. No direct detection has ever been performed, which would be a tremendous challenge due to their extremely low energy and low cross section. The most detailed proposal for a possible detection has been made by PTOLEMY [78].

1.4 High energy neutrino astronomy

The use of high energy neutrinos as cosmic messengers may present important advantages compared to very high energy photons or protons. Due to the interaction with ambient infra-red light and with the CMB, the maximum distance of the Universe which can be seen with photons of energies above 10^{12} eV varies between 200 and 0.03 Mpc (see Figure 1.7-top). This translates into a limitation of 100-1000 Mpc (distant galaxies) at 10^{12} eV or the local group at 10^{15} eV. Protons of very high energies ($\geq 10^{20}$) may only be deflected a few degrees from their original source after the interaction with galactic magnetic fields. However, due to the GZK effect described in Section 1.1.5, the observable Universe with these particles would only reach a distance of $\simeq$30 Mpc. None of these problems arise for high energy neutrinos. Since they only interact weakly, the Universe is effectively transparent to them.

Figure 1.7-bottom summarises the observed and estimated neutrino fluxes as a function of the energy for different sources. The sources described in Section 1.3 correspond to energies in the μeV–meV (Cosmic Neutrino Background) and 1eV–100 MeV (supernovae and solar neutrinos). In this chapter, the proposed mechanisms and sources for the range between 100 GeV and 10 PeV are described.

1.4.1 Hadronic and leptonic models

The regions which accelerate high energy cosmic rays are often hypothesised to yield high energy photons and neutrinos through pion production [19, 80],

$$p + nucleus \rightarrow \pi + X \tag{1.13}$$

$$p + \gamma \rightarrow \Delta^{+} \rightarrow \begin{cases} \pi^{0} + p \\ \pi^{\pm} + n \end{cases} . \tag{1.14}$$

The charged pions would decay producing neutrinos ($\pi^{\pm} \rightarrow \mu^{\pm} + \overset{(-)}{\nu}$, $\mu^{+} \rightarrow e^{+} + \bar{\nu}_{\mu} + \nu_{e}$, $\mu^{-} \rightarrow e^{-} + \nu_{\mu} + \bar{\nu}_{e}$), whereas each neutral pion would produce

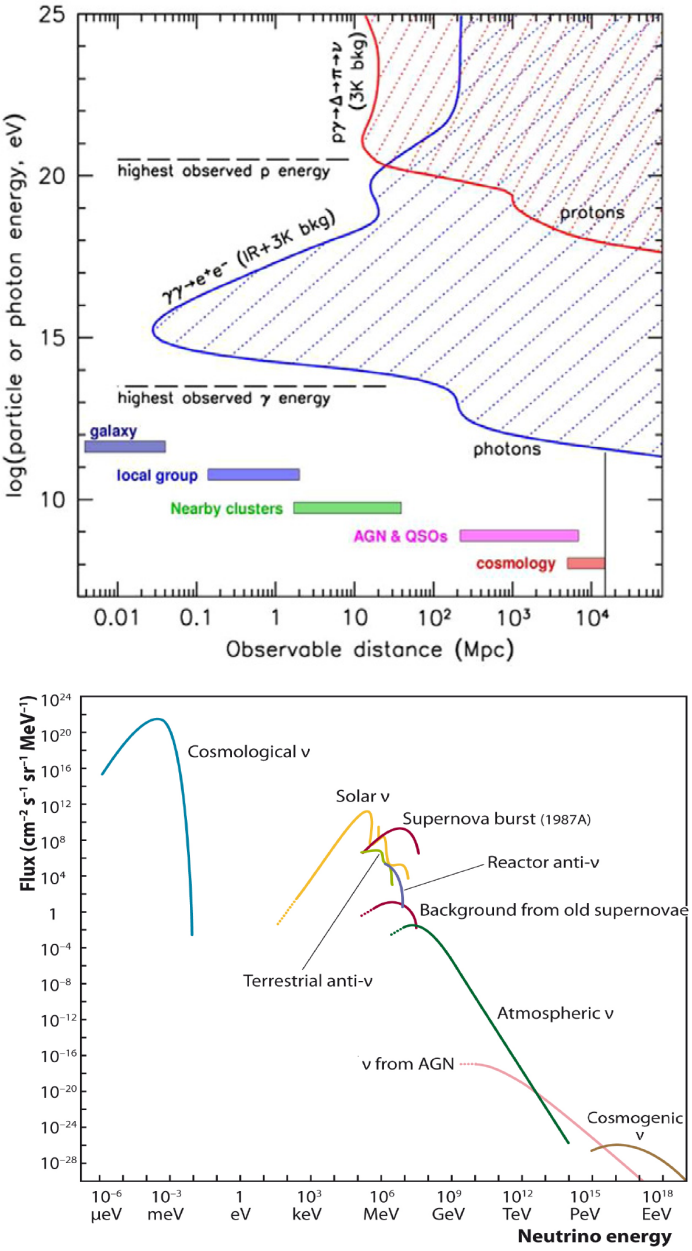

Fig. 1.7.: Top: Absorption length for photons (blue) and protons (red) for different energies. The regions filled with lines correspond to those invisible with the use of photons or protons. Figure taken from [79]. Bottom: Expected fluxes of neutrinos as a function of energy. High energy neutrino astronomy aims for the range between $\approx 10^2$ GeV and ≈ 10 PeV. Figure taken from [80].

a pair of photons ($\pi^0 \rightarrow 2\gamma$). Other mesons (K, η, ...) can be also produced via hadronic collisions and photoproduction ($p + \gamma$ collisions), although this happens in lower rates (10–20%) [81]. In this model, which is often referred as *hadronic model*, it is assumed that the sources present a size which is significantly larger than the proton mean free path, yet smaller than the pion decay length.

According to this explanation, acceleration sites of cosmic rays would also be production sites of high energy γ-rays and neutrinos. The rate of the different neutrino flavours at the production sites are obtained from the charged pion decays, which turns into a ratio of ($\nu_e : \nu_\mu : \nu_\tau$) $\simeq$ (1:2:0). After taking into account the effects due to neutrino oscillations, the expected neutrino flavour rate detected on Earth is approximately (1:1:1) [82, 83]. Some authors have suggested that a different flavour ratio could be produced in the production sites due to energy loss of the muons, (0:1:0), or directly suggest that neutrinos are produced from the decay of neutrons, (1:0:0) [84]. In these cases, a detected flavour ratio on Earth of (0.19:0.43:0.38) and (0.55:0.19:0.26) are expected, respectively.

The hadronic model is not the only one which explains the γ ray production. The *leptonic model* suggests that the source of γ-rays comes after the interaction of stable leptons with electromagnetic fields [33, 34]. Low-energy γ-ray photons can be produced due to the synchrotron radiation produced due to the movement of electrons around a magnetic field. The remaining part of the energy spectrum can be explained from lower energy photons through inverse compton (IC) scattering:

$$e^- + \gamma \rightarrow e^- + \gamma. \tag{1.15}$$

Leptonic models can explain the acceleration of gamma-rays up to energies of 100 TeV, but not higher. Most of the TeV sources observed have been reported to be compatible with these models. However, the leptonic processes are disfavoured to explain the spectrum of a few of them. The FERMI Collaboration reported in 2013 that the spectra of the SNRs IC443 and W44 are better explained with the use of hadronic processes, since the leptonic processes would not be able to explain the measurements for

photon energies below 1 GeV [85]. Multiwavelength studies of the energy spectrum of Tycho's SNR (SNR 1572) and of Cassiopea A suggest hadronic scenarios [86, 87, 88, 89] for these sources, although more complex leptonic scenarios have shown compatible results [90, 91]. More recently, the H.E.S.S. Collaboration reported strong evidence of a PeVatron in the Galactic Centre [92]. Figure 1.8 shows the observed gamma-ray flux, which extends up to tens of TeV without an evidence of a cutoff. Additionally, the positive results from the Auger observatory mentioned in Section 1.1.4 also show regions with likely hadronic acceleration.

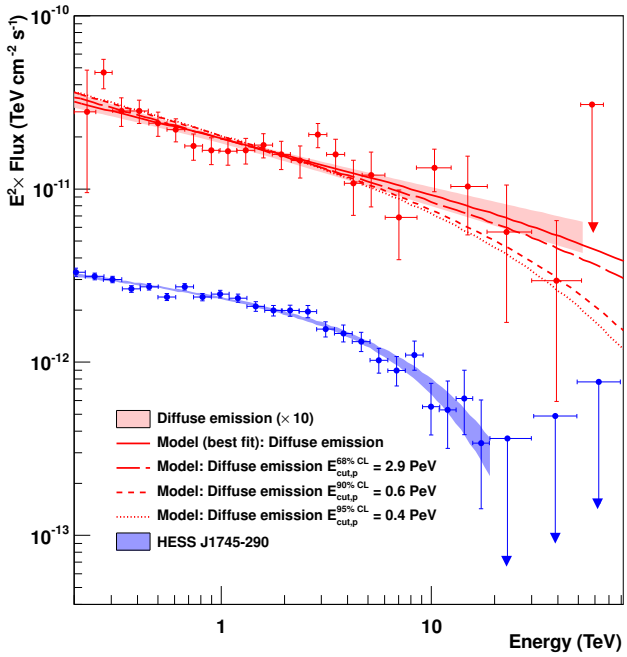

Fig. 1.8.: Observed energy spectrum by H.E.S.S. for the diffuse emission around the Galactic Centre (red) and for the point-source HESSJ1745-290 which could be correlated with SgrA* (blue). Figure taken from [92].

No clear confirmation of further sources with hadronic processes has been obtained. A clear detection of a high energy neutrino source would unambiguously indicate the presence of this process. Several sources have been proposed as such, although the absence of a signal correlated with an astrophysical object has resulted in several upper limits for some of them.

1.4.2 Galactic neutrino source candidates

Shell-type supernova remnants. This type of SNR presents a morphology with an expanding outer-shell which dominates the light emission [93]. The outer shell is formed as the shock-wave from the supernova explosion expands throughout the interstellar medium (ISM) and it heats the material it encounters. This type of SNRs is one of the preferred candidate sources of hadronic acceleration, since they would explain the acceleration of cosmic rays up to the knee (see Section 1.1.3). Apart from the two SNRs already mentioned (IC443 and W44), the SNR RX J1713.7–3946 has been proposed by several authors as a neutrino source candidate [94, 95, 96], since it is the brightest shell-type supernova remnant in the TeV γ–ray sky. Currently, leptonic models can fully explain the spectrum observed by Fermi-LAT and H.E.S.S. for this source [97], although hadronic models with a hard energy spectrum for hadrons can still explain it. Neutrino emission models are usually based on a primary proton spectrum and/or on the observed γ-ray spectrum. The model proposed by Kappes et al. [95] assumes a primary proton spectrum of the form,

$$\frac{dN_p}{dE_p} = k_p \left(\frac{E_p}{1\mathrm{TeV}}\right)^{-\alpha} \exp\left(-\frac{E_p}{\epsilon_p}\right), \tag{1.16}$$

where E_p is the proton energy, ϵ_p represents the energy cutoff (with values between 10 TeV and 1 PeV), α is the spectral index (between 1.8 and 3.0) and k_p is a normalisation constant. A low radiation and matter density, a low magnetic field, and a pion spectrum similar to the one of protons are further assumed. From this spectrum, the neutrino and γ-ray spectrum is transformed into:

$$\frac{dN_{\nu/\gamma}}{dE_{\nu/\gamma}} = k_{\nu/\gamma} \left(\frac{E_{\nu/\gamma}}{1\mathrm{TeV}}\right)^{-\Gamma} \exp\left(-\sqrt{\frac{E_{\nu/\gamma}}{\epsilon_{\nu/\gamma}}}\right). \tag{1.17}$$

A relationship of the k, Γ and ϵ parameters are obtained between the neutrino and the γ-ray spectrum ($k_\nu = (0.71 - 0.16\alpha)k_\gamma$, $\Gamma_\nu \approx \Gamma_\gamma \approx \alpha - 1$, $\epsilon_\nu \approx 0.59\epsilon_\gamma \approx \epsilon_p/40$). The final values for the predicted neutrino flux for

SNR RX J1713.7-3949 are $k_\nu = 15.52 \cdot 10^{-12}$ TeV^{-1}cm^{-2}s^{-1}, $\Gamma_\nu = 1.72$ and $\epsilon_\nu = 1.135$ TeV.

A second model has been recently introduced for KM3NeT neutrino source search estimations based on the methods described by Vissani et al. [96, 98, 99]. By using the last reported H.E.S.S. fluxes [100], the neutrino flux spectrum has been calculated as [101],

$$\frac{dN}{dE_\nu} = 0.895 \times 10^{-14} \left(\frac{E_\nu}{1\mathrm{GeV}}\right)^{-2.06} \exp\left(-\sqrt{\frac{E_\nu}{8.04\mathrm{TeV}}}\right) \mathrm{GeV}^{-1}\mathrm{cm}^{-2}\mathrm{s}^{-1}. \tag{1.18}$$

The Galactic Centre. The Galactic Centre is a region of interest for high-energy neutrino astronomy because of various reasons. First of all, a supermassive black hole is reported to be in the location of SgrA* [102]. Secondly, the region around the centre is known to have a high density of astrophysical objects (shell-type and pulsar wind nebula SNRs, X-ray binaries, etc.). Finally, as it has been mentioned in Section 1.4.1, it is the only known source to produce PeV photons (and therefore, PeV protons) in our Galaxy.

Pulse-wind nebulae. Pulse-wind nebulae (PWNe) are a type of SNRs in which the predominant emission is due to a pulsar located in their centre, and therefore not due to thermal processes [93, 103]. The energy spectrum of the brightest PWNe is well described by leptonic processes (bremsstrahlung up to X-rays, and SSC for γ-rays). The closest PWN is the Crab Nebula, whose photon energy spectrum is fully compatible with a purely leptonic model [104]. Hadronic processes may still happen, although at smaller rates. Another very bright γ-ray PWN is Vela X. Several neutrino emission models have been suggested for this source despite the agreement of the leptonic models with its photon spectrum [105]. In the neutrino models, the γ-ray spectrum is assumed to be fully produced from hadronic origin, and therefore they should be treated as optimistic predictions. The

methods summarised here are the same as for the SNR RX J713.7–3946. The model by Kappes et al. predicts a neutrino energy spectra of the form,

$$\frac{dN}{dE_\nu} = 11.75 \left(\frac{E_{\nu/\gamma}}{1\mathrm{TeV}}\right)^{-0.98} \exp\left(-\sqrt{\frac{E_{\nu/\gamma}}{0.84\mathrm{TeV}}}\right) \mathrm{TeV}^{-1}\mathrm{cm}^{-2}\mathrm{s}^{-1}, \quad (1.19)$$

whereas the derivation considered by the KM3NeT Collaboration for the Letter of Intent [106] using the Vissani et al. prescription is,

$$\frac{dN}{dE_\nu} = 7.2 \times 10^{-15} \left(\frac{E_\nu}{1\mathrm{GeV}}\right)^{-1.36} \exp\left(-\sqrt{\frac{E_\nu}{7\mathrm{TeV}}}\right) \mathrm{GeV}^{-1}\mathrm{cm}^{-2}\mathrm{s}^{-1}. \quad (1.20)$$

X-ray binaries/microquasars. X-ray binaries are binary systems typically formed by a massive object (a neutron star or a black hole of a few solar masses) and a companion object [65]. The more massive object absorbs matter from its companion, which produces an accretion disk. In case a relativistic jet is present, the object is known as microquasar [107].

Most of the energy is released in X-rays due to the synchrotron acceleration, although a γ-ray component is also observed. Due to the γ-ray observations and the possible hadronic scenario, some neutrino emission models have been suggested [108, 109]. So far, no evidences of neutrino emissions have been found either in ANTARES [110, 111] or IceCube [112, 113].

Galactic plane. The interaction of galactic cosmic rays with the ISM has been proposed as an important source of neutrinos. In particular, the large density of dust present in the Galactic Plane has been predicted to produce a signal which could be detected in neutrino telescopes [114, 115, 116]. Recent searches by the ANTARES and IceCube Collaborations have not found this neutrino spectrum, and upper limits on its flux have been set [117, 118].

1.4.3 Extragalactic sources

Gamma-ray bursts. Gamma-ray bursts (GRBs) correspond to the most energetic processes observed in the Universe (energies of $\sim 10^{44-47}$ J) [119]. Their origin is thought to be different depending on their time duration. Those which last a period of minutes are thought to be produced in the late stages of fast rotating stars with masses larger than $30M_{\odot}$, whereas the origin of the shorter ones is due to the merging of two neutron stars, as it was confirmed by the recent observation of gravitational waves GW170817 in coincidence with the γ-ray burst GRB170817A [120]. GRBs were one of the preferred candidate sources of neutrinos. According to the "fireball" models [121], the radiation pressure accelerates a *fireball* at relativistic speeds. Hadrons would lose energy by photo-meson interactions in the shock-waves of the fireball, leading to neutrino production. A high density of photons would be expected, which would end up in a large number of proton-photon interactions. However, the lack of observed neutrinos in the IceCube searches have set stringent fluxes to these models [122]. The recently observed merging of two neutron stars by LIGO, GW170817, did not translate into a neutrino detection in ANTARES or IceCube, yet the observations are compatible with an off-axis angle [123].

Active Galactic Nuclei. Active Galactic Nuclei (AGNs) consist of very luminous cores present at the centre of some galaxies [124, 65]. The brightness is assumed to be produced due to the accretion of matter because of the presence of a supermassive black hole ($M_{BH} > 10^5 M_{\odot}$) in the centre. In this manner, the gravitational energy would be released in the form of photons and other particles. In order to be classified as an AGN, the bolometric luminosity must be $\mathcal{L}_{bol}/\mathcal{L}_{Edd} \geq 10^{-5}$, where $\mathcal{L}_{Edd} \approx 1.5 \times 10^{31} W(M/M_{\odot})$ is the luminosity of a source in hydrostatic equilibrium (Eddington luminosity). A common classification of AGNs is done according to the strength of its radio signal [125]. Radio-loud AGNs present a radio flux at 5 GHz ten times larger than in the optical B-band. Otherwise, they are classified as radio-quiet. They are also usually classified depending on its orientation with respect to the observer. Figure 1.9 shows a scheme of this classification.

Blazars are a particularly interesting type of AGNs for neutrino detection. They consist of AGNs which have a jet pointing towards the observer ($\theta \leq$

12°), and therefore present higher fluxes. They tend to produce a two-bump flux spectrum. The radio to X-ray flux is thought to be produced by synchrotron acceleration. For higher energies, both leptonic [126, 127, 128] and hadronic [128] models have been used to fit the photon spectral energy distribution of blazars observed by FERMI.

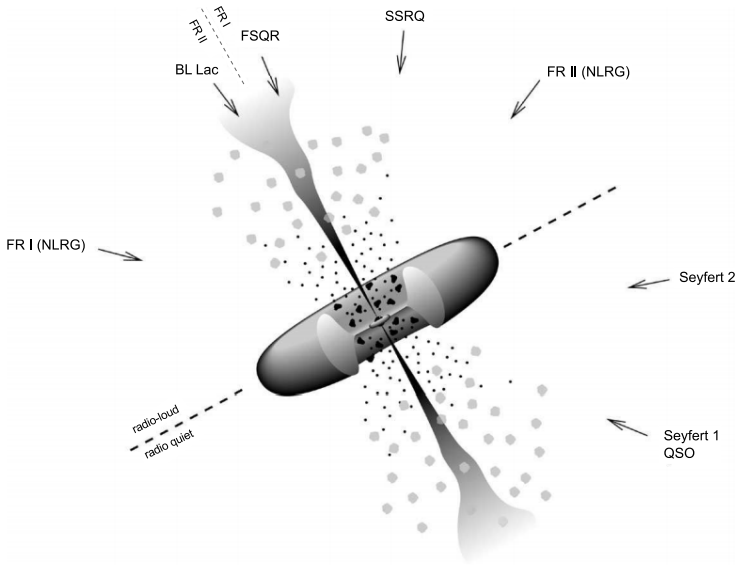

Fig. 1.9.: Classification of AGNs depending on the strength of its radio signal and the orientation with respect to the observer. Figure taken from [23].

1.5 The IceCube high energy neutrino flux

The IceCube Collaboration reported in 2013 the first evidence of a high energy neutrino flux [2]. This analysis considered only events with an interaction vertex inside the detector volume. Experimentally, this means that the first photons are detected by PMTs in the inner part of the detector. In other words, the first photons detected from a given event could not come from the outer layers of the detector (see Figure 1.10 for the volume defined for this analysis, and section 2.3 for a description of the IceCube detector). Furthermore, a minimum total detected charge of 6000 photoelectrons from all the photomultipliers was required per each event to ensure a selection of high energy events. These conditions reduce drastically the background

of atmospheric events (which have typically lower energies), and limit the sample to neutrino events above $\sim$ 10 TeV. A total of 28 events were observed in this first search (livetime of 662 days), in which only $10.6^{+5.0}_{-3.6}$ atmospheric events (neutrinos and atmospheric muons) were expected. This led to a significance of the order of 4σ.

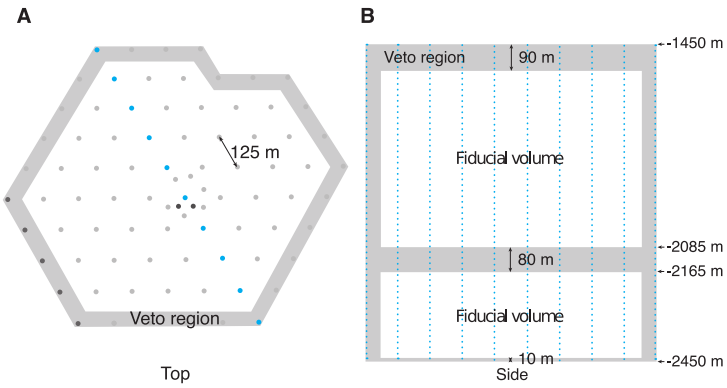

Fig. 1.10.: Scheme of the veto region defined for the High Energy Starting Events sample. Figure taken from [2].

This analysis has been updated several times with extended livetimes [3, 4, 5], each one increasing the significance of a flux compatible with an astrophysical origin. The last analysis (livetime of 2078 days) includes 82 events with an expected background of 25.2 ± 7.3 atmospheric muons and $15.6^{+11.4}_{-3.9}$ atmospheric neutrinos. Figure 1.11 shows the distribution of events from the most recent High Energy Starting Events (HESE) sample.

Several analyses inside and outside the IceCube Collaboration have attempted to establish or constrain the origin of these events. In the first analysis, a non statistically significant, yet intriguing accumulation of events was observed near the Galactic Centre at (α, δ) = (–79°, –23°). Some authors proposed they could originate from a point or an extended source in the region [129]. This hypothesis was further discouraged after the 2007-2012 point and extended source search using ANTARES data [130]. A specific search in a cone of 20° around the centre of the hypothetical source was performed, although no significant cluster was observed. The 90% CL upper limits, shown in Figure 1.12, discarded with >90% CL several point and extended source hypotheses for an E^{-2} energy spectrum. More

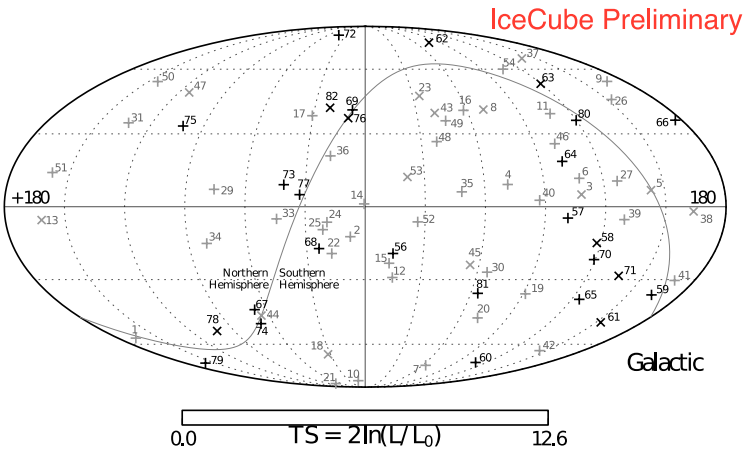

Fig. 1.11.: Event distribution of the High Energy Starting Events sample in galactic coordinates. Figure taken from [5].

stringent limits around this region are set in the last point and extended source analysis using ANTARES data, and are described in Section 6.2.

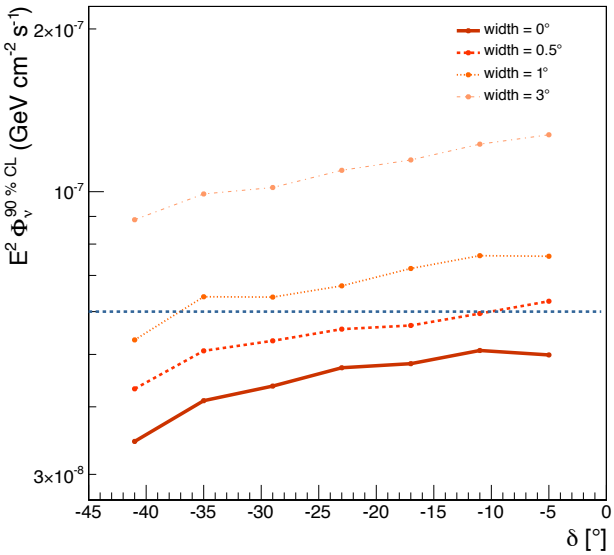

Fig. 1.12.: Limits imposed for an E^{-2} neutrino source with the use of ANTARES data between 2007 and 2012 as a function of the declination of the source [130]. The horizontal line corresponds to the source flux proposed in [129].

The significance of this hypothetical cluster has decreased in the following updates of the HESE sample, and no other significant accumulation of events has been observed. The poor angular resolution for cascade events (10°–20°), which correspond to ∼80% of the HESE events, may partially explain the absence of an observed preferred direction (see Section 2.1 for a description of the event signatures that can be observed in neutrino telescopes).

Additional IceCube searches with different methodologies have reported an astrophysical flux. The 8-year muon neutrino diffuse flux search [131], the 4-year search using neutrino-induced cascades [132] and the starting event sample with events above 1 TeV [133] are some recent examples. None of them have shown an evidence of a preferred sky location. Even if the angular resolution for the muon neutrino diffuse flux search is of the order of 1°, the small amount of statistics may still be covering the possibility of a point or extended neutrino source. The ANTARES telescope cannot claim to have observed this flux, but a "mild excess" with a significance of 1.6σ was reported in the last search for diffuse fluxes, and with physical properties similar to those reported by IceCube.

The origin of this flux still remains a mystery. The search over the 2nd year Fermi-LAT catalogue using IceCube data sets a maximum contribution of 27% to the astrophysical flux from these blazars [134]. The ANTARES and IceCube searches around the Galactic Plane have not found any significant evidence, and have set a maximum contribution of a Galactic Plane flux at the level of ∼15% of the total HESE flux. The lack of observations of neutrinos coming from GRBs [122] limits the contribution of these sources at the level of $<1\%$. The observed isotropy of the flux makes it compatible with an all-sky flux, which may lead to an extragalactic origin, although the poor angular resolution for most of the events and the low amount of statistics still makes some room for a subdominant galactic component.

The only physical information available about this flux corresponds to the energy spectrum and flavour ratio calculations done by the different IceCube searches. In the last HESE search [5], the unbroken power-law fit showed a neutrino energy spectrum with a best-fit value of $\gamma = 2.9$, although with a considerably large error bar. The result from the muon-neutrino diffuse

flux search presents the best fit, in which a value of $\gamma = 2.19$ is observed for an unbroken power-law fit, and an energy cutoff of $\sim$ 4 PeV is needed for a spectrum of the form $\propto exp(-E_\nu/E_{cut})E^{-2.0}$.

Measurements of the flavour ratio of this high energy neutrino flux have been carried out in different analyses [135, 136, 137]. The last published IceCube flavour ratio results used data from six different searches by employing a binned Poisson-likelihood method. As can be seen in Figure 1.13, the $(\nu_e{:}\nu_\mu{:}\nu_\tau)$ = (1:2:0) ratio expected from the pion decay hadronic model is compatible with the data within a 68% confidence region.

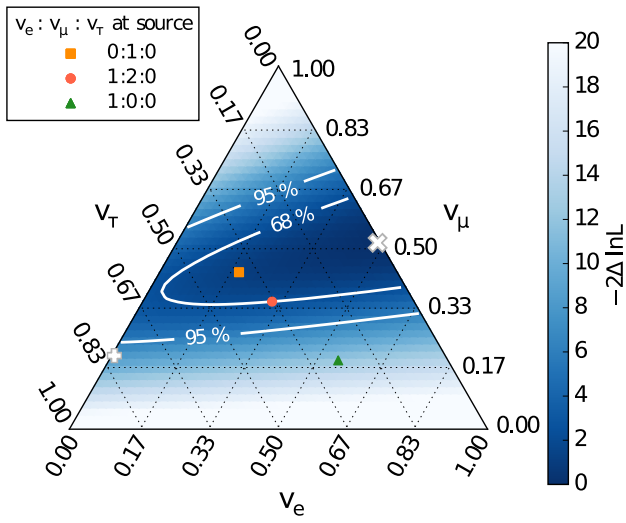

Fig. 1.13.: Flavour ratio composition as measured from maximum likelihood search using six different samples. The three most likely hadronic scenarios are marked with a square (0:1:0), circle (1:2:0) and triangle (1:0:0). Figure taken from [137].

2

Neutrino telescopes. Detection principles and description.

> *We propose setting up apparatus in an underground lake or deep in the ocean in order to separate charged particle directions by Cherenkov radiation*
>
> **— M. A. Markov**
> On high energy neutrino physics, ICHEP60 (1960)

In this chapter, a description of the neutrino telescopes which are currently in operation is presented. Neutrino telescopes consist of an array of photomultiplier tubes (PMTs) laid in a large volume of a natural and transparent medium (ice or water), which detect the Cherenkov light produced after a neutrino interaction. This idea was first attributed to Moisey A. Markov in 1960 [138].

The first attempts to build a neutrino telescope correspond to the DUMAND project [139], which was initially aimed to be a 1 km^3 volume detector in Hawai, but it was cancelled due to the lack of funds and different technical problems. The first atmospheric muons measured by a neutrino telescope were detected with a prototype string of the Baikal neutrino telescope [140], located in Lake Baikal (Russia). Afterwards, the AMANDA detector [141] was installed between 1996 and 2000 at the South Pole. AMANDA served as a prototype of the IceCube detector [142], which is currently the largest neutrino telescope in operation. The largest neutrino telescope in the Northern Hemisphere is ANTARES [143], which has been in a continuous and steady operation since 2007. Like AMANDA, ANTARES has been the prototype of a larger project, KM3NeT [106], which aims to build the

largest network of neutrino telescopes in the Mediterranean Sea and it may probably become the flagship of neutrino astronomy in the near future.

The detection principles of neutrino telescopes are introduced in section 2.1, while sections 2.2, 2.3, 2.4 and 2.5 describe the ANTARES, IceCube, KM3NeT and Baikal/GVD experiments, respectively.

2.1 Detection principle of neutrino telescopes

Neutrinos can only be detected through the weak interaction, via neutral current (NC) or charged current (CC) interactions, depending on the force carrier. These interactions can be described as

$$\textbf{NC: } \nu_l + N \xrightarrow{Z^0} \nu_l + X, \tag{2.1}$$

$$\textbf{CC: } \nu_l + N \xrightarrow{W^{\pm}} l + X, \tag{2.2}$$

where l denotes a lepton, N is the target nucleus and X indicates a hadronic cascade. The cross sections for these interactions can be seen in Figure 2.1, which have been obtained by using the CTEQ6 parton distributions [144, 145]. The cross section for CC interactions is a factor $\sim$3 larger than in NC interactions. An asymmetry on the neutrino and antineutrino cross sections is also observed for energies under 10^5 GeV. The peak observed at energies between 10^6–10^7 GeV corresponds to the Glashow resonance. This latter reaction occurs when an electron antineutrino with an energy of $\sim$ 6 PeV interacts with an electron to produce a W^- boson:

$$\bar{\nu_e} + e^- \rightarrow W^-. \tag{2.3}$$

Different signatures can be distinguished depending on the type of interaction (CC, NC or Glashow resonance), the neutrino flavour involved (ν_e, ν_μ or ν_τ), the possible decay of an outgoing lepton and the part of the interaction which is observed in the detector. A summary of all possible signatures can be seen in Figure 2.2, and a brief description is given below [147].

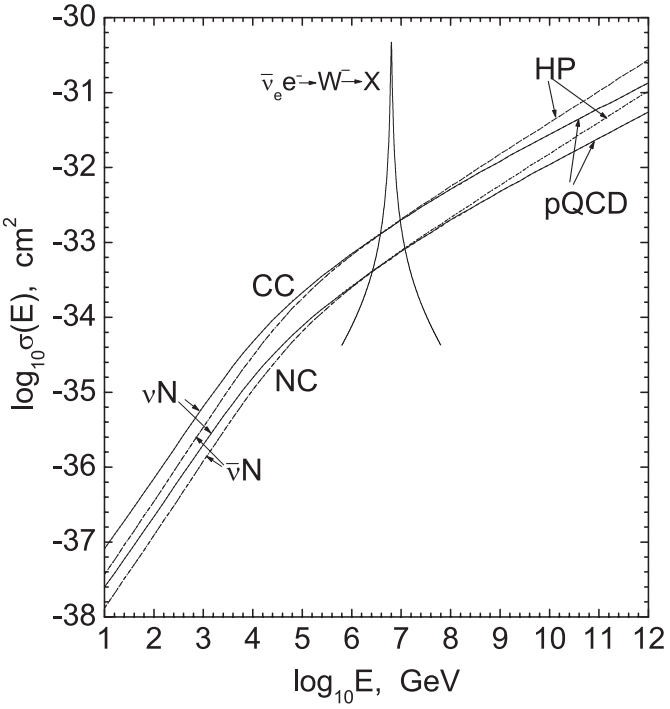

Fig. 2.1.: Cross sections for neutrino-matter interactions according to the CTEQ6-parton distributions. At energies above 10^6 GeV, different extrapolations are performed depending on the model (pQCD or HP). Figure taken from [146].

Neutrinos interacting through NC. In a NC interaction, a large fraction of the energy is transferred to the outgoing neutrino, and only a fraction is transferred to the nucleus. Because of this, it is not possible to obtain the total energy of the incoming neutrino, but just the deposited energy. This remaining energy is seen as a hadronic cascade. The event signature produced in these interactions is often referred to as *shower* or *cascade*.

Muon neutrinos interacting through CC. In this case, a hadronic cascade and an outgoing muon are produced. Since the muon moves at a relativistic speed, it can travel up to several kilometers before decaying (2.2 μs). This muon polarises the atoms and molecules in the media, producing Cherenkov radiation (see Section 2.1.1). The average angular distance between the

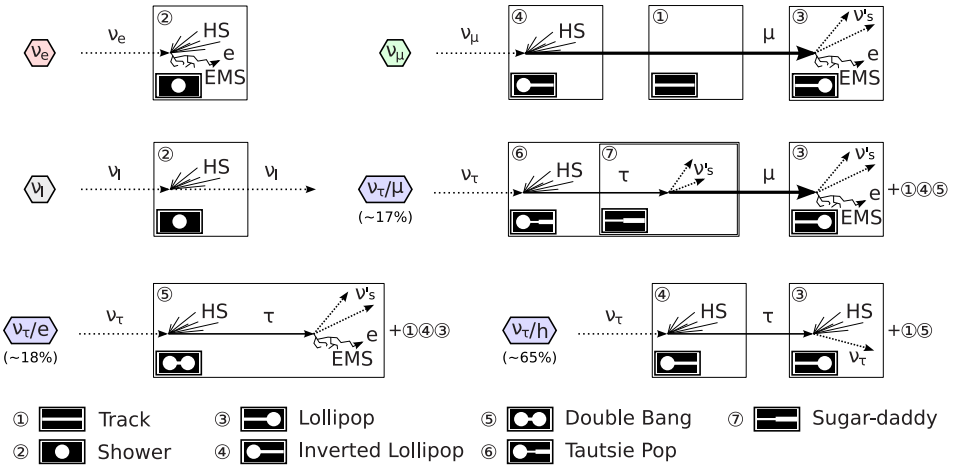

Fig. 2.2.: Types of events observed in neutrino telescopes depending on the type of interaction, incoming neutrino flavour and part of the interaction which is observed. HS denotes hadronic shower and EMS, electromagnetic shower. Figure obtained from [148].

incoming neutrino and the outgoing muon, $< \alpha_{\nu\mu} >$, can be expressed as [147]

$$< \alpha_{\nu\mu} >= \frac{0.6^\circ}{\sqrt{E_\nu / 1\,\mathrm{TeV}}}, \tag{2.4}$$

where E_ν is the energy of the incoming neutrino. For energies above 10 TeV, the median angular distance is smaller than 0.2°. Since the outgoing muon is almost collinear with the incoming neutrino, the reconstruction of the muon gives an estimate of the direction of the original neutrino.

Usually, only the Cherenkov light produced after the interaction is detected. This event signature is often referred to as *track*. When the muon decay or the neutrino interaction is observed inside the detector volume, the event signature is called *lollipop* or *inverted lollipop*, respectively. In both cases, a cascade and a track can be identified.

Electron neutrinos through CC with nucleons. An electron is produced after the neutrino interaction. In this case, two types of showers can be seen at the interaction vertex. On one hand, a hadronic cascade is produced from the "break-up" of the nucleon. On the other hand, an electromagnetic shower is produced due to the interaction of the outgoing electron with

matter via bremsstrahlung and pair production. Since both cascades are produced in the same interaction vertex, it is not possible to distinguish between them. As in NC interactions, a shower or cascade event type is observed.

Glashow resonance. A W^- boson is produced after the interaction of an electron anti-neutrino with an electron. The W^- then decays into hadrons in $\sim$2/3 of the times, whereas it produces a $\bar{\nu}_l\, l^-$ pair in the other $\sim$1/3 of the times.

Tau neutrinos through CC. A hadronic cascade and a τ lepton are produced in the interaction vertex. Due to the different decays of the τ particle, different topologies can be seen at the decay vertex. There is a 65% chance that a τ decays into pions and kaons, producing a hadronic cascade. On the other hand, there is a 35% chance of decaying into a lepton (electron or muon) with equal probabilities. In the cases in which the tau decays into hadrons or into an electron, a second cascade due to the τ decay is observed. The short lifetime of the tau ($2.906{\cdot}10^{-13}$ s) makes it impossible to distinguish both cascades for energies under $\sim$2 PeV. Both cascades can be observed at the short energy range between $\sim$2 and $\sim$20 PeV, leading to the *double-bang* pattern [149]. At larger energies, the length of the tau path is larger than the scale of km^3 neutrino telescopes, and therefore only a cascade and a track signature (*lollipop*) are observed.

2.1.1 Cherenkov radiation

The detection of the particles produced after a neutrino interaction is possible due to the Cherenkov radiation. This radiation is emitted when a charged particle crosses a transparent medium at a speed higher than the group velocity of light in this medium. The charged particle polarises the molecules and atoms of the media, which turn back to equilibrium once the particle has passed. If the particle crosses at a speed larger than the group velocity, the light due to the depolarisation is emitted in a coherent front, as seen in Figure 2.3. This coherent front forms a cone with an angle with respect to the lepton track (θ_C) given by

$$cos\theta_C = \frac{1}{\beta n}, \tag{2.5}$$

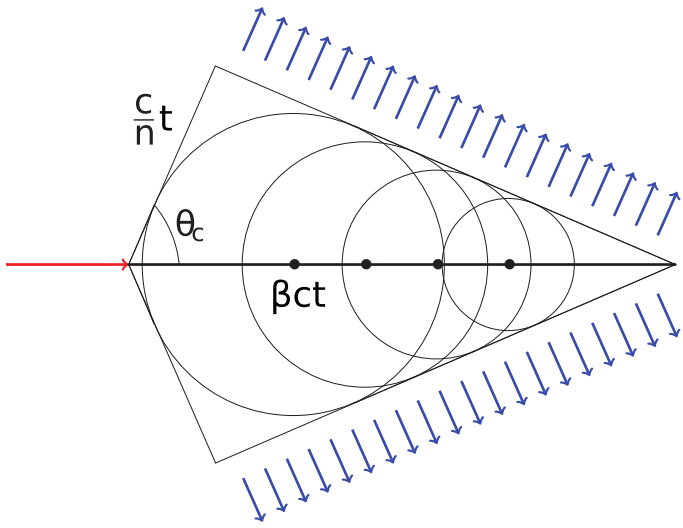

Fig. 2.3.: Scheme of the wavefront created through Cherenkov radiation. Figure obtained from [150].

where β is the ratio between the lepton velocity and the speed of light in vacuum, and n is the refractive index of water. The Cherenkov cone angle is of 43-46° in water, and 40° in ice.

The expected amount of photons emitted per unit of length, x, and wavelength, λ, can be expressed as

$$\frac{d^2N}{d\lambda dx} = \frac{2\pi\alpha Z^2}{\lambda^2}\left(1 - \frac{1}{\beta^2 n^2}\right), \tag{2.6}$$

where α is the fine-structure constant and Z is the charge of the particle. From this formula, it can be seen that the intensity of Cherenkov light is larger in the blue and UV range. Therefore, PMTs which are sensitive to these wavelengths are used in neutrino telescopes.

2.1.2 Physical backgrounds

Cosmic rays interact with nuclei present in the upper layers of the atmosphere, giving place to, amongst other particles, muons and neutrinos. These are the two main sources of physical background in neutrino telescopes.

Neutrino telescopes are placed at large depths to reduce the background of atmospheric muons. However, these particles can reach up to several kilometres deep in water. In the analyses which deal with muon neutrino events, atmospheric muons can be rejected by requiring an upward direction for the reconstructed events, since only neutrinos can cross the Earth without interacting. Nevertheless, atmospheric muons may be wrongly reconstructed as up-going, and then, additional conditions on the reconstruction are needed. The signature of shower-like events is different from that of atmospheric muons. It is therefore possible to consider down-going shower events in some analyses, while reducing at the same time the background of atmospheric muons.

Atmospheric neutrinos can cross the Earth without interacting, so they constitute an irreducible background which complicates the signal detection from cosmic sources. This detection can be performed in different manners depending on the analysis. Since the atmospheric neutrinos are distributed isotropically over the sky, accumulation of events into clusters are expected for point and extended cosmic neutrino sources. In the case of a diffuse cosmic neutrino flux from unresolved sources, cosmic neutrinos have a harder energy spectrum than atmospheric neutrinos [131, 151]. Additional procedures, such as the use of multivariate classifiers or event containment have been followed in some analyses [2, 106].

2.2 The ANTARES neutrino telescope

ANTARES [143] is the first neutrino telescope which operates in the sea, and it is currently the largest in the Northern Hemisphere. It is located at coordinates (42° 48' N, 6° 10' E), 40 km south of the coast of Toulon (France). It constists of an array of 885 PMTs distributed in 12 lines (or strings) at a depth of 2475 m. It also contains an instrumentation line (IL) with several sensors to study environmental conditions. The first line was deployed in 2006 and the detector was completed in May 2008. Figure 2.4 shows a scheme of the ANTARES detector.

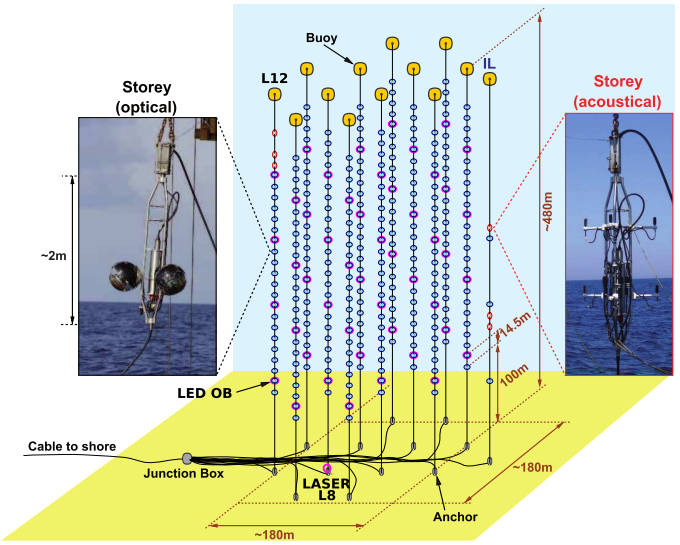

Fig. 2.4.: Scheme of the ANTARES detector. The two types of storeys are shown. Figure obtained from [148].

2.2.1 The Optical Module

The Optical Module (OM) [152] is the most basic element of the ANTARES telescope. It consists of a glass (borosilicate) sphere of 17 in diameter and a thickness of 15 mm which contains a Hammamatsu R7081-20 PMT of 10" (see Figure 2.5). This sphere has been designed to withstand up to 260 atm in order to resist the large pressures at the sea depth. A gel of 1.4 refractive index is used to fill the space between the PMT and the glass sphere. A magnetic μ-metal cage shield to avoid the effects of the Earth's magnetic

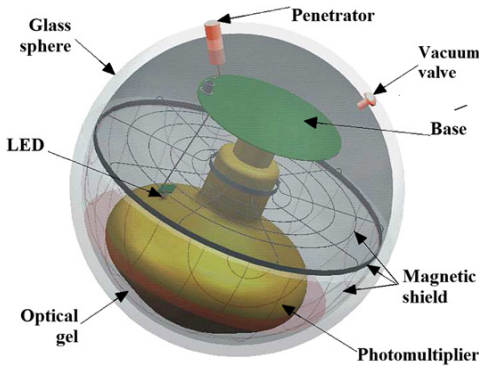

Fig. 2.5.: An ANTARES Optical Module. Figure obtained from [152].

field is located surrounding the PMT. The rear hemisphere of the OM is painted in black in order to avoid inner light reflections.

The Hammamatsu PMT model was selected after detailed comparison studies with other models during the R&D phase [153]. This model can detect photons from 300 nm to 600 nm with a Transit Time Spread (TTS) under 3 ns (FWHM) and a quantum efficiency of ∼25% for a 400 nm wavelength.

2.2.2 Storey

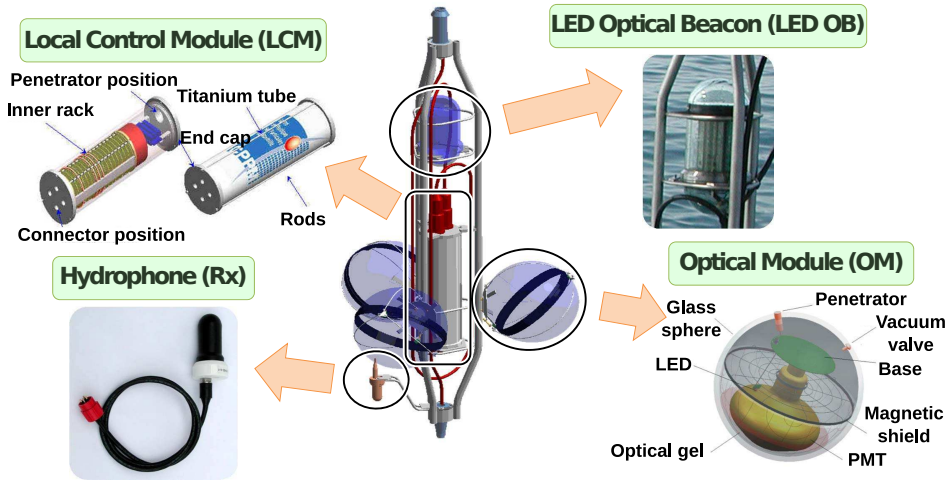

Fig. 2.6.: Scheme of a storey in the ANTARES telescope. All storeys consist of a titanium structure which contains 3 OMs facing downwards. Four storeys in each line contain a LED Optical Beacon, and five in each line contain a hydrophone.

A storey is a titanium structure that holds three OMs which face 45° downwards (see Figure 2.6 for a representation of a storey). This structure also sustains a local control module (LCM) located at the centre, which consists of a titanium cylinder that includes the electronics to control the equipment of the storey. Depending on the floor where the storey is located, additional equipment can be found. A Rx hydrophone is located every 5 storeys in each line in order to produce the acoustic positioning of the detector. LED Optical Beacons are also found in 4 storeys of each line (except in line 12, where one is missing since there is an acoustic sector), which are used for time calibration and for the monitoring of the water optical properties.

The electronic commands, the clock signal, the slow control, the HV suply and the readout are sent to the OMs via the electronics contained in the LCM. Each OM is linked to two Analogue Ring Samplers (ARSs) located in the LCM, which digitize the signal produced in the OM and provides its time and amplitude.

2.2.3 Line

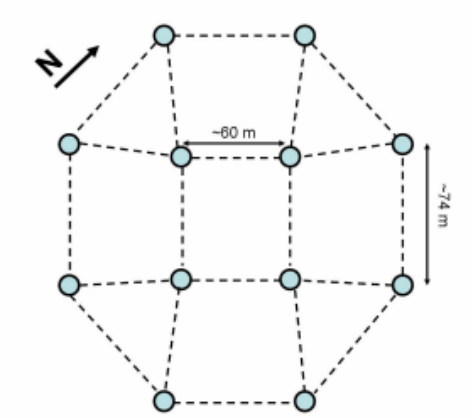

Fig. 2.7.: The 12 lines of ANTARES are configured on an octagonal layout with distances between lines of 60 to 75 m.

ANTARES consists of 12 detection lines and an instrumentation line which holds equipment for environment research. The 12 detection lines are placed on an octagonal layout with inter-line distances between 60 and 75 m (see Figure 2.7). They are kept vertical with a buoy on its top and they are anchored to the seabed by the weight of the Bottom String Socket (BSS), which is made of a titanium structure. Each detection line contains 25 storeys (except line 12, which has only 20) with a separation of 14.5 m between storeys, and a total height of 450 m. In each line, storeys are grouped in 5 sectors (4 in line 12). Each sector is controlled by a Master Local Control Module (MLCM), which holds both the LCM electronics and an Ethernet switch which receives data from all the LCMs of its corresponding sector.

A String Power Module (SPM) located in the BSS provides the power needed for the whole string, while the String Control Module (SCM) contains the electronics for the data transfer between the string and the the Junction Box (JB) with an electro-optical interlink cable. This JB serves as a connection between the strings and the shore station. In addition, a Laser Beacon is located on the bottom of lines 7 and 8 for time calibration purposes.

Connection with the shore station

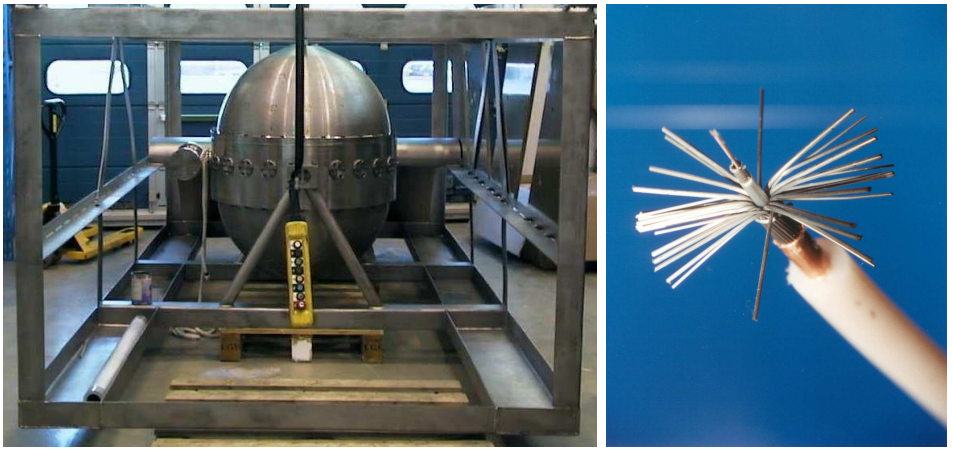

Fig. 2.8.: Left: Picture of the Junction Box before being deployed. Right: Section of the MEOC, which connects the shore station with the JB.

The Main Electro-Optical Cable (MEOC) connects the shore station with the JB. It consists of a 42 km long and 58 mm diameter cable made of 48 mono-mode pure silica optical fibres. The JB provides the power supply to the detector. It is also responsible of the data transfer and the commands between the shore station and the strings. Figure 2.8 shows a picture of the JB and a section of the MEOC.

2.2.4 Data Acquisition System

The aim of the Data Acquisition System (DAQ) [152] is to convert the signal from the PMTs to readable information for the analysis (see Figure 2.9). The ANTARES DAQ system follows the “all-data-to-shore” strategy, in which all the information recorded is transferred to the shore station, where it is processed, filtered and stored. The DAQ begins with the digitisation of

the time and the integrated charge of the PMT signals, which is done by the ARS chips in the LCMs. The combined information of the time and integrated charge corresponds to a single *hit*. A charge threshold above 0.3 photoelectrons (pe) is set in order to reduce the dark current noise of the PMT (L0 threshold). The charge integration is performed with an Analog-to-Voltage Converter (AVC), which integrates the charge collected within 35 ns. Considering that each AVC contains 256 channels, the charge in photoelectrons can be expressed as:

$$Q_{pe} = \frac{AVC - AVC_{0pe}}{AVC_{1pe} - AVC_{0pe}}, \tag{2.7}$$

where AVC_{0pe} corresponds to the lowest working channel and AVC_{1pe} the channel for a mean charge of 1 pe.

Additionally, the time information is obtained with the use of an internal clock and two time-to-voltage converters (TVCs) present in each ARS. The internal clock produces a clock pulse every 50 ns. If the L0 threshold is surpassed, a Time-Stamp (TS) value is generated according to this clock signal. Every TVC contains a 8-bit ADC which divides each clock phase into 256 channels, leading to a precision of about 200 ps. As a consequence, the time recorded from a TVC is obtained as

$$t(ns) = 50 \times \frac{TVC - TVC_{min}}{TVC_{max} - TVC_{min}}. \tag{2.8}$$

After the integration time is performed, the ARS has a dead time of 200 ns. In order to reduce this dead time, two ARS are assigned to a single PMT, working on a token ring configuration.

Apart from the Single Photo-Electron (SPE) mode, the ARS can work in the WaveForm (WF) mode, which is used for complex calibration purposes. In this case, a 150 MHz - 1 GHz sample shape of the pulse can be obtained.

The information collected by each LCM is sent to its corresponding MLCM via an Ethernet link. From the MLCM, this information is transferred to the SCMs, which send it to the JB via a 1 Gb/s connection. A Dense Wavelength Division Multiplexing (DWDM) technique is used to transfer the data from the JB to the shore station. This station contains a farm of PCs to filter and

store the data. It also contains the master clock generator, which sends a 20 MHz clock signal to the ARS chips. The signal is synchronised to the GPS time within 100 ns accuracy.

Triggers and data filtering

Different types of triggers can be applied to the data depending on the desired analysis [154]. The most relevant are summarised in Table 2.1.

The L0 threshold can be triggered by photons produced from ^{40}K decay or bioluminescence. In order to limit this background, some of the ANTARES triggers require hit coincidences on the same storey within a time window of $20\,\mathrm{ns}$ or hits exceeding $3\,\mathrm{pe}$. This is known as *L1 trigger*.

The standard or general purpose muon trigger uses the causality relation between two hits [143],

$$|t_i - t_j| \leq r_{ij}\frac{n}{c}, \tag{2.9}$$

where t_i and t_j are the time of two hits, r_{ij} is the distance between them, n is the refraction index in water, and c is the speed of light in vacuum. In order to be taken into consideration, at least five L1 triggers must fulfil this requirement. The *3N trigger* goes one step further [155]. Once the standard trigger is obtained, it checks causality relations considering 210 directions isotropically distributed in all sky. If five or more L1 triggers still fulfil at least one of the considered directions, the event is recorded with this trigger. This trigger is dominated by the background of atmospheric muons, with a typical rate between 5 to 10 Hz.

The *T3 trigger* [156] is aimed for events of lower energies compared to the 3N trigger. In this case, at least two coincidence L1 clusters within a time windows of 100 ns, or 200 ns for next-to-adjacent storeys are required. The *2T3* trigger is more commonly used in ANTARES analyses, which requires two T3 triggers between 2.2 μs in the whole detector with at least three L1 triggers in the same line, or four in the whole detector.

The point and extended source search analyses carried out in this Thesis with ANTARES data, only consider events recorded with the 2T3 and 3N

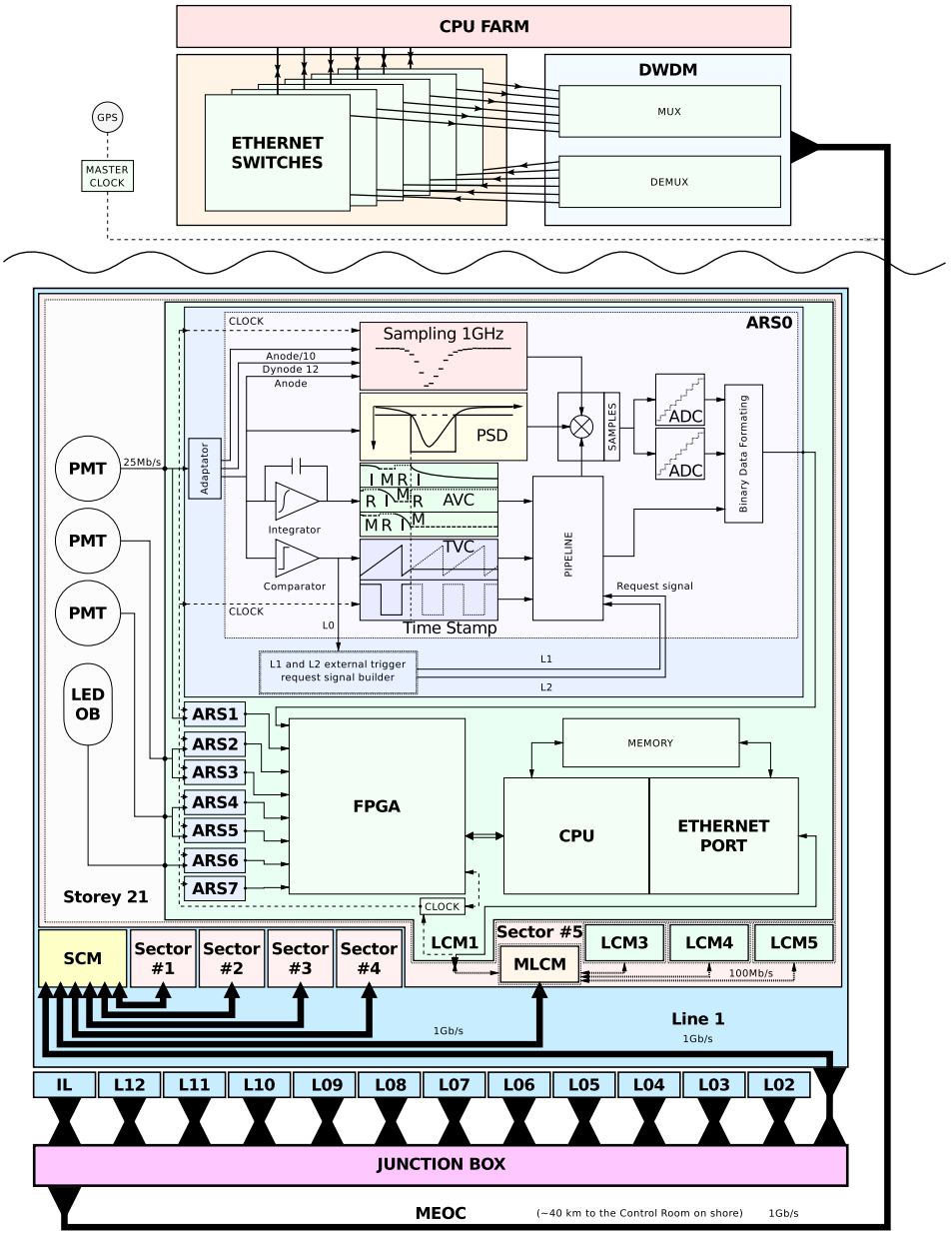

Fig. 2.9.: An example of the DAQ for storey 21 in line 1. The PMT signal is sent to one of its two ARS. The FPGA in the LCM sends the information through an Ethernet port to the MCLM. This is afterwards sent to the SCMs, which is connected to the JB. The JB distributes the signals and commands between the lines and the MEOC that connects the JB to the shore station. A CPU farm in the shore station filters and stores the data. Figure from [148].

triggers. Further triggers have been used in other analyses, such as the *TQ trigger*. The TQ trigger works similarly to 3N, but it considers only events pointing to an upward direction with at least two L1 triggers and four additional L0 hits.

Other triggers not directly focused on neutrino events are defined, such as the *K40* and *OB triggers*. The K40 trigger [157] considers coincidences of two L0 hits between two OMs in the same storey within 20 ns. These are mainly produced after the decay of ^{40}K nuclei. Moreover, the OB trigger is considered for the photons emitted from the LED Optical Beacons (see Section 4.1.2) for time calibration purposes.

Tab. 2.1.: Summary of the triggers used in ANTARES.

Trigger	Description
3N	5 L1 hits in at least one of the 210 predefined directions within 20 ns from coincidence relation.
T3	2 L1 hits in adjacent (within 100 ns) or next-to-adjacent storeys within 200 ns.
2T3	2 T3 triggers with at least three (one line) or four L1 (whole detector) in 2μs.
TQ	2 L1 triggers + 4 L0 hits in at least one of the 105 upward directions within 20 ns from coincidence relation.
K40	Coincidence between 2 L0 hits (same storey) in 20 ns.

2.2.5 Detector calibration

The charge, time and location information of each hit detected by the OMs are vital for the reconstruction of the events. An initial dark-room calibration of charge/time before the deployment was performed [158], but in situ calibrations are needed, especially after changes in the voltage of the OMs and the connection of lines. Different systems and devices have been developed for the continuous calibration and monitoring of the detector.

Time calibration

The time calibration of the ANTARES telescope consists in the calibration of the TVC channels and the time offset determination of each ARS.

Calibration of TVCs. A perfectly working TVC should have 256 channels, but missing channels may appear. The TVC time calibration consists of looking which are the minimum (TVC_{min}) and maximum (TVC_{max}) channels for each TVC pair of each ARS.

Time offset determination. A set of pulsed light sources, basically LEDs and lasers (Optical Beacon System), have been installed for the determination of the time offsets of the ARSs and the lines. This time calibration can also be performed with the use of reconstructed atmospheric muons and with ^{40}K events. A detailed description of these calibration methods is given in Chapter 4.

Position of the OMs

The sea current can move the top of the line up to 15 m. In order to know exactly the position of the OMs, a calibration system based on acoustic devices, a tiltmeter and a compass are used [159]. The acoustic system consists of RxTx hydrophonic emitters (located at the BSS) which emit 40-60 kHz acoustic signals every 2 minutes. These signals are detected by receptors located at 5 different floors in the detection lines. Figure 2.10 shows the horizontal positions of 5 storeys in line 4 for the February-April period in 2007.

Charge calibration

The gain of the PMTs is monitored during data taking. In order to maintain the 0.3 pe threshold, High Voltage (HV) tunings are occasionally performed. These changes in the HV tuning forces a recalibration of the AVC_{0pe} and AVC_{1pe} values defined in Equation 2.7. The AVC_{1pe} value is obtained from the background optical activity (namely bioluminescence and ^{40}K events as described in Section 2.2.6). Dedicated runs in which the PMT current is digitized at random times are needed for the recalibration of the AVC_{0pe} parameter.

A further correction is needed in order to obtain the charge. It has been observed that the time measurement of the TVCs affects the collected charge

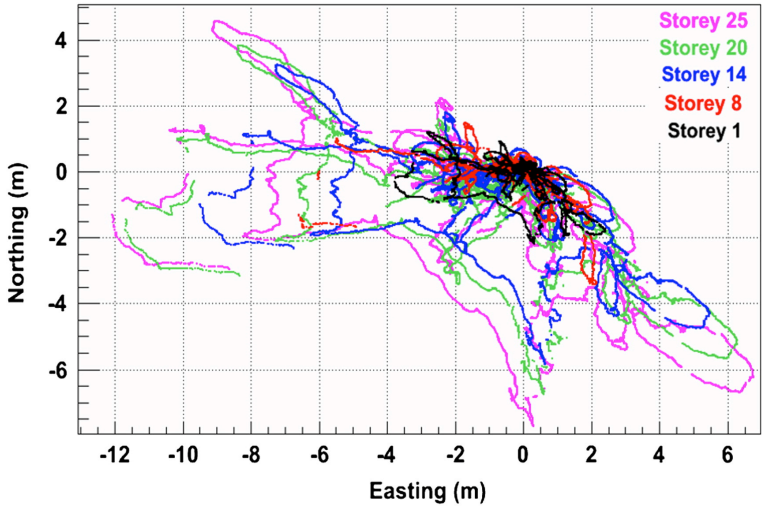

Fig. 2.10.: Tracking of the horizontal position for five different storeys in line 4 for the February-April period in 2007. Figure taken from [143].

by the AVCs. The maximum correction which is due to this *cross-talk* effect is in the order of 0.2 pe.

2.2.6 Optical properties

Detailed studies of the ANTARES site were performed during the R&D stage of the detector. In these studies, optical and environmental properties which are relevant for the detector performance were measured.

Optical properties of water

Scattering and absorption of light in water are relevant processes for the detection of the Cherenkov light. Cherenkov photons are deviated due to scattering processes, while the absorption decreases the number of photons detected. Since both happen at the same time, an effective attenuation length can be defined as,

$$\frac{1}{\lambda_{att}} = \frac{1}{\lambda_{abs}} + \frac{1}{\lambda_{scat}^{eff}}, \tag{2.10}$$

where λ_{abs} is the absorption length of water, and the effective scattering length, λ_{scat}^{eff}, is related to the scattering length, $\lambda_{scat}^{eff} = \lambda_{scat}/(1 - \langle \cos\theta \rangle)$,

where $\langle \cos\theta \rangle$ is the average cosine of the scattering angle. The latter approximation is only valid when $\langle \cos\theta \rangle \sim 1$, which is the case for sea water.

An autonomous line was deployed at the ANTARES site to determine both parameters before the detector deployment. This line had isotropic and pulsed light sources of UV and blue wavelengths at different distances from a 1" PMT. The results from these measurements can be seen in Figure 2.11 [160]. Moreover, during the ANTARES operations, the LED optical beacons have been used to monitor these parameters [161]. In the most dedicated ANTARES internal note regarding this topic [162], a thorough comparison between Monte Carlo time distributions for different values of the optical parameters and the photon arrival time distributions of data taken by using the LED OB system was carried out. The Monte Carlo simulations used the `Calibob` package, which considered the light propagation, absorption and scattering, the detector geometry and relevant acquisition parameters. Simulations were performed for different scattering and absorption lengths between 35 and 75 m in steps of 5 m. The output of seven LED optical beacon runs was compared with the output of the simulations by means of a χ^2 parametrisation. Figure 2.12 shows the results obtained from a particular run. From the χ^2 minimisation, the average absorption and scattering lengths obtained with all the runs were $\lambda_{abs} = 48 \pm 8$ m and $\lambda_{scat} = 57 \pm 8$ m, respectively.

Additionally, the velocity of light in sea water is also measured. This velocity can be defined as

$$v_g = \frac{c}{n_g} - \frac{ck}{n_g^2}\frac{dn_p}{d\omega}, \tag{2.11}$$

where n_g is the group refractive index, k is the wave number and ω is the frequency of a wave packet. This parameter has also been measured with the Optical Beacon system [163].

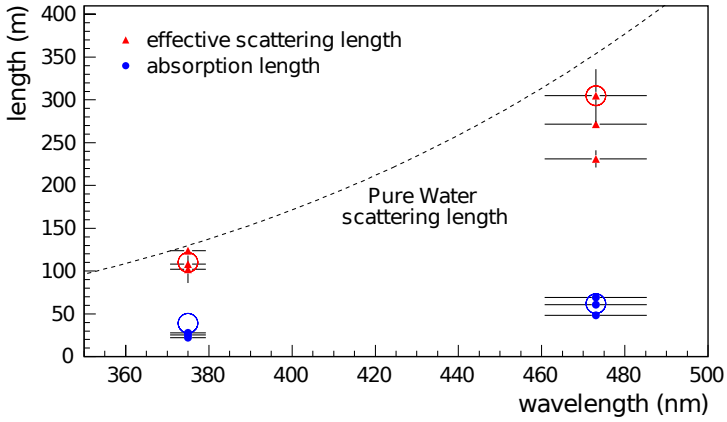

Fig. 2.11.: Effective scattering and absorption lengths measured in the location of ANTARES prior to its deployment for UV and blue wavelengths. The blue and red circles indicate estimated values for pure seawater, whereas the dashed line indicates the scattering length in sea water. The data points (triangles and dots) indicate measurements performed at different periods. The horizontal error bars show the spectral resolution at the 1σ level. Figure obtained from [160].

Optical background

The decay of ^{40}K nuclei is an unavoidable source of background in the ANTARES site. This isotope corresponds to 0.012% of all the present potassium in nature. Its concentration depends on the sea water salinity. ^{40}K can decay through the following beta decays:

$$\beta^- : \ {}^{40}\mathrm{K} \rightarrow {}^{40}\mathrm{Ca} + e^- + \bar{\nu_e} \ \ B.R. = 89.3\%, \tag{2.12}$$

$$EC : \ {}^{40}\mathrm{K} + e^- \rightarrow {}^{40}\mathrm{Ar} + \gamma + \nu_e \ \ B.R. = 10.7\%, \tag{2.13}$$

$$\beta^+ : \ {}^{40}\mathrm{K} \rightarrow {}^{40}\mathrm{Ar} + e^+ + \nu_e \ \ B.R. = 0.001\%. \tag{2.14}$$

The electron emitted after the β^- decay produces Cherenkov radiation of low amplitude (1 pe) which can be detected by the PMTs.

On the other hand, bioluminescence produced by bacteria and other microorganisms through chemical processes represents another environmental optical background. The higher the concentration of microorganisms, the

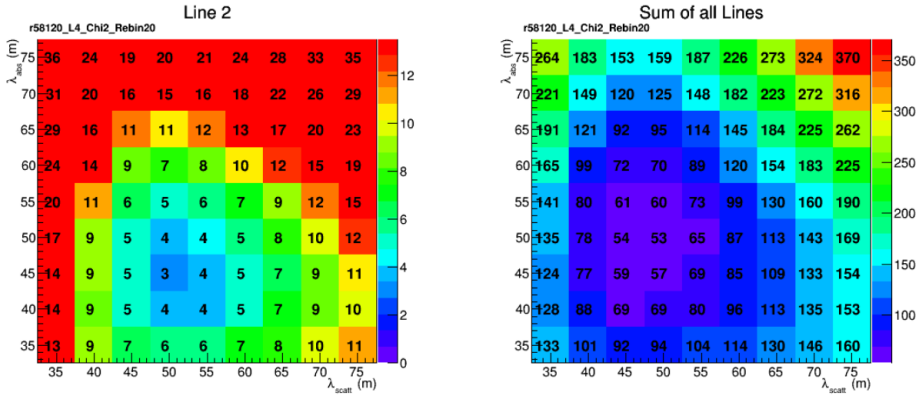

Fig. 2.12.: Left: χ^2 values obtained for different sets of absorption and scattering lengths by using the information of line 2 for a particular run. Right: sum of the χ^2 values for all lines and for the same run. Figure obtained from [162].

higher the bioluminescence. The rates of bioluminescence increase with the sea current velocity and the deep water renewal [164].

The total average rate from both backgrounds is ∼60 kHz, though seasonal bioluminescence effects are observed. Figure 2.13 shows the baseline rate of each run as a function of time. Higher rates and a higher bioluminescence are more frequent in Spring.

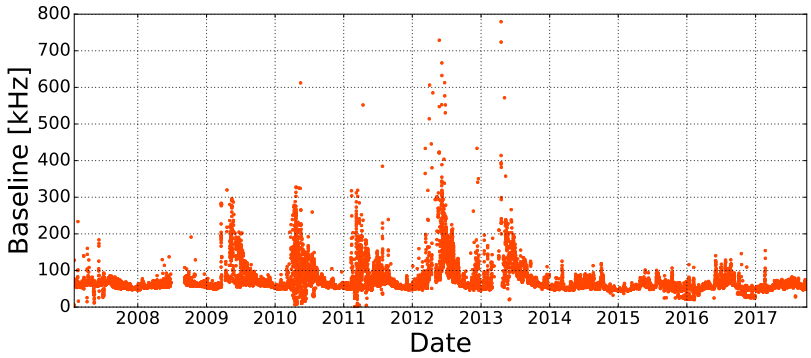

Fig. 2.13.: Baseline (in kHz) of each run as a function of time. From 2009 to 2013, higher rates are present during Spring.

2.3 The IceCube detector

IceCube [142, 165] is a neutrino detector which follows the efforts of AMANDA. Located at the South Pole, it is currently the largest neutrino telescope in the world. It consists of 5160 PMTs distributed over 86 strings in a cubic kilometer volume. Eight of these strings comprise the so-called DeepCore detector, an infill which is aimed for lower energy studies (starting at 10 GeV). A set of ice tanks in the surface are present (IceTop) to detect the products of the cosmic ray interactions in the upper layers of the atmosphere. The first string was deployed in 2005, reaching the completion of the detector in 2011. Figure 2.14 shows a scheme of the IceCube detector.

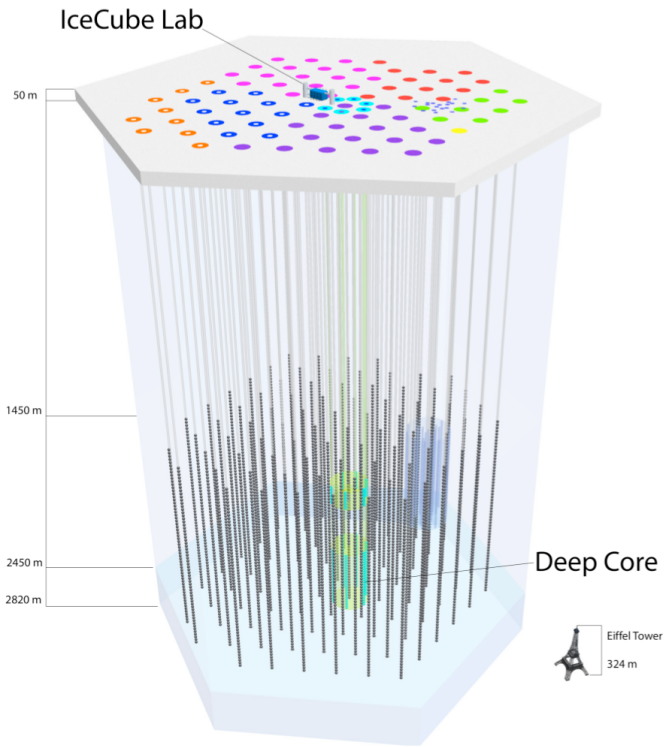

Fig. 2.14.: The IceCube detector is made of 86 strings and 81 IceTop stations. The bottom of the strings are at a depth of 2450 m. Figure obtained from [166].

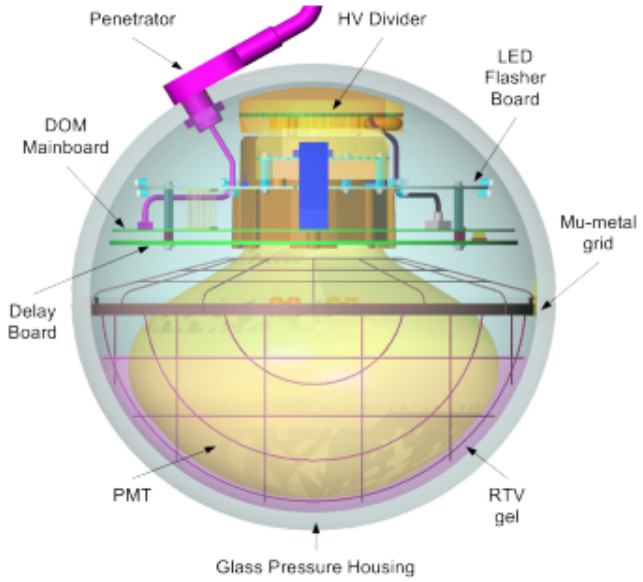

Fig. 2.15.: A Digital Optical Module from IceCube. Figure obtained from [167].

2.3.1 Digital Optical Module

A Digital Optical Module (DOM) [167] consists of a 35 cm diameter borosilicate glass sphere which contains a 10-inch PMT with its own DAQ system and readout electronics (see Figure 2.15). The glass sphere is made so to withstand pressures up to 600 atm. DOMs contain a μ-metal cage for the same reasons as in the ANTARES OMs, and a set of LEDs are included for calibration and determination of the ice optical properties.

The selected PMT for IceCube was the Hammamatsu R7081-02 model, which detects photons betweeen 300 and 650 nm with a quantum efficiency of $\sim$25%. For the DeepCore strings, the R7081MOD model was chosen, which have the same properties but with a 40% higher quantum efficiency. The DOMs were prepared so to have a maximum noise rate from the PMTs of 500 Hz and a TTS of $\sim$2.5 ns for single photoelectron pulses [165, 168]. They are also required to withstand temperatures between -55°C up to room temperature.

2.3.2 Strings

IceCube consists of 86 strings of 1 km length with their lowest position at a depth of 2450 m. 78 of these strings are placed in a hexagonal shaped grid with distances between lines of 125 m. Each string consists of 60 DOMs with a separation between them of 17 m. The 8 remaining DeepCore strings are located in the inner part of the detector. The spacing between adjacent DOMs in these strings is different: there are 50 DOMs under the dust layer (depth lower than 2100 m) with distances between DOMs of 7 m, and 10 DOMs above this layer (depth above 2000 m) with 10 m spacing.

2.3.3 IceTop

The IceTop surface array [169] consists of 81 pairs of ice tanks placed on the same grid as the IceCube strings. Each tank has a diameter of 1.8 m and a depth of 50 cm and contains two IceCube DOMs. The distance between adjacent tanks is of 10 m. IceTop detects particle cascades which come from the cosmic ray interactions with the nuclei of the atmosphere. It can be used as a partial veto to reject the atmospheric muon background in neutrino searches.

2.3.4 Optical properties

Unlike ANTARES, KM3NeT, Baikal or the original DUMAND project, IceCube uses ice as the medium to detect the Cherenkov light from the outputs of the neutrino interactions. As in water, the Cherenkov light is also absorbed or scattered in ice. Both effects have to be taken into account for the reconstruction and simulation of events.

The ice in the South Pole has been deposited throughout millennia, and different layers of multiple ages with different concentrations of impurities are present. As a consequence, the absorption and scattering lengths also change with the depth. The optical properties of ice have been measured with a system of LEDs located in the DOMs [170]. Figure 2.16 shows the effective scattering and absorption lengths (defined in the same way as in ANTARES) as a function of the depth. At most depths, the absorption length is larger than in water, leading to a smaller absorption. However, the inhomogeneities in the ice lead to strong variations, and specially important

is the short absorption length between 2000–2200 m in the so called “dust layer” region. However, the scattering length of ice is smaller than in water, which results into a worse angular reconstruction accuracy with respect to experiments which use water as medium (see for instance Figure 6.1 from Section 6.1.1).

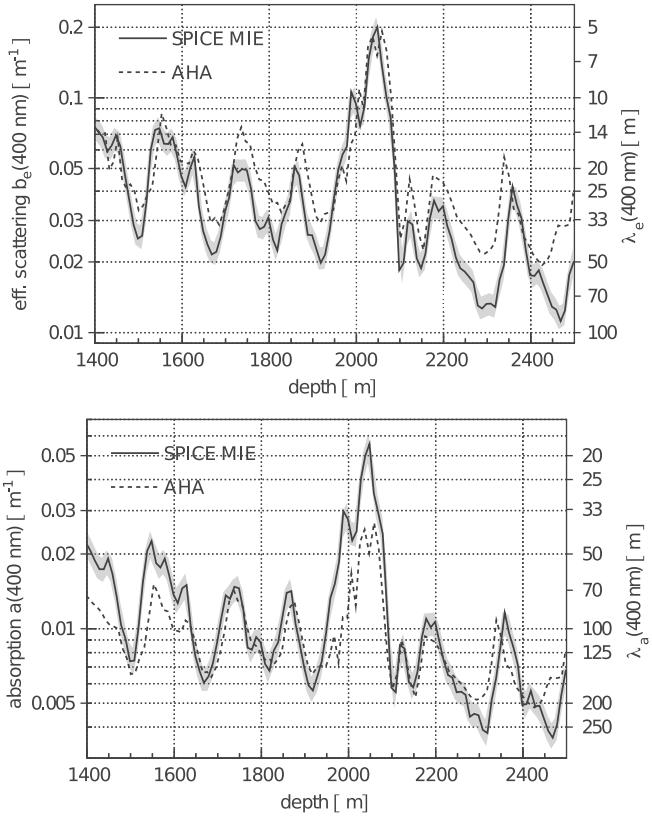

Fig. 2.16.: Absorption and effective scattering lengths for light at 400 nm as a function of the depth in the IceCube location. In this figure, different models are compared [170, 171]. Figure obtained from [170].

2.4 The KM3NeT neutrino telescope

The KM3NeT Collaboration [106] aims to build a network of neutrino telescopes in the Mediterranean Sea with two main goals: the detection of high energy neutrinos of cosmic origin, and the determination of the neutrino mass hierarchy. This network follows a modular design made of

detection blocks of 115 strings. The different spacing between strings allows to target for different neutrino energies. When completed, the network will be composed of 7 building blocks. Phase 2.0, which is aimed to be finished in 2022, will consist of two blocks dedicated to high-energy neutrino astronomy in Capo Passero (KM3NeT/ARCA), and one single block for the determination of neutrino mass hierarchy in Toulon (KM3NeT/ORCA).

2.4.1 Digital Optical Module

Fig. 2.17.: Left: Picture of a KM3NeT DOM. Right: Example of a KM3NeT DU. Figures obtained from [106].

The Digital Optical Module (DOM) is the most basic element of the KM3NeT building blocks (see Figure-left 2.17 for an example). It consists of a glass sphere of 17 in which contains 31 PMTs with their corresponding readout electronics.

The PMTs used are the ETEL D792KFL and Hammamatsu R12199-02 models. Their diameter is at least of 72 mm with a total length smaller than 122 mm. They present a TTS of 4.5 ns and a quantum efficiency of $\sim$27% for a 404 nm wavelength. No μ-metal shield has been added to the DOM, since

the effect of the Earth's magnetic field is negligible due to the small size of the PMTs. The PMTs are distributed on the DOM surface in 5 rings of 6 PMTs each. The vertical separation between rings is of 30° and they are equally spaced within the same ring. As in ANTARES, an optical gel is placed between the PMT and the glass sphere.

The use of multiple PMTs per each DOM presents important advantages compared to the traditional use of one single PMT. The photocatode area increases by a factor 3 to 4 compared to the former. It also permits the identification of more than one photon arriving to the same DOM. This feature further allows a better rejection of the optical background, either due to bioluminescence or ^{40}K decay.

Each DOM also contains an LED in the upper hemisphere for time calibration purposes, a compass/tiltmeter in order to determine the orientation of the DOM and an acoustic piezo sensor for the positioning determination.

2.4.2 Detection Unit

A string or Detection Unit (DU) consists of 18 DOMs attached to two parallel 4 mm diameter Dyneema^{TM} ropes (see Figure-right 2.17 for an example of a DU). The length of the DUs and the vertical separation between DOMs are different for the KM3NeT/ARCA and KM3NeT/ORCA detection blocks. In KM3NeT/ARCA, the total length of the string is of 700 m, with a separation of 36 m between DOMs and starting at 80 m from the sea bottom. In KM3NeT/ORCA, the total length of each line is of 200 m with a 9 m separation between DOMs, starting at 40 m.

The information and power are transferred with the use of an electro-optical cable. This cable is made of a plastic tube which contains two copper wires, which provide the power supply, and 18 optical fibres for data transmission. The DU keeps itself vertical by design, although an additional buoy is placed on the top to help keeping it upright during fast sea currents.

2.4.3 KM3NeT/ORCA and KM3NeT/ARCA layouts

Once Phase 2 is finished, KM3NeT/ARCA will be made of two blocks of 115 strings, which are being placed at (36° 16' N, 16° 06' E) and at a depth of 3500 m. This location is at a distance of 100 km from Porto Palo di Cappo

Passero (Italy), where the on-shore station is located. Figure 2.18 shows the location and the layout for the KM3NeT/ARCA detector.

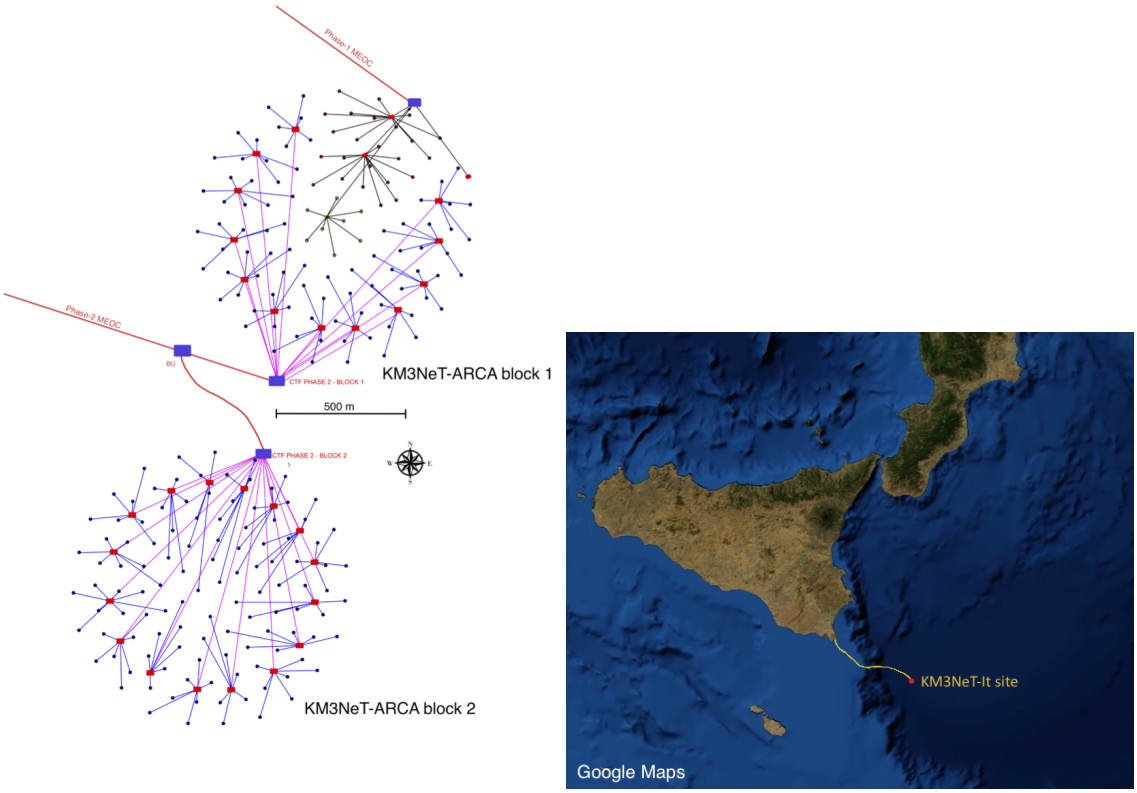

Fig. 2.18.: Left: Layout of the complete KM3NeT/ARCA detector with the two detection blocks in Phase 2. Right: Location of the KM3NeT/ARCA detector. Figure taken from [106].

Two Main Electro-Optical Cables (MEOCs) will connect the shore station with the detector. These are split into two branches that are connected to a Cable Termination Frame (CTF). These CTFs are connected to different Junction Boxes (12 for block2 and 16 for block1). A total of 7 DUs can be connected to each JB, with an average separation between DUs of 95 m.

In Phase 2, KM3NeT/ORCA will consist of one single block to be deployed at (42° 48' N, 06° 02' E) and at a depth of 2450 m. The shore station is located in La Seyne Sur Mer (France), 40 km away from the detector, where the current ANTARES station is. A scheme of the layout and its location can be seen in Figure 2.19. Two MEOCs will connect the station with the

detection block. Five JBs located at the surroundings of the DUs provide the power to the DUs. Each JB has eight connectors, and each connector can power up to 4 strings.

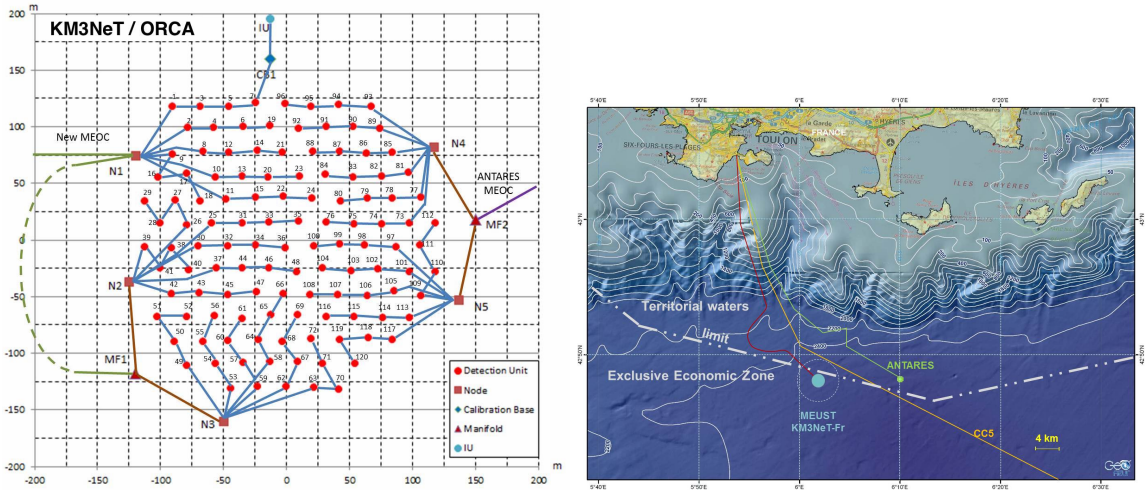

Fig. 2.19.: Left: Layout of the complete KM3NeT/ORCA detector. Right: Location of the KM3NeT/ORCA detector. Figure taken from [106].

2.4.4 Data Acquisition System

As in ANTARES, the KM3NeT DAQ follows the "all-data-to-shore" strategy, so that all signals above 0.3 pe are sent to the shore station. The information of each hit given by the PMTs consists of the arrival time and the Time over Theshold (ToT), which is the time the PMT signal is above a threshold of $0.3\,\mathrm{pe}$. The information of each hit is stored in 6 bytes of data. The first byte corresponds to the address of the PMT, 4 bytes correspond to the time information (where the least significant bit corresponds to 1 ns) and 1 byte for the ToT. A total of 25 GB/s are sent per builiding block, so this data needs to be filtered and reduced in order to be stored. Apart from physics data, a sampling of the rates of all PMTs is sent with a frequency of 10 Hz. This sampling is used in order to know the optical background for its implementation in the reconstruction and in the Monte Carlo simulations.

Trigger

The L0 trigger denotes the most basic trigger, which corresponds to a hit with a signal above 0.3 pe. This is the only trigger which is performed off-shore. The L1 filter consits on a coincidence of at least 2 L0 hits in the same DOM within a time window (typically, defined as $\Delta t = 10$ ns). The expected rate of L1 hits for a detection block is of 1000 Hz, where 600 Hz corresponds to ^{40}K decays. The remaining is due to random coincidences. These random coincidences can be reduced with the L2 filter, in which the information of the orientation of the PMTs is used.

A muon track and a shower triggers have been also developed. The muon track trigger consists of a scan around the visible sky which is combined with an assumed directional filter for the muon track. In this case, only PMTs within distances to the track smaller than a few times the absorption length of water are taken into account. A field of view of 10° degrees is considered in this filter, so that a scan in 200 different directions is needed to cover the full sky. The shower trigger is applied without a directional filter, and with a maximum light distance.

2.5 Baikal NT200 and GVD

Baikal has the first successful proof-of-concept attempt, after the detection of atmospheric muons with a stationary string placed in the Southern part of Lake Baikal in 1984 [140]. A first small PMT array of 36 PMTs in 3 strings, NT36, was deployed in 1994 [172]. These strings constitute the first ones of the NT200 Baikal Neutrino Telescope, which has been taking data since 1998. NT200 consists of 192 photomultipliers encapsulated into glass spheres (also called Optical Modules or OMs) in 8 strings. The OMs are located at depths between 1115 and 1195 m, with the anchor located at 1350 m deep. Three additional strings were added in 2005 as a first step towards a km^3 detector, leading to the NT-200+ telescope. Figure 2.20 shows a scheme of the detector.

The NT-200+ project is being upgraded to a much larger detector, Baikal-GVD, which is currently under construction [173]. It will consist of an array of $\sim 10^4$ OMs in a instrumental volume of ~ 2 km^3. The detector will be

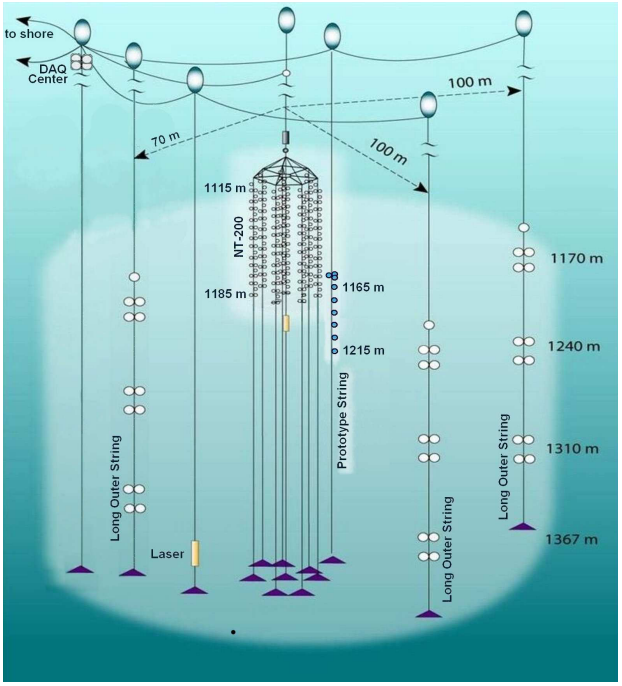

Fig. 2.20.: Scheme of the NT200+ detector. The inner strings correspond to the NT200 detector. Figure from [172].

divided into clusters of 8 strings. The first phase will be completed in 2020, with a total of 8 clusters (see Figure 2.21). A first prototype, DUBNA, was completed in 2015, and the first results of its operation were presented in the ICRC2017 [174].

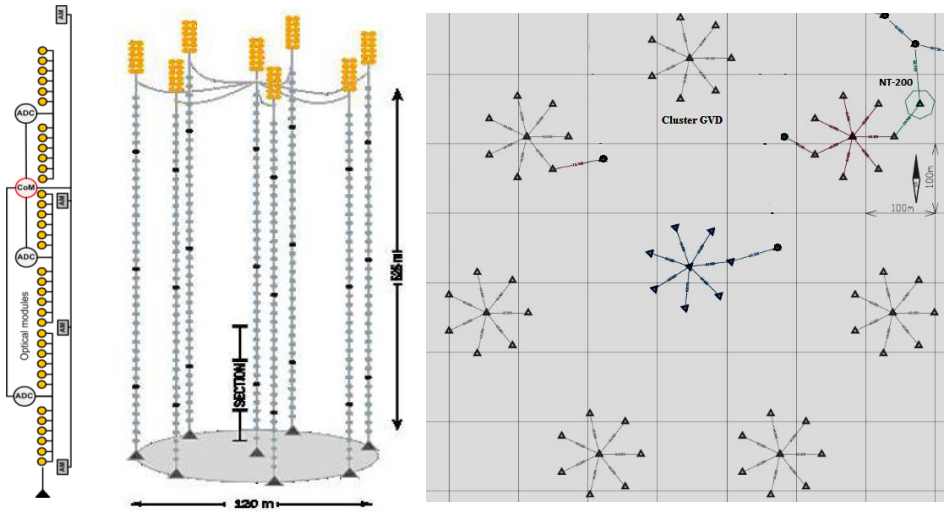

Fig. 2.21.: Baikal-GVD detector. The left figure shows a scheme of a GVD string. The second figure shows the configuration of a GVD cluster of 8 strings. The right figure shows a group of 8 clusters. Figure taken from [174].

3 Simulations and event reconstruction methods

Simulations are needed in order to estimate the performance and the response of the detectors. More specifically, they are used to obtain the efficiency of the event reconstruction algorithms, to know the probability density distributions of relevant parameters, and to estimate the parameters needed to compute the sensitivity of a specific neutrino flux, such as the effective area. In this chapter, the simulation chains which are used for the ANTARES, KM3NeT and IceCube detectors are described, with a particular emphasis on the point and extended source search analyses. The most relevant reconstruction algorithms used for these searches are also explained.

The simulation chains can be divided into three different steps. First, the events are generated and the Cherenkov light which is produced from these events is propagated through water or ice (Section 3.1). Afterwards, the response of the detector is simulated (Section 3.2). Finally, the reconstruction algorithms for both data and simulation are performed (Sections 3.3, 3.4 and 3.5).

3.1 Event generation and propagation

Simulations have to take into account all the events which can produce a response in the detector (see Section 2.1 from Chapter 2 for a summary on event signatures detected in neutrino telescopes, and Sections 2.1.2 and 2.2.6 in the same chapter for the main sources of background).

The instrumented volume is defined as the cylinder that surrounds the detector layout. An additional cylinder (the *can*) defines the volume where the emitted Cherenkov light can reach the detector (instrumental volume). In ANTARES and KM3NeT, the can volume is set so that its surface is at a distance of three times the light absorption length in water, approximately

($\sim 3\lambda_{abs}$) [175, 106]. A full simulation is performed inside this volume, whereas only energy losses of particles are considered outside. Figure 3.1 shows these volumes as defined in the ANTARES simulations.

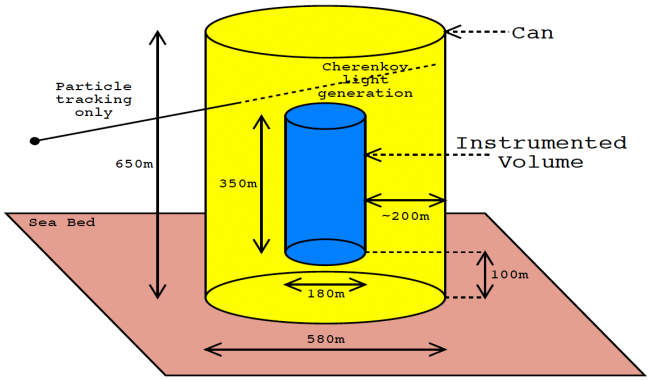

Fig. 3.1.: Detector geometry of ANTARES as defined in the simulation chain. A similar procedure is followed in the KM3NeT and IceCube simulations. Figure from [175].

3.1.1 Simulation of atmospheric muons

In IceCube, the atmospheric muons are simulated with the CORSIKA [176, 177] software, which allows the generation of muons from showers produced in the atmosphere and their propagation up to the sea level. In ANTARES and KM3NeT, atmospheric muons are generated using the MUPAGE [178] package, which is based on CORSIKA parametrisations. These parametrisations use the angular distribution and the energy spectrum of underwater muon bundles. The simulations produced by MUPAGE are valid for depths between 1.5 and 5.0 water-equivalent kilometers, and for zenith angles under 85°. In ANTARES, a single production of atmospheric muons with muon energy bundles above 0.5 TeV is produced. In KM3NeT, two different productions of muon bundles exceeding 10 TeV and 50 TeV are used instead. A sample with energies exceeding 1 TeV was also produced, and its contribution was shown to be completely suppressed with the background removal procedures of the 10 TeV sample.

3.1.2 Simulation of neutrinos

A similar procedure is followed for the simulation of neutrinos in the three detectors. A large number of neutrinos ($\sim 10^{11}$) are produced uniformly from all directions and for a large energy range, which is different for each detector. These neutrinos interact via charged or neutral current interactions following the CTEQ6-D [144] parton distribution functions, which are used to calculate the deep inelastic scattering (DIS) cross sections, and validated up to energies of 10 PeV. The same generated events are used for the simulations of atmospheric and cosmic neutrinos. As a result, an event weight is associated to each event to calculate the event rate for any neutrino flux either from cosmic or atmospheric origin.

In ANTARES and KM3NeT, the `GENHEN` [175] package is used for the generation of all neutrino flavours, both for CC and NC interactions. The `LEPTO` [179] software is used for the calculation of the differential cross sections. Neutrinos with energies between 10 and 10^8 GeV are considered for the high-energy simulations of ANTARES, and between 10^2 and 10^8 GeV for KM3NeT/ARCA simulations. Neutrinos are simulated with an energy spectrum of $\mathrm{E}^{-1.4}$, except in the ν_τ event simulations, in which a E^{-1} spectrum was preferred in order to have more high-energy events.

Since up-going neutrinos may interact with the Earth, the probability for a neutrino to reach the detector after traversing the Earth needs to be calculated. This is parametrised as a function of the zenith direction, θ_ν, and the neutrino energy, E_ν, as

$$P_{Earth} = e^{-N_A \sigma_\nu(E_\nu) \rho(\theta_\nu)}, \tag{3.1}$$

where N_A is the Avogadro number, $\sigma_\nu(E_\nu)$ is the cross section of the neutrino interaction with matter and ρ is the matter density along the neutrino trajectory. A representation of this probability can be seen in Figure 3.2.

In IceCube, the generation of neutrinos is produced with the NuGen software, which is based on `ANIS` [146]. In this case, neutrinos with energies between 10^2 and 10^9 GeV are produced with a spectrum of E^{-2}.

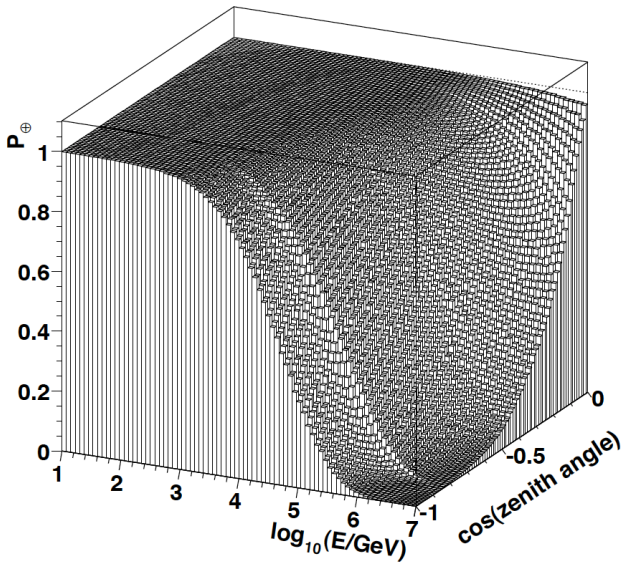

Fig. 3.2.: Probability for a neutrino to cross the Earth without interacting as a function of the neutrino energy, E_ν, and the zenith direction, θ_ν. Figure obtained from [180].

Atmospheric neutrino fluxes

Different assumptions on the atmospheric neutrino flux can be made. In the ANTARES analyses, the Bartol flux [181] has been assumed. However, in the KM3NeT analyses the HONDA flux [182] with the prompt component described in [183] has been taken into account for the atmospheric neutrino simulations. The comparison with data and simulations for the IceCube samples has been done by assuming the HONDA flux for the simulated events [184].

Calculation of weights

A different procedure for the event weight calculation is performed between ANTARES/KM3NeT and the IceCube simulations, although they present large similarities. In ANTARES and KM3NeT simulations, the generation weight associated to each generated neutrino is defined as [185],

$$W_{gen} = V_{gen} I_\theta I_E E_\nu^\gamma \sigma(E_\nu) \rho N_A P_{Earth} t_{sim}, \tag{3.2}$$

where:

- V_{gen} is the generation volume,
- I_θ is the angular space factor, which takes into account the solid angle from which the neutrinos are generated (typically, 4π),
- γ is the spectral index of the neutrino generation,
- I_E is the energy space factor, which takes into account the total energy range. It is defined as $I_E = \int_{E_{min}}^{E_{max}} E^{-\gamma} dE$, where E_{min} and E_{max} are the minimum and maximum generated energy,
- $\sigma(E_\nu)$ is the neutrino-matter cross section,
- ρN_A is the target nucleon number density,
- P_{Earth} is the probability for a neutrino to reach the detector volume after it crsses the Earth,
- t_{sim} is the equivalent livetime of the simulation.

The units of W_{gen} in the ANTARES/KM3NeT simulations are GeV·m^2·s·sr·year^{-1}. Given a neutrino flux $\frac{d\phi}{dEdSdtd\Omega}$ in units of GeV^{-1}m^{-2}s^{-1}sr^{-1}, the equivalent total number of neutrinos per year can be calculated as

$$N = W_{gen} \frac{d\phi}{dEdtdSd\Omega}. \tag{3.3}$$

The IceCube Collaboration uses a slightly different definition for the associated weight to each generated neutrino [186]. This generated weight, called OneWeight, can be expressed as

$$OneWeight = \frac{P(E_\nu, \theta_\nu)}{E_\nu^{-\gamma}} \int_{E_{min}}^{E_{max}} E^{-\gamma} dE A_{gen} \Omega, \tag{3.4}$$

where

- $P(E_\nu, \theta_\nu)$ is the probability of not interacting for a neutrino of a given energy E_ν and direction θ_ν,
- A_{gen} is the generation area of the simulation,
- γ is the spectral index of the neutrino generation,

- Ω is the total solid angle of the generation,
- E_{min}, E_{max} are the minimum and maximum generated energy of the simulation.

The units of OneWeight are expressed as GeV·cm^2·sr. The total amount of neutrinos associated to a generated event for a given flux $\frac{d\phi}{dEdtdSd\Omega}$ during an amount of time T can be expressed as,

$$N = OneWeight \frac{d\phi}{dEdtdSd\Omega} T. \tag{3.5}$$

3.1.3 Light and lepton propagation

Particles are tracked in ANTARES and KM3NeT with the KM3 [187] package, which is based on the `GEANT` [188] software. The relevant physical processes such as energy losses, hadronic interactions, light emission and multiple scattering are considered. When simulating muon tracks, the emission of the Cherenkov light is performed on a statistical basis. The probability of a photon to produce a hit on a OM is based on tables which include distributions of the number of hits and the arrival hit times for different distances, positions and orientations of the OM with the muon track. These tables are obtained from simulations of propagation of photons coming from muons.

The propagation of muons from the sea level to the detector volume is done with an additional software, `MUSIC` [189], which calculates the muon energy loss and the Cherenkov light emission in one metre steps.

In the IceCube simulations, the lepton propagation is performed with the `PROPOSAL` [190] package. These simulations assume a homogeneous model of ice and takes into account the energy losses via continuous and stochastic processes. The photon propagation is done with the Photonics [191] software. The approach is similar to the KM3 package, which as a matter of fact was developed from the Photonics software. In order to save calculation time, photons are not propagated individually. Instead, tables with information of the number of hits and hit arrival times for different depths and light sources are followed. The light sources can be either muons which start

or stop inside the detector volume or cross it, and from electromagnetic or hadronic cascades. These tables include the information of ice properties.

3.2 Detector simulations

Two additional steps have to be included in the simulations: the background due to environmental conditions and the detector response to individual hits.

The optical background due to the environmental conditions in ANTARES and KM3NeT corresponds to the light produced by the decay of ^{40}K nuclei and by living beings (bioluminiscence) which are present in sea water. In ANTARES, this information is evaluated with the `TriggerEfficiency` [192] program, assuming a mean rate obtained from the counting rate of the real detector. In KM3NeT, this is done with the `JTriggerEfficiency` [193] program, which is part of the `JPP` package. A 5 kHz rate per PMT is simulated, which produces correlated hits of 2, 3 and 4 coincidences between PMTs in the same DOM at frequencies of 500, 50 and 5 Hz.

The `TriggerEfficiency` program takes into account the time resolution, which for a single photo-electron is dominated by the TTS of the PMT($\sigma_{TTS} = 1.3$ ns for ANTARES). This value decreases when considering multiple photo-electrons, and it can be simulated by assuming a Gaussian smearing with a width of $\sigma = 1.3/\sqrt{N_\gamma}$, where N_γ is the number of photons arriving simultaneously.

In the IceCube simulations, no events due to the decay of isotopes are observed due to the purity of the Antarctic ice. However, the variability of the scattering and absorption lengths due to the presence of dust layers, as discussed in Section 2.3.4 from Chapter 2, plays an important role in the light propagation. The largest contribution of background noise is, therefore, due to the dark and thermal noises of the PMTs [186].

3.3 ANTARES and KM3NeT track reconstruction methods

Many event reconstruction algorithms have been developed to obtain the most relevant information of the event signatures produced after the neutrino or the atmospheric muon interactions. The ANTARES and KM3NeT track reconstruction algorithms which have been used for the analyses presented in Chapter 6 are discussed in this Section.

3.3.1 AAfit

There are several track reconstruction algorithms developed for ANTARES detector: `BBFit` [194], `GridFit` [195], `AAFit` [180], and `RECO` [196]. `AAFit` is the one which is currently used in point-like source searches, due to its better detection efficiency at high energies and its excellent angular resolution. It is based on a multi-step procedure which consists on a linear prefit, an M-estimator fit and a maximum likelihood fit with a simplified PDF to obtain the starting point for the final maximum likelihood fit, which gives the direction of the reconstructed track.

The muon trajectory can be characterised by a direction, $\vec{d}$ (which can be expressed as a function of the zenith, θ, and azimuth, ϕ, angles) and a position $\vec{p} = (p_x, p_y, p_z)$ at a given time, t_0. For a given OM and a given track, it can be shown that the expected arrival time of a photon to an OM is given by

$$t^{th} = t_0 + \frac{1}{c}\left(l - \frac{k}{tan\theta_c}\right) + \frac{1}{v_g}\left(\frac{k}{sin\theta_c}\right), \tag{3.6}$$

where v_g is the group velocity of light in water, θ_C is the Cherenkov angle and k is the shortest distance between the track and the OM (see Figure 3.3 for a representation of a muon track). The input information required for this reconstruction mechanism consists of the time residual of each hit (difference between the observed hit time and the expected one), the amplitude, the photon path length ($b = k/sin\theta_C$) and the angle of incidence of the photon into the OM (a).

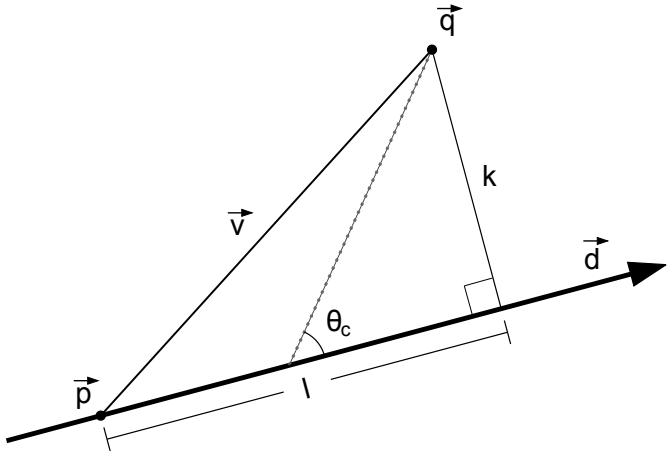

Fig. 3.3.: Scheme of a muon passing through the detector coming from a direction $\vec{d}$ at a position $\vec{p}$ for a given time t_0. This muon emits Cherenkov radiation with an angle θ_c (dotted grey line). The $\vec{q}$ vector shows the location of a particular OM. The vector $\vec{v} = \vec{q} - \vec{p}$ shows the distance between the point $\vec{p}$ and the OM. The k and l segments indicate the perpendicular and parallel components of $\vec{v}$ with respect to the direction of the muon. Figure taken from [197].

Reconstruction chain

First of all, a pre-selection of hits is performed by considering all the hits with $|\Delta t| \leq \frac{d}{v_g} + 100$ ns, where Δt is the time difference between a given hit with the one having the largest amplitude, and d denotes the distance between the OMs. With this sample, a linear pre-fit is performed under the assumption that the position of the selected hits coincide with points located on the muon trajectory. This linear fit is performed by means of a χ^2 minimisation.

With the information of the linear pre-fit, an M-estimator minimisation is performed. In this case, the considered hits must correspond to time residuals between -150 $\leq t_{res} \leq$ 150 ns and within distances from the fitted track smaller than 100 m, or to amplitudes larger than 2.3 pe. The function which is maximised depends on the time residuals of the hits, t_{res}, and the angular response function of the optical module, f_{ang}, as

$$M = \sum_i K(-2\sqrt{1 + A_i t_{res,i}^2/2}) - (1 - K) f_{ang}(a_i), \tag{3.7}$$

where A_i is the amplitude of the hit, a_i is the cosine of the angle of incidence of the photon and K is a constant value. This constant was set to 0.05 after being optimised with simulations.

The best fit parameters from the M-estimator are used for a maximum likelihood fit. In this case, only hits between -$0.5t^{RMS} < t_{res} < t^{RMS}$ are considered, where t^{RMS} is the root mean square of the time residuals obtained from the M-estimator fit. The likelihood can be described as a product of the probabilities of each individual hit:

$$L = \prod_i P(t_i|t_i^{th}, a_i, b_i, A_i). \tag{3.8}$$

For this particular step, only the information of the hit time and the expected arrival time are considered. This likelihood maximisation is sensitive to the starting point position. Because of this, the previous two steps are repeated for eight alternative additional starting points, which are chosen by rotating or translating the track direction from the pre-fit. The number of starting points providing a track within an agreement of 1° from the preferred result (the one with the largest likelihood) is kept (N_{comp}).

The final step consists on a maximum likelihood fit by considering the complete information from Equation 3.8 and by taking the direction and position of the best fit from the previous step. For this maximisation, all hits with time residuals between $-250 < t_{res} < 250$ ns, amplitudes higher than 2.5 p.e. or with local coincidences, are taken into account.

The goodness of the reconstruction is given by the Λ quality parameter,

$$\Lambda = \frac{\log L}{N_{dof}} + 0.1(N_{comp} - 1), \tag{3.9}$$

where N_{dof} is the number of degrees of freedom ($N_{hits} - 5$).

The angular error estimate of the track can be obtained from the covariance matrix after the last likelihood maximisation. This is done by assuming that the likelihood behaves as a multivariate Gaussian function around the

fitted maximum. As a result, from the error estimates on the zenith, β_θ, and azimuth, β_ϕ, the angular error estimate can be defined as

$$\beta = \sqrt{\beta_\theta^2 + \sin^2\theta\beta_\phi^2}. \tag{3.10}$$

Energy reconstruction

The `dEdX` energy reconstruction method [198, 199] was developed in order to obtain the energy of the events reconstructed by `AAFit`. Although muons coming from ν_μ CC interactions can release a large fraction of their energy outside the detector volume, a correlation can be established between the amount of energy deposited per unit length and the actual energy of the event. The `dEdX` reconstruction approximates the energy by calculating the parameter

$$\rho = \frac{\sum_i^{N_{hits}} Q_i}{\epsilon(\vec{x}_i)} \frac{1}{L_\mu}, \tag{3.11}$$

where Q_i is the charge collected from the hit i, L_μ is the reconstructed track length of the muon within a volume defined by the cylinder of the ANTARES instrumented volume increased by twice the light attenuation length, and $\epsilon(\vec{x}_i)$ is the ANTARES light detection efficiency. Only hits used in the last part of the `AAFit` reconstruction mechanisms are used to compute the ρ parameter.

Performance

Figure 3.4-top shows the angular resolution for events coming from ν_μ CC interactions after the set of cuts applied to the last analysis of point-like source searches ($\Lambda > -5.2$, $\cos(\theta) > -0.1$, $\beta < 1^\circ$, $\log 10(\rho) > 1.6$, $L_\mu > 380$ m). An angular resolution better than 0.4° can be established for energies above 10 TeV. Figure 3.4-bottom shows the dependence between the ρ parameter of the `dEdX` energy reconstruction and the original neutrino energy.

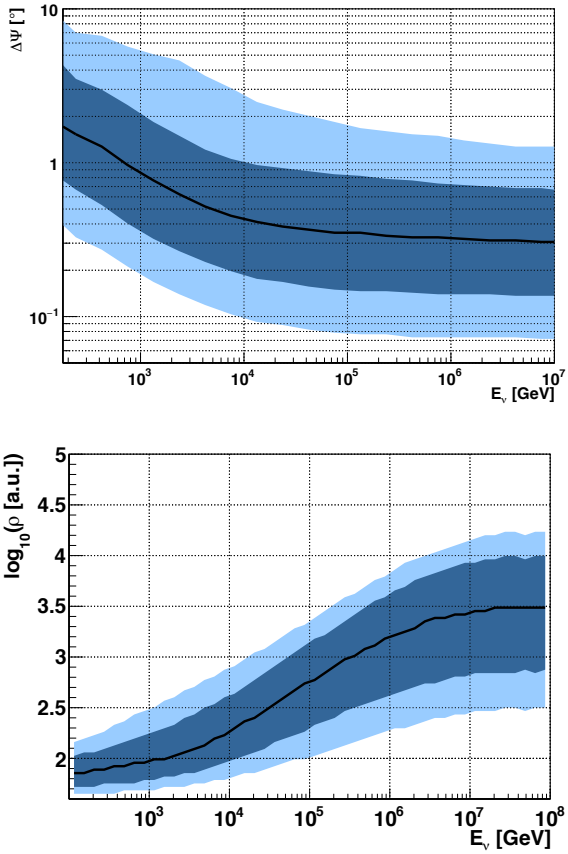

Fig. 3.4.: Top: Angular resolution for track events coming from ν_μ CC interactions using `AAFit` events. Bottom: correlation between the ρ energy proxy and the original neutrino energy for events coming from ν_μ CC interactions. In both cases, a cut on $\Lambda >$ -5.2, $\beta < 1°$, cos$\theta >$ -0.1, $L_\mu >$ 380 m and $\log_{10}(\rho) >$ 1.6 have been applied. The dark blue area shows the 1σ region, whereas the light blue area shows the 90% belt.

3.3.2 Track reconstruction mechanisms: JGandalf

`JGandalf` [200] is the most recent track reconstruction algorithm developed for KM3NeT. As in the `AAFit` algorithm, the first step is also a prefit. This consists of a linear fit in which causally connected hits are used to avoid those coming from optical backgrounds or light scattering. Based on the χ^2

minimisation values, different permutations of hit selections are done from the causally connected hits. A best fit value, Q, is defined as

$$Q = NDF - 0.25 \times \frac{\chi^2}{NDF}, \tag{3.12}$$

where NDF is the number of degrees of freedom. After a direction is selected, the prefit procedure is repeated for different directions within 1° from the selected prefit. From these, the twelve with a best fit value are chosen.

A muon trajectory fit based on a likelihood maximisation is evaluated for these twelve directions. This likelihood takes as information the PMT response as a function of the minimum distance of the muon to the PMT i, ρ_i, the orientation of the PMT, ϕ_i and θ_i, and the time residual of the hit, t_{res}:

$$L = \prod_{hits} \left[\frac{\partial P}{\partial t}(\rho_i, \theta_i, \phi_i, t_{res}) \right]. \tag{3.13}$$

The PDF used for the likelihood is calculated semi-analytically from simulations, in which the unscattered and single-scattered Cherenkov photons, the muon energy losses, the dispersion of photons, the optical background rate, and the properties of the PMTs are considered.

This likelihood is built to estimate the reconstructed vertex and the direction of the muon. The estimated deposited energy is performed in a final step by taking into account the reconstructed direction from the likelihood maximisation, and the distribution of the PMTs which have and have not detected hits and are no further than 200 m from the muon trajectory.

The median angular and energy resolutions are shown in Figure 3.5. An excellent median angular resolution lower than $\leq 0.1^\circ$ is achieved for energies above 100 TeV, and an energy resolution of $\sim$30% is obtained for energies between 10 TeV and 1 PeV.

3.3.3 recoLNS

`recoLNS` [201] is a KM3NeT track-like event reconstruction method heavily based on `AAfit`, with a radical change on the hit selection and in the PDFs

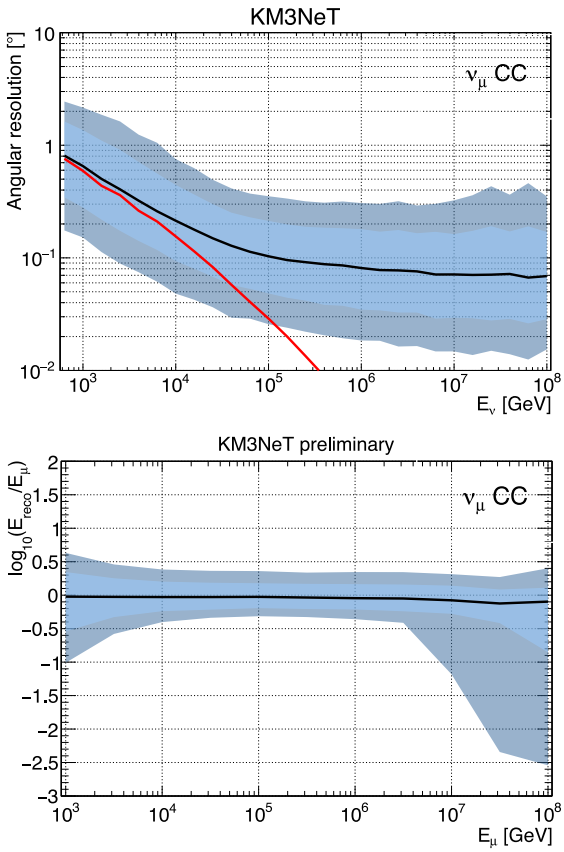

Fig. 3.5.: Top: Angular resolution of `JGandalf` for track events coming from ν_μ CC. The red line indicates the median deviation between the neutrino and the outcoming muon. Bottom: Energy resolution as a function of the outcoming muon for the same type of events. The dark blue area shows the 1σ region, whereas the light blue area shows the 90% belt. Figure taken from [200]

used. The hit selection is performed introducing a set of trigger patterns of hits with decreasing probability of being produced by the optical background. An angular resolution below 0.3° is achieved for events above 10 TeV.

As in AAfit, a four-step reconstruction strategy with few conceptual differences has been followed. Apart from changes in the hit selection in each step, the repetition of steps 3 (M-estimator) and 4 (likelihood maximisation with reduced information) are now produced in 7200 different starting track positions by rotating the prefit track in steps of 3° from the initial point. The

one with the highest value of $\Lambda_{recoLNS}$, defined as $\Lambda_{recoLNS} = -\frac{logL}{N_{hit}-5}$ is taken as the starting point for the last maximum likelihood minimisation.

3.4 ANTARES and KM3NeT cascade reconstruction methods

Several reconstruction algorithms for cascade events have also been developed for ANTARES and KM3NeT. Some of the algorithms used in KM3NeT were first applied in ANTARES. The ones which have been used for the analyses presented in Chapter 6 are discussed in this section.

3.4.1 TANTRA

`TANTRA` [202, 203] is the cascade reconstruction algorithm which gives the best directional reconstruction in ANTARES. It is based on a two-step procedure. First, the vertex of the interaction is reconstructed. In the second step, the direction of the cascade is fitted. Each of these steps is preceded by a specific selection of the hits.

The reconstruction of the interaction vertex

The `TANTRA` interaction-vertex reconstruction algorithm checks all the possible groups of hits from a triggered event that are causally connected with a common source in a fraction. In other words, each pair of hits inside the selection must fulfil the condition

$$|\vec{r_i} - \vec{r_j}| \geq c_W |t_i - t_j|, \tag{3.14}$$

where $\vec{r_i}$ is the position of the OM where the hit i has been detected, t_i is the recorded time of the hit, and c_W is the speed of light in water. From these groups, the one with the largest sum of detected hit charges is selected.

Once the hit selection is done, a pre-fit is performed to obtain the location of the position vertex. All selected hits are supposed to come from the same interaction vertex. This means that per each hit we will have

$$(\vec{r_i} - \vec{r}_{vertex})^2 = c_W^2(t_i - t_{vertex}), \tag{3.15}$$

where $\vec{r}_{vertex}$ and t_{vertex} indicate the location and time of the vertex we want to fit, and i is the index of any of the N selected hits. From this information, a least square fit minimization is done to obtain the pre-fitted vertex position and time. These values are used as an initial point for the M-estimator fit, which minimises the function

$$M_{Est} = \sum_i^N \left(q_i \sqrt{1 + t_{i-res}^2/2} \right), \tag{3.16}$$

where q_i and $t_{i-res} = t_i - t_{Shower} - |\vec{r_i} - \vec{r_{Shower}}|/c_W$ denote the charge and the time residual of the hit i, respectively.

Reconstruction of the cascade direction

A different hit selection is done for the reconstruction of the cascade direction. In this case, all the hits of a triggered event in a time residual window of -200 < t_{res} < 500 ns are considered, where t_{res} is the time residual with respect to the previously fitted vertex. Hits arriving to the same PMT are merged: the charge of the merged hits corresponds to the sum of the individual ones, and the time is taken as the one of the first detected hit in the PMT.

The direction of the cascade is then obtained by performing a maximisation of a likelihood, defined as

$$\log L = \sum_{i=1}^{N_{selected}} \log\left[P_{q_i>0}(q_i|E_\nu, d_i, \phi_i, \alpha_i) + P_{bg}(q_i)\right] + \sum_{i}^{N_{PMTswithouthits}} \log\left[P_{q=0}(E_\nu, d_i, \phi_i)\right]. \quad (3.17)$$

In this equation, $P_{q_i>0}$ denotes the probability for a PMT i to have measured a charge q_i, $P_{q=0}$ is the probability of not detecting the charge, and P_{bg} is the probability for a PMT i to detect a hit with charge q_i from background. All of these probabilities depend on the charge of the hit, q_i. Also, $P_{q_i>0}$ and $P_{q=0}$ depend on the neutrino energy, E_ν, the distance between the PMT i and the vertex of the interaction, d_i, the angle between the neutrino direction and the vector which connects the PMT i and the vertex of the interaction, ϕ_i, and the angle between the direction of the PMT with the incident photon, α_i.

Performance

The performance of this reconstruction method can be seen in Figure 3.6. A median angular resolution between 2° and 4° degrees can be achieved for contained events (events within $|Z_{vertex}| < 300$ m, $\rho_{vertex} < 250$ m from the detector centre) with neutrino energies,E_ν, between 10^3 and 10^6 GeV for ν_e CC events according to the simulations.

3.4.2 AAshowerfit

`AAshowerfit` [204] is the main cascade reconstruction mechanism used in KM3NeT/ARCA for point-like source analyses due to its superior angular resolution. As `TANTRA`, it is based on an initial position fit followed by a direction fit, where the information of the previous fit is used.

The hit selection is performed in two steps. First, hits occurring in one PMT within a time window of 350 ns are merged into a single hit, whose arrival time is the time of the first hit. Afterwards, merged hits which coincide in

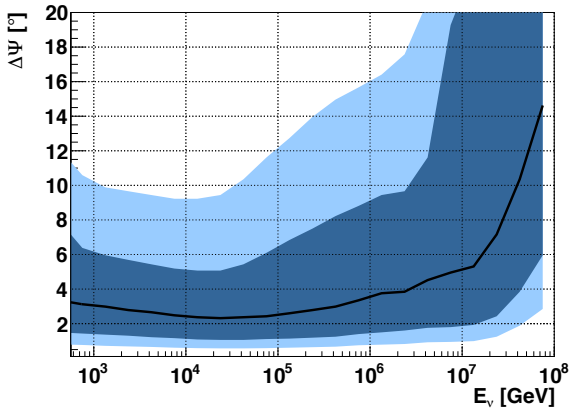

Fig. 3.6.: Angular resolution for cascades coming from ν_e CC interactions for events selected with the cuts of the last ANTARES point-source analysis (see Section 6.2 from Chapter 6) using the TANTRA reconstruction method. The dark blue area shows the 1σ region, whereas the light blue area shows the 90% belt.

the same DOM within 20 ns are used for the vertex fit, which is based on an M-estimator which maximises the following function:

$$M = \sum_{i}^{N_{hits}} \sqrt{1 + r_i^2}. \tag{3.18}$$

The starting point of the M-Estimator is taken as the centre of gravity of all the selected hits, and the starting interaction time is taken as the mean of the hit times minus 500 ns.

With the reconstructed interaction vertex from the M-Estimator fit, a new hit selection is performed for the direction and energy fit. In this selection, all coincidence hits with time residuals between -100 $< t_{res} <$ 900 ns are considered.

Even if the likelihood does not take into account the ToT information, the energy can be estimated by counting the number of hits detected in each DOM. The PDF used in this likelihood has been built by calculating the mean number of photons which are expected to be detected from a cascade, μ_{sig}. This quantity has been expressed as a function of the vector which connects the interaction vertex to the centre of the DOM, the direction of

the cascade, the direction to where the PMT is facing and the energy of the event. If Poisson statistics is assumed, the probability to obtain a null observation by a given PMT can be expressed as $P_0 = \exp(-\mu_{sig})$. From this probability, as in the TANTRA mechanism, an on/off information approach has been developed for the likelihood maximisation, which is defined as,

$$\log L = \sum_{empty-PMTs} \log P_0 + \sum_{hit-PMTs} \log(1 - P_0). \tag{3.19}$$

Figure 3.7 shows the angular and energy resolution for cascade events coming from ν_e CC interactions. Angular resolutions better than 2° are observed for energies above 100 TeV, which is a significant improvement compared to the angular resolutions observed in ice by IceCube ($\sim 10° - 20°$). A remarkable energy resolution of the order of the 10% is also observed for the same energy region.

3.4.3 Dusj

Dusj [205, 206, 207] is a cascade reconstruction mechanism used in ANTARES, which was originally developed for diffuse flux searches. Due to its worse angular resolution compared to TANTRA, it is not the main reconstruction algorithm used for point-like source searches. However, some of its variables are included into multivariate techniques in order to distinguish between cascades and background of atmospheric muons.

The Dusj reconstruction is divided into three main steps: hit selection, maximum likelihood fits and calculation of additional quality parameters. In ANTARES, some Dusj parameters are used in an event classification via a random decision forest (RDF) algorithm.

Hit selection

The hit selection is performed in two steps. First, only hits from direct photons (i.e., not suffering scattering) are kept. From these, only those which are coincident within a time window of 20 ns and with a detected charge larger than 1.2 pe are considered, in order to avoid hits due to ^{40}K or bioluminescence. The second step tries to identify those hits originated

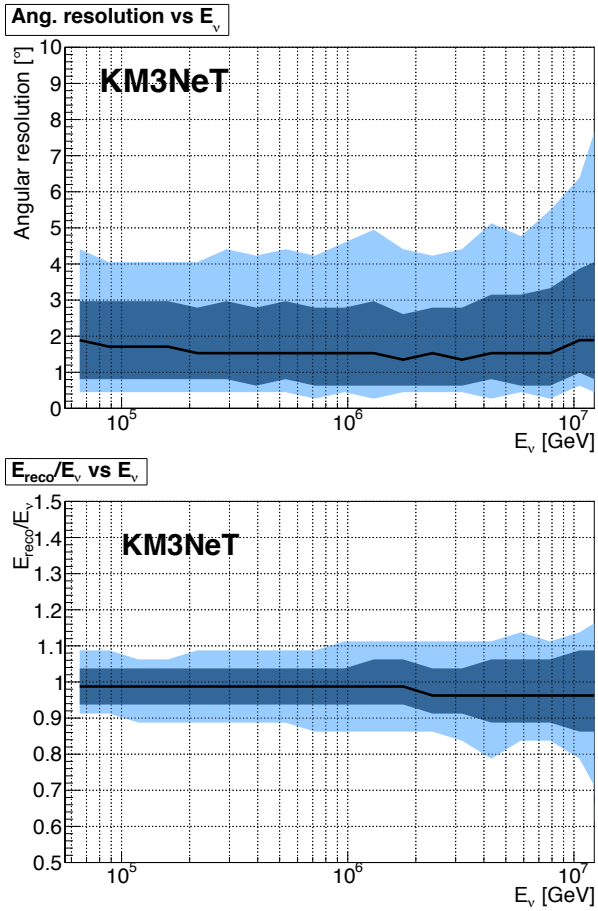

Fig. 3.7.: Top: angular resolution for cascade events coming from ν_e CC interactions and for a containment of $\rho_{aashow} < 500$ m and $|z_{aashow}| < 250$ m. The dark blue area shows the 1σ region, whereas the light blue area shows the 90% CL area. Bottom: energy resolution for the same sample. The `AAShowerFit` reconstruction method has been used in both cases.

from the cascade. This is done by an approximate scan fit of the location and time of the interaction vertex. From all the possible vertices, the one which minimises the reduced χ^2_{pre} is taken, which has been defined as

$$\chi^2_{pre} = \frac{\sum_{i=0}^{N_{hits}} t^2_{res,i}}{N_{hits} - 4}, \tag{3.20}$$

where $t_{res,i}$ is the time residual for a given hit, and $N_{hits} - 4$ takes into account the number of degrees of freedom in the fit.

Likelihood maximisation fit

To obtain the interaction vertex location, the time, and the energy and direction of the original neutrino, two consecutive maximisations are performed. The first one obtains the information regarding the interaction vertex, and the second one calculates the direction and energy of the neutrino by taking as initial parameter the information obtained from the first fit.

Per each hit i, the probability p of being originated from a cascade is estimated from PDFs obtained from simulations, so that the likelihood for a hit selection to come from the same cascade is defined as $LH = \prod_{i=1}^{N_{hits}} p_i$. The reduced likelihood, which gives the quality of the fit, is obtained by dividing the LLH with the number of degrees of freedom, N_{dof}, $LLH_{red} = \frac{\log(LH)}{N_{dof}}$.

For the interaction vertex fit, the PDF considered contains information of the distance from the interaction vertex at a given time since this interaction occurred. For the direction fit, information of the total charge at the vertex, the emission angle of hits' photons and the original simulated cascade energy are considered.

In ANTARES, a Random Forest Classifier (RFC) method to reject atmospheric muons is used. This RFC considers the reduced χ^2_{pre} parameter from the hit selection, the vertex and direction reduced likelihood values, the χ^2_{fin} value of the final reconstructed vertex and the quadrupole moment of the cascade hits. The χ^2_{fin} value of the final reconstructed vertex is defined as

$$\chi^2_{fin} = \frac{1}{N_{hits}} \sum_{i=1}^{N_{hits}} t^2_{res,i}. \tag{3.21}$$

The quadrupole moment of the cascade hits is obtained once all the reconstruction steps are performed. This quadrupole moment measures the charge distribution in comparison with the one of a track with the same neutrino direction.

3.4.4 Qstrategy

Q-Strategy [208] [209] is the first cascade reconstruction mechanism available in ANTARES, and it was also developed initially for diffuse flux searches. This algorithm has also been adapted for KM3NeT/ARCA.

For the prefit, all 3N triggered hits are considered, and a first fit of the interaction vertex is calculated. After this first fit, all L0 hits with time residuals between –10 $< \Delta t <$ 14 ns and/or with a charge larger than 2.5 p.e. are taken.

The reconstruction of the cascade vertex is performed in two stages. The first one consists on a mean space-time estimation, in which the cascade is assumed to come from a point-like light source. If hits are detected on the correct time, the interval between the expected hit detection and the actual hit time must be zero. It can be shown that this can be transformed into a set of N-1 equations, which can be expressed in matricial form as,

$$\boldsymbol{\chi_s} = b_i \frac{1}{2} \begin{pmatrix} \vec{r}_{i+1} - \vec{r}_i \\ \frac{ic}{n}(t_{i+1} - t_i) \end{pmatrix}^{-1} = b_i \boldsymbol{A}^{-1}, \tag{3.22}$$

where $\vec{r}_i$ and t_i are the location and the time of the hit i, n is the refractive index of sea water, c is the speed of light, **A** is a matrix with (N-1)×2 dimensions, and b_i can be expressed as $b_i = r_{i+1}^2 - r_i^2 - \frac{c^2}{n^2}(t_{i+1}^2 - t_i^2)$.

Since there are four parameters that have to be estimated (x_s, y_s, z_s, t_s), at least five hits from two different lines are needed. If the event has more than five hits, the residual parameter is minimised with the following definition:

$$R = \sqrt{(\boldsymbol{\chi}_s - b\boldsymbol{A}^{-1}) \cdot (\boldsymbol{\chi}_s - b\boldsymbol{A}^{-1})^T}. \tag{3.23}$$

After this, an M-estimator minimisation is performed. Q-Strategy uses a L_1–L_2 M-estimator which is defined as

$$M = 2 \cdot \sqrt{1 + \frac{\Delta T^2}{2\sigma^2}} - 2, \tag{3.24}$$

where σ is the estimated time resolution of the detector ($\sim$1 ns).

For the direction reconstruction, it is assumed that the resulting direction of the particles produced by the neutrino interaction follows the direction of the original neutrino. This is done by calculating the so-called *Light Direction* vector, defined as the average direction of all vectors which connect the first selected hit with the i-th one.

A correlation between the total charge amplitude of the event and the deposited energy is assumed in order to calculate a parameter correlated with the deposited energy. This parameter is calculated as

$$\rho = \frac{A^{tot}}{\frac{1}{N}\sum_{i=1}^{N} \frac{\alpha_i}{|\vec{r}_i - \vec{r}_s|} e^{-|\vec{r}_i - \vec{r}_s|/\tau}}. \tag{3.25}$$

Apart from the total charge amplitude, A^{tot}, this energy estimator takes into account two factors. On the one hand, the acceptance of each PMT, α_i, depends on the angle of incidence of the hit. On the other hand, light attenuation produces an exponential loss on the deposited energy, where τ is the attenuation factor.

3.5 Track reconstruction algorithms in IceCube

As in ANTARES and KM3NeT, most track reconstruction methods in IceCube are likelihood based algorithms. The methods applied to the data samples used for the analysis described in Section 6.1 in Chapter 6 use the algorithms explained in [210], which were originally adopted for the AMANDA detector.

As in the algorithms mentioned in the previous sections, an initial fit (*first guess*) is performed in order to provide a starting point. The *line-fit* first guess algorithm assumes that all the hits in a track-like event follow a linear track given by $\vec{r}_i = \vec{r}_0 + \vec{v}t_i$, where t_i and $\vec{r}_i$ denote the detection time and the position of each hit. This method performs a χ^2 minimisation to obtain a vertex point, $\vec{r}_0$, and an initial direction, $\vec{v}$.

A single photoelectron likelihood maximisation which uses only the time information of the first photon detected by each PMT is performed in several iterations [184]. The direction and vertex obtained from the maximisation is then used as the starting point of a multi-photoelectron likelihood, which takes into account the time residual and amplitude information of the considered detected hits. The final value of the reconstructed direction and vertex are obtained from this maximisation. Furthermore, the angular error estimate of the reconstructed track can be obtained from the covariance matrix. The angular error is defined as $\sigma = \sqrt{\sigma_1 \sigma_2}$, where 1 and 2 are defined by the semi-major and semi-minor axes of the ellipse defined by a decrease of 1/2 in the maximum log-likelihood value [211].

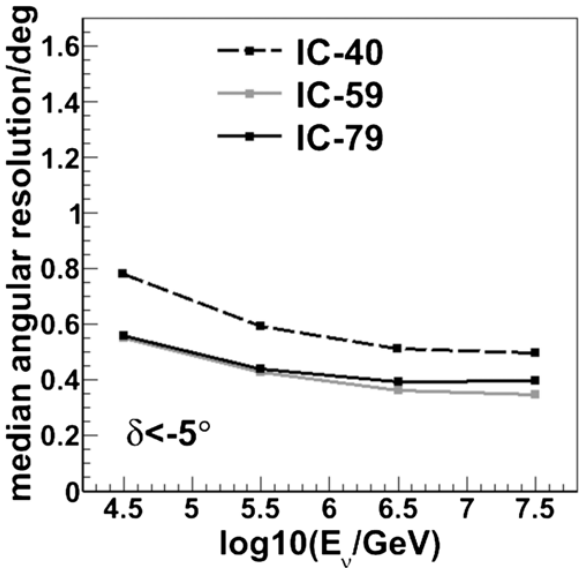

Fig. 3.8.: Median angular resolution for ν_μ CC track events in the IceCube 40, 59 and 79 string configurations for neutrino sources coming from the southern sky.

The reconstructed energy estimation is similar to the `dEdX` algorithm explained in Section 3.3.1. In the IC40 and IC59 configurations, named after the number of strings which IceCube had in the intermediate stages of construction, the average density of photons along the reconstructed track is used to obtain the final value [212]. The scattering and absorption lengths of light in ice, the angular acceptance of the PMTs and the distance of the DOM to the reconstructed track are taken into account. For the IC79

configuration, a more elaborate method was developed [213], in which the reconstructed energy is calculated by dividing the track into bins, and by considering the ratio of observed and expected photoelectrons (for a given energy) in each bin.

The pointing accuracy of the track reconstruction method is different in each of the IceCube configurations, as it can be seen in Figure 3.8. A comparison with the 2007-2012 ANTARES point-source analysis sample is shown in Section 6.1 in Chapter 6.

4 Time calibration in the ANTARES neutrino telescope

The time calibration of ANTARES is vital for its proper operation. On one hand, the reconstruction of the detected events requires a precise calibration between OMs to be performed. On the other hand, the time of these events needs to be measured with precision to be able to correlate them with those observed from other experiments. In this chapter, the different methods used for the time calibration of the ANTARES telescope are described. The final results of the time calibration are also presented.

4.1 Time calibration methods in ANTARES

Two main types of time calibration need to be taken into account in ANTARES [158]. The first one is related to the absolute timing of an event with respect to the universal time (absolute time calibration). This is required to correlate the events in the detector with any phenomena observed by other experiments. The second type of time calibration corresponds to the relative calibration between PMTs. This is a more demanding calibration, since a $\sim$1 ns level accuracy is required to obtain an angular resolution of $\sim 0.3^{\circ}$ for reconstructed muon neutrino events above 10 TeV.

4.1.1 Absolute time calibration: The echo-based clock system

An echo-based clock system was developed to provide a time synchronisation of all the electronic modules of the ANTARES detector. The absolute time is synchronised with respect to the GPS signal at the level of 100 ns. This system is implemented to also measure the time delays due to the electronic paths from the shore station to each LCM, which corresponds to the main source of miscalibration for the determination of the absolute time.

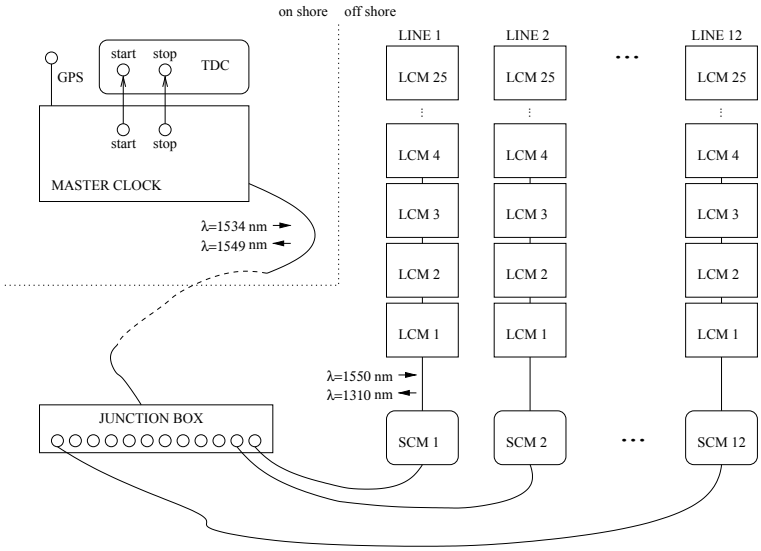

Fig. 4.1.: Schematic view of the echo-based clock system in ANTARES. Figure obtained from [158].

Figure 4.1 shows a schematic view of the clock system, which provides a synchronisation of all the electronic modules. The master clock sends an infrarred signal of $\lambda = 1535$ nm to all SCMs at a frequency of 20 MHz. Then, each SCM sends a $\lambda = 1550$ nm signal to the LCMs of its correspoding line. The LCMs send back a signal of 1310 nm to the SCM, which transmits a 1549 nm signal to the master clock.

The time delays due to the electronic paths are measured using round-trip signals which are sent to each LCM every hour. The total round-trip signal time corresponds to twice the time to reach an individual LCM. Figures 4.2 and 4.3 show the time delay evolution for the round trip signals sent from the shore station to the SCM and from an SCM to an LCM, respectively. A global variation of the order of a few hundreds of picoseconds is observed.

4.1.2 Relative time calibration

Relative time calibration between OMs is crucial for the reconstruction of events. The precision of this time calibration is limited by several unavoidable factors coming from the electronics and environmental factors [158]. The optical properties of water at a level of 1 pe (especially the chromatic dispersion and light scattering) produce an uncertainty of $\sigma_{water} \approx 1.5$ ns

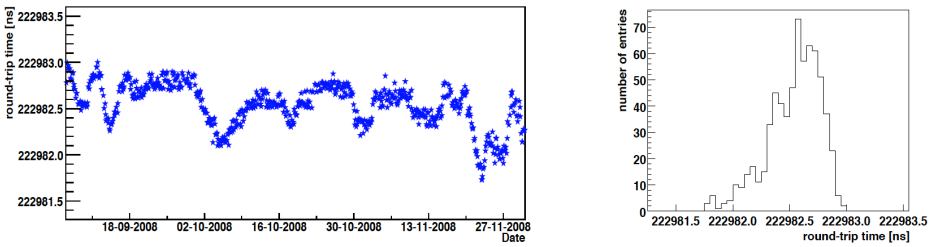

Fig. 4.2.: Time evolution of the round-trip signal sent from the shore station to an SCM. Variations of the order of a few hundreds of picoseconds are seen. Figure obtained from [158].

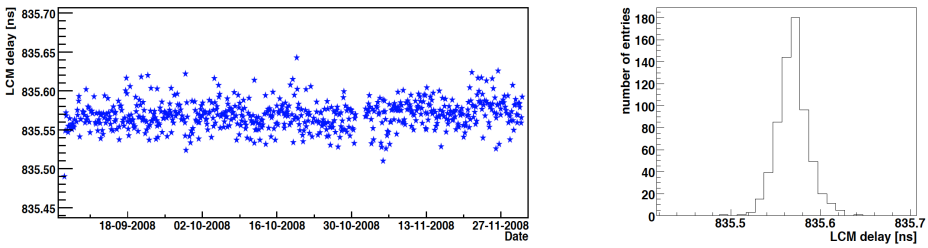

Fig. 4.3.: Time evolution of the round-trip signal sent from an SCM to an LCM on the same line. Deviations of the order of tens of picoseconds are seen. Figure obtained from [158].

for Cherenkov photons produced at a distance of 40 m from a PMT. The uncertainty due to the transit time spread (TTS) of the PMTs is $\sigma_{TTS} \approx$ 1.3 ns. The electronic effects, which we estimate with the time calibration methods presented in this chapter, have an overall time uncertainty of $\sigma_e \sim$ 0.5 ns. If we combine these effects, the global uncertainty for the time measurements obtained can be expressed as [148],

$$\sigma^2 = \frac{\sigma^2_{water}}{N_\gamma} + \frac{\sigma^2_{TTS}}{N_{pe}} + \sigma^2_e \,, \tag{4.1}$$

where N_{pe} is the number of photoelectrons arriving to a PMT, and N_γ is the number of Cherenkov photons emitted. Assuming that both N_{pe} and $N_\gamma >>$ 1, uncertainties under the 1 ns level can be achieved.

Prior to the deployment of each line, the time calibration of all the ARSs is performed in order to calculate its T0 values. A T0 value is defined as the time between a photon hits a PMT and its signal reaches the shore

station. Due to environmental reasons, the degradation of the electronics and the PMTs, and the changes in the voltage supply of the PMTs, the T0 values may change over time. Because of this, every time there is a change in the voltage supply of the PMTs, a new table of T0 values needs to be provided. Furthermore, it has been shown that the connection of a line has produced changes in the time offsets between lines. Because of these reasons, in-situ calibrations need to be carried out. For this purpose, different methodologies, such as the use of renconstructed muon tracks, coincident events coming from the radioactive decay of ^{40}K nuclei and the Optical Beacon system have been used.

On-shore time calibration

A complete time calibration is performed before a line is deployed. This procedure consists on the simultaneous illumination of a group of OMs by using short pulses from the same source. The actual experimental setup can be seen in Figure 4.4. A Nd-YAG laser which emits short (FWHM $\approx$ 0.8 ns), green ($\lambda = 532$ nm) and intense (1 μJ) pulses at a frequency of 1 kHz was used. A photodiode is attached to this laser, which permits the measurement of the pulse time emission. The light emitted by the laser is splitted via a 1-to-16 splitter to reach the 15 OMs of a given sector. The light is then transmitted through optical fibers, which have been set up to add a maximum of a 0.3 ns delay. The light is afterwards distributed over the surface of the destination PMT by means of a Lambertian[1] diffuser.

Laser and LED Optical Beacon Systems

The idea behind the Optical Beacon (OB) system [214] is similar to the on-shore calibration: it uses the pulsed light emitted from a laser or a LED to obtain the time offsets. These time offsets are calculated by using the information of the time residual between the time of the emission of the pulse and the detection time in the destination ARS. Once the time residual distributions have been obtained for all the ARSs or lines to be calibrated, a

[1] A Lambertian diffuser produces an intensity proportional to the cosine of the angle between the direction of the incident light and the surface normal.

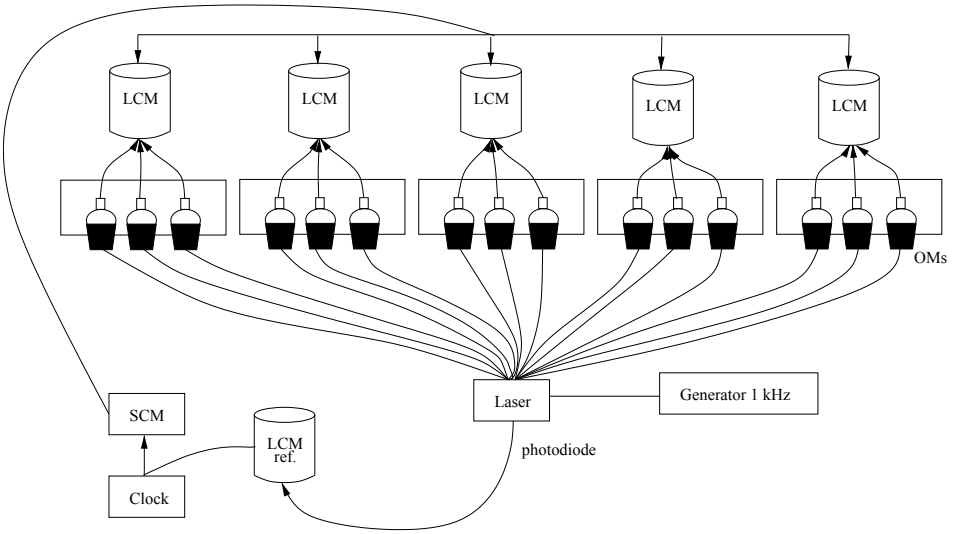

Fig. 4.4.: Schematic view of the on-shore time calibration. Figure obtained from [158].

fit to a convoluted Gaussian with an exponential is performed, from which the peak time residual is obtained. A more detailed description of the procedure can be found at [148].

Apart from its use for time calibration purposes, this system has also been used to perform measurements of the optical properties of water, as mentioned in Section 2.2.6.

The Laser Optical Beacons

The Laser Optical Beacons or LOBs (see Figure 4.5) contain a Nd YAG laser which emits green ($\lambda = 532$ nm) and high intensity ($\approx 1\ \mu$J) short (< 1 ns) pulses. The laser is encapsulated in a Titanium cylinder (70 cm height, 17 cm diameter) with a Lambertian diffuser on its top, so to spread the light pulse over a cosine distribution. A quartz rod is located on the top of the cylinder so that the light exits laterally and the effect of the sedimentation of microorganisms is avoided. An internal photodiode is also found at the laser head to measure the pulse emission time. There is a laser beacon at the bottom of three lines (line 7, line 8 and the Instrumentation Line). Due

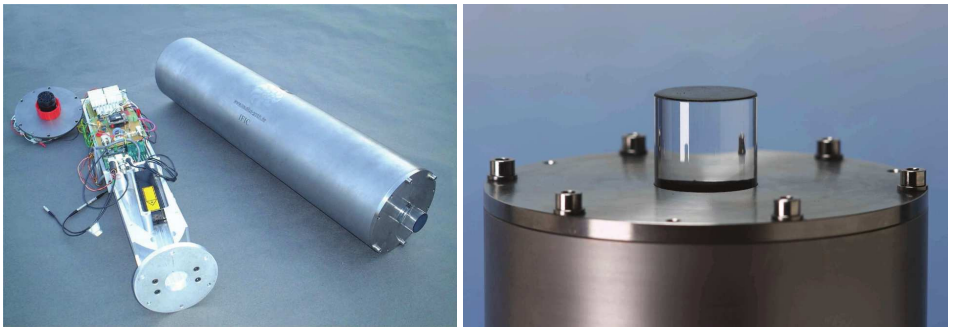

Fig. 4.5.: Left: The Laser OB. Right: The upper part of the Laser OB. Figures obtained from [214].

to the high intensity of the pulses, they can be detected up to at least the 10th floor of all the lines.

The LOB system has been used for the calculation of the time offsets between lines (inter-line calibration). For this purpose, only the OMs which are at distances between 150 and 250 m from the LOB are considered, so that the detected hits correspond to single photoelectrons. Currently, one run of 5-10 minutes is taken every Monday.

The LED Optical Beacons

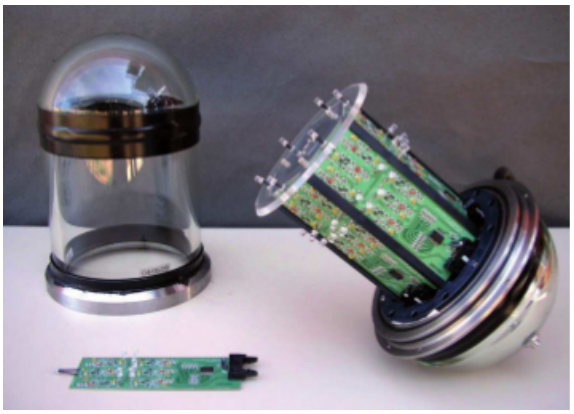

Fig. 4.6.: A photograph of an LED OB. Figure obtained from [158].

A LED Optical Beacon or LED OB (see Figure 4.6) consists on 36 blue (λ = 472 nm) LEDs placed on an hexagonal prism. These LEDs emit 4 ns width (FWHM) pulses with intensities of 160 pJ per flash. Six LEDs are placed per

each face of the hexagonal prism. In each face, one LED is located at the top, one at the centre of the surface, and four around the latter. An 8 mm surface photocatode is located inside of the prism to detect the light emitted by the LED OB. In order to withstand the high pressures at the depth of ANTARES, the prism is encapsulated over a glass cylinder with two hemispheres at the extremes.

A total of four LED beacons (at storeys 2, 9, 15 and 21) are installed per each line. The LEDs located on top can illuminate distances up to 8 floors above (distances up to 120 m from the LED OB), although only the information from the 7 farthest are used in the time calibration procedure (the OMs of the floor which are just above the LED OB are not considered, since the light of the LED OB saturates them). The hits detected by the OMs at these distances from the LED OB correspond to multi photo-electron hits, and therefore are subject to the early photon effect (see Section 4.1.3). Because of this, a linear dependence of the peak time residual with respect to the distance is observed.

The LED OB runs are taken every two months. A 5-10 minute duration run flashing two alternate OBs is performed in every line.

A few disadvantages appear in the LED OB time calibration. The lowest three floors of each line cannot be calibrated with this method due to the absence of a LED OB under them. Furthermore, the last sector (floors 23-25) has only three floors to measure the linear dependence caused by the early-photon effect (see Section 4.1.3). Due to the degradation of the OMs, similar problems have appeared in other sectors of the detector.

^{40}K calibration

The ^{40}K calibration [215] [216] relies on the Cherenkov photons produced after the decay of ^{40}K nuclei. If a decay is produced within a few meters from a storey, a coincident signal can be observed simultaneously in a pair of its OMs (ARSs). Figure 4.7 shows an example of the time differences of events with coincidences smaller than 50 ns. A Gaussian peak is observed in the centre, which corresponds to coincident ^{40}K events. This peak is observed

on top of a flat background, which is attributed to non-correlated ^{40}K hits from different nuclei which were observed in the same time window.

This time calibration method is the simplest and least model dependent which can be performed. Furthermore, it does not require the use of dedicated runs. Therefore, data taking is not interrupted. However, it is only limited to the relative calibration between ARSs in the same storey.

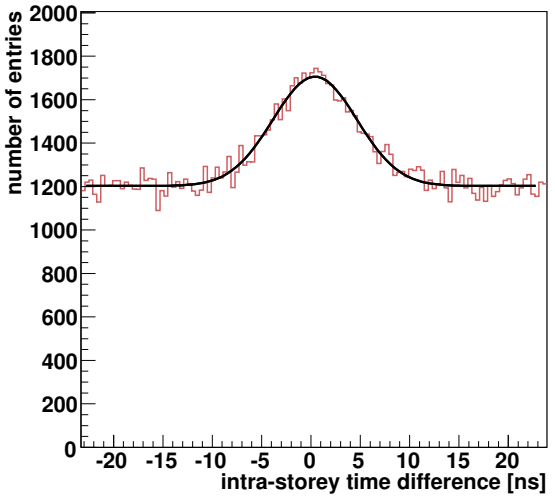

Fig. 4.7.: Distribution of the time differences on hits detected from two different OMs in the same storey within a maximum time range of 50 ns. Figure obtained from [217].

Calibration with atmospheric muons

The calibration with atmospheric muons relies on the time information of the hits coming from reconstructed muon tracks (mostly, down-going atmospheric muons). In ANTARES, the rate of triggered atmospheric muons ranges between 1-10 Hz. In this calibration, the muon track is reconstructed by using all the hits from the ARSs/Storeys/lines except the ones recorded by the element to be calibrated. The time offsets are afterwards calculated by considering the time difference between the expected hit time according to the reconstructed time and the actual arrival hit time. The complete procedure is explained with more detail in Section 4.2.

Both the inter-line (determination of time offsets between lines) and the intra-line (determination of time offsets between ARSs or storeys) calibrations can be performed with this method (including the sectors that cannot be calibrated with the LED OB system) without interrupting the physics data taking. However, it requires the use of several runs (of at least 1 week). Furthermore, in order to require enough statistics, the use of down-going tracks is required, and therefore the scattering effects may play a negative role.

Nanobeacon

As an experimental procedure to evaluate an alternative type of calibration to the LED OB system to be used in KM3NeT, the nanobeacon system was developed [218]. A nanobeacon consist of a blue LED ($\lambda = 470$ nm) which is located inside and at the top of an OM. Nanobeacons have only been installed at the OMs of the first floor in line 9. It has been shown that the light emitted from the nanobeacons can reach up to floor 20 (275 m). A similar procedure to the LED OB system can be followed to perform the calibration. Since no dedicated PMT is attached to the nanobeacon, an OM of an upper floor needs to be used as reference. The presented results in different Collaboration Meetings [219] [220] [221] show the feasibility of this method.

Internal LED calibration

An internal LED to measure, evaluate and monitor the PMT transit times is located inside all the OMs. The LED model is the same as the one used for the LED OBs, and they are placed at the back of the phototube. In the internal LED runs, the internal LEDs are triggered by the clock signal and illuminate the PMTs. Variations with RMS smaller than 0.2 ns have been observed over time [158].

4.1.3 Time measurement corrections

Limitations on the electronics used in ANTARES have shown to produce non negligible effects on the time measurement of hits. The most relevant effects are described below.

Walk effect

The time of a recorded hit corresponds to the time in which the detected signal is above the 0.3 photoelectron threshold. As it is shown in Figure 4.8-left, hits with higher detected charge amplitudes surpass this threshold earlier. Figure 4.8-right shows the time recorded as a function of the pulse amplitude. This effect is more relevant for hits with lower collected charges, as seen on these figures.

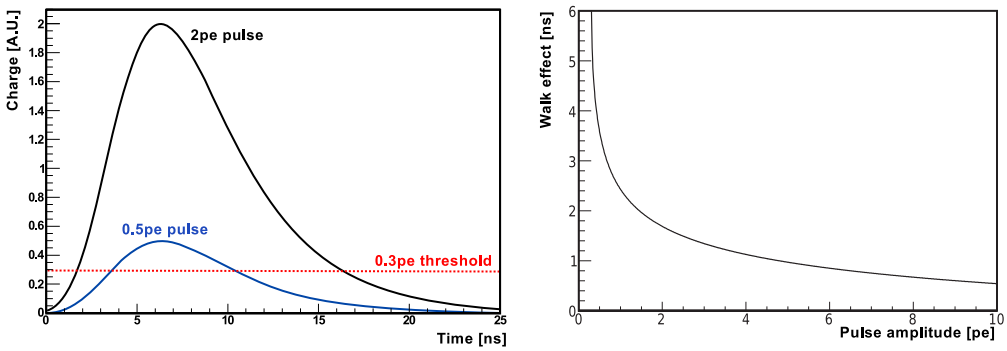

Fig. 4.8.: Examples of the walk effect. Left: Schematic view of the walk effect. Right: Time recorded as a function of the pulse amplitude. Figures obtained from [148] and [158], respectively.

TVC calibration and Differential-non-linearities

A perfectly operating TVC should have its 256 channels in operation. Since this is usually not the case, the minimum and maximum working channels have to be obtained in order to estimate the recorded hit time between two consecutive clock phases (see Equation 2.8 from Chapter 2). The determination of these values can be obtained using physics runs (standard data taking runs) in which the TVC channels are filled randomly.

An example of a TVC distribution can be found in Figure 4.9. Ideally, all the TVC channels should contain the same amount of entries. However, caused by the non-uniform answer of the ADC of each ARS, an unequal distribution is observed. This is usually known as the Differential-non-linearities (DNL) effect. An error of $\sim$0.3 ns is attributed to this effect. This could be avoided by using the cumulative TVC distribution of each TVC. As a consequence, the hit time would be assigned depending on the bin size. Although this solution could improve the hit time error ($\sim$0.1 ns), it is currently not implemented, since it would require the addition of $\sim$ 1 million values in the TVC calibration tables.

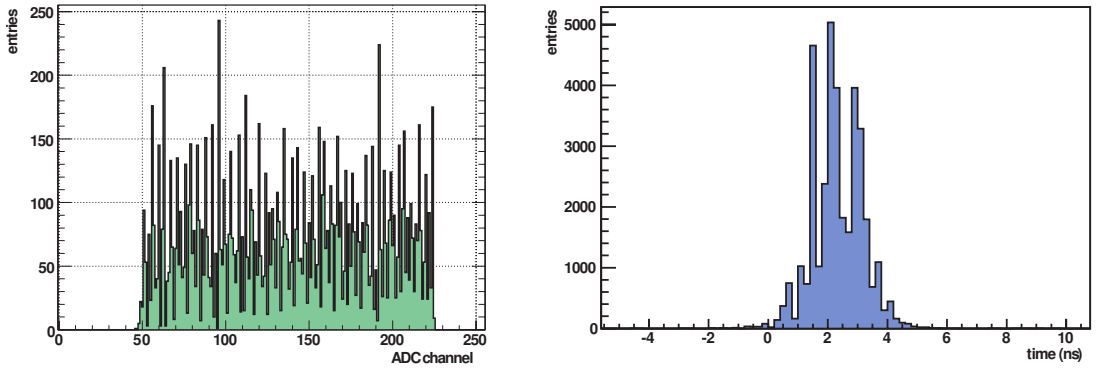

Fig. 4.9.: Left: Example of a TVC distribution on a physics run showing the DNL effect. Right: Hit time arrival distribution due to the flashing of the LED OB in line 12 floor 9 observed in the ARS 1 of line 12 floor 12. The peaked shaped distribution is due to the DNL effect. Figures obtained from [148].

Token-ring effect

As mentioned in Section 2.2.4, the two ARS associated with a particular OM work under a token-ring protocol. Once a hit is detected by an OM, one of the ARS begins a 40 ns integration time. The following ARS begins the data taking 10 to 20 ns after this integration time. If there is still a charge to be integrated, a new hit is registered by the second ARS. This effect is especially important for the LED and nanobeacon hits, since they happen in the multi photo-electron region.

Early photon effect

The PMTs cannot resolve the arrival of many photons coming in a very short period of time. In these situations, the time recorded for the flash is the time of the first arrival photon. This is of particular relevance in the LED OB and nanobeacon calibrations, in which very intense pulses are emitted with a width smaller than the integration time of the PMTs, but larger than their time resolution for single photoelectron hits. Therefore, a PMT close to a flashing LED OB records the time of the first arriving photon, which corresponds to one of the first photons emitted in each pulse. In other words, most of the pulse photons will arrive to the PMT once the charge integration has begun. However, the hit time distribution recorded by a PMT far enough so that it only detects less than one photon per flash in average, will correspond to the one of the emitted pulse. As a consequence, an approximately linear effect in the time delay is observed with respect to the distance between the source and the PMTs [222].

4.2 Update on the ANTARES time calibration procedure

During the studies of the efficiency loss of the optical modules by using coincident events from ^{40}K decays, a cross-check of the time calibration was performed [216]. In this cross-check, the hit time differences between OM pairs of the same storey were evaluated. This showed a discrepancy in the results: Figure 4.10 shows the time differences between OM pairs using physics runs from November 2010, in which a perfect calibration would correspond to a single peak centred at 0 ns. The level of discrepancy is not crucial for the reconstruction, since the RMS of the distribution is of the order of the 1 ns level. However, the evolution of the time offsets showed unexpected behaviours over time for a considerable amount of OM pairs, as seen in Figure 4.11.

Discrepancies on the three first and the three last storeys of all lines are expected. As mentioned in Section 4.1.2, these correspond to floors which cannot be calibrated or which can be calibrated with difficulties by the OB system. However, these discrepancies are also found on OMs from storeys

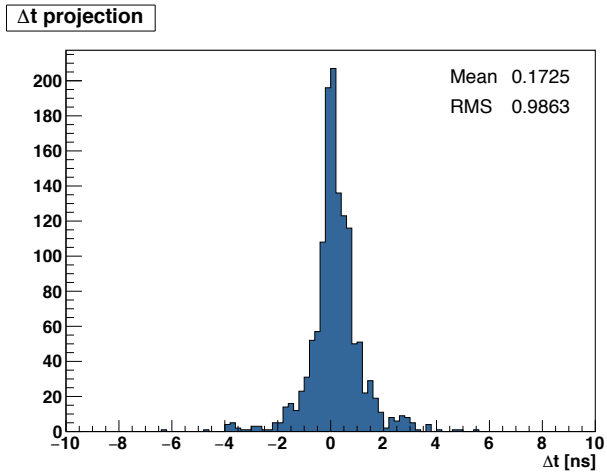

Fig. 4.10.: Distribution of the time differences between OM pairs obtained using ^{40}K coincident events from runs in November 2010.

properly illuminated by the LED OBs. Changes in the time offsets over time take place when a High Voltage tuning is performed, which may show a small bias of the LED OB method. However, gradual increases and decreases show effects which cannot be correlated with this.

To verify the validity of the ^{40}K cross-check results, an independent analysis using the information of reconstructed muon tracks was performed. This was obtained in the following procedure:

- Only reconstructed tracks with Λ > -6.5 were considered.
- All hits detected at the floor of the OM pair to be considered are excluded from the muon track reconstruction.
- Time residuals of the rest of the hits are calculated. The difference between the time residuals for a pair of OMs is taken (see Figure 4.12).
- Once this is repeated for several events and for all possible OM pairs, a Gaussian fit over the distributions of the time differences between each pair is done, as it is done in the ^{40}K calibration.

The comparisons of the OM pair time differences with ^{40}K calibration and muon calibration for November 2010 are shown in Figure 4.13. The difference between both calibrations present a distribution with a statistical

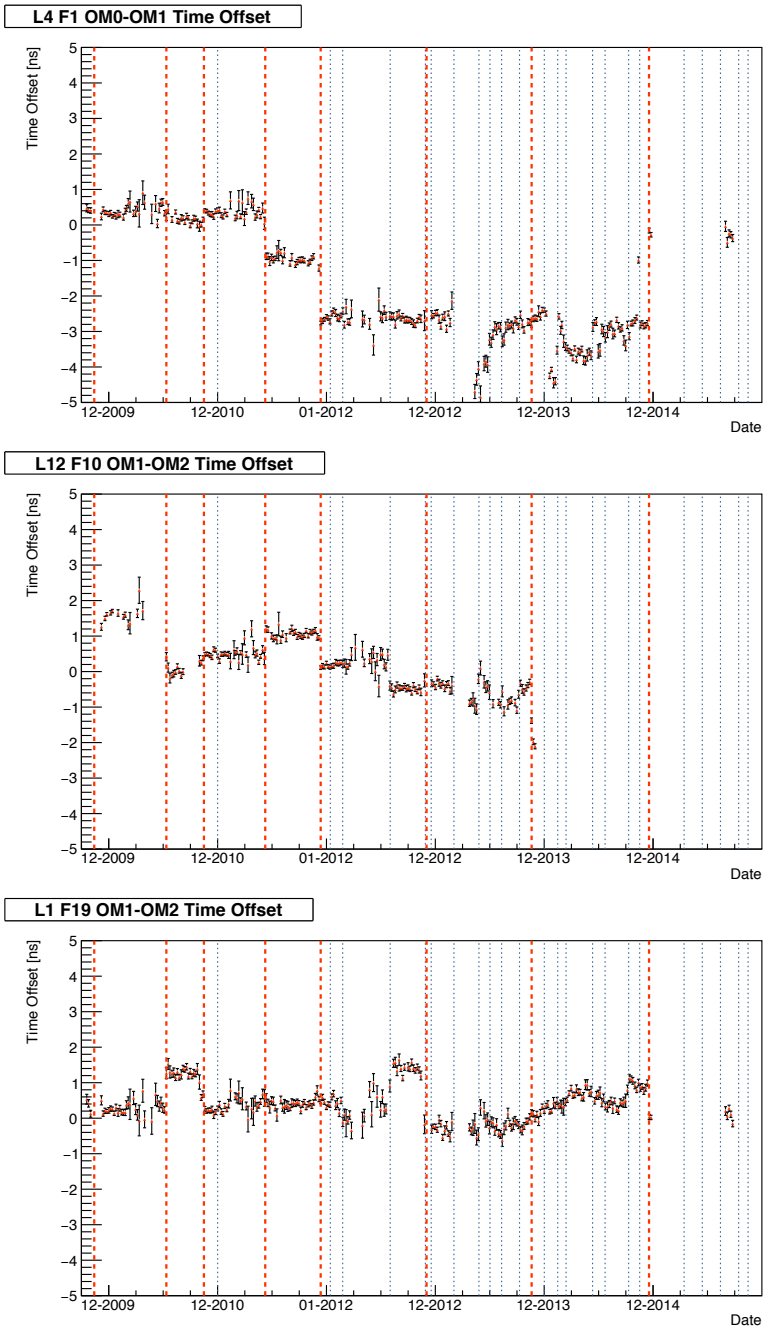

Fig. 4.11.: Evolution of the time offsets calculated with ^{40}K coincidences. Each vertical red line corresponds to a high voltage tuning. The blue lines correspond to other changes (either due to the connection of a line or simply a change after a set of LED OBs runs).

deviation smaller than 0.5 ns, which is smaller than the difference with the LED OB calibration. The specific case obtained for the OM pairs in Line 6 is shown in Figure 4.14.

The time evolution of these time differences was also calculated using reconstructed atmospheric muon tracks from data taken in 2010. The data was divided in steps of two months. Per each step, only a total amount of data runs corresponding to a total livetime between one and two weeks was considered. Examples for three different cases are shown in Figure 4.15. A similar evolution over time is observed with both methods.

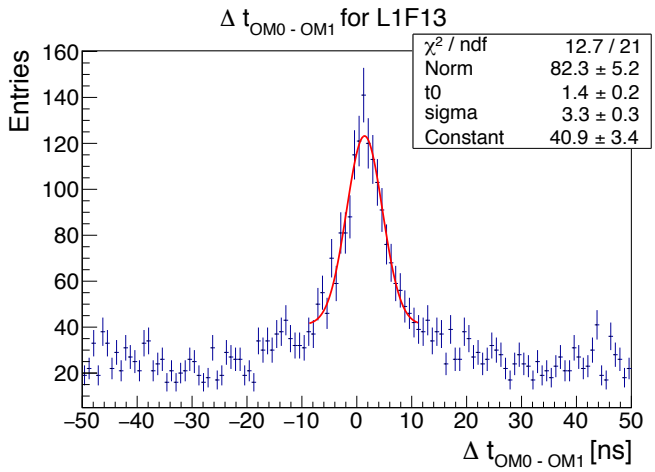

Fig. 4.12.: Distribution of the time differences from coincidence hits coming from reconstructed muon tracks for OM0 and OM1 in line 1, floor 13.

4.2.1 Procedure

Given the previous results, a new calibration procedure which combines the calibration with reconstructed atmospheric muon tracks and with ^{40}K events is proposed. This calibration is divided in three steps:

1. **Inter-line calibration with atmospheric muons**, in which the time offsets between lines are calculated.
2. **Intra-storey calibration with ^{40}K events**, which allows to obtain the time offsets between ARSs in the same storey.
3. **Inter-storey calibration with atmospheric muons**. This procedure is used to obtain the time offsets between storeys. In this step, the

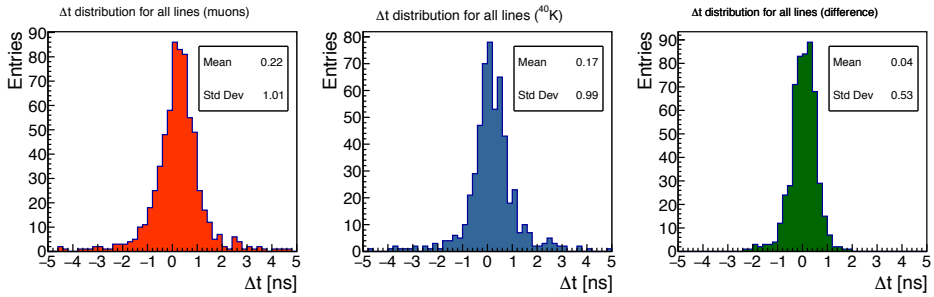

Fig. 4.13.: Time differences for OM pairs obtained using atmospheric muon tracks (left) and ^{40}K events (centre). The figure on the right shows the difference between the time differences obtained with both methods.

time offsets calculated in the inter-line and intra-storey calibrations are included.

Inter-line calibration with atmospheric muon tracks

The inter-line calibration consists in the calculation of the time offsets between lines. The procedure is similar to the one described in [217] and [197], although calculated in a much larger interval (beginning of 2007 until the end of 2016). Since the inter-line offsets are not constant over time, the whole 2007-2016 data taking period was divided in steps of one month. In each monthly step, the values of the time offsets between lines were calculated. The amount of runs considered in each step was taken so that the sum of their livetimes corresponds to a time range between one and two weeks. In order to be considered, the runs had to fulfil the same quality criteria as in the ANTARES physics analyses. However, in the very few cases in which there were not enough good quality runs so to reach this livetime, an attempt to calculate the time offsets was still carried out.

Per each considered monthly step, the inter-line calibration is performed as follows. In a given iteration, only events with $\Lambda >$ -6.0 are considered. Per each event, a line is selected randomly, and the hits from that line (*probe hits*) are excluded from the reconstruction, which is performed with the remaining hits (*reco hits*). The time residuals are calculated for the probe hits. After repeating this procedure for several events, time residual distributions for all lines in operation are obtained. A fit to a Gaussian plus

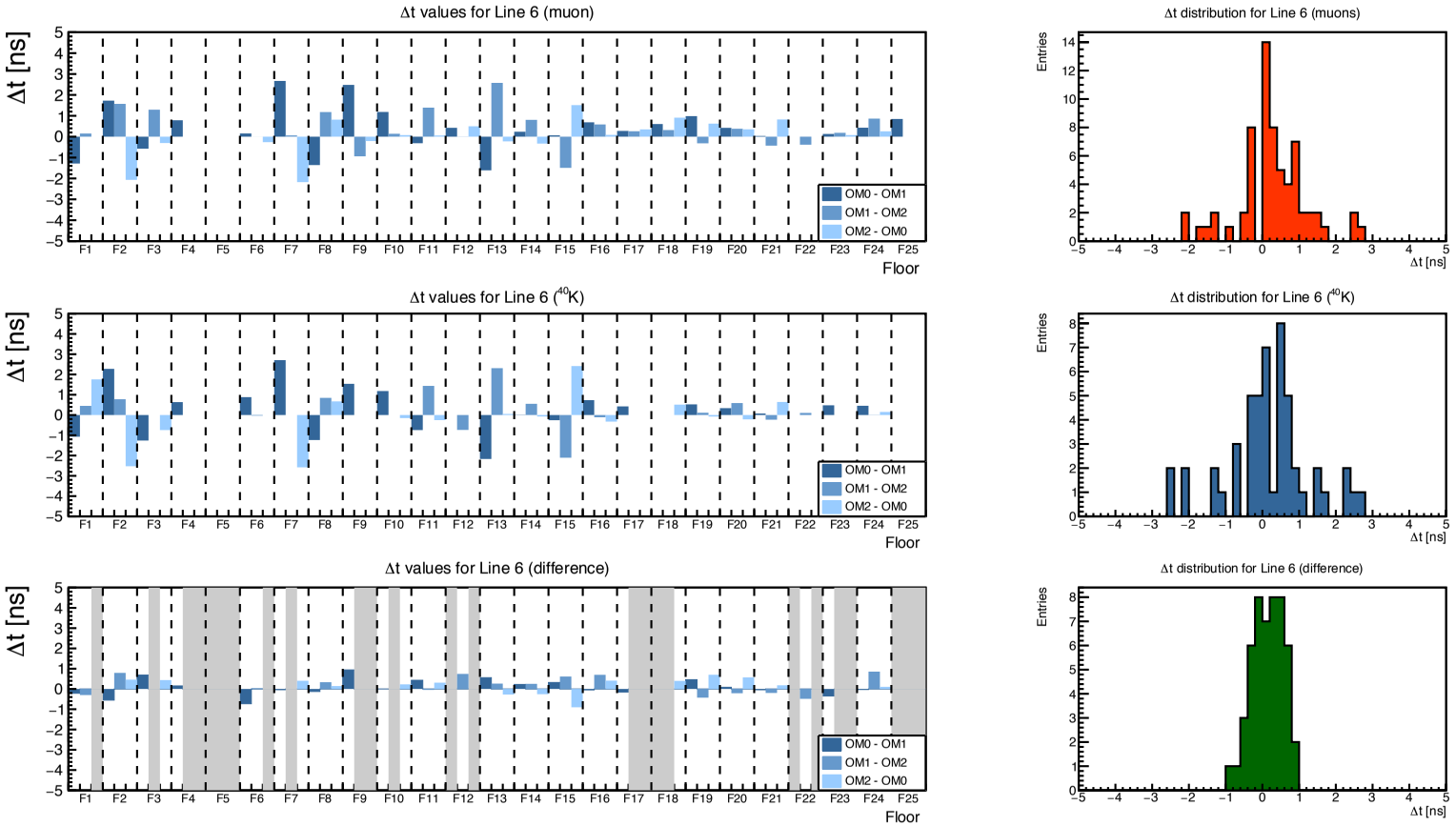

Fig. 4.14.: Time differences for OM pairs in Line 6 obtained with the atmospheric muon calibration (top left), the ^{40}K calibration (middle left), and their difference (bottom left). The distributions on the right are the projections of the plots on the left.

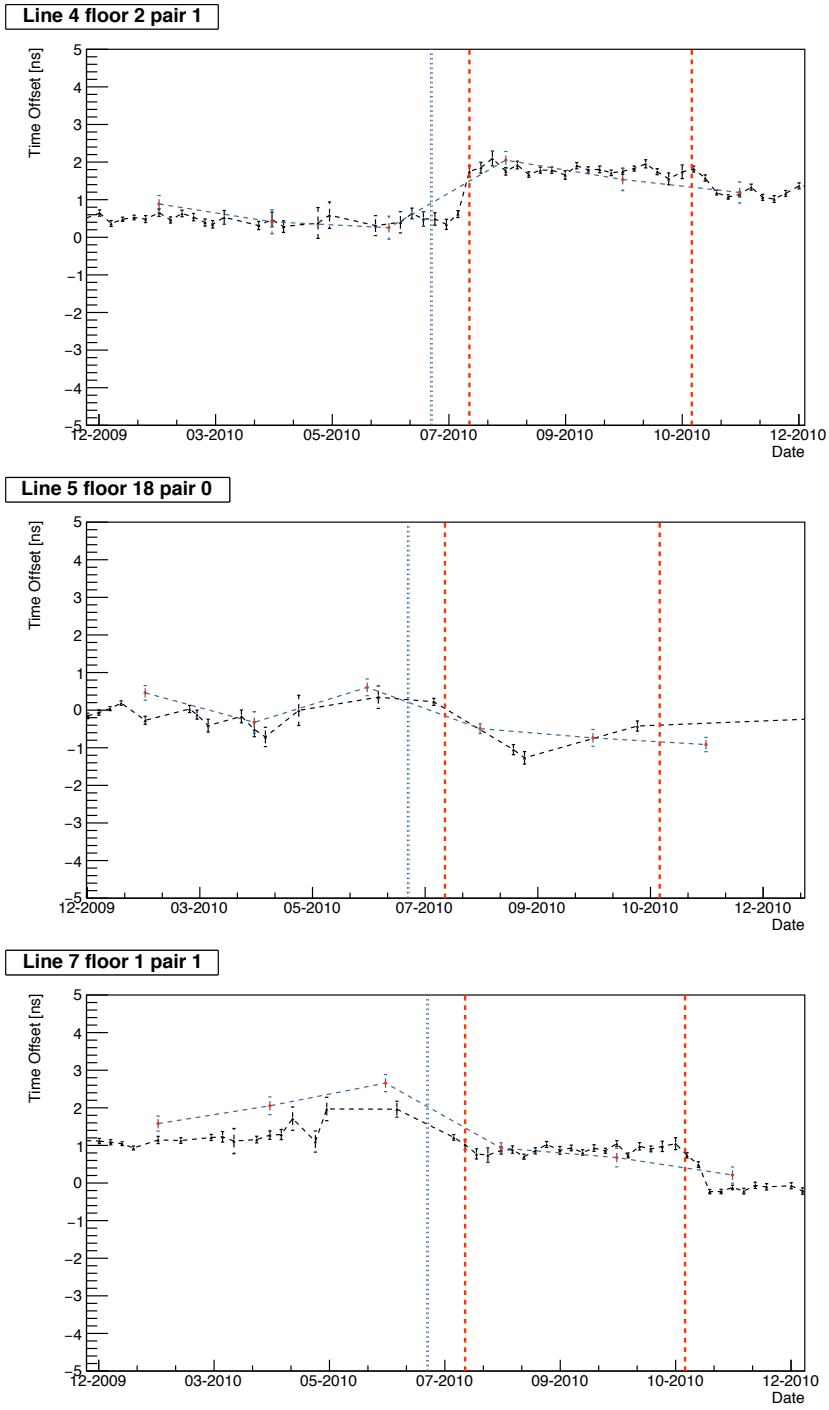

Fig. 4.15.: Evolution of the time offsets calculated with ^{40}K coincidences (black points) and with atmospheric muon tracks (red points) for three different OM pairs. Each vertical red line corresponds to a high voltage tuning. The vertical blue lines correspond to changes due to other reasons (either a connection of a line or after a set of LED OB runs).

a constant is made around the peak of the distribution (see Figure 4.18 as an example). The mean value of the Gaussian fit, $t_{i,fit}$, is extracted for each i line. Since the average of these mean values, $\bar{t}_{fit}$, is usually non-zero, the correction to be applied to each line is taken as $t_{i,corr} = t_{i,fit} - \bar{t}_{fit}$.

These corrections are then introduced in the following iteration. The procedure is repeated until a convergence is assured. In order to evaluate the convergence, the following quantities have been defined:

- The average time correction for a given line using all the iterations until a given iteration ($t_{i,corr,avg}$).
- The standard deviation of the difference between $t_{i,corr,avg}$ and $t_{i,corr}$ for a given iteration ($\sigma_{\Delta T}$).

The convergence limit was set to $\sigma_{\Delta T} \leq 0.4$ ns. After a total of seven iterations, a few of the monthly steps did not reach to this convergence. These months correspond to moments with high bioluminescence, and therefore, with a smaller amount of available runs.

The evolution of the inter-line time offsets as a function of the iteration for January 2011 is shown in Figure 4.16. The corresponding time residual distributions for line 8 in the first and last iterations is shown in Figure 4.18. A decrease of the statistical deviation of the corrections is seen when the number of number of iterations increases, as shown in Figure 4.17.

Results of the inter-line offsets obtained in each of the monthly steps considered for all lines are shown in Figures 4.19, 4.20 and 4.21. Each point corresponds to the last iteration value of $t_{i,corr,avg}$ per each considered monthly step. As it can be seen in these figures, similar values are obtained for different months: the time offsets only change after a line is connected, with only one exception at the beginning of 2011. In this case, a significant deviation is observed, especially in lines 1 and 8. This deviation is present because the official T0 tables contained the inter-line offsets calculated using the Laser OB calibration instead of the calibration using atmospheric muons from [217] and [197].

The final values considered for the inter-line offsets in the official ANTARES database have been calculated by considering the average of seven inter-line

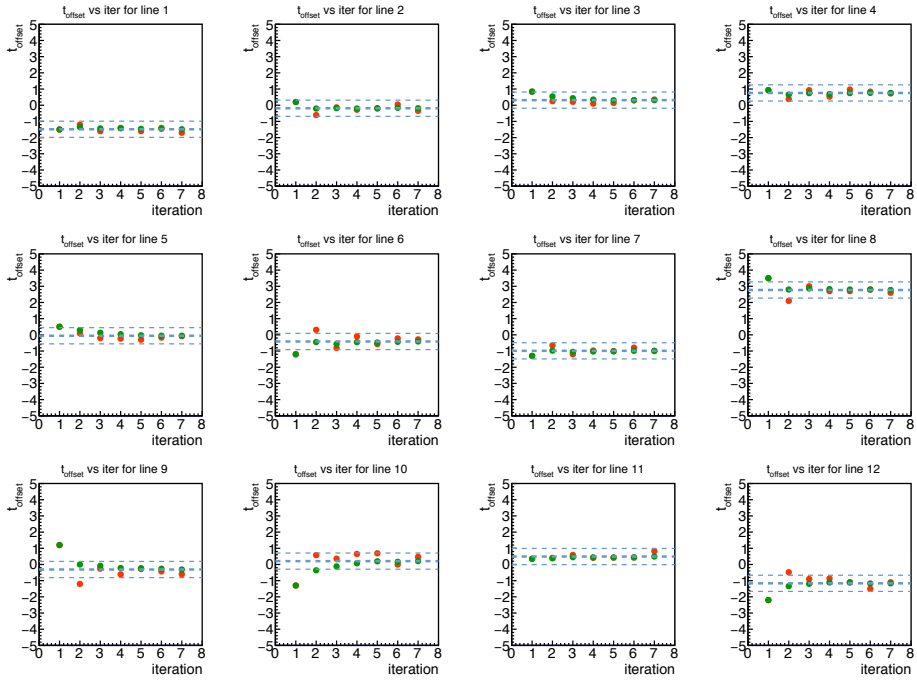

Fig. 4.16.: Inter-line time offsets calculated in January 2011 for all lines as a function of the iteration. The red dots indicate the value which is introduced in the following iteration. The green dots correspond to the average until a given iteration.

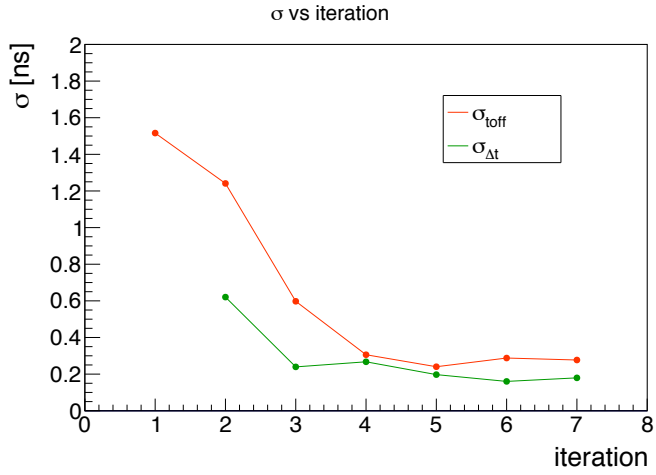

Fig. 4.17.: The green line ($\sigma_{\Delta t}$) shows the mean difference between the correction applied in a given iteration and the average correction. As a comparison, the statistical deviation of the differences on the time corrections between two consecutive iterations (σ_{toff}) is shown in red.

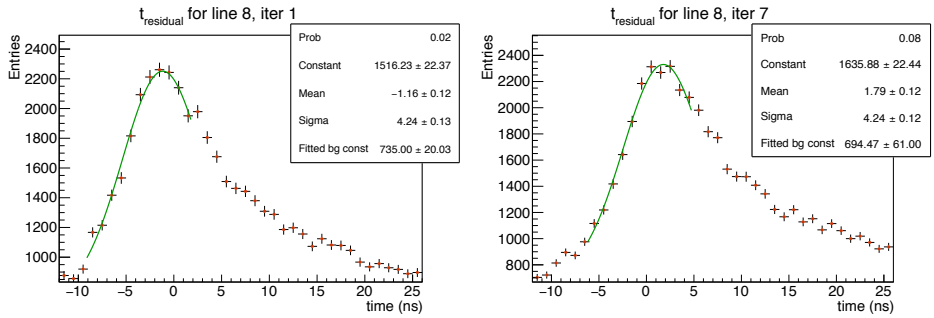

Fig. 4.18.: Time residual distribution for line 8 using runs from January 2011 after one (left) and seven (right) iterations. The green line shows the fitted curve.

periods, corresponding to the main variations in the inter-line offsets. These values and the corresponding periods of validity are included in Table 4.1.

Start date	Final date	L1	L2	L3	L4	L5	L6	L7	L8	L9	L10	L11	L12
01/01/2007	07/12/2007	0.44	-2.50	0.93	0.56	0.54	0.00	0.00	0.00	0.00	0.00	0.00	0.00
07/12/2007	17/05/2008	0.42	-2.10	0.13	0.51	0.16	-0.52	0.39	0.13	0.28	0.73	0.00	0.00
17/05/2008	07/11/2009	0.55	-1.30	0.01	0.63	0.03	-0.04	0.29	-0.16	-0.39	0.54	-0.16	0.45
07/11/2009	04/11/2010	0.27	-0.78	-0.13	0.85	0.12	0.00	0.23	-0.13	0.00	-0.05	-0.19	-0.20
06/11/2010	01/01/2012	-1.80	-0.34	0.35	0.88	0.03	0.01	-0.89	2.70	-0.33	-0.03	0.61	-1.00
01/01/2012	02/08/2012	-0.29	-0.72	-0.18	1.40	-0.10	-0.47	-0.03	0.71	0.30	-0.61	0.41	-0.47
02/08/2012	01/01/2017	-0.45	-0.60	-0.42	1.40	-0.01	-0.68	-0.11	0.83	0.60	-0.19	-0.56	-0.17

Tab. 4.1.: Final values (in ns) of the inter-line offsets for each considered period.

Intra-storey calibration with ^{40}K events

The time offsets between ARSs in the same storey are obtained with the use of ^{40}K events. As described in Section 4.1.2, this method is based on coincident ^{40}K events which are observed in two ARSs of the same floor within a time window of 50 ns. Once the average time difference is obtained after the Gaussian fit, one ARS is taken as reference, in such a way that the time offset between this ARS and any other OM in the same storey is obtained (Δt_{ri}, where r corresponds to the reference and i is another ARS in the same floor). Since the two ARS of the reference OM are never operating at the same time, the time offset between them is computed with the help of a third ARS from another OM in the same storey. In this case, the time offset can be calculated as $\Delta t_{rk} = \Delta t_{rj} - \Delta t_{jk}$, where r is the reference

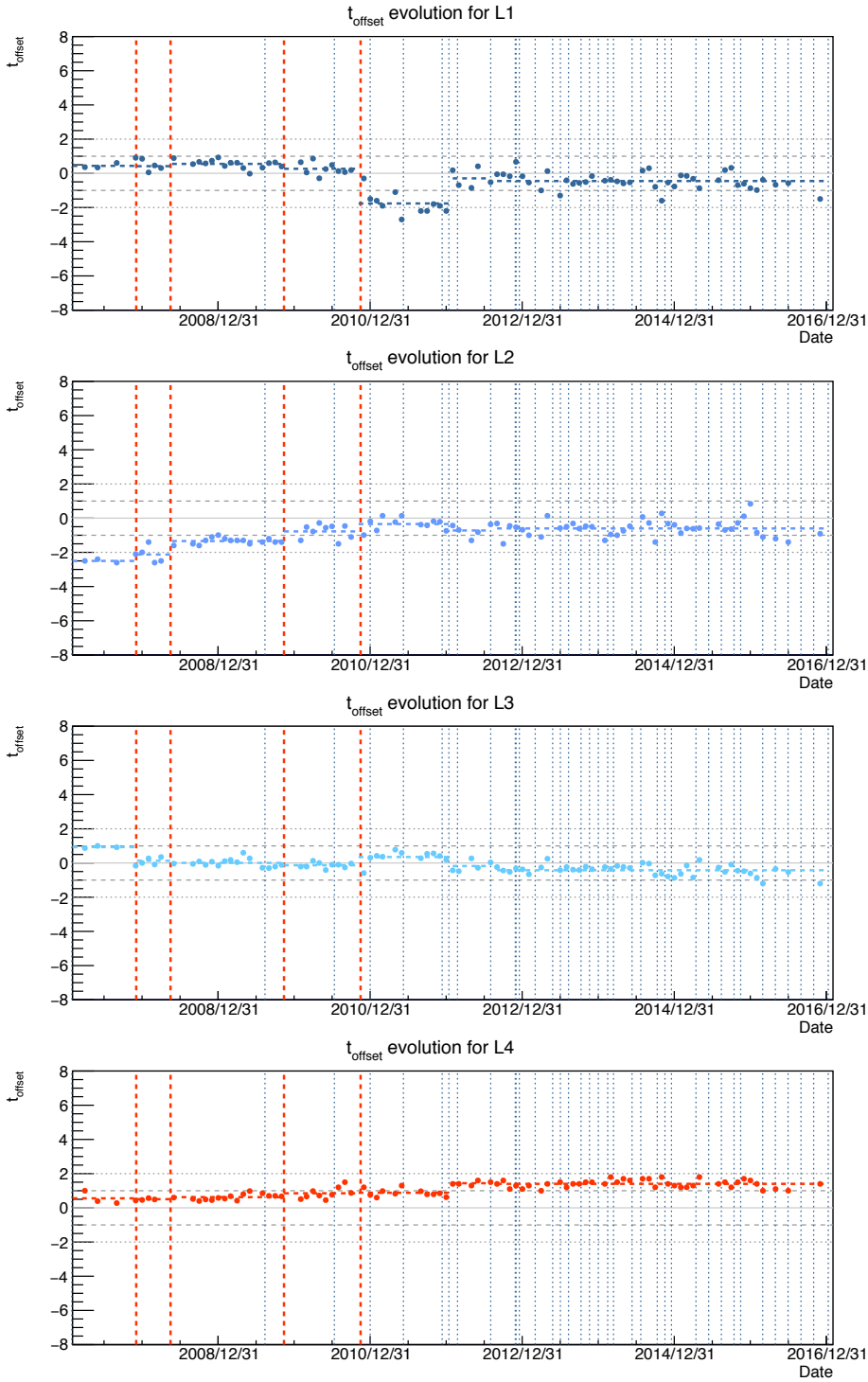

Fig. 4.19.: Evolution of the inter-line time offsets for lines 1, 2, 3 and 4. The red vertical lines denote the changes in the T0 tables due to the connection of a line. The blue vertical lines indicate the starting periods of other changes in the T0 tables.

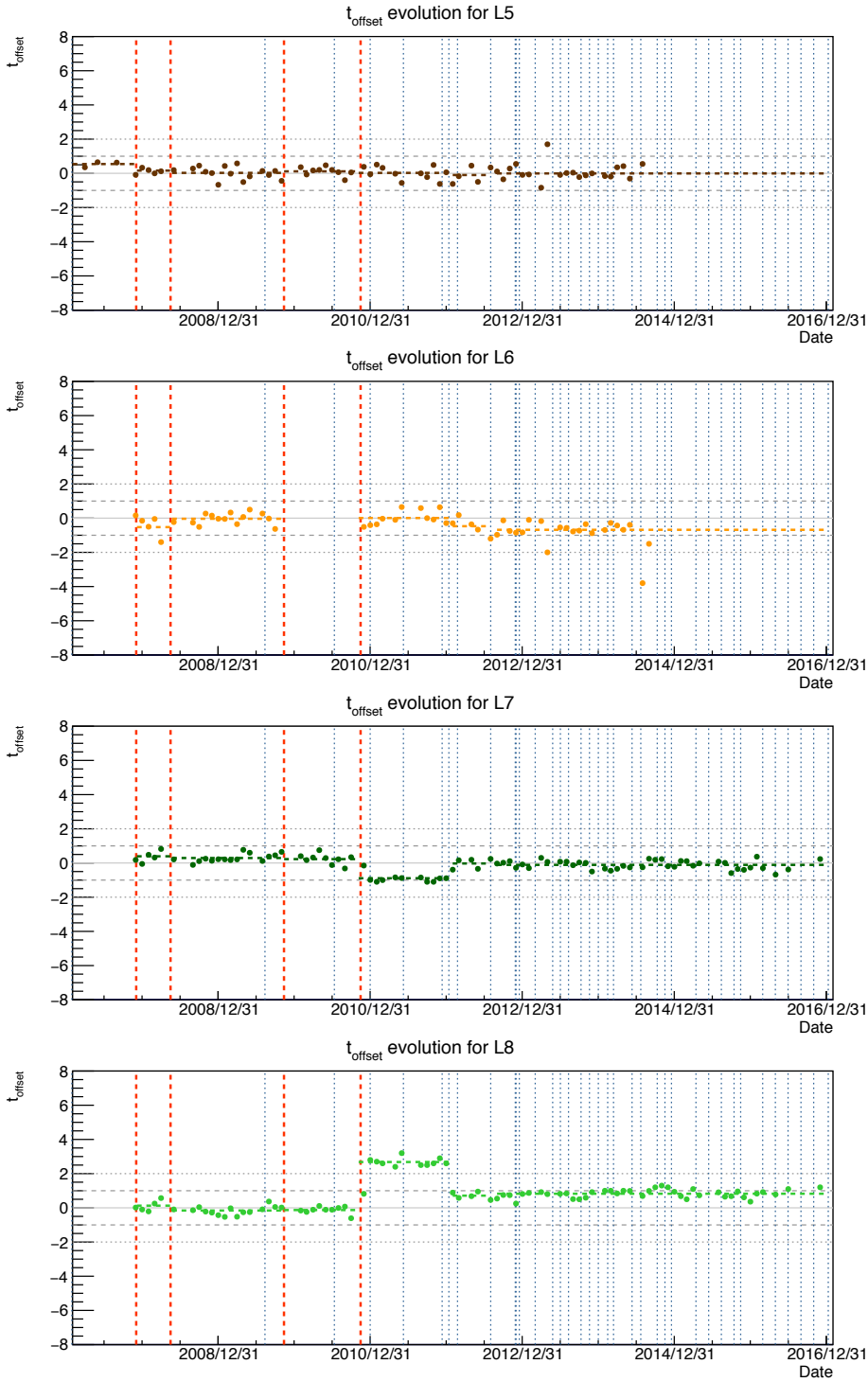

Fig. 4.20.: Evolution of the inter-line time offsets for lines 5, 6, 7 and 8. The red vertical lines denote the changes in the T0 tables due to the connection of a line. The blue vertical lines indicate the starting periods of other changes in the T0 tables.

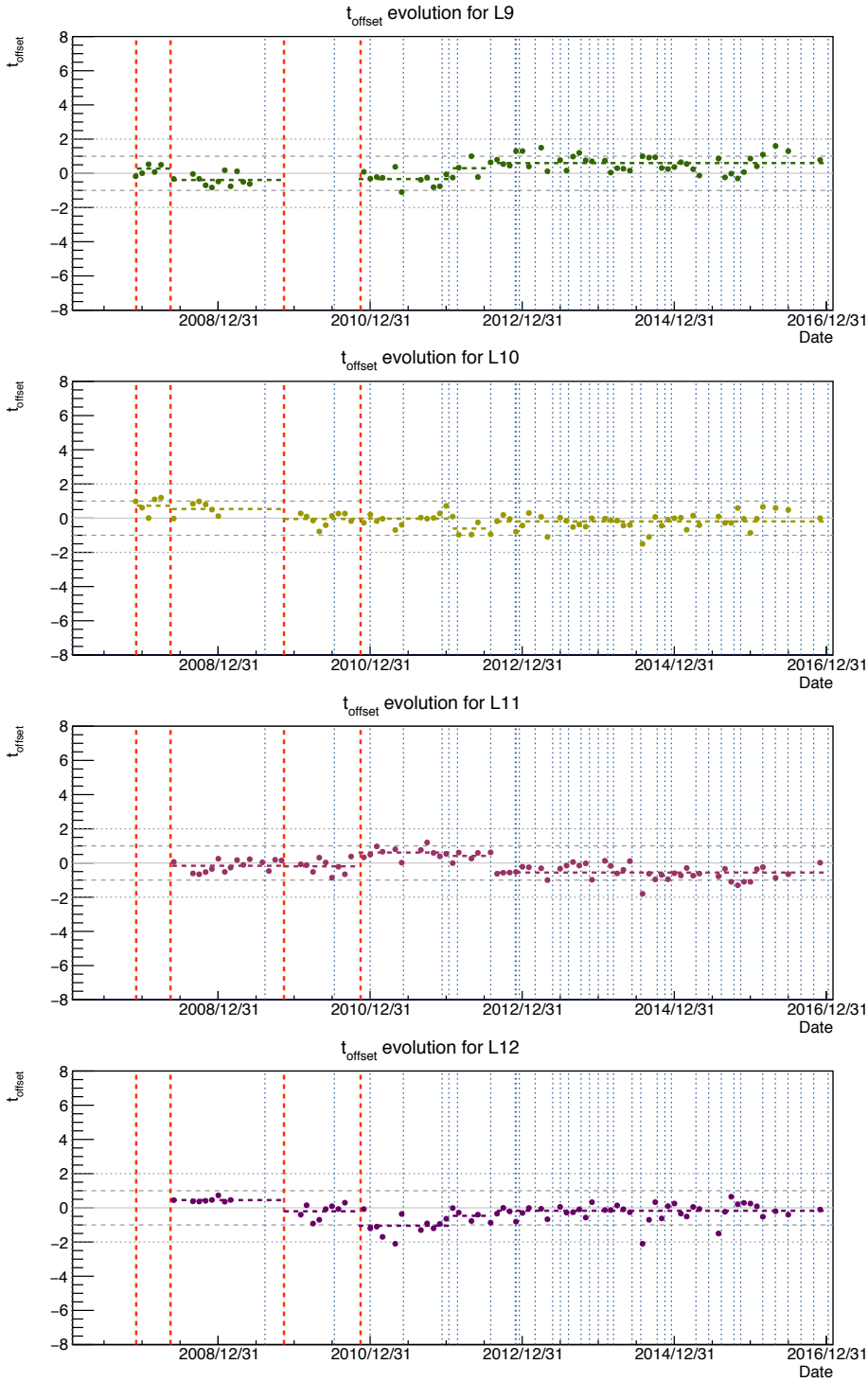

Fig. 4.21.: Evolution of the inter-line time offsets for lines 9, 10, 11 and 12. The red vertical lines denote the changes in the T0 tables due to the connection of a line. The blue vertical lines indicate the starting periods of other changes in the T0 tables.

ARS, k is the other ARS which is located at the same OM, and j is another ARS from the same floor used as auxiliary.

For a given floor, all active ARSs can act as the reference. The one with the largest number of ARS pairs with a successful fit was chosen as reference. If more than one ARS fulfil this condition, the one with the lowest ARS number was taken.

As only relative differences between ARSs are needed, a constant can be added to all the time differences obtained in a given floor. Because of this, the Δt_{rj} values are set so that the average value of all of them equals to 0. Extreme values (those larger than 4 ns from the average) are excluded in the average calculation.

Inter-storey calibration using atmospheric muon tracks

This step consists in the calculation of the time offsets of all the storeys. For this purpose, the results obtained in the previous inter-line and intra-storey calibration are taken into account. As in the inter-line calibration, this is an iterative method based on the time information obtained from reconstructed muon tracks. Since the convergence is obtained faster, in this case only three iterations were performed for each period considered in the inter-storey calibration.

The inter-storey periods considered were chosen with the aim to obtain a time calibration on a monthly basis. The duration of each period is not the same, since some of them had to begin after a high voltage tuning or after a connection of a line. Some others are set so to make them coincident with the periods of the charge calibration tables. For a list of all the inter-storey periods, see Appendix A. The calibration for a given period is performed as follows:

- Only reconstructed events with $\Lambda >$ -6.5 are considered. For each of these events, a loop over all storeys is performed. If a storey does not have a detected hit, the loop advances to the next storey. If there are hits, they are excluded from the new reconstruction (*probe hits*), which is performed with the remaining hits (*reco hits*). The time residuals

are then calculated for the probe hits, and the loop continues to the next floor.

- After several loops over different events, distributions of time residuals of the probe hits are made for each available storey. A Gaussian plus a constant fit function is performed around the peak region.
- A distribution of all the mean values obtained from the fits is made, from which the average value is extracted and taken as a reference to compute the corrections. The correction applied to a given storey in the following iteration is the difference between the residual of the storey and the average value obtained from the fit of the time residual distribution.

Figure 4.22 shows an example of the time residual distribution for the storey L1F21 for the first iteration considered by using runs from period 4 in 2010 (see Appendix A). The corresponding distributions of the mean fitted values for the first and the last iteration for this period can be seen in Figure 4.23. The last iteration is always set so that the standard deviation of the mean fitted values is ≤ 0.35 ns.

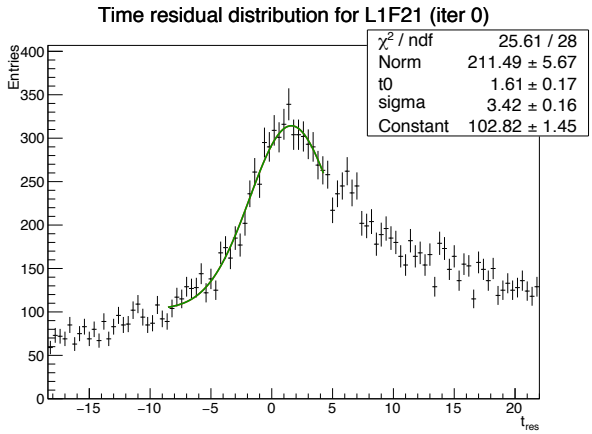

Fig. 4.22.: Time residual distribution for storey L1F21 for the first iteration using runs from 2010, period 4 (see Appendix A).

4.2.2 Effects on the reconstruction

An increase on the number of well-reconstructed down-going events is observed after the update on the time calibration. Figure 4.24-left shows

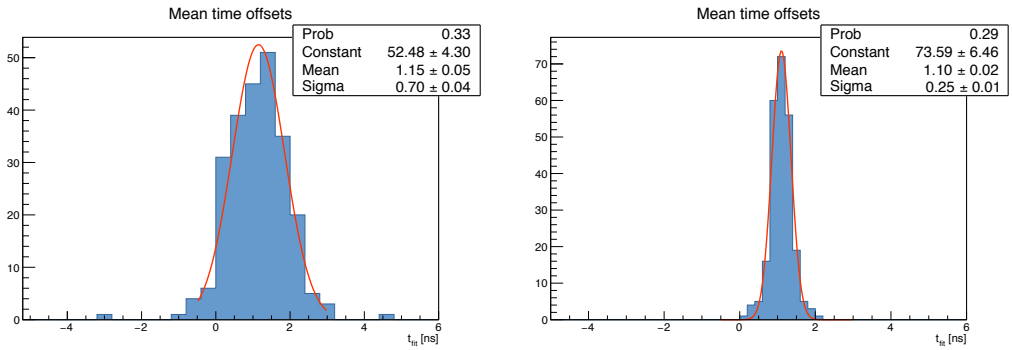

Fig. 4.23.: Distribution of the mean fitted values after the first iteration (left) and the last (right) for period 4 in 2010 (see Appendix A for the periods considered). The statistical deviation is reduced from ∼0.70 to ∼0.25 ns.

the comparison on the number of down-going reconstructed events between the previous and the new calibration for around ∼10% of the runs taken in 2009. For a cut on $\Lambda >$ -5.2, the observed increase is of ∼7%. Figure 4.24-right shows the same comparison for a ∼30% of the runs in 2011. A larger increase is observed in this case due to the bigger difference in the inter-line offsets for this year.

An increase is also observed for well reconstructed upgoing events, as shown in Figure 4.25. The figures represent the same periods as in Figure 4.24. In this case, the number of events after a $\Lambda >$ -5.0 cut is known to be dominated by atmospheric neutrinos, where a clear increase is seen for 2011. The increase observed in 2009 is smaller. Since the increase is also smaller for the down-going events, and the livetime considered is smaller compared to the 2011 periods, the increase observed after a cut on $\Lambda >$ -5.2 or $\Lambda > -5.0$ is not statistically significant.

Changes in the time calibration are known to modify the angular reconstruction of the events. Figure 4.26 shows the changes between the current and the former T0 tables in the same period as in 4.24-left for down-going events after a cut on $\Lambda >$-5.5 (left) and $\Lambda >$-5.2 (right). For the latter case, only around 10% of the events show a change larger than 1°. A similar behaviour is observed for up-going events, as shown in Figure 4.27. In this case, the comparison in the $\Lambda >$ -5.5 cut shows a larger amount of events

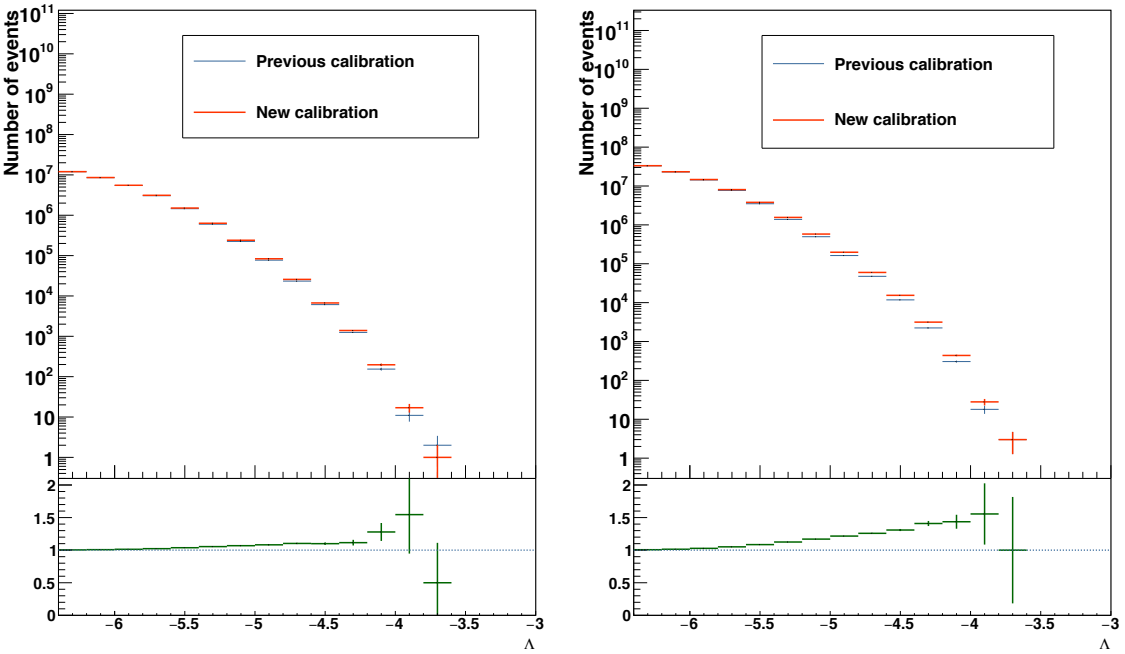

Fig. 4.24.: Comparison on the number of down-going reconstructed events between the previous calibration (blue) and the currently used calibration (red) as a function of the Λ cut applied. The livetime corresponds to $\sim$10% of the runs in 2009 (left) and $\sim$30% of the runs in 2011 (right). The bottom plot shows the ratio between the number of events obtained with the current and the previous calibration.

which change their direction more than 1°. This is most likely produced due to the large presence of mis-reconstructed atmospheric muons.

A similar trend can be observed in simulated neutrino events after adding a Gaussian smearing of $\sigma = 1.0$ ns on the ARS T0 values, as shown in Figure 4.28. Even if a change in the angular reconstruction is made, no relevant changes are seen in the median angular distance between the original and the reconstructed angles for a $\Lambda >$ -5.2 cut. However, a smaller amount of reconstructed events is observed after the σ =1.0 ns smearing.

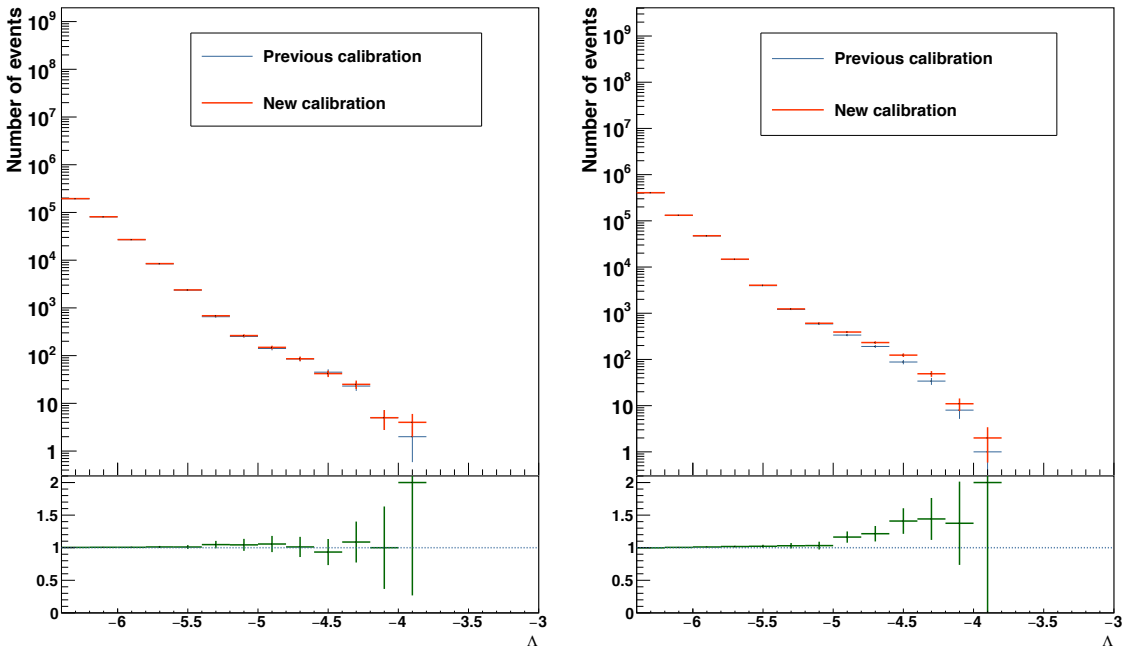

Fig. 4.25.: Comparison on the number of up-going reconstructed events between the previous calibration (blue) and the currently used calibration (red) as a function of the Λ cut applied. The livetime corresponds to $\sim$10% of the runs in 2009 (left) and to $\sim$30% of the runs in 2011 (right). The bottom plot shows the ratio between the number of events obtained with the current and the previous calibration.

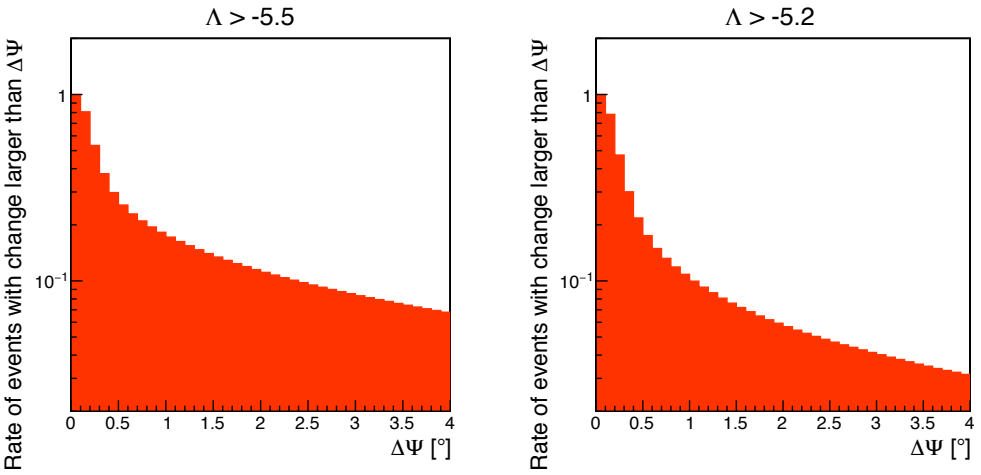

Fig. 4.26.: Rate of events which have an angular change of $\Delta\Psi$ or larger between the current and the former T0 tables for down-going events and for two different Λ cuts. Less than $\sim$10% of the events present a variation larger than 1° for $\Lambda >$ -5.2 .

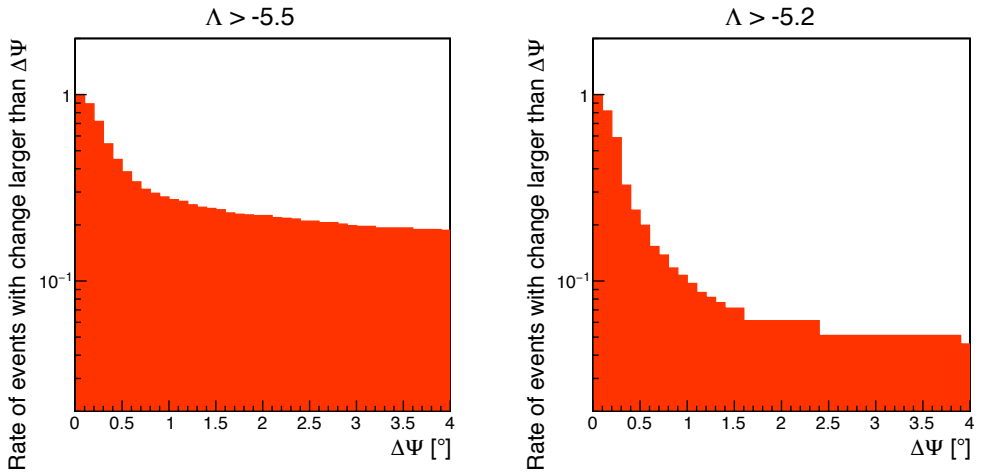

Fig. 4.27.: Rate of events which have an angular change of $\Delta\Psi$ or larger after the new T0 tables for up-going events and for two different Λ cuts. Less than $\sim$10% of the events present a variation larger than 1° for $\Lambda >$ -5.2.

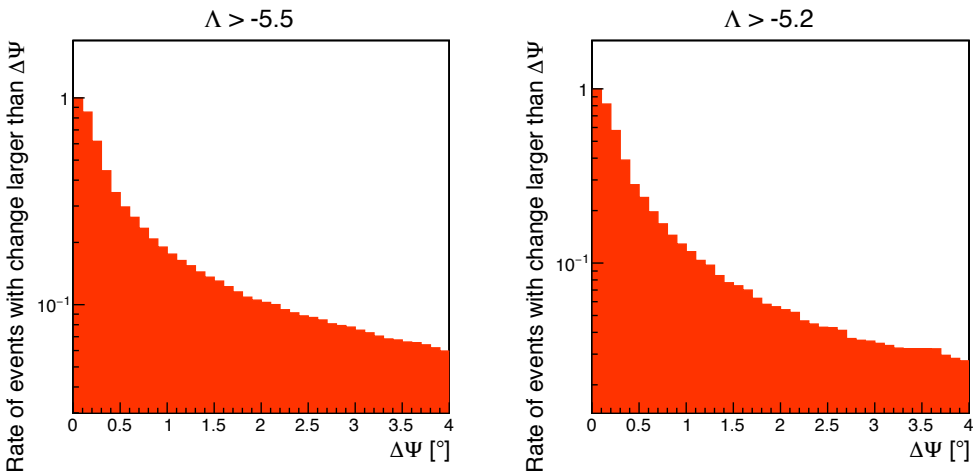

Fig. 4.28.: Rate of events which have an angular change of $\Delta\Psi$ or larger for simulated up-going atmospheric neutrino events and for two different Λ cuts after adding a smearing of 1 ns in the T0 tables of each ARS. Around $\sim$10% of the events present a variation larger than 1° for $\Lambda >$ -5.2.

5 Search methods for point and extended neutrino sources

> *Ora che ho perso la vista, ci vedo di più*
>
> — **Giuseppe Tornatore**
> Cinema Paradiso (1988)

This chapter focuses on the methods used for the search of point and extended-like cosmic neutrino sources performed in this thesis. The specific details of each analysis are explained in Chapter 6, which also contains the results.

Basically, the methods which attempt to find cosmic neutrino sources are based on the search for accumulations of events (clusters) coming from specific sky locations. While the atmospheric neutrino background is distributed uniformly in right ascension, and approximately follows the visibility distribution of the detector in declination, the events coming from a point or extended source are expected to gather into a cluster around its centre. In order to estimate the signal strength of a candidate signal cluster, an unbinned maximum likelihood method has been used (Section 5.1). For this purpose, the likelihood takes advantage of the information from relevant parameters which help to distinguish between the assumed signal and the expected background. In order to estimate the significance of a cluster, a hypothesis test based on the likelihood ratio between the maximised value of the likelihood and its value for the only-background hypothesis (null hypothesis) has been followed (Section 5.1.3).

To avoid biases in the analysis, a large number of simulations with data sets of randomly generated events (pseudo-data sets or pseudo-experiments) are performed before the unblinding of the final data sample (Section 5.2). These simulations are also used to estimate the sensitivity of the searches and to optimize the event selection which maximises a discovery (Sections 5.3 and 5.4). The event selection relies on cuts on threshold values of some

of the parameters described in Chapter 3. In some cases, a Random Forest Classifier has also been used to help in the optimisation process (Section 5.4.1).

5.1 Unbinned maximum likelihood search method

An unbinned maximum likelihood estimation method has been used to evaluate the significance of an accumulation of neutrino signal events over the background. Different definitions of the likelihood have been used in each analysis. In the point-source analysis which combines the data from the ANTARES and IceCube detectors (Section 6.1), a standard likelihood definition has been considered, whereas for remaining searches an extended likelihood definition has been adopted (Sections 6.2 and 6.3).

5.1.1 Standard likelihood definition

Given a set of N independent observations, $\boldsymbol{X} = \{\vec{x}_1, \vec{x}_2, ..., \vec{x}_N\}$, for a set of p unknown parameters, $\boldsymbol{\Theta} = \theta_1, \theta_2, ..., \theta_p$, the probability to obtain these particular observations is given by the product of the individual values of the probability density functions (PDFs) of each observable, $f(\vec{x}_i|\boldsymbol{\Theta})$ [223]:

$$\mathcal{L}(\boldsymbol{\Theta}) = P(\boldsymbol{X}|\boldsymbol{\Theta}) = \prod_i^N f(\vec{x}_i|\boldsymbol{\Theta}), \tag{5.1}$$

where $\vec{x}_i$ indicates the considered features of the observable i. This function is called *likelihood* when $\mathbf{X}$ corresponds to the set of measurements.

In the standard likelihood definition, the integral of each individual PDF over the full range of allowed values is normalised to 1:

$$\int f(\vec{x}_i|\boldsymbol{\Theta}) d\vec{x}_i = 1. \tag{5.2}$$

In every search, each observation corresponds to a detected event of the sample. The corresponding PDF of each event is defined as

$$f(\vec{x}_i|n_s,\vec{z}_s,\gamma) = \frac{n_s}{N} S_i(\vec{x}_i|\vec{z}_s,\gamma) + \left(1-\frac{n_s}{N}\right) B_i(\vec{x}_i), \tag{5.3}$$

where n_s stands for the (unknown) number of detected signal events, $\vec{z}_s$ is the location of the assumed source, γ represents the spectral index of the energy spectrum of the source, N is the total number of events in the sample, and $S(\vec{x}|\vec{z}_s,\gamma)$, $B(\vec{x})$ denote the signal and background probability functions. In all the analyses described in Chapter 6, the energy spectrum of the source has been assumed fixed in the likelihood maximisation (γ = constant).

The signal PDF can be expressed as

$$S(\vec{x}_i|\vec{z}_s,\gamma) = A(\Delta\Psi_i|\gamma,\sigma_i) P_{sg}(E_{proxy,i},\sigma_i), \tag{5.4}$$

where the function $A(\Delta\Psi|\gamma,\sigma)$ corresponds to the PDF for an event to be reconstructed at an angular distance $\Delta\Psi_i$ from the source. When a point-source is assumed, it is equivalent to the point spread function (PSF). The dependence of the energy spectrum of the source and on the reconstructed angular error estimate of the event, σ_i, is not always considered.

The $P_{sg}(E_{proxy,i},\sigma_i)$ function takes into account the probability for an event to be reconstructed as signal given an energy proxy, such as the total number of hits used for the reconstruction or the reconstructed energy, and an angular error estimate (if used).

The background probability density function can be described as

$$B(\vec{x}_i) = \frac{1}{2\pi} R(sin\delta) P_{bg}(E_{proxy,i},\sigma_i). \tag{5.5}$$

The $\frac{1}{2\pi}$ term takes into account that the background events are uniformly distributed in right ascension. The $R(sin\delta)$ function corresponds to the background rate of events as a function of the declination. Finally, the function $P_{bg}(E_{proxy,i},\sigma_i)$ provides the probability for an event to be reconstructed as background given an energy proxy and an angular error estimate.

5.1.2 Extended likelihood definition

A different normalisation for the PDFs is considered in the extended likelihood definition [224]. In this case, the normalisation is constrained to the total number of observed events, which is considered to vary depending on the unknown $\mathbf{\Theta}$ parameters:

$$\int F(\vec{x}|\mathbf{\Theta})d\vec{x} = N(\mathbf{\Theta}). \tag{5.6}$$

A simple substitution of $f(\vec{x}|\mathbf{\Theta})$ by $F(\vec{x}|\mathbf{\Theta})$ may lead to a too large normalisation in the process of the likelihood maximisation. A solution to this problem is given in [224]. Let us assume the one dimensional problem, in which $\vec{x} \to x$. In this case, the whole range of x can be divided in N segments. Since the N segments are arbitrary, they are set to a length Δx so small that having 2 events in the same segment is practically impossible. The probability to obtain 0 or 1 events are, then, given by the Poisson distribution:

$$P_0(x) = e^{-\Delta x P(x)}, \;\; P_1(x) = \Delta x P(x) e^{-\Delta x P(x)}. \tag{5.7}$$

If i runs for the segments which contain one event, and j corresponds to the index for any segment, the likelihood is given by

$$\mathcal{L} = \prod_i \Delta x P(x_i) \prod_j e^{-\Delta x P(x_j)}. \tag{5.8}$$

This equation can be simplified as

$$\mathcal{L} = \left[\prod_i \Delta x P(x_i)\right] e^{-N}. \tag{5.9}$$

If we make the $\Delta x \to dx$ transformation, we end up obtaining $\mathcal{L} = e^{-N} \prod_i P(x)$. Or, taking the logarithm:

$$\log \mathcal{L} = \sum_i \log P(x) - N. \tag{5.10}$$

Therefore, in point and extended source searches, the logarithm of the extended likelihood is expressed as

$$\log \mathcal{L}(n_s, \vec{z}_s, \gamma) = \sum_i \left[\log(n_s S(\vec{x}_i|\vec{z}_s, \gamma) + N_b B(\vec{x}_i))\right] - n_s - N_b, \quad (5.11)$$

where the signal and background PDFs take the same form as in Equations 5.4 and 5.5, respectively, and N_b is the number of background events.

5.1.3 Likelihood maximisation and test statistic definition

Whether the standard or the extended definition are used, the likelihood $\mathcal{L}(n_s, \vec{z}_s, \gamma)$ is maximised for the set of unknown parameters. The values which maximise this function indicate the most likely solution, but they do not give information about the significance of an observation. For this purpose, a Test Statistic (TS) variable is defined based on the the likelihood ratio between the maximised value over the expected value considering only background ($n_s = 0$):

$$TS = -2 \log \left(\frac{\mathcal{L}_{bg}}{\mathcal{L}_{max}} \right) = 2 \left(\log \mathcal{L}_{max} - \log \mathcal{L}_{bg} \right), \quad (5.12)$$

where $\mathcal{L}_{bg} = \mathcal{L}(n_s = 0, \vec{z}_s, \gamma)$ and $\mathcal{L}_{max} = \mathcal{L}(n_s^{max}, \vec{z}_s, \gamma)$.

Distributions of the TS values are needed in order to perform a hypothesis test. Two opposed hypotheses are considered. The H_0 hypothesis or null hypothesis corresponds to the case where no signal events are present ($n_s = 0$), whereas the H_1 hypothesis or alternative hypothesis corresponds to the case in which $n_s > 0$. Two types of errors are usually identified in hypothesis testing: the type-I error corresponds to the case in which the H_0 hypothesis is rejected while being true. The type-II error happens when the null hypothesis is wrongly non discarded. In order to quantify the frequency of these errors, the following quantities are often defined:

- The significance gives the probability to falsely reject the null hypothesis.

- The power is defined as the probability to avoid a type-II error given that H_1 is true.

For further clarification on the meaning of these quantities when considering the TS distributions for the H_0 and H_1 hypotheses, see Figure 5.1.

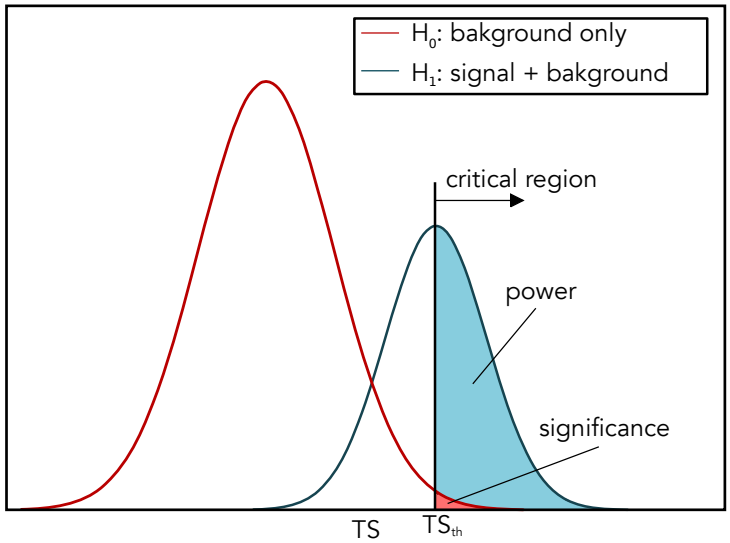

Fig. 5.1.: Example of a hypothesis test. The red (blue) curve corresponds to a given TS distribution for the H_0 (H_1) hypothesis. Given a TS threshold value, TS_{th}, the significance is defined as the area of the H_0 distribution for which $\mathrm{TS} > \mathrm{TS}_{th}$. The power is defined as the area of the H_1 distribution for which $\mathrm{TS} > \mathrm{TS}_{th}$.

5.2 Pseudo-experiments

The distributions of the TS values for different hypotheses are obtained from pseudo-experiments, in which only partial information of the data is considered. In each pseudo-experiment, a randomised data-set (or skymap) which resembles the data is performed. Signal and background events are simulated differently.

The declination of background events are generated randomly by using the declination dependent rate of events from the data sample (see Figure 5.2 for an example). The right ascension is generated by assuming a uniform distribution between 0° and 360°. Further observables, such as the angular error estimate and the energy proxy or energy estimator are also generated

if they are included in the likelihood definition. In that case, they are generated randomly from histograms obtained from the data sample.

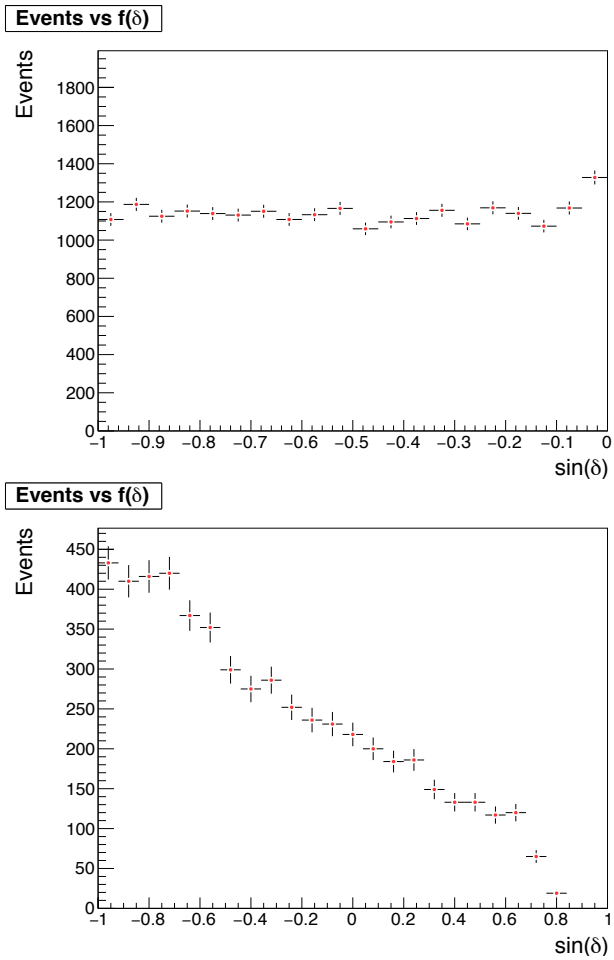

Fig. 5.2.: Number of events obtained from data for the IC40 (top) and the ANTARES 2007-12 (bottom) data samples as a function of the declination. More information on these samples can be found in Section 6.1.

The location of signal events are generated taking into account the distribution of the angular distance between the reconstructed and the original neutrino direction for the assumed energy spectrum of the source. These distributions are obtained by considering reconstructed events from Monte Carlo neutrino event simulations. If a point-source is assumed, the distance to the centre of the source is randomly generated from the angular distance

distribution. In the case of an extended source, first the location of the original neutrino by assuming the extended source profile is generated. Afterwards, the reconstructed direction is obtained randomly from the angular distance distribution. The angular distance distribution can be correlated with other variables, such as the energy proxy used, and/or the angular error estimate. Because of this, these variables are generated from 2D or 3D histograms which take into account the correlation between the angular distance with the corresponding extra variables. These histograms are also considered for different declinations, in order to take into account the different performance of the reconstruction depending on the source location. Figure 5.3 shows an example of a 3D histogram used for the last ANTARES point-source search (see Section 6.2).

Typically, the number of pseudo-experiments per each signal strength is $O(10^4 - 10^5)$. In each set of simulations, a fixed number of signal events coming from a source at a specific location in the sky are generated. Since the number of signal events is expected to follow a Poisson distribution, a transformation to calculate the TS distribution for a mean number of signal events, μ_s, is needed:

$$\frac{dP(\mu_s)}{d(TS)} = \sum_i^N \frac{dP(n_i)}{d(TS)} P(n_i|\mu_s), \tag{5.13}$$

where N is the maximum number of signal events generated (typically, 30 signal events), $\frac{dP(n_i)}{d(TS)}$ is the TS distribution for a fixed number of signal events n_i, and $P(n_i|\mu_s)$ is the Poisson probability to detect n_i events given a mean of μ_s events. In the ANTARES searches, the systematic on the number of detected events is added in this step by means of a Gaussian smearing, leading to the following formula:

$$\frac{dP(\mu_s)}{d(TS)} = \sum_i^N \frac{dP(n_i)}{d(TS)} \int P(n_i|\bar{\mu}) G(\bar{\mu}|\mu_s, \sigma_\mu) d\bar{\mu}, \tag{5.14}$$

where σ_μ is the uncertainty on the mean number of signal events, and $\bar{\mu}$ is a variable which ranges between $[\mu_s - 4\sigma_\mu, \mu_s + 4\sigma_\mu]$. Figure 5.4 shows an example of TS distributions using the ANTARES 2007-15 data sample.

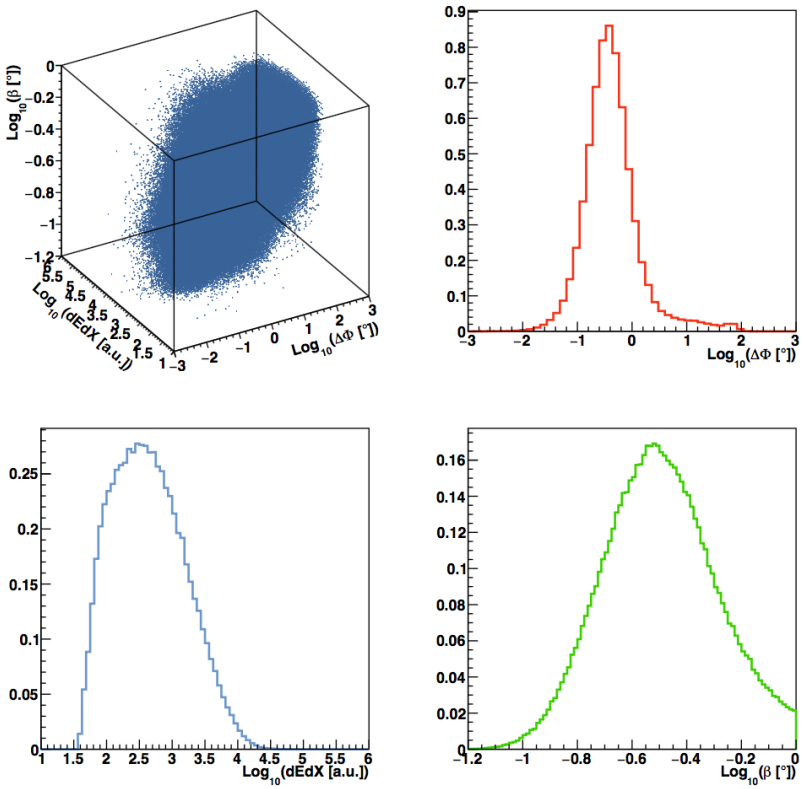

Fig. 5.3.: 3D histogram used to generate neutrino events from a source with a declination between $-0.8 \leq sin(\delta) < -0.6$ in the last ANTARES point-source search (see Section 6.2 for more information about this search). The top right, bottom left and bottom right figures represent the projections of the top left histogram on the angular distance, the energy proxy and the angular error estimate, respectively.

5.3 Upper-limits and discovery fluxes

The discovery potential is defined as the signal strength which leads to a 5σ discovery in 50% of the trials. The threshold value of the TS which leads to a 5σ discovery is obtained from a fit performed over the background TS distribution. According to the Wilk's theorem [225], the background TS distribution assymptotically follows a χ^2 distribution with n degrees of freedom, where n is the number of parameters which are fitted in the likelihood maximisation. In this case, only the number of signal events, n_s, is left as a free parameter, and therefore, the background TS distribution is

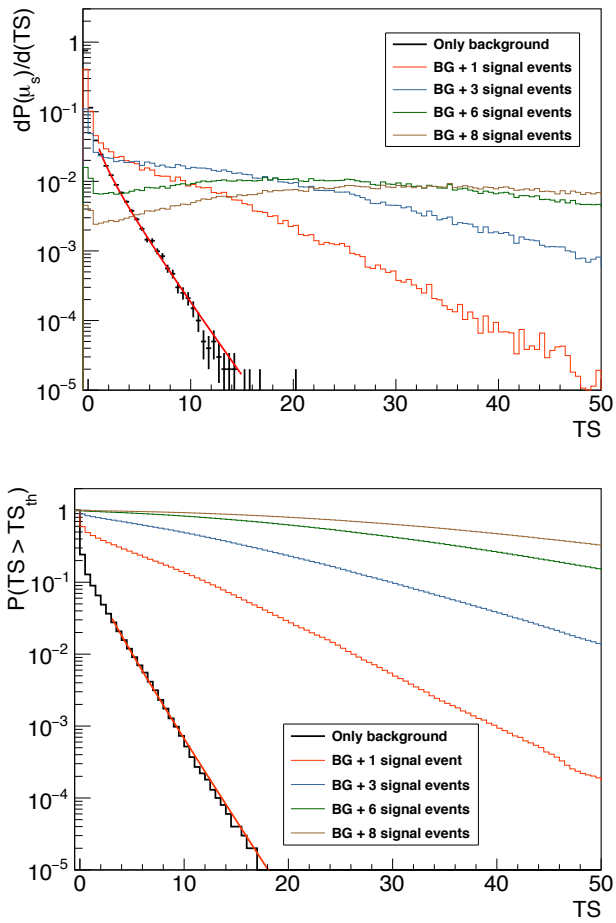

Fig. 5.4.: Top: TS distributions for the background only case (black) and for different cases of background + signal events. The red line shows a fit assuming a χ^2 distribution of 1 degree of freedom with a free normalisation. The figure on the bottom shows the probability to obtain a value larger than a given threshold TS value for the same cases.

fitted to a χ^2 distribution of one degree of freedom with a free normalisation. Figure 5.4 shows an example of this fit.

The significance of an observation is determined by comparing the observed TS value with the background TS distribution. From this, the p-value is quoted as the fraction of simulations in which a higher TS value is obtained.

The upper limit is the magnitude which provides the discarded signal strength within a given confidence level (CL). The frequentist approach proposed by Neyman [226] [227] is used for all the analyses. The aim is to obtain an interval $[n_1, n_2]$ which encloses the number of signal events, n^{true}, within a given confidence level, α:

$$P(n^{true} \in [n_1, n_2]) = \alpha. \tag{5.15}$$

It is said that a proper coverage is found when this condition is satisfied. In other words, the statement that n^{true} is constrained within $[n_1, n_2]$ has a probability of α to be true. Since it is not possible to obtain the actual true number of signal events, intervals of a physical parameter which depends on n^{true} are used. These intervals are known as *confidence belts*, and are defined as

$$P(x \in [x_1, x_2]|n^{true}) = \alpha, \tag{5.16}$$

where x is the physical parameter related to n^{true}, and $[x_1, x_2]$ corresponds to the interval. Different options to construct the $[x_1, x_2]$ range are possible. The one used in the analyses of this thesis correspond to

$$P(x < x_1|n^{true}) = 1 - \alpha, \tag{5.17}$$

which are usually known as *Neyman upper limits*. Other possible confidence belt constructions such as the Feldman & Cousins [228] or the CLS [229] methods are possible.

In order to estimate the performance of the detector, it is common to obtain the *median upper limit* or *sensitivity*. The sensitivity is defined as the upper limit which would be obtained if our observed result would be the median of the background-only case. A CL value of $\alpha = 0.9$ is used both for the upper-limit of a given location obtained from data and for the sensitivity.

The calculation of upper limits and discovery potentials in terms of the true number of signal events, n^{true}, is obtained from the TS distributions generated from pseudo-experiments after the transformations given in Equations

5.13 and 5.14. In order to compare with other detectors, or to obtain a relevant physical magnitude of the source, this number needs to be converted into the flux arriving to Earth. Given a specific source flux $\frac{d\Phi}{dE_\nu dt dS}$, the number of expected events is calculated as

$$N_{evts}(\delta) = \int\int \frac{d\Phi}{dE_\nu dt dS} A_{eff}(\delta, E_\nu) dE_\nu dt, \tag{5.18}$$

where $A_{eff}(\delta, E_\nu)$ is the effective area (i.e, the equivalent area of a detector with perfect efficiency) for a given neutrino energy and declination. The flux of a source is commonly assumed to follow a power-law relationship with the neutrino energy, $\frac{d\Phi}{dE_\nu dt dS} = \Phi_0 (E_\nu / E_0)^{-\gamma}$, where Φ_0 is a normalisation constant. In ANTARES and KM3NeT analyses, the magnitude which connects the number of expected events with a given flux, Φ_0 is called acceptance, $A(\delta)$, and it is defined as

$$A(\delta) = \frac{N_{evts}(\delta)}{\Phi_0}. \tag{5.19}$$

The upper limits and discovery potentials are transformed into a flux by considering the proportionality relation between the number of expected events, n_0, and the flux considered, Φ_0. Therefore, the corresponding flux for the n' events is

$$\Phi' = \frac{\Phi_0}{n_0} n'. \tag{5.20}$$

5.3.1 Median of the TS background distribution

Previously, the sensitivity has been defined as the median upper limit which would be obtain in case only background events are present in a sample. However, the median value of the TS background distribution for a single source at a fixed position is not trivial to calculate.

When considering the likelihood maximisation, it is important to fix the allowed range of values for the fitted number of signal events, n_s. A frequent boundary for n_s corresponds to $0 \leq n_s \leq n_s^{max}$, where n_s^{max} corresponds to the total number of events at distances smaller than the

search cone[1]. However, if this boundary is applied, more than 50% of the pseudoexperiments have a TS value which is exactly 0. This is shown in Figure 5.5, in which the TS background distribution is shown for three different cases: the first one is obtained with the ANTARES 2007-2015 track sample (7622 events) and assuming a source location at $\delta = -70^\circ$ with an E^{-2} energy spectrum in the signal part of the likelihood. In this case, ∼80% of the times the TS value was exactly 0. The second case is the same as the former, but the number of background events is increased to 10^6 events, with almost no reduction in the first bin (75%). The last case is the same as the first one, but assuming an E^{-3} source spectrum, leading to a reduction from 80% to ∼65%. The three cases are compared with a likelihood with no energy information used. For a background of 7622 events, there is almost no difference between the use of an E^{-3} spectrum compared to the likelihood without energy information. Furthermore, the first bin is further reduced in the case of increased statistics, in which the likelihood with no energy information produces TS values of exactly 0 in ∼56% of the cases.

These results show that the use of an E^{-2} source assumption in the likelihood tends to produce more values closer to TS = 0. The reason for this feature is likely to be due to the big difference between the energy spectra of the background ($\sim E^{-3.5}$) and the E^{-2} case. The fact that the number of trials with a TS = 0 for a larger number of background events (∼10^6) is considerably reduced in the case without the use of energy information also shows that the number of total background events plays a more limited role.

Overall, these results demonstrate that, if nothing else is changed, the median of the TS distribution cannot be determined. In order to be able to calculate the median value of the background TS distribution, two complementary approaches have been followed. In the first approach, the minimum bound for n_s in the likelihood maximisation is set to $n_s^{min} = 10^{-3}$. If the real maximum of the likelihood corresponds to a negative value, $n_s < 0$, according to equation 5.12, the TS will have a negative non-zero value. In

[1]The search cone corresponds to the cone angle in which we consider that the P_{sg} values can be larger than zero (i.e., the value of P_{sg} outside this cone is considered to be zero). The size of the cone is set depending on the median angular resolution of the events in the sample. In the ANTARES samples, the cone angle is set to 10° for track events and 30° for cascades.

other words, this approach produces TS $\neq 0$ values when underfluctuations of the signal are observed, which also permits the calculation of the median TS value for the background distribution. In order to ease the calculation of the median, the following transformation is performed to obtain the TS distributions:

$$TS^{new} = \log_{10}(TS + K), \tag{5.21}$$

where K is a constant with a value close to n_s^{min}. Different values of $n_s^{min} > 0$ and $|n_s^{min}| < 0.01$ have been used without significant changes in the calculation of the sensitivity (see Figure 5.6-top).

In the second approach, negative values of n_s are explicitally allowed in the likelihood maximisation (a limit on n_s^{min} = -100 is set), so that the TS values are:

$$TS^{new} = \begin{cases} -2\log\left(\frac{\mathcal{L}_{bg}}{\mathcal{L}_{max}}\right) & n_s \geq 0 \\ 2\log\left(\frac{\mathcal{L}_{bg}}{\mathcal{L}_{max}}\right) & n_s < 0 \end{cases}$$

Since both approaches are meant to be sensitive to negative fluctuations of n_s, both produce the same sensitivity calculations, as shown in Figure 5.6-bottom. In this respect, in the combined ANTARES & IceCube point-source search (Section 6.1, the first approach ($n_s^{min} = 10^{-3}$) is used. The second approach is followed in the other searches (Sections 6.2 and 6.3).

5.4 Event selection

The event selection must be optimised before the complete information of the final data sample is unblinded. In all the analyses, this has been done by obtaining the selection cuts which minimises the 5σ discovery flux at 50% of trials assuming an E^{-2} source spectrum for the signal. The background of atmospheric muons is removed using relevant reconstruction parameters able to distinguish this background from neutrino events. In the searches in which the number of parameters used is too large to consider different cuts, a cut on the output value given by a Random Forest Classifier (RFC) is used.

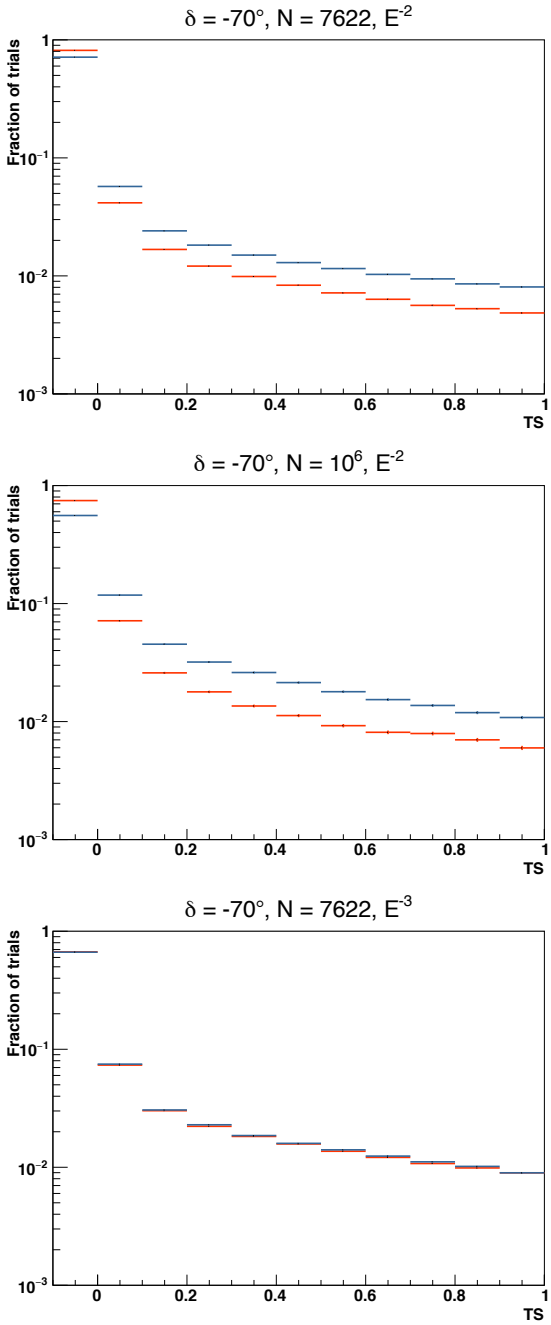

Fig. 5.5.: TS background distributions for a declination $\delta = -70°$ assuming an E^{-2} point-source in the signal PDF and with 7629 total events (top), with 10^6 total events (middle), and with 7629 events assuming an E^{-3} point-source in the signal PDF (bottom). In all cases, the red distribution corresponds to the TS obtained by adding to the likelihood the information of the energy proxy (blue if this information was not used). TS values of exactly 0 are set to the first bin (TS < 0) for clarification purposes.

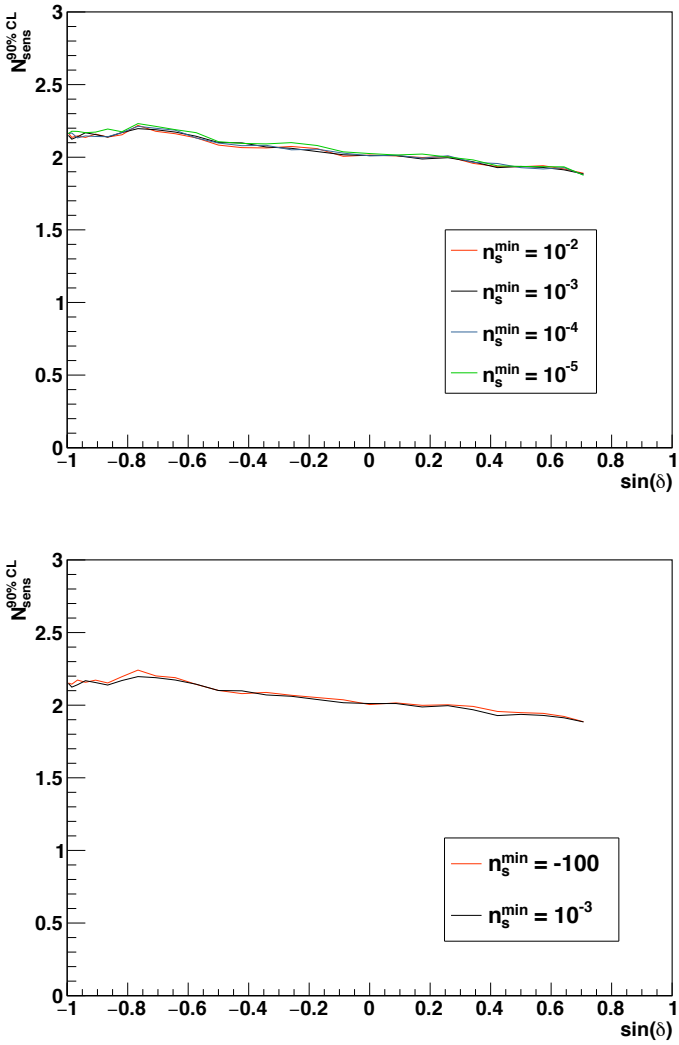

Fig. 5.6.: Median upper limits as a function of $\sin(\delta)$ for the 2007-2015 ANTARES track sample using different values of $n_s^{min} > 0$ and $|n_s^{min}| < 0.01$ (top) and allowing negative values of n_s compared to $n_s^{min} = 10^{-3}$ (bottom). No significant changes are observed.

5.4.1 Random Forest Classfier

The Random Forest Classifier (RFC) technique [230] is one of the many multivariate analysis algorithms which are currently available. A multivariate analysis algorithm (or MVA) simply stands for any statistical analysis algorithm which uses many variables on a studied object (for instance, the maximum likelihood method which has previously described can be understood as such). Depending on its purpose, MVA techniques can be divided into classification or regression models. Classification models are used to predict a category or *qualitative* output (such as "this event is predicted to be an atmospheric muon"), whereas regression models are used to predict a quantity ("the energy of an event is 10.1 TeV"). The RFC technique is also a machine learning (ML) algorithms, i.e., an algorithm which requires a learning process in order to compute an output. ML techniques can be divided into those which require to be trained with a sample in which the real output is known (*supervised learning*) and those in which no prior knowledge is required (*unsupervised methods*). In this sense, RFCs are a classifying method which requires supervised learning.

Decision trees

RFCs rely on the use of a large number of binary decision trees built via the CART algorithm [231]. A binary decision tree can be understood as a set of consecutive decisions which are split into two branches. Figure 5.7 shows a scheme of a decision tree. Each decision is represented by a *node*, which branches out into two destination nodes. The final destination nodes are usually referred as *leafs*.

The CART algorithm optimises the decision tree in the following manner. At each node, by starting on the root node, a split based on a cut on one of the selected variables is done. The selection cut is obtained by minimising the Gini index,

$$G = \sum_{k=1}^{K} p_k(1 - p_k), \tag{5.22}$$

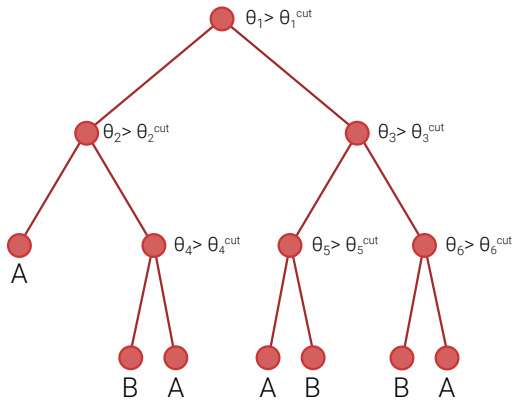

Fig. 5.7.: Example of a binary decision tree for a classification problem of classes A and B by using a set of parameters denoted as θ_i. Each node represents a condition, which is split into two subsequent nodes. The final nodes are labelled as *leafs*.

where K corresponds to the number of possible classes (classifications), and p_k is the fraction of events of the k class. The method is repeated with all the considered nodes. Typically, the process is stopped after a maximum number of nodes which was set previously is reached, or when a leaf contains a minimum number of events of a given class.

An additional step of the CART method is the *pruning* of the decision tree, which consists in deleting nodes according to a given criterion. The pruning algorithm is performed to reduce the *variance* of the tree. In other words, it reduces the variability when trained with different samples. However, the pruning of a tree is not performed when using RFCs.

Fully developed decision trees without pruning present a low *bias* (the difference between the predicted and the real classification is low), but a high variance. When considering a single decision tree, the variance can be reduced at the expense of the increase of the bias by prunning, setting a maximum number of nodes and/or a minimum number of events at a leaf.

The RFC method uses randomisation of multiple trees in order to reduce the variance. Other popular methods applied to decision forests, such as

Adaboost [232] are, in contrast, applied to reduce the bias, since they use decision trees which are pruned, low-depth and/or contain a large minimum number of events per leaf.

The Random Forest Classifier algorithm

Part of the randomisation in the RFC technique is performed via *bootstraping*, which consists on drawing N random subsamples from a given sample. Each of these samples is known as a *bootstraped* sample. The statistical method to be evaluated is then applied to these samples.

The algorithm of RFCs is, therefore, the following [233]. Per each of the N trees to be trained, a bootstraped subsample from the training sample is set. A decision tree is grown by following the CART algorithm, in which only m of the p classifying variables are used. These variables are randomly chosen. Then, every grown tree makes a prediction of the corresponding class per each event. The assigned class for each event corresponds to the majority vote of the trees.

To perform the RFC for the KM3NeT search the `scikit-learn` libraries were used [234]. These libraries present a small modification to the prior method, in which the majority vote is substituted by the average probabilistic prediction.

The recommended parameters of the RFCs to be optimised are the number of variables used in each tree and the total number of trees.

Cross validation

Even if the authors of the RFC algorithm claim it is much less prone to overfitting problems compared to other methods [230], differences in the misclassification errors obtained in a trained and a test (or error) sample may be significant. In a data rich situation, an ideal manner to evaluate this error would be to divide the whole sample into three subsamples [233]. Half of the sample would be used always for the training of the data, 25% to the validation of the method (that is, to evaluate the misclasification error

while optimising the classifier), and a final 25% to the final test sample from which the final test error would be obtained.

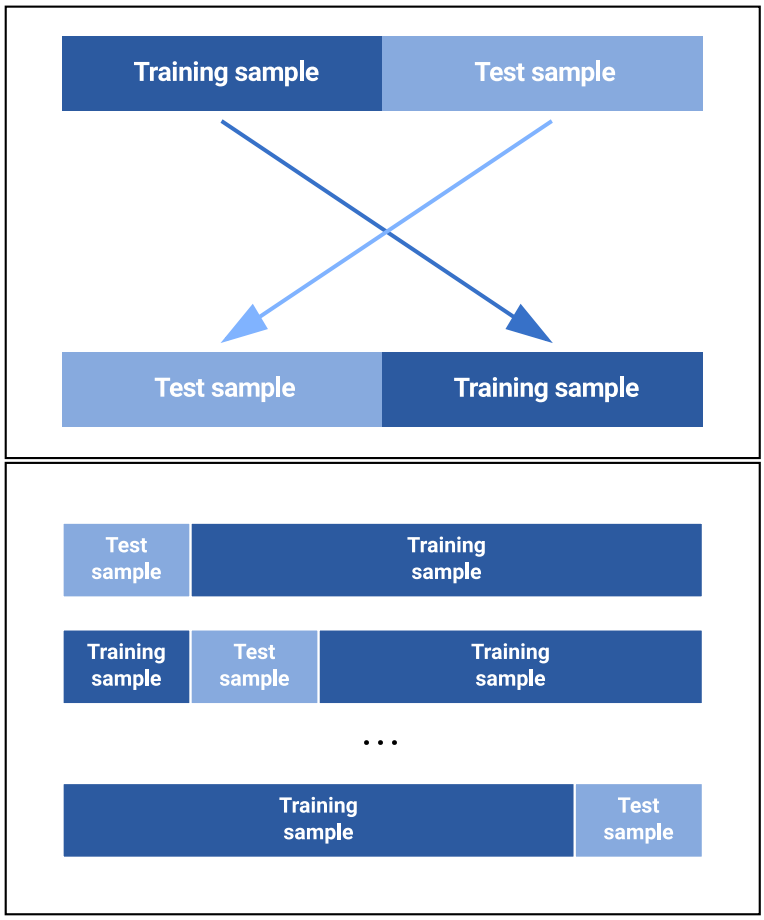

Fig. 5.8.: Top: Example of a 2-fold cross validation with two equal samples. Bottom: Example of a 5-fold cross validation process. The sample is divided into 5 equal parts, in which one corresponds to the test sample and the rest composes the training sample.

The time it takes to perform the simulations of reconstructed events is too large in order to perform the previous evaluation. Because of this, a cross-validation procedure is adopted. The most basic cross-validation procedure corresponds to the 2-fold case (see Figure 5.8-top). The whole sample is divided into two equal parts. The classifier is first trained with the information of the first half (training sample) and it is afterwards evaluated in the second half (test sample). In the next step, the training and test

samples are switched. This method allows to obtain the stability of the misclassification error by comparing the values obtained in the two test samples.

A more sophisticated manner corresponds to the n-fold cross validation (see Figure 5.8-bottom). In this case, the whole sample is divided in n subsamples, in which only one corresponds to the test sample for each iteration. The training sample would therefore correspond to the remaining $n - 1$ subsamples.

6 Searches of point-like and extended neutrino sources

The results of three different analyses of cosmic neutrino sources are presented in this chapter. In the first one, data from the two largest neutrino telescopes on Earth, ANTARES and IceCube, are combined for the first time (Section 6.1). These results were already published in the Astrophysical Journal [235] and presented in various conferences. The second one corresponds to an update of the point-source analysis using data of the ANTARES neutrino telescope (see Section 6.2), which includes the use of cascade events. This analysis has been published in Physical Review D [111]. A previous point and extended neutrino source search analysis was carried out for a shorter livetime of the ANTARES telescope. This analysis was published in the Astrophysical Journal Letters [130]. Since these results have been superseded by those presented in section 6.2, they are not described in this Thesis. Finally, the estimations of the KM3NeT/ARCA detector performance for searches of point and extended sources by using only events reconstructed as showers are presented in Section 6.3. An earlier version of this analysis was presented for the Letter of Intent of the KM3NeT collaboration [106].

6.1 First combined analysis with the ANTARES and IceCube neutrino telescopes

In this section, the results of the first combined search with data from the ANTARES and IceCube detectors are described. Although the IceCube detector is considerably larger, the location of the ANTARES telescope provides a better sensitivity to galactic sources. The reason is that for events coming from the Southern Sky, the IceCube detector needs to apply a stringent energy cut to suppress the huge background of atmospheric muons. Further

efforts have been performed by the IceCube Collaboration to improve the sensitivity towards this region of the sky, and large improvements have been achieved [236] [237]. However, the sensitivities for galactic sources obtained by ANTARES are currently the most stringent ones. In contrast, IceCube presents an improved sensitivity for energies higher than $E_\nu >$ 100 TeV for almost the whole Southern Sky. The main motivation for the combination relies on the fact that each detector has a better performance in different energy ranges, so that they are complementary.

The data samples are described in Section 6.1.1. A further extension of these samples is forseen in future searches, although it is out of the scope of this Thesis. Brief comments on the method are described in Sections 6.1.2 and 6.1.3. The results are finally described in Section 6.1.4.

6.1.1 Neutrino Data Samples

All the events coming from the Southern sky which were included in the three-year IceCube point-source analysis [184] and the 2007-2012 ANTARES point-source search [130] are included in the data sample. The recorded events of the ANTARES sample correspond to the time period between Jan 29, 2007 to Dec 31, 2012. The IceCube data sample contains events taken from Apr 5, 2008 until May 13, 2011, without the use of the Deep Core strings.

The IceCube detector was being constructed during this period. Therefore, the performance differs not only between the ANTARES and IceCube detectors, but also during the different periods of the IceCube data sets. Figure 6.1-left shows the effective area for each IceCube configuration (40, 59 and 79 strings) and for ANTARES for muon neutrinos coming from a source at δ = –30°. The effective area is larger for the IceCube samples in neutrino energies above 100 TeV due to its larger volume. The overwhelming down-going background of atmospheric muons in IceCube, forces a declination-dependent energy cut which reduces significantly the effective area at lower energies. Since the events of a δ = –30° source are up-going for the ANTARES detector, and therefore the Earth is used as a filter, the effective area for energies smaller than 100 TeV is larger in this detector. Another relevant difference between both detectors is the median angular

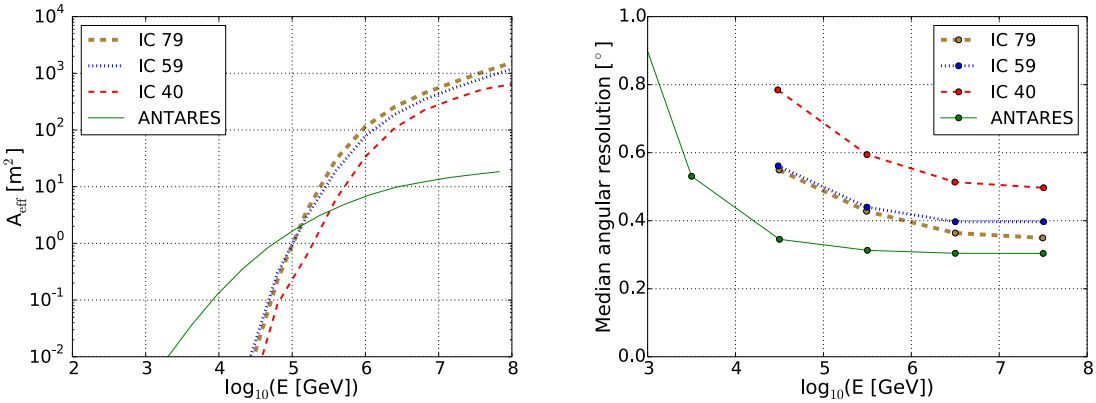

Fig. 6.1.: Left: Effective area for muon neutrinos coming from a point source at a declination $\delta = -30°$. Right: Median angular resolution for muon neutrino events for the samples used in this analysis after the final set of cuts. The median angular resolution is defined as the median of the distribution of the difference between the true and the reconstructed neutrino directions.

resolution, as can be seen in Figure 6.1-right. The longer photon scattering length in water compared to the one in ice provides a better angular resolution for the ANTARES sample.

A comparison of the sensitivities reported by both experiments for the whole sky using the Neyman method [226] can be seen in Figure 6.2.

On each sample, the events were selected using different criteria, although in all cases they were selected following a data blinding policy and with a set of selection cuts which minimised the neutrino flux required for a 5σ discovery in 50% of the experiments.

The 2007-2012 ANTARES sample

The ANTARES event sample is the one used in the ANTARES 2007-2012 point-source analysis [130]. The event selection optimisation was performed by applying cuts on the quality of the reconstructed track fit, Λ, the angular error estimate, σ, and the reconstructed zenith angle, θ. All these parameters are obtained from the `AAFit` reconstruction mechanism (see Section 3.3.1). The optimised event sample contains a total of 5516 events, where 4136

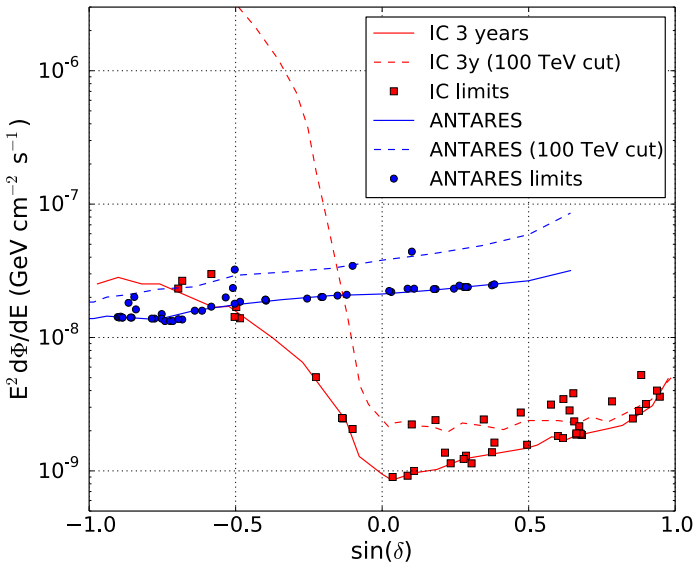

Fig. 6.2.: Sensitivities (lines) and 90% CL upper limits on the neutrino flux for a set of selected sources (squares and dots) at 90% CL assuming an E^{-2} source spectrum as reported in the 2007-2012 ANTARES (blue) [130] and IceCube 3 years (red) [184] point-source analyses. Dashed lines indicate the sensitivity for an E^{-2} spectrum with neutrino energies below 100 TeV. The sensitivities and upper limits are calculated using the Neyman method.

come from the Southern Hemisphere. Around 10% of these events are estimated to be mis-reconstructed atmospheric muons.

The 3–year IceCube sample

Table 6.1 shows the livetime, number of events and time period of the IceCube 40–, 59– and 79–string data samples used for this analysis. Only events from the Southern sky are considered. Unlike the ANTARES sample, the background of atmospheric muons is predominant over the background of atmospheric neutrinos in the IceCube's Southern sky events.

A total number of $\sim 10^{10}$ down-going events per year are reconstructed in IceCube. The events included in the data samples of Table 6.1 correspond only to high energy well-reconstructed muon tracks. This reduction makes

Sample	Start date	End date	Livetime [days]	# events
IC-40	2008 Apr 5	2009 May 20	376	22 779
IC-59	2009 May 20	2010 May 31	348	64 230
IC-79	2010 May 31	2011 May 13	316	59 009

Tab. 6.1.: Event sample information for the different IceCube configurations. Only events coming from the Southern-sky (numbers indicated in the last column) have been considered for this analysis.

possible to detect a neutrino source with a hard energy spectrum compared to the softer spectrum of the atmospheric muon background. The selection process is performed differently in each configuration. In the 40–string data sample, a set of cuts on the angular error estimate, σ, the reconstructed energy, and the reduced log-likelihood from the reconstructed track was performed (see [212] for further information). The IceTop vetoing capability was also included in the IceCube 59–string data sample [184]. A boosted decision tree combining 17 parameters and the IceTop vetoing capability were used instead in the IceCube 79–string configuration [184].

The total number of Southern sky events selected from the three year sample is 146 018 events.

6.1.2 Relative fraction of events for different source assumptions

Due to the different features of each sample, the fraction of expected source events for each sample varies according to the declination and source assumptions. This fraction is defined as the quotient between the expected number of signal events for a given sample and the one for all samples,

$$C^j(\delta, d\Phi/dE_\nu) = \frac{N^j(\delta, d\Phi/dE_\nu)}{\sum_i N^i(\delta, d\Phi/dE_\nu)}, \tag{6.1}$$

where $N^j(\delta, d\Phi/dE_\nu)$ is the total number of expected events for the j-th sample with a given source declination, δ, and a given source spectrum, $\frac{d\Phi}{dE_\nu}$. This number can be calculated from the effective area as denoted in Equation 5.18.

The relative fraction of signal events for an unbroken E^{-2} spectrum is shown in Figure 6.3. In this case, all samples have a significant contribution over most of the Southern Sky. The ANTARES contribution is more relevant for declinations closer to δ = –90°, while IceCube contributions are more significant for declinations closer to δ = 0°. This variability is due to the strong declination-dependent energy cut to reduce the background of atmospheric muons.

Apart from the E^{-2} case, further source spectra are considered in this analysis. The relative fraction of source events is also calculated for an unbroken $E^{-2.5}$ power-law spectrum, which favoured by recent IceCube diffuse-flux searches [2, 3, 4, 5]. Additionally, an E^{-2} source spectra with exponential square-root cut-offs ($\frac{d\Phi}{dE} \propto E^{-2} \exp\left[-\sqrt{\frac{E}{E_{\mathrm{cut-off}}}}\right]$) of 100 TeV, 300 TeV and 1 PeV have also been considered, since a square-root dependence may be expected from Galactic sources [95]. The relative fraction of source events for these cases are shown in Figure 6.4. As in the E^{-2} case, the ANTARES relative importance increases with declinations closer to δ = –90°. Furthermore, the ANTARES total contribution in these cases is larger, since the contribution of high energy neutrinos is suppressed for these source spectra.

6.1.3 Search method

The unbinned maximum likelihood method explained in Section 5.1 has been applied. The likelihood takes into account the reconstructed energy, the reconstructed direction and the estimated angular uncertainty to evaluate the significance of a cluster of events. It also considers different PDFs per each sample, due to the different detector response. Consequently, the likelihood as a function of the total number of fitted events, n_s, can be defined in the following way:

$$L(n_s) = \prod_{j=1}^{4} \prod_{i=1}^{N^j} \left[\frac{n_s^j}{N^j} S_i^j + \left(1 - \frac{n_s^j}{N^j}\right) B_i^j \right], \tag{6.2}$$

where j indicates the index of a data sample, i is an event contained in the j-th sample, S_i^j and B_i^j are the values of the signal and background PDFs for the i-th event, N^j is the total number of events observed in the j-th

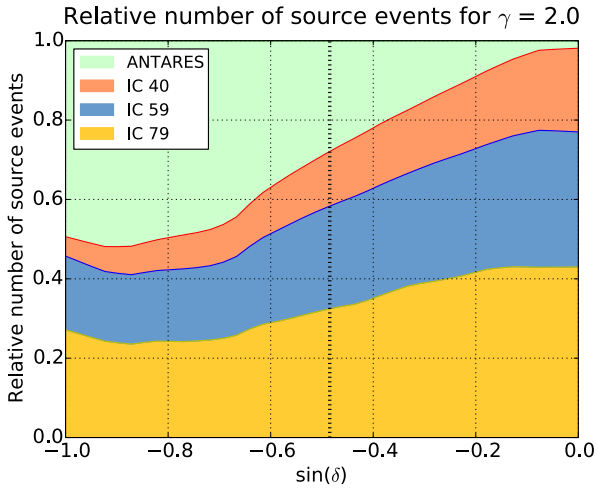

Fig. 6.3.: Relative fraction of signal events for each sample coming from an E^{-2} source as a function of the declination. The green shaded area corresponds to the 2007-2012 ANTARES contribution, whereas the orange, blue, and yellow areas to the IceCube 40–, 59– and 79–string samples. The vertical dashed line corresponds to the declination of the Galactic Centre.

sample, and n_s^j is the fitted number of signal events in the j-th sample. The n_s^j values are referred to the same source assumption, and therefore are related to the total number of fitted events, n_s, by the relative contribution of each sample, $n_s^j = n_s \cdot C^j(\delta, \frac{d\Phi}{dE})$.

The background and signal PDFs for the ANTARES and IceCube samples are defined differently. The ANTARES signal PDF is described as

$$S^{ANT} = \frac{1}{2\pi\sigma^2} \exp\left(-\frac{\Delta\Psi(\vec{z}_s)^2}{2\sigma^2}\right) P_s^{ANT}(\mathcal{N}^{hits}, \sigma), \tag{6.3}$$

where $\vec{z_s} = (\alpha_s, \delta_s)$ is the source location, $\Delta\Psi(\vec{z}_s)$ indicates the angular distance between the source and a given event, and $P_s^{ANT}(\mathcal{N}^{hits}, \sigma)$ is the probability for a signal event to be reconstructed with an angular error estimate of σ and a number of hits $\mathcal{N}^{hits}$. In this case, the number of hits is used as a proxy of the energy of the event. The larger the number of hits, the less likely to be produced by a background event.

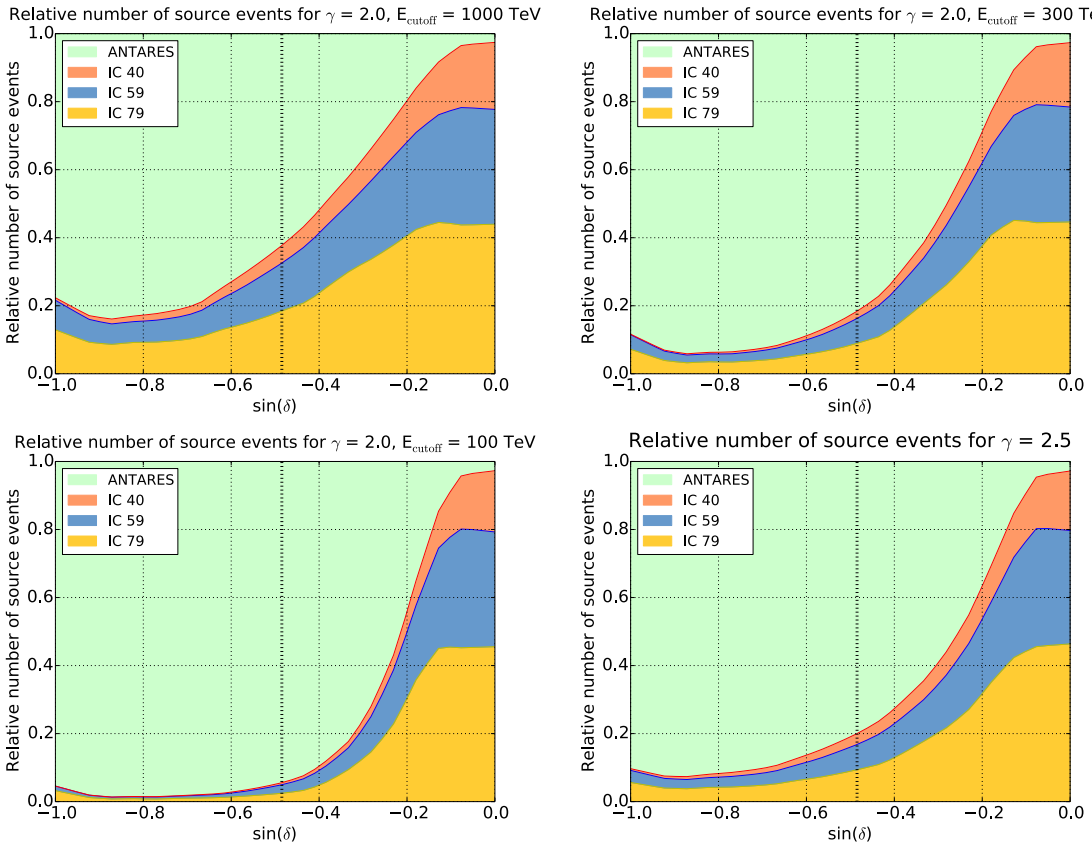

Fig. 6.4.: Relative fraction of signal events of each sample for different energy spectra: E^{-2} with energy cutoff E_{cutoff} of 1 PeV (top-left), 300 TeV (top-right), 100 TeV (bottom-left) and $E^{-2.5}$ spectrum (bottom-right). The green shaded area corresponds to the 2007-2012 ANTARES contribution, whereas the orange, blue, and yellow areas to the IceCube 40–, 59– and 79–string samples. The vertical dashed line corresponds to the declination of the Galactic Centre.

A similar PDF for of the IceCube signal is defined,

$$S^{IC} = \frac{1}{2\pi\sigma^2} \exp\left(-\frac{\Delta\Psi(\vec{z}_s)^2}{2\sigma^2}\right) P_s^{IC}(\mathcal{E}, \sigma|\delta). \tag{6.4}$$

The main difference with respect to the ANTARES signal PDF lies in the use of the reconstructed energy, $\mathcal{E}$. The dependence on declination comes from the declination dependent event selection cut on the reconstructed energy.

The definition of the background PDFs are:

$$B^{ANT} = \frac{R^{ANT}(\delta)}{2\pi} P_b^{ANT}(\mathcal{N}^{hits}, \sigma), \tag{6.5}$$

$$B^{IC} = \frac{R^{IC}(\delta)}{2\pi} P_b^{IC}(\mathcal{E}, \sigma|\delta), \tag{6.6}$$

where $R^j(\delta)$ is the rate of events as a function of the declination of the corresponding sample. $P_b^{ANT}(\mathcal{N}^{hits}, \sigma)$ and $P_b^{IC}(\mathcal{E}, \sigma|\delta)$ are the analogous background event distributions to the P_s^{ANT} and P_s^{IC} definitions given above.

The test statistics, TS, is defined as in Equation 5.12. The TS distributions can be different for each declination. Because of this, TS distributions have been calculated in steps of 1° from pseudo-experiments. The TS value obtained for a given location in the sky from the data, is turned into a pre-trial p-value by comparing it with the corresponding background TS distribution. The post-trial significance is estimated with pseudoexperiments according to the type of search, as explained in Section 6.1.4.

Two kind of searches have been carried out to find point-like sources. In the first one, the TS values are obtained at the location of 40 pre-selected neutrino source candidates. These correspond to those sources from the Southern sky which were considered in the ANTARES 2007-2012 and IceCube 3 years point-source searches. Since the position of these sources is known with an uncertainty below the angular resolution of each sample, their location is considered as a known parameter in the likelihood maximisation. The second one is a search over the Southern sky, where the TS is evaluated in steps of $1^\circ \times 1^\circ$ over the whole scanned region. The location of the source is left as an additional free parameter in the likelihood maximisation to fit the best position within the $1^\circ \times 1^\circ$ boundaries.

An E^{-2} source spectrum has been assumed in the signal PDFs for the full sky and candidate list searches. However, limits for the neutrino flux from the candidate sources have also been calculated for the source spectra referred to in Section 6.1.2.

6.1.4 Results

Results from the full Southern sky and candidate list searches are given below.

Full Southern-sky search

No significant excess is found over the background of atmospheric muons and neutrinos. The most significant accumulation is found at $\alpha = 332.8°$, δ=–46.1° with a pre-trial p-value of 6.0×10^{-7} and a best-fit value of $n_s = 7.9$. The pre-trial p-value distribution for the most significant clusters when only background events are present is obtained from simulations of pseudo-data sets. From this distribution, it is estimated that 24% of the background simulations present a smaller p-value, which leads to a significance of 0.7σ in the one sided convention (see Figure 6.5). The location of this cluster corresponds to the second most significant cluster in the 2007-2012 ANTARES point-source search. The map of pre-trial p-values for all directions in the Southern sky can be seen in Figure 6.6, in which a smaller step of $0.2° \times 0.2°$ is used.

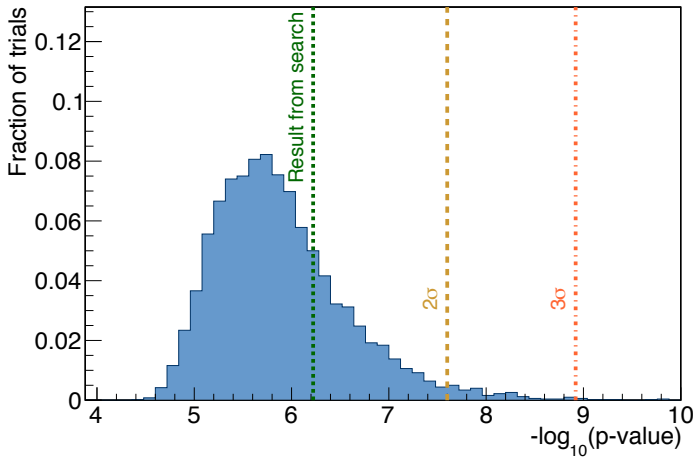

Fig. 6.5.: Smallest p-value distribution obtained from simulations of pseudo-data sets in the Southern sky (blue distribution) compared to the pre-trial p-value of the most significant cluster found in the full Southern Sky search (green dashed line). The yellow and the red dashed lines indicate the 2σ and 3σ significance thresholds using the one-sided convention.

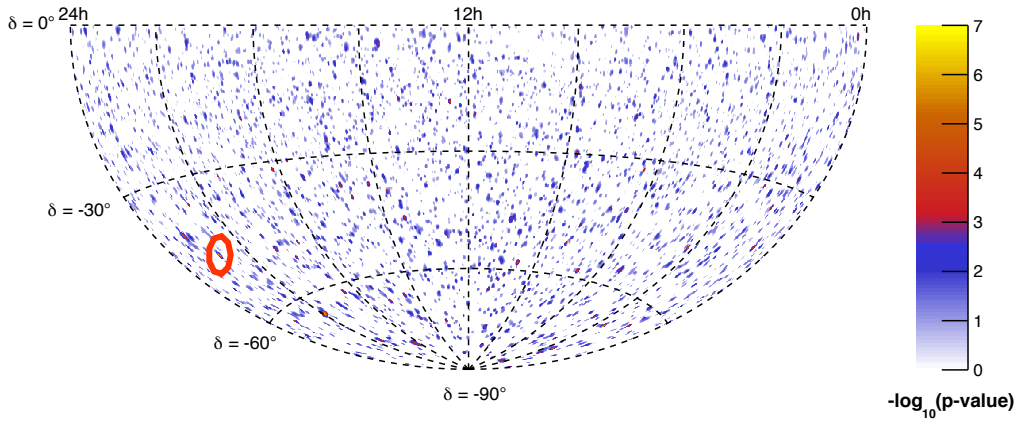

Fig. 6.6.: Pre-trial p-values represented over the Southern Sky. The red circle shows the location of the most significant cluster mentioned in the text.

Candidate list search

No statistically significant accumulation is observed. The most significant accumulation of events in the candidate list corresponds to HESS J1741-302 (pre-trial p-value of 0.003). In order to obtain the post-trial significance, a distribution of the smallest p-value obtained in the location of the candidate source lists after simulating only background events is made. A post-trial p-value of 11% (significance of 1.2σ in the one-sided convention), as seen in Figure 6.7, is found.

Table 6.2 shows the pre-trial p-values, fitted number of signal events, n_s, and flux upper limits for different energy spectra for all the candidate sources considered. The flux upper limits for an E^{-2} source spectrum, along the sensitivity of the combined analysis and the results of the ANTARES 2007-2012 and IceCube 3–year samples are shown in Figure 6.8. For this spectrum, the sensitivity improves in a larger scale in the region close to the Galactic centre ($\delta = -29°$). Similar gains in other regions of the sky can be seen for different energy spectra in Figure 6.9.

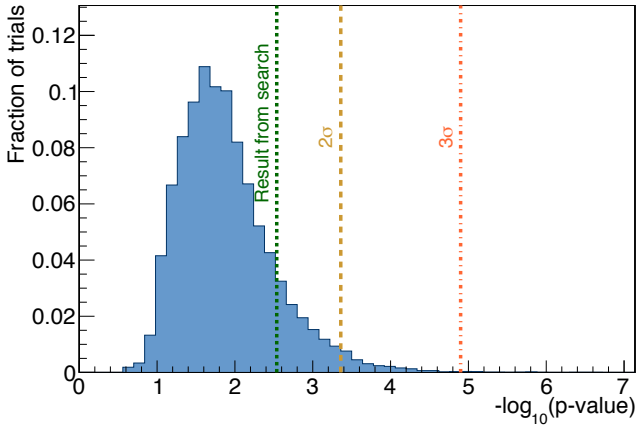

Fig. 6.7.: Smallest p-value distribution obtained from simulations of pseudo-data sets found using the locations of the source candidates (blue distribution) compared to the pre-trial p-value of the most significant cluster found in the candidate list search (green dashed line). the yellow and the red shaded lines indicate the 2σ and 3σ significance thresholds using the one-sided convention.

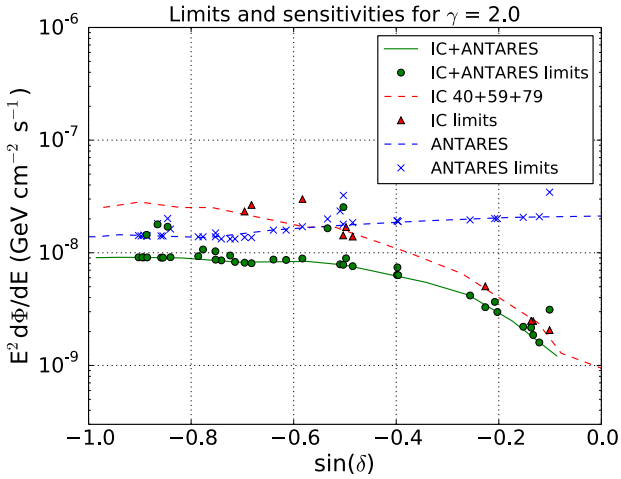

Fig. 6.8.: 90% CL upper limits (points) and sensitivities (lines) using the Neyman method for point-sources assuming an E^{-2} energy spectrum. In green, the results obtained for the combined search are shown. As a comparison, the results obtained in the ANTARES 2007-12 search and in the IceCube 3 years search are shown in blue and red, respectively. As reference, the Galactic Centre is at $\sin(\delta = -29°) \approx$ -0.48.

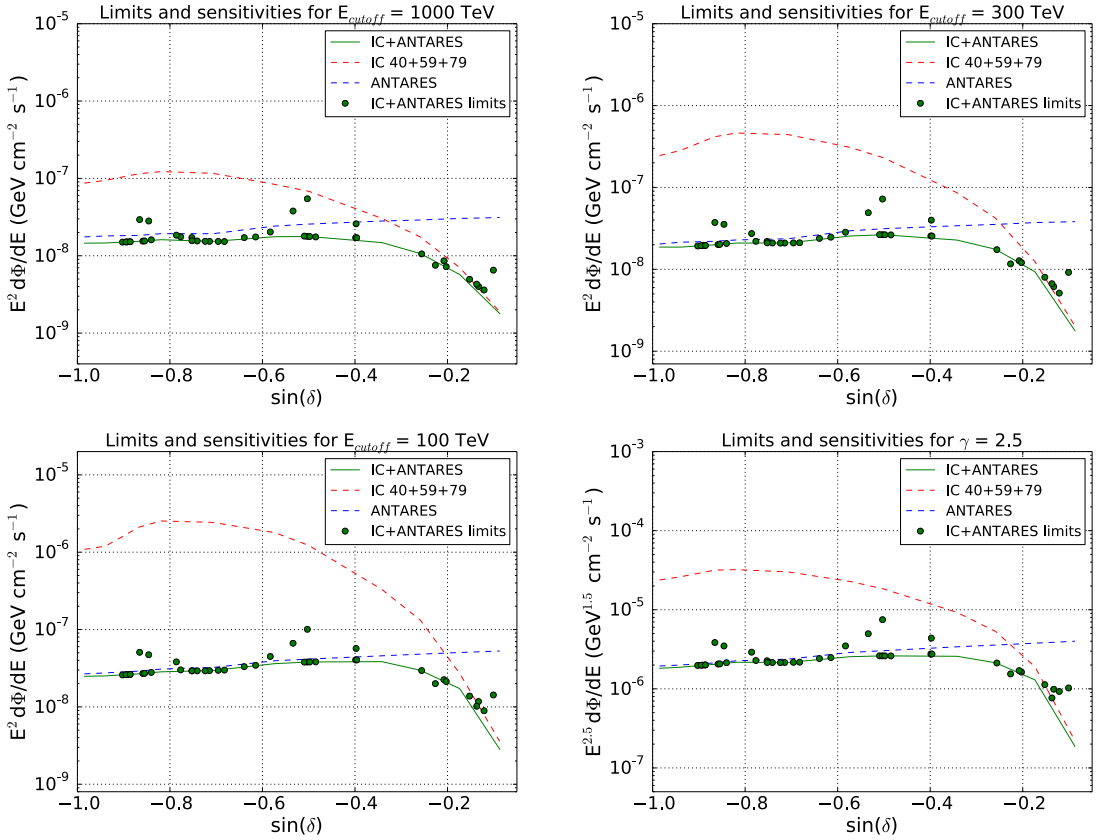

Fig. 6.9.: 90% CL upper limits (points) and sensitivities (curves) as in Fig. 6.8 but calculated for other energy spectra: E^{-2} with a square-root exponential cut-off at $E = 1\,\text{PeV}$ (top left), $E = 300\,\text{TeV}$ (top right), $E = 100\,\text{TeV}$ (bottom left) and $E^{-2.5}$ unbroken power-law (bottom right). In green, the results obtained for the combined search. The results of the ANTARES 2007-12 and the 3 years IceCube point-source searches are shown in blue and red, respectively. As reference, the declination of the Galactic Centre is approximately at $\sin(\delta = -29°) \approx$ -0.48.

Name	δ (°)	α (°)	n_s	p	$\phi^{90CL}_{E^{-2}}$	$\phi^{90CL}_{E^{-2.5}}$	$\phi^{90\%CL}_{E_c=1PeV}$	$\phi^{90CL}_{E_c=300TeV}$	$\phi^{90CL}_{E_c=100TeV}$
3C279	-5.8	-166	1.1	0.05	3.13E-09	1.03E-06	6.51E-09	9.17E-09	1.43E-08
HESSJ1837-069	-7.0	-80.6	-	-	1.60E-09	9.27E-07	3.61E-09	5.12E-09	8.91E-09
QSO2022-077	-7.6	-53.6	-	-	1.86E-09	9.89E-07	4.01E-09	6.14E-09	1.17E-08
PKS1406-076	-7.9	-147.8	-	-	2.17E-09	7.67E-07	4.29E-09	6.67E-09	1.02E-08
HESSJ1834-087	-8.8	-81.3	-	-	2.21E-09	1.13E-06	4.96E-09	8.00E-09	1.38E-08
PKS0727-11	-11.7	112.6	-	-	2.98E-09	1.63E-06	7.22E-09	1.21E-08	2.13E-08
1ES0347-121	-12.0	57.4	-	-	3.67E-09	1.70E-06	8.60E-09	1.27E-08	2.25E-08
QSO1730-130	-13.1	-96.7	-	-	3.29E-09	1.54E-06	7.53E-09	1.17E-08	2.00E-08
LS5039	-14.8	-83.4	-	-	4.17E-09	2.12E-06	1.06E-08	1.74E-08	2.95E-08
W28	-23.3	-89.6	-	-	6.32E-09	2.75E-06	1.71E-08	2.55E-08	4.05E-08
PKS0454-234	-23.4	74.3	-	-	7.42E-09	4.38E-06	2.59E-08	3.98E-08	5.69E-08
1ES1101-232	-23.5	165.9	-	-	6.36E-09	2.76E-06	1.72E-08	2.56E-08	4.05E-08
GalacticCentre	-29.0	-93.6	-	-	7.60E-09	2.61E-06	1.75E-08	2.63E-08	3.82E-08
PKS1622-297	-29.9	-113.5	-	-	8.93E-09	2.61E-06	1.77E-08	2.64E-08	3.81E-08
PKS2155.304	-30.2	-30.3	-	-	2.54E-08	7.49E-06	5.45E-08	7.22E-08	1.01E-07
HESSJ1741-302	-30.2	-94.8	1.6	0.003	7.82E-09	2.61E-06	1.78E-08	2.65E-08	3.80E-08
H2356-309	-30.6	-0.2	-	-	7.90E-09	2.61E-06	1.79E-08	2.65E-08	3.79E-08
PKS0548-322	-32.3	87.7	0.9	0.07	1.65E-08	4.97E-06	3.79E-08	4.91E-08	6.65E-08
PKS1454-354	-35.7	-135.6	-	-	8.89E-09	3.49E-06	2.03E-08	2.84E-08	4.49E-08
PKS0426-380	-37.9	67.2	-	-	8.64E-09	2.48E-06	1.75E-08	2.47E-08	3.45E-08
RXJ1713.7-3946	-39.8	-101.8	-	-	8.71E-09	2.42E-06	1.72E-08	2.39E-08	3.32E-08
CenA	-43.0	-158.6	-	-	8.07E-09	2.17E-06	1.53E-08	2.11E-08	2.99E-08
PKS0537-441	-44.1	84.7	-	-	8.16E-09	2.16E-06	1.53E-08	2.10E-08	2.97E-08
VelaX	-45.6	128.8	-	-	8.30E-09	2.15E-06	1.53E-08	2.09E-08	2.94E-08
RXJ0852.0-4622	-46.4	133	-	-	9.46E-09	2.15E-06	1.54E-08	2.09E-08	2.93E-08
HESSJ1632-478	-47.8	-112	-	-	8.56E-09	2.15E-06	1.55E-08	2.10E-08	2.93E-08
PKS2005-489	-48.8	-57.6	-	-	8.69E-09	2.15E-06	1.56E-08	2.11E-08	2.93E-08
GX339-4	-48.8	-104.3	-	-	1.03E-08	2.27E-06	1.72E-08	2.19E-08	2.93E-08
HESSJ1616-508	-51.0	-116	-	-	1.07E-08	2.28E-06	1.76E-08	2.20E-08	3.01E-08
HESSJ1614-518	-51.8	-116.4	-	-	9.32E-09	2.91E-06	1.85E-08	2.74E-08	3.82E-08
CirX-1	-57.2	-129.8	-	-	9.13E-09	2.14E-06	1.61E-08	2.07E-08	2.79E-08
HESSJ1023-575	-57.8	155.8	0.8	0.08	1.70E-08	3.48E-06	2.81E-08	3.54E-08	4.72E-08
HESSJ1503-582	-58.7	-133.6	-	-	9.05E-09	2.07E-06	1.55E-08	2.02E-08	2.71E-08
MSH15-52	-59.2	-131.5	-	-	9.06E-09	2.06E-06	1.55E-08	2.01E-08	2.70E-08
ESO139-G12	-59.9	-95.6	0.8	0.07	1.79E-08	3.85E-06	2.93E-08	3.73E-08	5.08E-08
HESSJ1507-622	-62.3	-133.3	-	-	9.09E-09	2.01E-06	1.52E-08	1.96E-08	2.63E-08
RCW86	-62.5	-139.3	0.2	0.11	1.44E-08	2.00E-06	1.52E-08	1.96E-08	2.63E-08
HESSJ1303-631	-63.2	-164.2	-	-	9.10E-09	1.99E-06	1.51E-08	1.95E-08	2.61E-08
PSRB1259-63	-63.5	-164.3	-	-	9.11E-09	1.99E-06	1.51E-08	1.94E-08	2.61E-08
HESSJ1356-645	-64.5	-151	-	-	9.12E-09	1.98E-06	1.50E-08	1.93E-08	2.59E-08

Tab. 6.2.: Fitted number of source events, n_s, pre-trial p-values, p, and 90% C.L. flux limits, Φ^{90CL}_{ν} for the different source spectra for the 40 considered candidate sources. Units for the flux limits for the $E^{-2.5}$ spectra, $\phi^{90CL}_{E^{-2.5}}$, are given in GeV$^{1.5}$cm^{-2}s^{-1}, whereas the rest are in GeV cm^{-2}s^{-1}. The sources are sorted by their declination. Dashes (-) in the fitted number of source events and pre-trial p-values indicate sources with $n_s \leq 0.001$.

6.2 Searches with the ANTARES neutrino telescope

This point and extended source search, which uses the ANTARES data taken between 2007 and 2015, is the first one published which includes neutrino events from all flavours. This is achieved by including events whose signal is due to the induced electromagnetic and/or hadronic shower produced in a neutrino interaction. The reconstruction of these events has been done using the TANTRA shower algorithm (see Section 3.4.1), which provides a median angular resolution between 2° and 3° for neutrinos with energies between 1 TeV and 1 PeV.

6.2.1 Event selection

The event selection is done with data taken between the 29th January 2007 and 31st December 2015, which comprises a total livetime of 2423.6 days. Two event samples based on the event types registered have been defined. The track-like sample is mainly composed by events coming after the CC interaction of $\overset{(-)}{\nu}_\mu$[1] and some $\overset{(-)}{\nu}_\tau$, whereas the remaining event types are included in the shower sample. The selection criteria for each sample is explained in Sections 6.2.2 and 6.2.3. The effective area for $\overset{(-)}{\nu}_\mu$ CC after the track selection cuts and for $\overset{(-)}{\nu}_e$ CC and $\overset{(-)}{\nu}_\mu$ NC events after the shower selection cuts is shown in Figure 6.10.

The ANTARES simulations produced to account for $\overset{(-)}{\nu}_\tau$ interactions only cover a limited livetime of the data. For this reason, the corresponding contributions due to the hadronic and leptonic channels after the interaction of $\overset{(-)}{\nu}_\tau$ are estimated by scaling the contribution of other flavor neutrino events. An E^{-2} neutrino flux is considered for this scaling. The rates obtained are the following: to take into account the decay of the outgoing τ into a μ (branching ratio of $\sim$ 17%) after a $\overset{(-)}{\nu}_\tau$ CC interaction, the number of events predicted by CC $\overset{(-)}{\nu}_\mu$ interactions is increased by 9%; to take into account the decay of the outgoing τ into an electron (branching ratio of $\sim$ 17%), the number of CC $\overset{(-)}{\nu}_e$ is increased by 12%; finally, to take into account the τ decaying into hadrons (branching ratio of $\sim$ 64%) after a

[1] The notation $\overset{(-)}{\nu}$ refers to both neutrinos and anti-neutrinos.

$\overset{(-)}{\nu}_\tau$ CC interaction and the $\overset{(-)}{\nu}_\tau$ NC interactions, the small number of events predicted by $\overset{(-)}{\nu}_\mu$ NC interactions is increased by 374%.

6.2.2 Muon track selection

Muon tracks are considered amongst the events reconstructed with `AAFit` (see Section 3.3.1). As in previous publications [130], a cut on the angular error estimate ($\beta_{tr} < 1°$), the reconstructed zenith angle ($\cos\theta_{tr} > -0.1$) and the Λ reconstruction quality parameter ($\Lambda > -5.2$) have been applied. The output value of the dEdX algorithm (see Section 3.3.1) has been used as the energy proxy of these events. This estimator fails for events with muon energies below ∼500 GeV (the critical region to produce significant energy losses due to radiative processes) and for estimated track lengths below 380 m. Therefore, these events are not included in the event sample. An overview of the selection cuts is shown in Table 6.3. The selection criteria yields a total of 7622 neutrino candidate events reconstructed as muon tracks.

Tab. 6.3.: Chain of selection cuts for the track channel and number of estimated events after each step for atmospheric muons (n_μ^{atm}), atmospheric neutrinos (n_ν^{atm}) and cosmic neutrinos ($n_\nu^{E^{-2}}$) reconstructed as a track. A flux according to $d\Phi/dE = 10^{-8}\,(E/\mathrm{GeV})^{-2}\,\mathrm{GeV}^{-1}\,\mathrm{cm}^{-2}\,\mathrm{s}^{-1}$ is assumed for cosmic neutrinos.

Criterion	Condition	n_μ^{atm}	n_ν^{atm}	$n_\nu^{E^{-2}}$
Trigger		4.9×10^8	6.3×10^4	204
Up-going	$\cos\theta_{tr} > -0.1$	4.3×10^7	5.0×10^4	151
Angular error estimate	$\beta_{tr} < 1°$	2.2×10^7	3.3×10^4	105
Track reconstruction quality	$\Lambda > -5.2$	1513	7475	44
Track length and energy cut	$L_\mu > 380$ m, $\log_{10}(\rho) > 1.6$	1117	7086	41

6.2.3 Shower selection

Shower events are reconstructed with the `TANTRA` algorithm (see Section 3.4.1). Since one event may be reconstructed both by `AAFit` and `TANTRA`, those events which have been selected for the track channel are excluded from the shower event selection. As in the track reconstruction mechanism, cuts on the reconstructed zenith angle ($\cos\theta_{sh} > -0.1$) and on the angular error estimate ($\beta_{sh} < 30°$) are applied. Moreover, only events with a

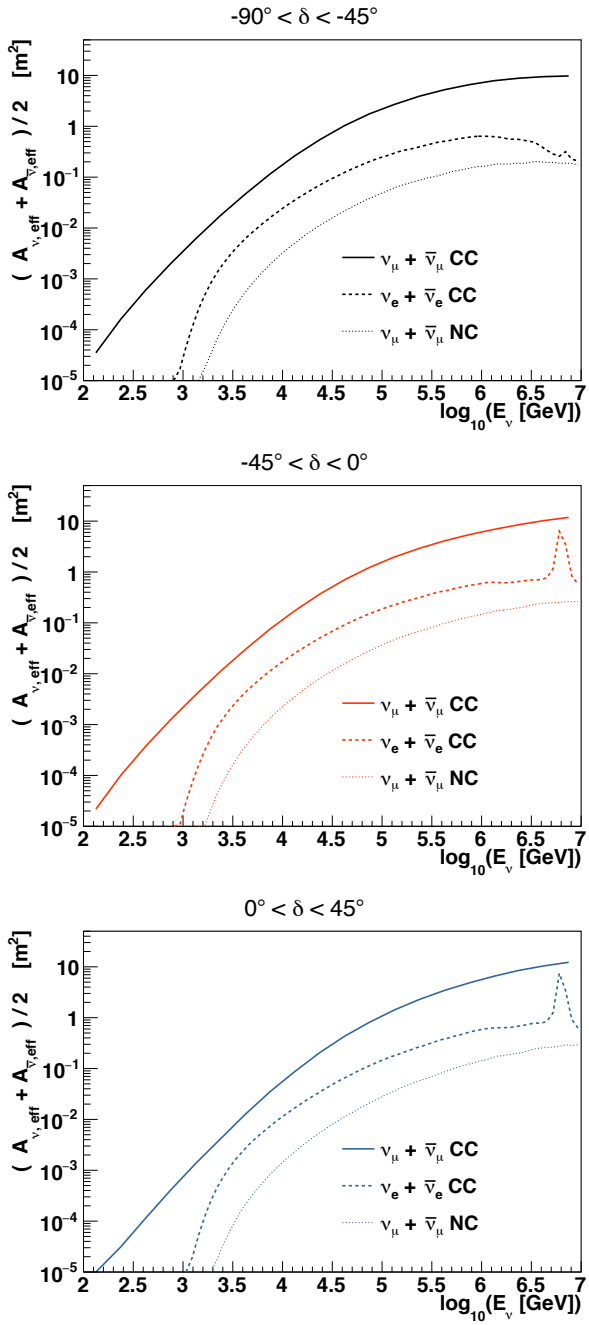

Fig. 6.10.: Effective area for $\nu_\mu+\bar{\nu}_\mu$ CC events after the track selection cuts (solid line) and for $\nu_e+\bar{\nu}_e$ CC and $\nu_\mu+\bar{\nu}_\mu$ NC events after the shower selection cuts (dashed lines) considering three declination ranges.

reconstructed interaction vertex close or inside the intrumented volume are considered.

Further requirements are needed to reduce the background of atmospheric muons. Additional cuts based on the TANTRA $M_{\rm est}$ value, on the RDF value provided by the Dusj reconstruction mechanism (see Section 3.4.3), and on an atmospheric muon veto likelihood, $\mathscr{L}_\mu$, which uses informations of the hits in the event, are applied. This muon likelihood only takes into account coincidence hits in the same storey within $20\,\mathrm{ns}$. Its PDF is based on the time residual of the hits, $t_{\rm res}$, the distance of the hits to the reconstructed vertex, d, and on the number of hits with time residuals between -20 ns and 60 ns, N, so that,

$$\mathscr{L}_\mu = \sum_{\rm hits} \log\{P_{\rm sig}/P_{\rm bkg}\}, \tag{6.7}$$

where $P_{\rm sig} = P(N, d, t_{\rm res}|\nu)$ and $P_{\rm bkg} = P(N, d, t_{\rm res}|\mu)$. The distribution of this muon likelihood veto for atmospheric muons, cosmic showers and data events after applying all cuts is shown in Figure 6.11-top. Figure 6.11-bottom contains the distributions for the Dusj RDF variable after the cuts prior to the RDF cut have been applied.

The list of selection cuts with the expected number of events per each contribution is included in Table 6.4. The final shower event sample contains a total of 180 events after all the cuts.

Tab. 6.4.: Chain of selection cuts for the shower channel and number of estimated events after each step for atmospheric muons (n_μ^{atm}), atmospheric neutrinos (n_ν^{atm}) and cosmic neutrinos ($n_\nu^{E^{-2}}$) reconstructed as a shower. A flux according to $d\Phi/dE = 10^{-8}\,(E/\mathrm{GeV})^{-2}\,\mathrm{GeV}^{-1}\,\mathrm{cm}^{-2}\,\mathrm{s}^{-1}$ is assumed for cosmic neutrinos.

Criterion	Condition	n_μ^{atm}	n_ν^{atm}	$n_\nu^{E^{-2}}$
Track Veto	not selected as muon track	4.9×10^8	5.6×10^4	160
Up-going	$\cos\theta_{sh} > -0.1$	1.5×10^8	2.3×10^4	90
Interaction vertex	$R_{sh} < 300\,\mathrm{m}$, $\lvert Z_{sh}\rvert < 250\,\mathrm{m}$	7.7×10^7	2.1×10^4	80
M-estimator	$M_{\rm est} < 1000$	7.2×10^7	2.0×10^4	80
RDF	$RDF > 0.3$	8.0×10^4	2044	24
Muon likelihood	$\mathscr{L}_\mu > 50$	90	109	12

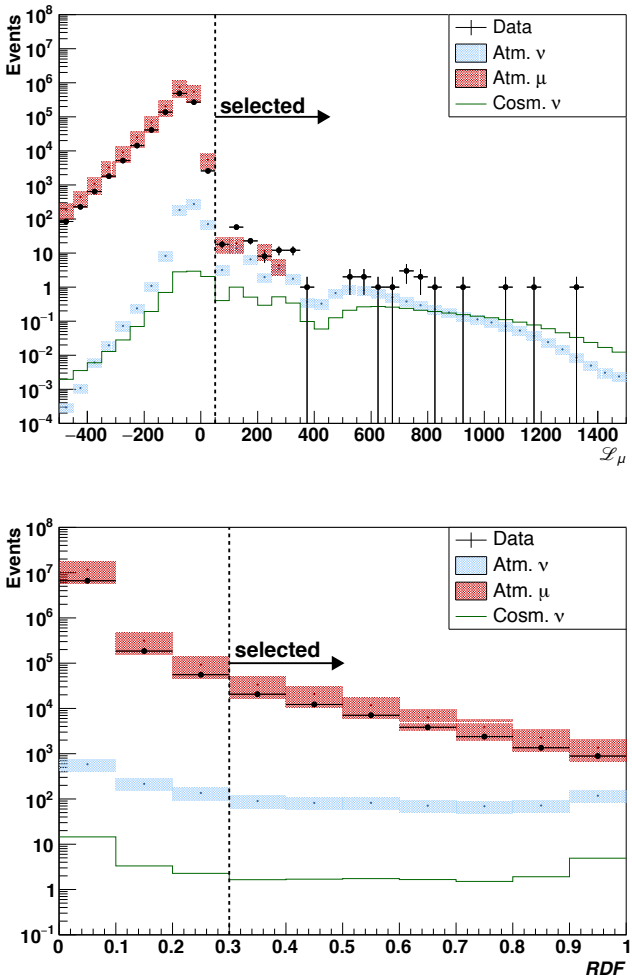

Fig. 6.11.: Top: atmospheric muon likelihood ratio parameter, $\mathscr{L}_\mu$, for data, cosmic neutrinos and atmospheric background. This figure corresponds to the event distributions after the RDF and all previous cuts listed in Table 6.4. Bottom: RDF parameter distribution for data, cosmic neutrinos and atmospheric background. This figure corresponds to the distributions obtained after applying all the cuts prior to the RDF shown in Table 6.4. The vertical dashed lines indicate the cut value.

6.2.4 Comparison between data and simulations

The comparison of the distributions between data and simulated events of the quality parameter for the track channel, Λ, and of the reconstructed zenith angle for the shower channel, are shown in Figure 6.12 and 6.13,

respectively. The background contamination of atmospheric muons in the track channel is estimated to be around 13%, whereas it is of $52\,\%$ for the shower channel.

An overestimate of the simulation on the number of events by $8\,\%$ ($17\,\%$) in the track (shower) channel is observed for the final event selection. This overestimate is within the overall systematic uncertainty of the atmospheric neutrino flux normalization [198]. The largest overestimation is mainly observed in the region where the atmospheric muon background is larger. In the cascade event sample, an underestimation of neutrinos is observed for $\cos(\theta_{sh}) > 0.4$, but again within the uncertainties of the atmospheric neutrino flux models. Even if there is a large contribution of atmospheric muons compared to atmospheric neutrinos in the region between $-0.1 < \cos(\theta_{sh}) < 0.1$, the current cuts enhance the discovery flux. To this respect, the point-source searches are more tolerant to higher levels of background contamination.

6.2.5 Acceptance

Figure 6.14 shows the acceptance as a function of the declination for both samples assuming an E^{-2} energy spectrum. With the assumed E^{-2} spectrum, 90% of the events are found in an energy range between 2 TeV and 3 PeV for the track channel (between 5 TeV and 4 PeV for the shower channel).

6.2.6 Search method

An extended maximum likelihood has been used for this analysis. The likelihood has been defined as,

$$\log \mathcal{L} = \sum_{S} \sum_{i \in S} \Big[\log(n_s^S F_i^S P_{i,sig}^S + N^S R_i^S P_{i,bkg}^S) \Big] - n_s, \qquad (6.8)$$

where S denotes the sample (in the following, *tr* for tracks, *sh* for showers), i is an event of the sample S, n_s^S is the number of signal events detected in the sample S, F_i^S is the point-spread function, $P_{i,sig}^S$ is the energy estimator PDF value for the event i if considered as a signal event, R_i^S is the background rate of events, $P_{i,bkg}^S$ is the energy estimator PDF value for the event i if

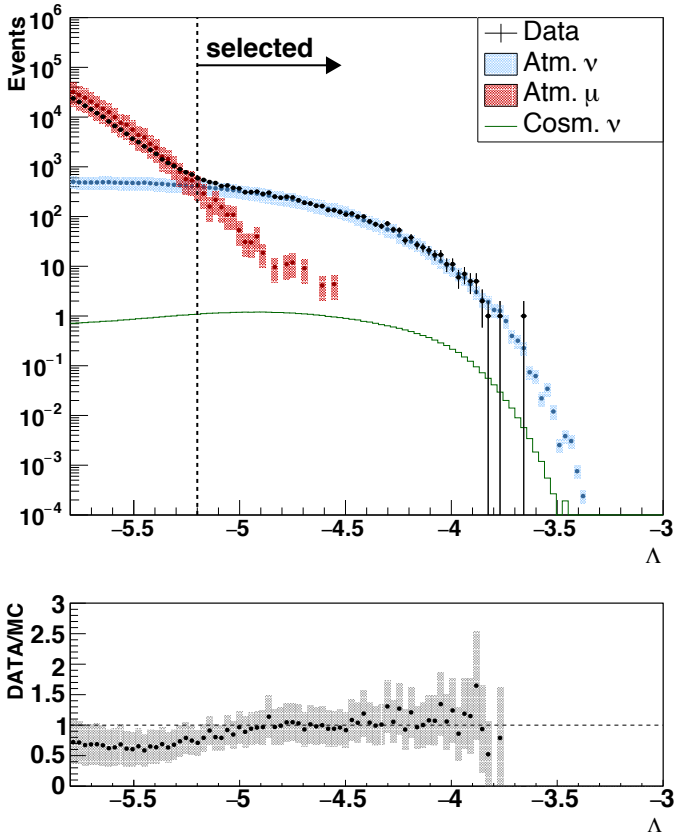

Fig. 6.12.: Monte Carlo (MC) and data distributions of the quality parameter Λ after a cut on the zenith angle ($\cos\theta_{tr} >$ -0.1) and on the angular error estimate ($\beta_{tr} < 1°$). For the cosmic neutrino distribution, a flux according to $d\Phi/dE = 10^{-8}\,(E/\mathrm{GeV})^{-2}\,\mathrm{GeV}^{-1}\,\mathrm{cm}^{-2}\,\mathrm{s}^{-1}$ is assumed. The figure on the bottom shows the ratio between the data and the MC, where the MC contribution corresponds to the sum of atmospheric muons and atmospheric neutrinos.

considered as a background event, and n_s is the sum of the number of signal events from all samples, $n_s = n_s^{tr} + n_s^{sh}$.

6.2.7 Point spread function and background rate

The Point Spread Function (PSF) describes the distribution of signal events around the location of a point-like source. It is defined as the PDF to reconstruct an event at a given angular distance $\Delta\Psi$ from its original direction,

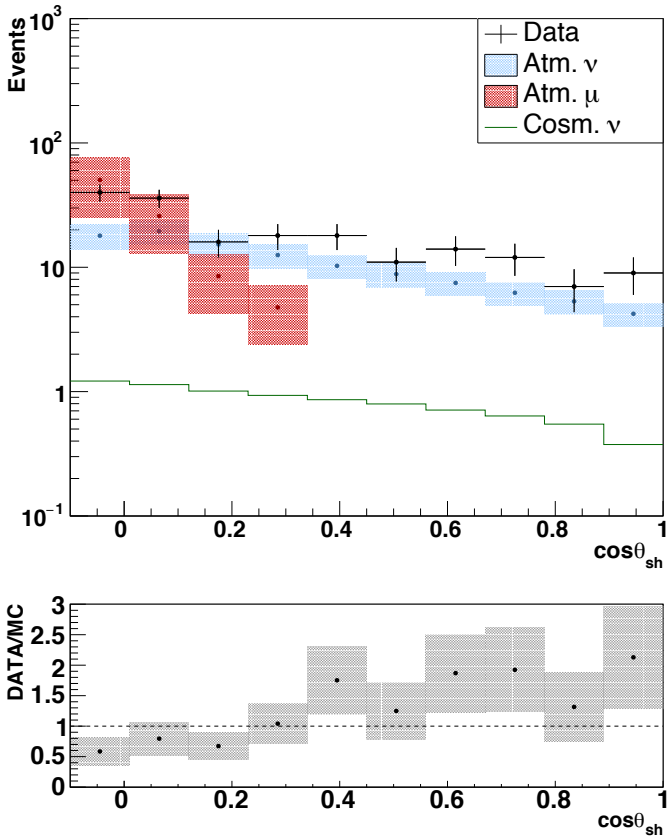

Fig. 6.13.: Monte Carlo (MC) simulations and data distributions of the zenith of the reconstructed shower direction, θ_{sh}, after all cuts are applied on the shower sample. For the cosmic neutrino distributions, a flux according to $d\Phi/dE = 10^{-8}\,(E/\mathrm{GeV})^{-2}\,\mathrm{GeV}^{-1}\,\mathrm{cm}^{-2}\,\mathrm{s}^{-1}$ is assumed. The figure on the bottom shows the ratio between the data and the MC, where the MC contribution corresponds to the sum of atmospheric muons and atmospheric neutrinos.

and depends on the angular resolution of the detector. However, the angular resolution is found to be correlated with the estimated angular error, β. Because of this, a PSF which depends also on β is considered to improve the pointing accuracy in the track channel. The cumulative distribution of the angular distance between the reconstructed and the original direction for track and shower events assuming a source with an E^{-2} energy spec-

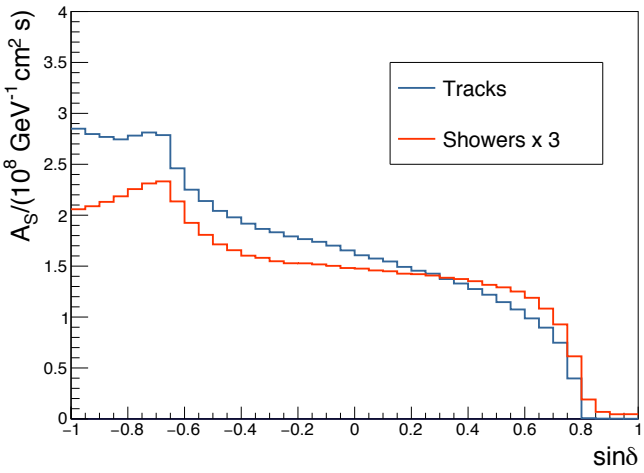

Fig. 6.14.: The acceptance as a function of the source declination for an E^{-2} energy spectrum with a flux normalization factor of $\Phi_0 = 10^{-8}\,\mathrm{GeV\,cm^{-2}\,s^{-1}}$ for the track (blue) and shower (red) samples. For better visibility, the acceptance for showers is scaled up to a factor 3.

trum is shown in Figure 6.15. About 50% of the track (shower) events are reconstructed within $0.4°$ ($3°$) of the real neutrino direction.

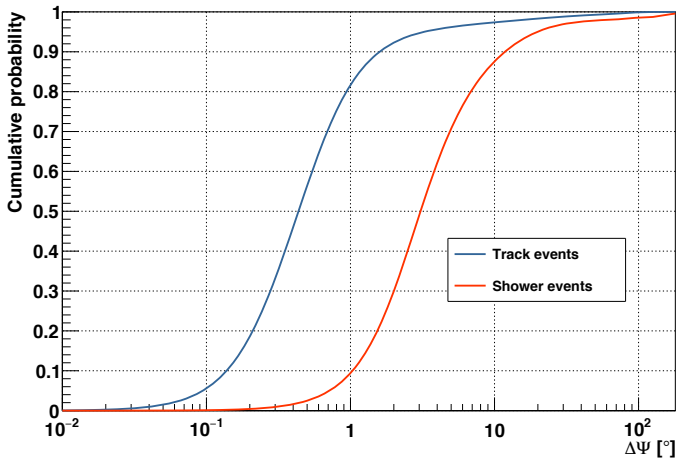

Fig. 6.15.: Probability to obtain a reconstructed angle within $\Delta\Psi$ between the reconstructed direction and the original neutrino direction for track-like (blue) and shower-like (red) events, assuming a neutrino flux with an E^{-2} energy spectrum.

The background rate for the track and shower samples, shown in Figure 6.16, is obtained directly from the measured data, since a low cosmic contribution is expected.

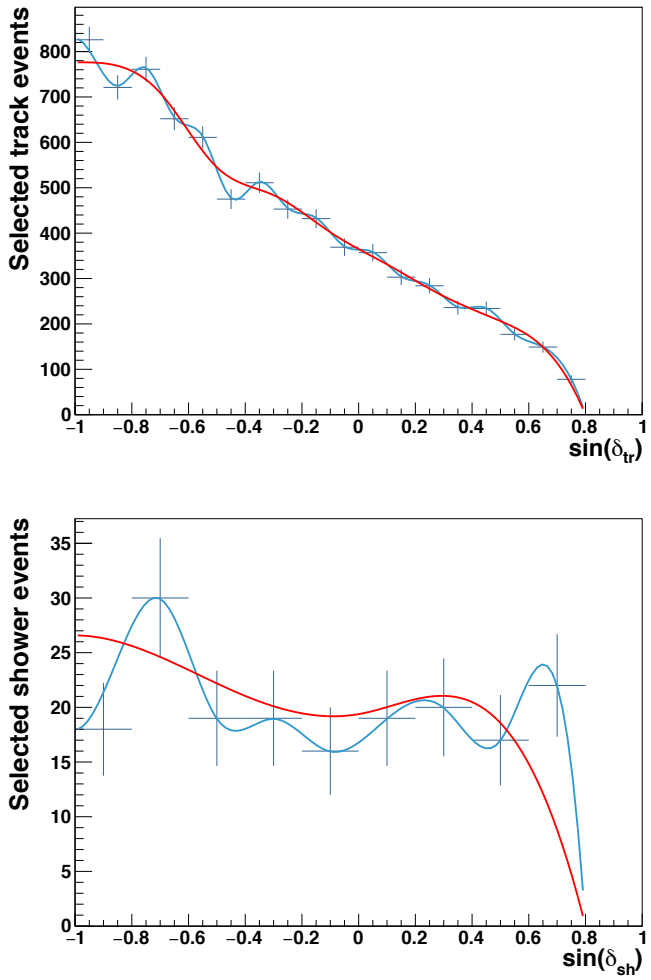

Fig. 6.16.: Number of selected track-like (top) and shower-like (bottom) events as a function of the reconstructed declination. The red and blue lines are different spline parametrisations (see Section 6.2.15). The different shape for showers is mainly due to a higher relative contamination of atmospheric muons in the sample.

6.2.8 Energy estimator

The energy spectrum of atmospheric neutrinos ($\propto E^{-3.7}$) is significantly softer compared to the expected astrophysical fluxes ($\propto E^{-2} - E^{-2.5}$). Because of this, the information provided by the energy estimator helps to distinguish between signal and background events. For the shower events, the number of hits (N_{sh}) entering into the TANTRA algorithm is used as an energy proxy. A more elaborate approach is considered for the track channel, in which both, the ρ parameter from the dEdX energy estimator (Section 3.3.1) and the angular error estimate, are considered. Since a significant declination dependence is observed for the ρ parameter, the signal and background PDFs for the track channel are taken into account in steps of 0.2 over $\sin\delta$.

6.2.9 Implementation

The significance of an accumulation of events is determined from the TS definition in Equation 5.12. In the maximisation of the likelihood, the location of the source is either kept fixed or fitted within boundaries depending on the type of search (see Section 6.2.10). The values of n_s^{tr} and n_s^{sh} are always left free in the likelihood maximisation.

6.2.10 Search for neutrino sources

Four approaches to search for astrophysical neutrinos sources have been followed.

1 *Full sky search.* The visible sky of ANTARES is inspected to find the most significant cluster of events.

2 *Candidate list search.* The directions of 106 neutrino source candidates is considered to search a significant accumulation of events. Upper limits on the neutrino fluxes are also determined.

3 *Galactic Centre region.* The algorithm is the same as the full sky search, but the scanned region is limited to a region defined by an ellipse centred in the origin of the galactic coordinate system (α, δ) = (266.40°,–28.94°) with a semi-axis of 15° in the direction of the galactic latitude and a semi-axis of 20° in galactic longitude. This search is motivated

by the appearance of high-energy neutrino events observed by IceCube [3, 4] that may cluster in this region. In addition, an accelerator of PeV protons (which could induce high-energy neutrinos) was recently discovered by the HESS Collaboration in the Galactic Centre [92].

4 *Sagittarius A**. The location of Saggitarius A* is considered by assuming a Gaussian emission profile of various widths.

Figure 6.17 shows both the track and shower event samples in equatorial coordinates. The location of the considered neutrino source candidates and the region of the Galactic Centre search are also indicated.

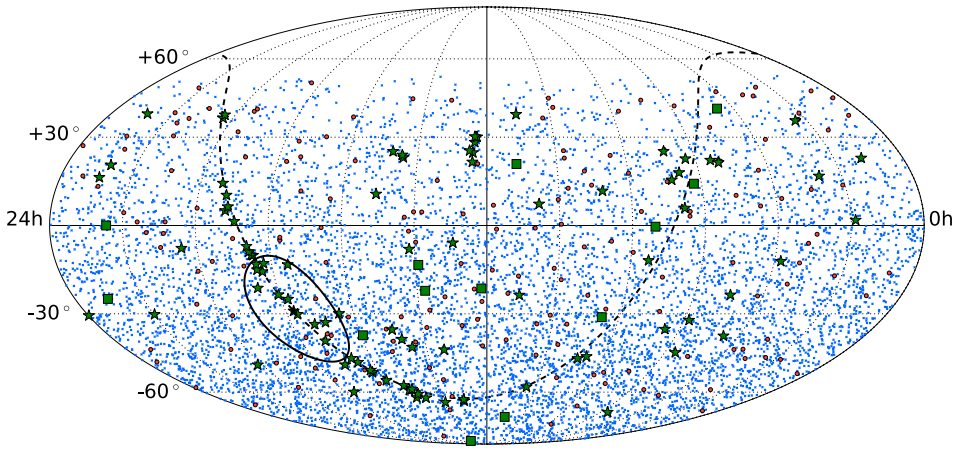

Fig. 6.17.: Representation in equatorial coordinates of the 7622 track (blue crosses) and 180 shower (red circles) events passing the selection cuts. The 106 candidate neutrino sources are indicated with green stars. Green squares are used to show the location of the 13 considered tracks from the IceCube high energy starting events or HESE. The black solid ellipse represents the search area around the Galactic Centre, in which the origin of the galactic coordinates is shown with a black star. The galactic equator is also shown with a black dashed line.

6.2.11 Full sky search

The whole visible sky of ANTARES is divided in a grid in which each tile has a size of $1^\circ \times 1^\circ$ in right ascension and declination. The TS is evaluated in each tile by letting the most likely location of the fitted cluster free between the $1^\circ \times 1^\circ$ boundaries. The pre-trial p-value of each tile is obtained by comparing the TS value with the background TS distribution obtained from pseudodata sets at the corresponding declination.

The location of the most significant cluster and the obtained pre-trial p-values for all the visible sky is shown in Figure 6.18. The most significant cluster is found at equatorial coordinates $(\delta, \alpha) = (23.5^\circ, 343.8^\circ)$ with a pre-trial p-value of 3.84×10^{-6}. This pre-trial p-value is compared to the distribution of the smallest p-values found over all locations when performing the same algorithm on pseudo-experiments. The obtained post-trial p-value is of 5.9% (significance of 1.9σ in the two-sided convention, 1.5σ in the one-sided convention). The 90% CL upper limit on the neutrino flux at this sky location is $E^2 d\Phi/dE = 3.8 \times 10^{-8}\,\mathrm{GeV\,cm^{-2}\,s^{-1}}$. The accumulation of events around the most significant location is shown in Figure 6.19-top-left. A total of 16(3) track events within $5^\circ(1^\circ)$ and 1 shower event within 5° are detected. 90% CL upper limits of the most significant cluster in bands of 1° in declination are shown in Figure 6.20.

The location of this cluster is coincident within 1.1° from event ID 3 of the 6–year Northern Hemisphere Cosmic Neutrino (NHCN) flux sample from IceCube [238]. A simplified simulation is carried out to obtain the significance of this coincidence. In the NHCN sample, 26 out of the 29 events are located in declinations between –5° and 30°. The remaining events are located in declinations with a smaller event density. By considering a random distribution of 26 events within these declinations, the probability of a random coincidence within 1° between the most significant cluster of this search and at least one event is of $\sim$1%.

6.2.12 Candidate list

The candidate list used in the last ANTARES point-source analysis [130] is updated in this search. This list included neutrino source candidates of Galactic and extragalactic origin listed in the TeVCat catalogue [239]. These

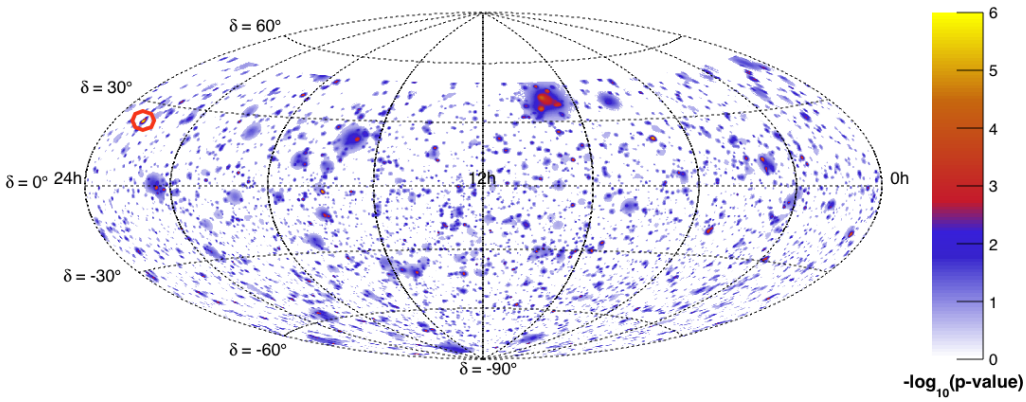

Fig. 6.18.: Sky map in equatorial coordinates of pre-trial p-values for a point-like source of the ANTARES visible sky. The red circle indicates the location of the most significant cluster of the full sky search. For this map, a smaller grid size of $0.2^\circ \times 0.2^\circ$ was used.

source candidates were confirmed gamma-ray sources observed by γ-ray telescopes in the 0.1–100 TeV energy range with declinations lower than 20° in dates prior to July 2011. Since the energy of photons from extragalactic TeV emitters can be degraded until they reach the Earth, also extra-Galactic candidates which were detected by gamma-ray satellites between energies of 1–100 GeV were included. 56 more sources are added, including the newly observed sources between the 0.1–100 TeV energy range after July 2011, and also some bright sources with declinations between 20° and 40° which had not been considered previously. Furthermore, the muon track with the highest energy recorded from IceCube [238] and the 2HWC sources which are not coincident with any known source from other catalogues [240] have also been included. Finally, seven more sources are considered: the three blazars with highest intensity observed by the TANAMI Collaboration that coincide with three events from the IceCube HESE sample [241, 242, 243], and the four gravitationally lensed Flat Spectrum Radio Quasars with the highest magnification factor analysed in a previous work [244].

Table 6.5 includes the 106 considered neutrino source candidates along with their equatorial coordinates, fitted number of signal events and upper limits on the flux.

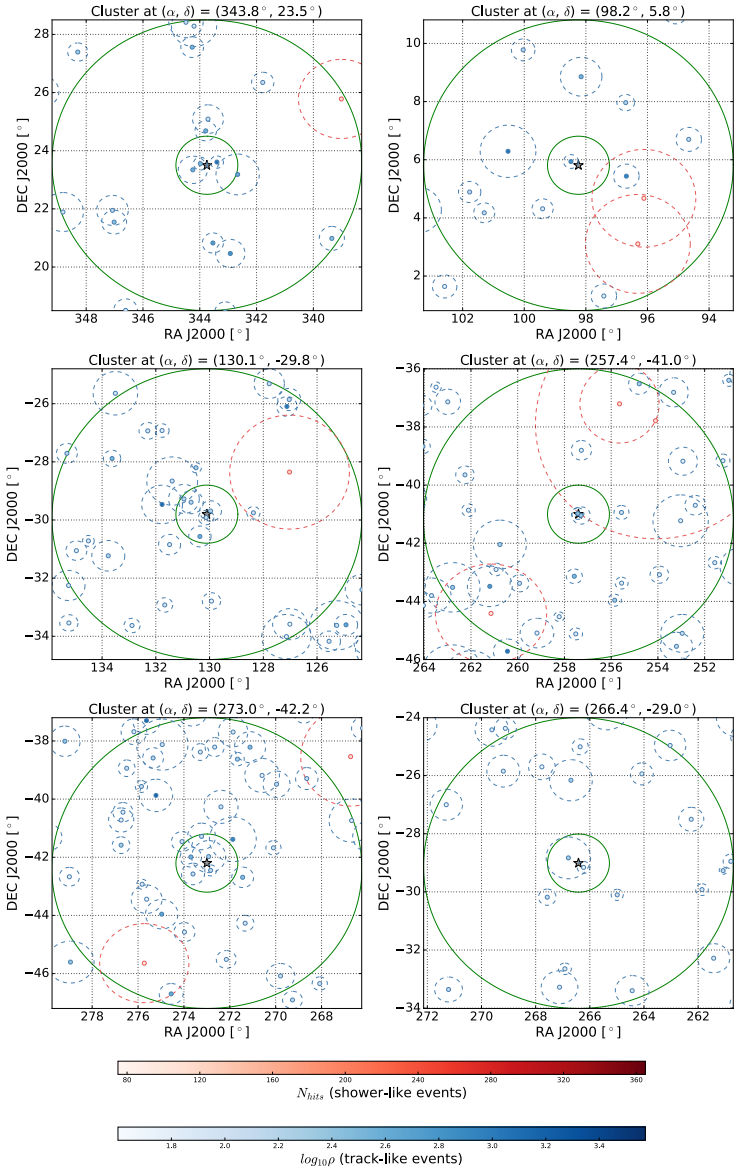

Fig. 6.19.: Distribution of event in the (α, δ) (RA, DEC) coordinates for the most significant clusters found in the full sky search (top left), the candidate list search (HESSJ0632+057) (top right), the search over the track events from the IceCube HESE sample (track with ID = 3) (middle left), the search around the Galactic Centre for an E^{-2} point-like source (middle right), the search around the Galactic Centre for an $E^{-2.5}$ point-like source (bottom left) and at the location of Sagittarius A* (bottom right). In all figures, the inner (outer) green line depicts the one (five) degree distance from the position of the best fit or known location, indicated as a grey star. The red points denote shower-like events, whereas the blue points indicate track-like events. Different tones of red and blue correspond to the values assumed by the energy estimators: the number of hits (shower-like events) and the ρ parameter (track-like events) as shown in the legend. The dashed circles around the events indicate the angular error estimate.

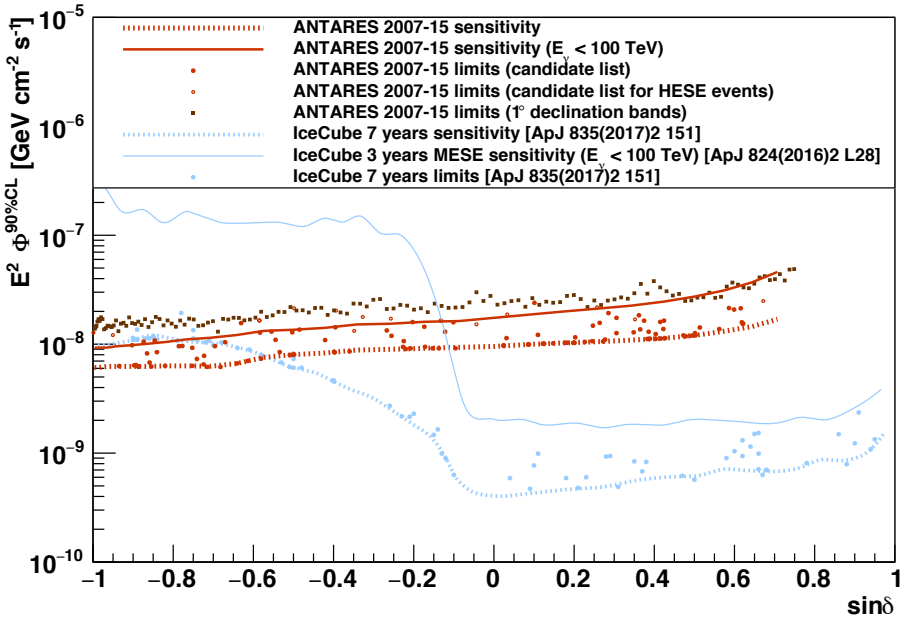

Fig. 6.20.: Upper limits at a $90\,\%$ C.L. on the signal flux from the investigated candidates assuming an E^{-2} spectrum (red circles). The dashed red line shows the ANTARES sensitivity and the blue dashed line the sensitivity of the seven years point-like source analysis by the IceCube Collaboration for comparison [113]. The upper-limits obtained in this analysis are also included (blue dots). The curve for the sensitivity for neutrino energies under 100 TeV is also included (solid red line). The IceCube curve for energies under 100 TeV (solid blue line) is obtained from the 3 years MESE analysis [236]. The limits of the most significant cluster obtained in bands of 1° in declination (dark red squares) are also shown.

The most significant accumulation corresponds to HESSJ0632+057, located at $(\alpha, \delta) = (98.24^\circ, 5.81^\circ)$. The pre-trial p-value is 0.16%. The distribution of events around this source is shown in Figure 6.19-top-right. A total of 11(1) track events within $5^\circ(1^\circ)$ and 2 shower events within 5° around the source candidate are observed. The second and third most significant sources are found at the locations of PKS1440-389 and PKS0235+164, with pre-trial p-values of 0.5% and 5%, respectively. The same search is carried out in pseudo-experiments of only background events to account for trial factors. A total of 13% of the simulated pseudo-data sets have a more significant

accumulation to the one found in the data, which corresponds to a post-trial significance of 1.5σ in the two-sided convention, 1.1σ in the one-sided.

The sensitivity, the 90% CL upper-limit fluxes and the 5σ discovery flux for this search by assuming an E^{-2} energy spectrum are represented in Figure 6.20.

A separate candidate list search with the location of the 13 event tracks observed in the IceCube HESE sample [245, 4] is also done. In this case, the angular error is larger than the angular resolution of the ANTARES detector, and therefore the direction parameters in the likelihood are not fixed but fitted within a cone of twice their angular error estimate around the direction given by the IceCube tracks. The number of fitted signal events and the upper limits on the flux for the location of the 13 HESE tracks are shown in Table 6.6.

The muon track candidate from the HESE sample with the highest significance in our search corresponds to IceCube track ID 3. The fitted cluster is found at $(\alpha, \delta) = (130.1°, -29.8°)$ and at a distance of 1.5° from the original HESE track at $(\alpha, \delta) = (127.9°, -31.2°)$. The post-trial p-value is 20% (1.2σ significance in the two-sided convention, 0.8σ in the one-sided). The upper-limit associated with this location is $\Phi_0^{90\,\%} = 2.1 \times 10^{-8}\,\mathrm{GeV\,cm^{-2}\,s^{-1}}$. The accumulation of events from this cluster is shown in Figure 6.19-middle-left.

6.2.13 Galactic Centre region

In this analysis, the search region has been defined as an ellipse centred around the origin of the galactic coordinate system, (α, δ) = (266.40°, -28.94°), with semiaxis of $15°$ and $20°$ in galactic latitude and longitude, respectively. A specific search around the Galactic Centre is more sensitive than a full sky search, since it is less likely that background events accumulate randomly in a cluster.

The most significant cluster assuming an E^{-2} spectrum and a point-like source is found at $(\alpha, \delta) = (257.4°, -41.0°)$. The fitted number of signal events is 2.3 and the obtained pre-trial p-value is of 0.09%. The obtained post-trial p-value is 60%. Apart from the E^{-2} assumption, other spectral indices (γ = 2.1, 2.3, 2.5) are tested. For the E^{-2} case, several source

Tab. 6.5.: List of astrophysical objects used in the candidate list search. The first column reports the type of source: *Binary* means X-Ray binary, *GC* means Galactic Centre, *Radio* means Radio Galaxy, *Sey2* means Seyfert 2 Galaxy, *UNID* means unidentified. The last two columns show the sum of the fitted number of signal track and shower events $\mu_{\rm sig} = \mu_{\rm sig}^{tr} + \mu_{\rm sig}^{sh}$, and the $90\,\%$ C.L. upper limits on the flux normalization factor $\Phi_0^{90\,\%}$ (in units of 10^{-8} GeV cm^{-2} s^{-1}). Candidates of the same type are sorted by declination.

Type	Name	$\delta[^\circ]$	$\alpha[^\circ]$	$\mu_{\rm sig}$	$\Phi_0^{90\,\%}$	Type	Name	$\delta[^\circ]$	$\alpha[^\circ]$	$\mu_{\rm sig}$	$\Phi_0^{90\,\%}$
BLLac	PKS2005-489	-48.82	302.37	0.3	0.93		PKS1406-076	-7.90	212.20	–	0.92
	PKS0537-441	-44.08	84.71	0.6	0.96		QSO2022-077	-7.60	306.40	1.0	1.64
	PKS1440-389	-39.14	220.99	2.9	1.56		3C279	-5.79	194.05	0.8	1.59
	PKS0426-380	-37.93	67.17	–	0.70		B1030+074	7.19	158.39	–	1.01
	PKS1454-354	-35.67	224.36	1.2	1.28		PKS1502+106	10.52	226.10	–	1.03
	TXS1714-336	-33.70	259.40	0.8	1.31		3C454.3	16.15	343.50	–	1.10
	PKS0548-322	-32.27	87.67	–	0.85		4C+21.35	21.38	186.23	–	1.37
	H2356-309	-30.63	359.78	–	0.79		B1422+231	22.93	216.16	–	1.12
	PKS2155-304	-30.22	329.72	–	0.80		PKS1441+25	25.03	220.99	–	1.38
	1ES1101-232	-23.49	165.91	–	0.85	Radio	PKS0625-35	-35.49	96.78	–	0.74
	1ES0347-121	-11.99	57.35	–	0.92	SNR	LHA120-N-157B	-69.16	84.43	–	0.63
	RGBJ0152+017	1.79	28.17	–	1.14		RCW86	-62.48	220.68	–	0.62
	RBS0723	11.56	131.80	–	1.03		MSH15-52	-59.16	228.53	–	0.68
	PKS0235+164	16.61	39.66	2.1	1.93		SNRG327.1-01.1	-55.08	238.65	–	0.63
	RGBJ2243+203	20.35	340.98	–	1.29		RXJ0852.0-4622	-46.37	133.00	–	0.65
	VERJ0521+211	21.21	80.44	1.2	1.84		RXJ1713.7-3946	-39.75	258.25	–	0.67
	S20109+22	22.74	18.02	–	1.30		W28	-23.34	270.43	0.8	1.43
	PKS1424+240	23.79	216.75	–	1.12		SNRG015.4+00.1	-15.47	274.52	0.2	1.34
	MS1221.8+2452	24.61	186.10	–	1.13		W44	1.38	284.04	–	0.97
	1ES0647+250	25.05	102.69	–	1.65		HESSJ1912+101	10.15	288.21	–	1.03
	S31227+25	25.30	187.56	–	1.14		W51C	14.19	290.75	–	1.07
	WComae	28.23	185.38	–	1.20		IC443	22.50	94.21	–	1.12
	1ES1215+303	30.10	184.45	–	1.26	Sey2	ESO139-G12	-59.94	264.41	–	0.82
	1ES1218+304	30.19	185.36	–	1.21		CentaurusA	-43.02	201.36	–	0.62
	Markarian421	38.19	166.08	–	1.59	UNID	HESSJ1507-622	-62.34	226.72	–	0.62
Binary	CirX-1	-57.17	230.17	–	0.84		HESSJ1503-582	-58.74	226.46	–	0.62
	GX339-4	-48.79	255.70	–	0.63		HESSJ1023-575	-57.76	155.83	1.5	1.08
	LS5039	-14.83	276.56	–	1.19		HESSJ1614-518	-51.82	243.58	0.7	0.96
	SS433	4.98	287.96	–	0.99		HESSJ1641-463	-46.30	250.26	–	0.78
	HESSJ0632+057	5.81	98.24	2.7	2.40		HESSJ1741-302	-30.20	265.25	0.6	1.29
FSRQ	S30218+35	35.94	35.27	0.7	2.15		HESSJ1826-130	-13.01	276.51	–	1.07
	B32247+381	38.43	342.53	–	1.54		HESSJ1813-126	-12.68	273.34	–	0.90
GC	GalacticCentre	-29.01	266.42	1.1	1.36		HESSJ1828-099	-9.99	277.24	0.7	1.45
PWN	HESSJ1356-645	-64.50	209.00	0.4	0.98		HESSJ1834-087	-8.76	278.69	–	0.92
	HESSJ1303-631	-63.20	195.75	–	0.64		2HWCJ1309-054	-5.49	197.31	–	0.92
	HESSJ1458-608	-60.88	224.54	1.2	1.05		2HWCJ1852+013*	1.38	283.01	–	0.97
	HESSJ1616-508	-50.97	243.97	0.5	0.96		2HWCJ1902+048*	4.86	285.51	–	0.99
	HESSJ1632-478	-47.82	248.04	–	0.73		MGROJ1908+06	6.27	286.99	–	1.22
	VelaX	-45.60	128.75	–	0.62		2HWCJ1829+070	7.03	277.34	–	1.01
	HESSJ1831-098	-9.90	277.85	–	0.95		2HWCJ1907+084*	8.50	286.79	–	1.02
	HESSJ1837-069	-6.95	279.41	–	1.30		ICPeV	11.42	110.63	–	1.03
	MGROJ2019+37	36.83	304.64	0.4	2.08		2HWCJ1914+117	11.72	288.68	–	1.16
Pulsar	PSRB1259-63	-63.83	195.70	–	0.64		2HWCJ1921+131	13.13	290.30	–	1.05
	Terzan5	-24.90	266.95	–	1.09		2HWCJ0700+143	14.32	105.12	–	1.48
	Geminga	17.77	98.47	0.9	1.75		VERJ0648+152	15.27	102.20	–	1.57
	Crab	22.01	83.63	0.1	1.64		2HWCJ0819+157	15.79	124.98	–	1.06
Quasar	PKS1424-418	-42.10	216.98	1.1	1.04		2HWCJ1928+177	17.78	292.15	–	1.26
	SwiftJ1656.3-3302	-33.04	254.07	–	1.10		2HWCJ1938+238	23.81	294.74	–	1.24
	PKS1622-297	-29.90	246.50	–	0.80		2HWCJ1949+244	24.46	297.42	–	1.60
	PKS0454-234	-23.43	74.27	–	0.84		2HWCJ1955+285	28.59	298.83	–	1.18
	PKS1830-211	-21.07	278.42	–	0.86		2HWCJ1953+294	29.48	298.26	–	1.20
	QSO1730-130	-13.10	263.30	–	0.94		2HWCJ1040+308	30.87	160.22	–	1.42
	PKS0727-11	-11.70	112.58	1.3	1.59		2HWCJ2006+341	34.18	301.55	–	1.38

Tab. 6.6.: The 13 IceCube muon track candidates from the IceCube HESE sample [245, 4] that are in the field of view of the ANTARES detector. The table gives the equatorial coordinates, the angular error estimate β_{IC} of the event and the $90\,\%$ C.L. upper limits on flux $\Phi_0^{90\,\%}$ (in units of 10^{-8} GeV cm^{-2} s^{-1}).

HESE ID	$\delta[^\circ]$	$\alpha[^\circ]$	$\beta_{\mathrm{IC}}[^\circ]$	$\Phi_0^{90\,\%}$
3	-31.2	127.9	1.4	2.1
5	-0.4	110.6	1.2	1.5
8	-21.2	182.4	1.3	1.7
13	40.3	67.9	1.2	2.4
18	-24.8	345.6	1.3	2.0
23	-13.2	208.7	1.9	1.7
28	-71.5	164.8	1.3	1.2
37	20.7	167.3	1.2	1.7
38	14.0	93.3	1.2	2.1
43	-22.0	206.6	1.3	1.3
44	0.0	336.7	1.2	1.8
45	-86.3	219.0	1.2	1.2
53	-37.7	239.0	1.2	1.6

extensions ($\sigma = 0.5^\circ$, 1.0°, 2.0°) are considered. In all the cases, a Gaussian profile has been assumed for the source extension.

The most significant excess for a spectral index of $\gamma = 2.5$ and a point-source is found at $(\alpha, \delta) = (273.0^\circ, -42.2^\circ)$, with a pre-trial p-value of 0.02% and a post-trial significance of 30%. Figure 6.19-middle-right shows the distribution of events for the two mentioned clusters. The location of the most significant cluster for the remaining spectral indices and source extensions are within 1° from the latter with similar TS values.

Figure 6.21 shows the declination-dependent upper limit for these searches. A worsening of the upper limits with increasing values of γ and with the source extension is observed. Softer energy spectra of cosmic neutrinos are less distinguishable from atmospheric neutrinos, and so is a source with a larger extension.

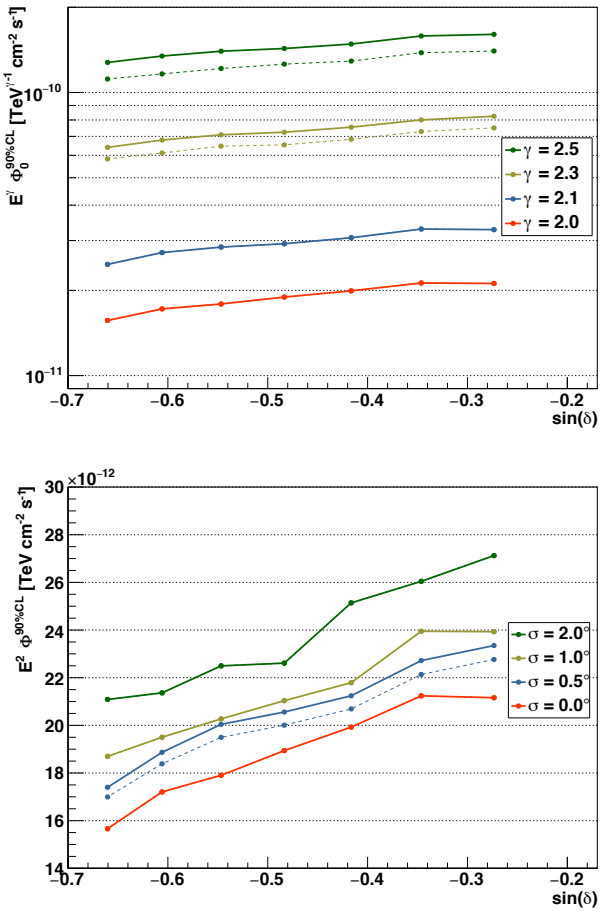

Fig. 6.21.: 90% C.L. upper limits of a search restricted to the region around the origin of the galactic coordinates at $(\alpha, \delta) = (266.40°, –28.94°)$ assuming different spectral indices for the neutrino flux (top) and different source extensions for $\gamma = 2$ (bottom).

6.2.14 Sagittarius A*

Super-massive black holes are strong candidates to be accelerators of very-high energy cosmic rays and, therefore, cosmic neutrino producers [246]. Furthermore, the presence of gas and the high concentration of candidate sources around the Galactic Centre (GC) makes possible the detection of a diffuse signal more likely than a point-like source.

Because of these reasons, a dedicated search over the location of Sagittarius A*, $(\alpha, \delta) = (266.42°, -29.01°)$, is considered as an extended source with widths between $0.5°$ and $5°$. Unlike in the previous search, this is the only sky location which is inspected. The distribution of events around Sagittarius A* is shown in Figure 6.19-bottom-right. The sensitivity and upper limits for the assumption of different source extensions can be seen in Figure 6.22. The sensitivity degrades with increasing extension but an improvement of up to a factor of 2.7 can be achieved by assuming an extended source with the simulated extension. The largest excess above the background is found at an extension of $0°$ with a pre-trial p-value of 22%.

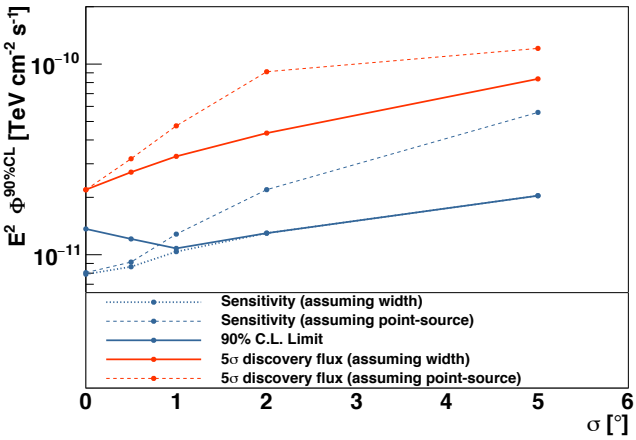

Fig. 6.22.: Discovery flux (dotted red), median sensitivity (dotted blue) and 90 % C.L. upper limits (solid blue) for a search for an extended source at Sagittarius A* at $(\alpha, \delta) = (266.42°, -29.01°)$ assuming different angular extensions σ. The dashed lines correspond to the point-like source assumption.

6.2.15 Systematic uncertainties

In this section, the effects of systematic uncertainties on the absolute pointing accuracy, angular resolution, acceptance and the background rate distribution of events are evaluated.

Absolute Pointing Accuracy Uncertainty. An uncertainty of 0.13° and 0.06° on the horizontal (ϕ) and vertical (θ) directions, respectively, was established in a previous study [247]. To take this into account, randomly generated

offsets have been added to the ϕ and θ variables of the simulated events. The offsets are generated according to two Gaussian distributions with the aforementioned uncertainties as sigmas.

Angular Resolution Uncertainty. The angular resolution of the track reconstruction algorithm can be affected by the accuracy of the detected hit times. A smearing of these times leads to a 15% degradation on the angular resolution in the track channel [248]. For neutrinos of the shower sample, the reconstruction of the direction depends most significantly on the recorded charge. A smearing in the measured charges [249] leads to a 12% degradation of the angular resolution for the shower channel.

Acceptance Uncertainty. A 15% uncertainty on the acceptance has been considered for the calculation of the reported fluxes. This uncertainty was calculated after performing simulations with a reduction of the OM efficiency by 15% [248].

Background Uncertainty. In order to account for possible systematic uncertainties on the background, the distribution of the background rates in Figure 6.16 are parametrised by two different spline functions, $R(\delta)$ and $B(\delta)$ (red and blue lines). The declination-dependent distribution of background events of the pseudo-experiments is determined as $\mathscr{B}(\delta) = B(\delta) + r \cdot (R(\delta) - B(\delta))$, with r being a random number drawn for each pseudo-experiment from a uniform distribution between -1 and 1.

It is found that not considering these uncertainties would improve the median sensitivity at $90\,\%$ C.L. and the 5σ discovery potential by less than $5\,\%$.

6.3 Estimations for the KM3NeT/ARCA detector

After the addition of the shower channel in the ANTARES point and extended source analyses, the impact of this channel in KM3NeT was studied. This section describes the estimation of the performance of the KM3NeT/ARCA detector for point-like sources and for two candidate galactic sources by using only the shower channel.

6.3.1 Sample selection

The shower channel presents a lower background compared to the track channel, since the amount of atmospheric electron neutrino events is considerably smaller compared to atmospheric muon neutrinos, and the amount of atmospheric tau neutrinos is negligible. However, atmospheric muons have been observed to produce shower events, and therefore they are also reconstructed as cascade events by the reconstruction mechanisms. Because of this, a strong suppression of this background needs to be performed. This background has been tackled in two steps. First, preliminary cuts on the values of some parameters obtained from the reconstruction algorithms explained in Chapter 3 are applied. After this, a training of a random forest classification algorithm, RFC, is performed in order to further reduce the background.

Preliminary cuts

The strategy followed for the preliminary cut selection is similar to the diffuse-flux search presented in the KM3NeT LoI [106]. Two different samples, denoted as samples A and B, are defined using different cuts on the reconstructed zenith angle and the interaction vertex given by the JGandalf track reconstruction mechanism, the cumulative ToT value obtained from the triggered hits by Q-Strategy and the Λ parameter reconstructed by recoLNS track reconstruction mechanism.

Figure 6.23-left shows the distribution of the reconstructed zenith angle, θ_{JG} given by JGandalf both for the atmospheric muon background (blue)

Tab. 6.7.: Amount of ν_e CC events for a diffuse cosmic flux of $\phi_{\nu_e} = 10^{-8}\mathrm{GeVcm}^{-2}\mathrm{s}^{-1}\mathrm{sr}^{-1}$ and atmospheric muons per year and per KM3NeT/ARCA block after each cut in sample A.

Cut applied	N_{ν_e} (E^{-2} flux)	$N_{\mu_{atm}}(E_{th} > 10\mathrm{TeV})$
$\cos(\theta) > -0.4$	34.9	1.1×10^6
Containment	25.9	9.1×10^5
CumToT $> 2\mu$s	10.9	76000

Tab. 6.8.: Amount of ν_e CC events for a diffuse cosmic flux of $\phi_{\nu_e} = 10^{-8}\mathrm{GeVcm}^{-2}\mathrm{s}^{-1}\mathrm{sr}^{-1}$ and atmospheric muons per year and per KM3NeT/ARCA block after each cut in sample B.

Cut applied	N_{ν_e} (E^{-2} flux)	$N_{\mu_{atm}}(E_{th} > 10\mathrm{TeV})$
$\cos(\theta) < -0.4$	10.7	2.7×10^7
Containment	8.1	2.1×10^7
CumToT $> 2\mu$s	4.5	7.2×10^6
$\Lambda <$ -5.8	4.4	2.2×10^6

and E^{-2} cosmic neutrinos (red). Since a much larger contribution of atmospheric muons is expected for $\cos(\theta_{JG})$ < -0.4, a division of the samples A and B is defined after this value, so that sample A considers those events with $\cos(\theta_{JG}) > -0.4$, and sample B those with $\cos(\theta_{JG}) < -0.4$. The cut on the reconstructed vertex is the same for both samples, consisting on a volume defined by a vertical direction from the center of $Z_{JG} < 324$ m and a radial direction of $R_{JG} = \sqrt{X_{JG}^2 + Y_{JG}^2} < 500$ m. Figure 6.23-bottom shows the distribution of the cumulative ToT values for contained events for atmospheric muon events and events coming from the CC interaction of cosmic ν_e. Only those events which have a cumulative ToT value larger than 2 μs are considered. In the case of sample B, an additional cut on $\Lambda_{recoLNS} < -5.8$ has been applied to further reduce the background of atmospheric muons (see Figure 6.24). Tables 6.7 and 6.8 show the amount of cosmic ν_e CC and atmospheric muon events which are expected per year of operation and per KM3NeT/ARCA block after each cut is applied.

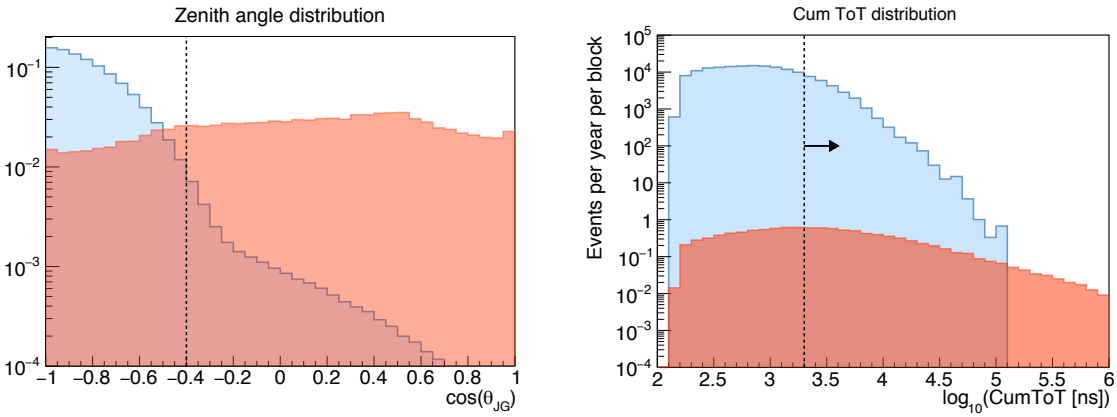

Fig. 6.23.: Left: reconstructed nadir angle distribution for atmospheric muons (blue) and cosmic CC electron neutrinos (red). These distributions are normalised to unity. Right: distribution of the cumulative ToT value for atmospheric muons (blue) and cosmic electron neutrinos (red). A cosmic energy spectrum of $\phi_{\nu_e} = 10^{-8}\mathrm{GeVcm}^{-2}\mathrm{s}^{-1}\mathrm{sr}^{-1}$ is assumed.

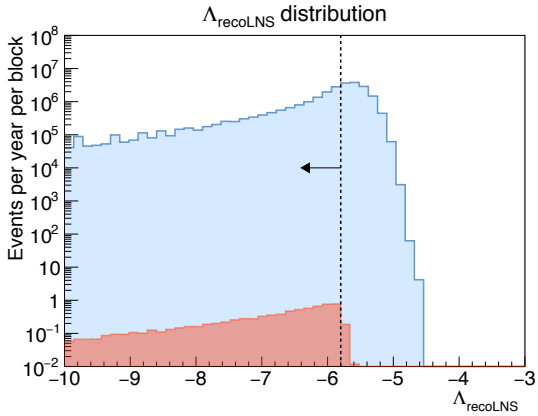

Fig. 6.24.: Λ value obtained by the recoLNS reconstruction mechanism for atmospheric muons (blue) and cosmic CC electron neutrinos (red). A cosmic energy spectrum of $\phi_{\nu_e} = 10^{-8}\mathrm{GeVcm}^{-2}\mathrm{s}^{-1}\mathrm{sr}^{-1}$ is assumed.

Random Forest Classifier training

A Random Forest Classifier (RFC) is trained in both samples. In order to test the validity of the training, a cross-validation technique is applied (see Section 5.4.1 from Chapter 5). The parameters used for the training are the ones used in the `JGandalf`, `QStrategy` and `AAShowerFit` mechanisms

explained in Chapter 3. Additionally, some of the parameters included in the event ID classification analysis of KM3NeT [106, 250] are considered.

The RFC is trained for samples A and B with a similar procedure. Two different categories, atmospheric muon background and cascade-like neutrinos, are considered for the training. For the first category, atmospheric muon events with energies larger than 10 TeV and 50 TeV are considered. For the cascade-like neutrinos, the training is performed by using both NC and CC electron neutrinos. A cross-validation technique is used to obtain the best set of parameters, and to avoid biases in the output RFC distribution. The events considered for the training in samples A and B are divided into two subsamples with equal number of events. In order to obtain the optimal number of trees and the optimal number of features to be used in each tree, a 5-fold cross-validation is performed in one of these subsamples. The results of the optimisation process for sample A can be found in Figure 6.25. The test error keeps stable starting at 50 number of trees, whereas the optimal value for the maximum number of features is between 5-10 (consistent with the default value of $\sqrt{N_{features}}$). The final number of trees considered for the analysis is, however, much larger (200). Despite the lack of improvement in the cross validation error (although without deterioration), the larger the number of trees, the finer the RFC value distribution.

After the optimal parameters are obtained, the classifier is trained in each subsample. Each classifier is used to predict the RFC output value distribution for the subsample which is not used for the training of the corresponding classifier. Even if no muon or tau neutrinos are used in the training, the distribution of the output RFC parameter is also obtained for these type of events.

The electron neutrinos have been weighted for an E^{-2} energy source flux. An error of 0.6% was obtained in both samples, where the error is defined as the ratio between the number of wrongly classified events (i.e., events with a probability lower than 0.5 of being the real category) over the total number of events. Figure 6.26-left shows the RFC distribution for atmospheric muons (blue) and electron neutrinos (red) for both test subsamples in sample A. Figure 6.26-right shows the same figure for the test subsamples in sample B.

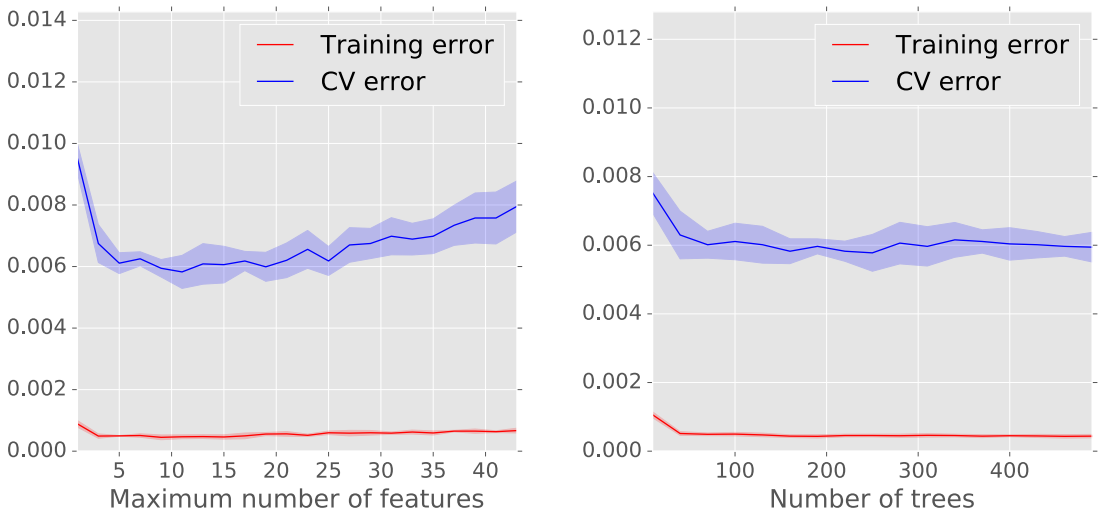

Fig. 6.25.: Misclassification error (ratio between the events with a probability lower than 0.5 of being the correct type over the total number of events in the considered sample) in the training (red) and in the error subsets (blue) after performing a 5-fold cross validation. The figure on the left shows the errors obtained as a function of the maximum number of features. On the right figure, as a function of the number of trees used in the RFC.

Reduction of the muon neutrino contribution

The training of the RFC only considers two categories (atmospheric muons and electron neutrinos). A large contamination ($\sim$ 20%) of muon neutrinos is still present in sample A even after applying stringent cuts of the RFC value. In order to minimise this contribution, a combined cut on the reconstructed energy by `AAShowerFit` and the number of L1 hits with time residuals between -1000 and -50 ns is set. The cut for sample A is shown in Figure 6.27. The RFC algorithm can be applied over more than two categories, although this is not the case for this analysis. This could be an alternative which in principle should lead to better results to distinguish between the signal of CC muon neutrino events and the signal of electron neutrino events.

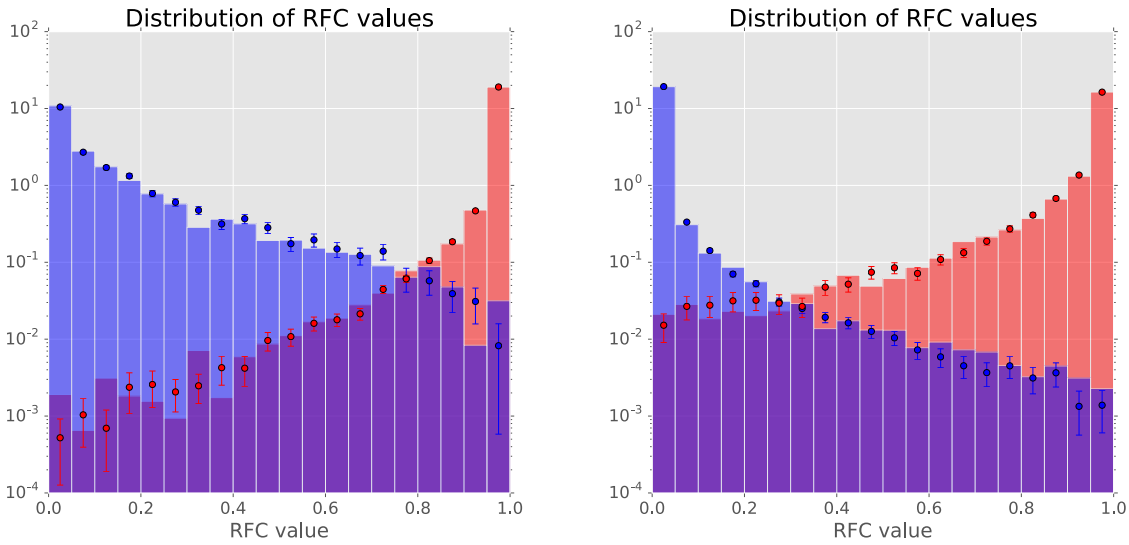

Fig. 6.26.: RFC output value distribution in sample A (top) and B (bottom). The blue color indicates the distributions for atmospheric muons, whereas the red color does it for ν_e events. The bars represent the RFC value distributions of a given subsample by training the complementary. The dots show the result when training and test subsamples are interchanged.

6.3.2 Search method

An extended maximum likelihood is considered for this analysis, which can be expressed as

$$L = \prod_{j}^{N_{samp}} \prod_{i}^{N_{evts}^{j}} \left[n_{sg}^{j} PSF^{j}(\Delta\alpha_i) P_{sg}^{j}(E_i) + N_{bg}^{j} B^{j}(\delta) P_{bg}^{j}(E_i) \right] - n_{sg} - N_{bg}. \tag{6.9}$$

In this likelihood, j indicates the index of the sample (A or B), i corresponds to the index of an event of the sample j, n_{sg} is the fitted number of signal events, N_{bg}^{j} is the number of background events for a given sample, PSF($\Delta\alpha$) is the point spread function as a function of the angular distance of a given event from an hypothetical source location, $\Delta\alpha$, $B_j(\delta)$ is the background rate as a function of the declination, and $P_{sg}(E)$ and $P_{bg}(E)$ are the probability

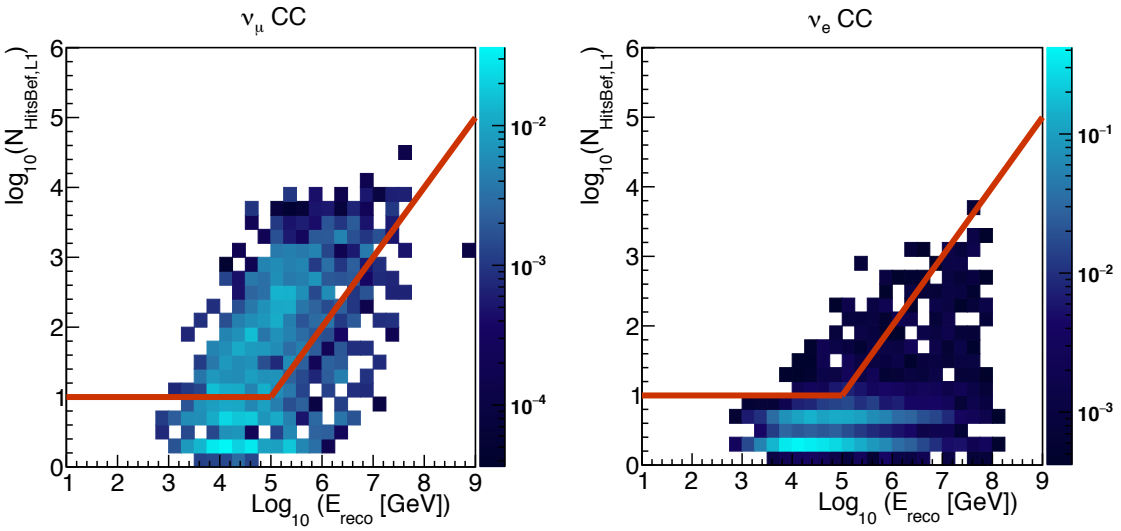

Fig. 6.27.: Distribution of the number of L1 hits with time residuals between -1000 and -50 ns versus the reconstructed energy by considering the information provided by `AAShowerFit`. The left figure shows the distribution for ν_μ CC events, whereas the right figure does it for ν_e CC events. The exclusion cut is defined by the red line, so that only the events below it are considered.

functions for an event to be reconstructed as signal or background given their reconstructed energy, respectively.

Figure 6.28 shows the point-spread function for samples A and B for those events with an output RFC value larger than 0.95. The angular median resolution for ν_e CC events as a function of the neutrino energy is also shown. A median angular resolution of $\sim$2–3° is achieved for energies above 10 TeV. The background rates of events per building block[2] and per year for the same RFC cut are shown in Figure 6.29-top. The blue and red curves show two different spline parametrisations obtained as in the ANTARES point-source analysis. In this analysis, only the red curve is used for the estimation of the background rate. A total number of 144 atmospheric muon and neutrinos per year and per KM3NeT/ARCA buliding block are expected in sample A, whereas this number is reduced to a total of 42 in sample B. The atmospheric neutrino flux has been estimated by considering the Honda

[2]Reminder: KM3NeT/ARCA will be composed of two building blocks of 115 strings each in Phase 2.

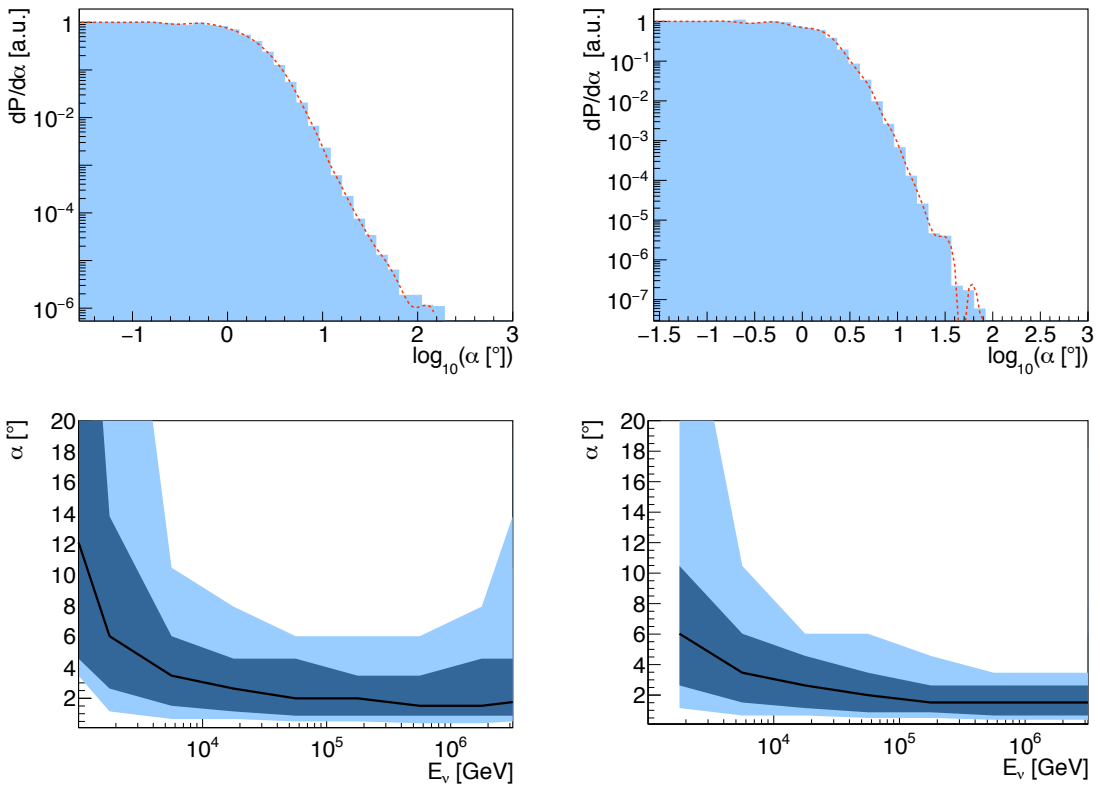

Fig. 6.28.: Point Spread Function (PSF) obtained for sample A (top-left) and sample B (top-right) for events with a RFC value larger than 0.95. Median angular resolution of ν_e CC neutrinos versus the neutrino energy for sample A (bottom-left) and sample B (bottom-right). The dark blue and light blue areas indicate the 1σ and 90% belts.

[251] and the prompt [252] flux, as reported in the KM3NeT LoI [106]. The reconstructed energy distributions for a cosmic E^{-2} point-source spectrum and for the atmospheric muon and neutrino backgrounds are shown in Figure 6.29-bottom.

The acceptance per year and per KM3NeT/ARCA block for sources with an E^{-2} energy spectrum for both samples is represented in Figure 6.30-left. The differential acceptance (number of events expected per energy bin) for a source at a declination range between $-0.6 < \sin(\delta) < -0.4$ is shown in Figure 6.30-right, where it can be seen that these events correspond mostly to neutrinos with energies above $\sim$ 10 TeV.

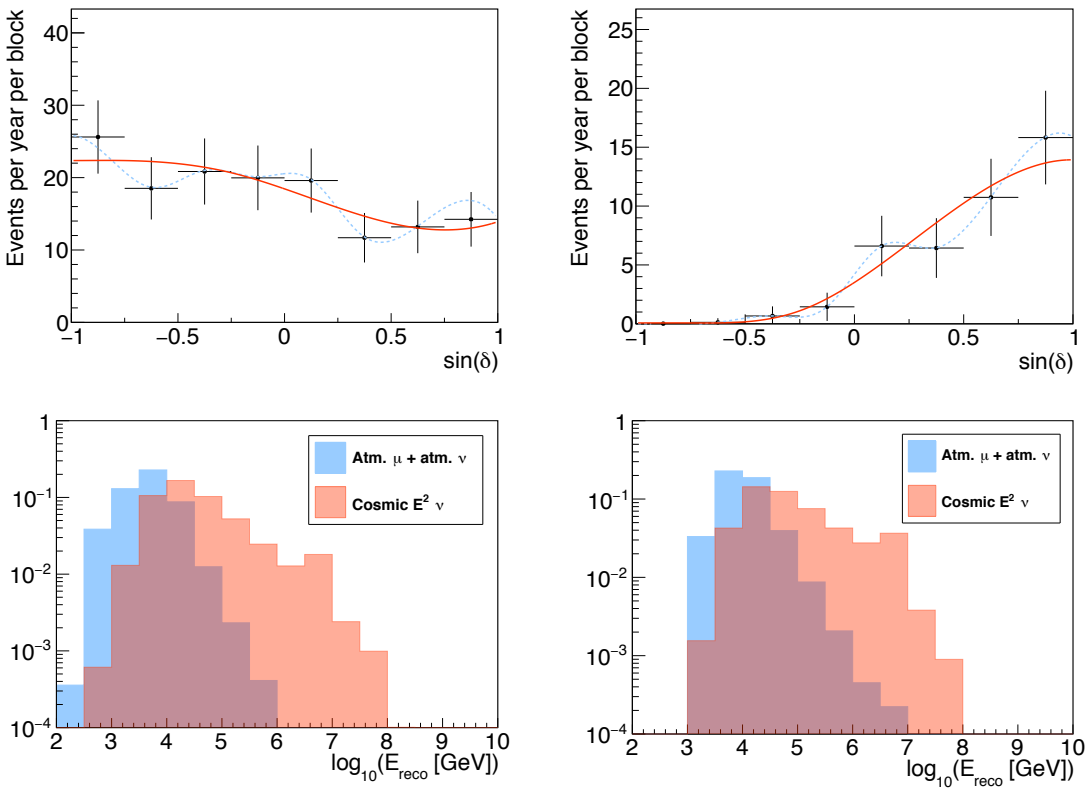

Fig. 6.29.: Background rate of events per year per KM3NeT/ARCA block as a function of the declination for sample A (top-left) and sample B (top-right). Reconstructed energy distribution for background events (blue) and signal events (red) in sample A (bottom-left) and sample B (bottom-right). Atmospheric muon and neutrinos are considered for background events, whereas an E^{-2} energy spectrum has been considered for signal events.

The definition of the TS is the same as in Equation 5.12. Only a fixed-source search is attempted to estimate the performance of KM3NeT/ARCA, and therefore the location of the fitted source is kept fixed. The values of n_{sg}^{j} are left free to vary in the likelihood.

6.3.3 Results for point-like sources

Different set of cuts on the RFC value have been applied in both samples to minimise the 5σ discovery flux. The optimal cut value is found to be 0.95 both for sample A and sample B. The result of the sensitivity, the 5σ and the

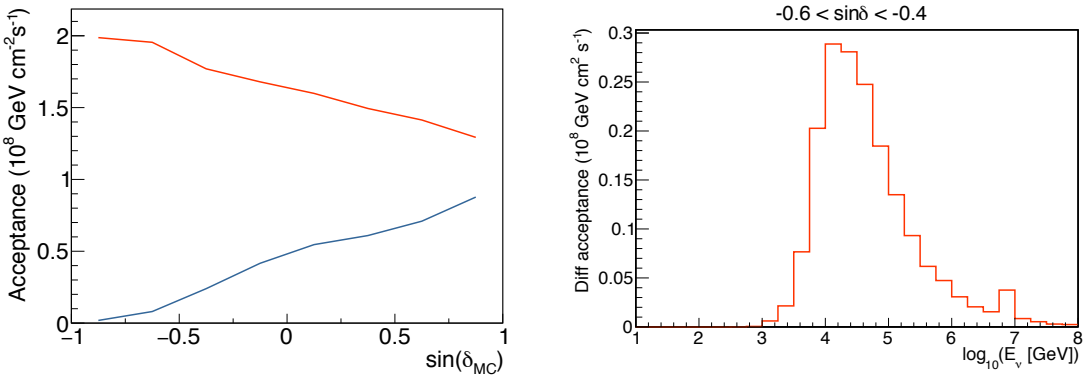

Fig. 6.30.: Left: acceptance for sample A (red) and sample B (blue) assuming an E^{-2} energy source spectrum per year of operation and per KM3NeT/ARCA building block as a function of the declination. Right: Differential acceptance per year and per block for the same spectrum for a point-source bewteen –0.6 $<$ sin(δ) $<$ –0.4.

3σ discovery fluxes for 6 years of operation of a complete KM3NeT/ARCA detector (two blocks) is shown in Figure 6.31-top. The error bands shown in the figure correspond to a case with $\pm$ 50% difference in the number of total background events. Figure 6.31-bottom shows the comparison of the sensitivity and the 5σ discovery flux with the track analysis [101]. The point-source sensitivity using the shower channel is around 15–30 % compared to the track channel. The dependence of the discovery flux as a function of time for a point-source at a declination of δ = –30° (almost at the declination of the Galactic Centre) is shown in Figure 6.32. As expected for a low-background case, the values obtained lie between a squared-root and a linear evolution over the observation time.

6.3.4 Results for Vela X and SNR RXJ 1713.7-3946

A dedicated analysis is done both for Vela X and SNR RXJ 1713.7-3946. As mentioned in Section 1.4.2, these sources correspond to two of the brightest SNRs which can be observed in the field of view of KM3NeT. The flux assumed for both sources correspond to the procedure calculated by Vessani et al [96, 98, 99] (Equations 1.18 and 1.20). Furthermore, a disc extension of 0.6° and 0.8° degrees are considered for RXJ 1713.7-3946 and Vela X, respectively.

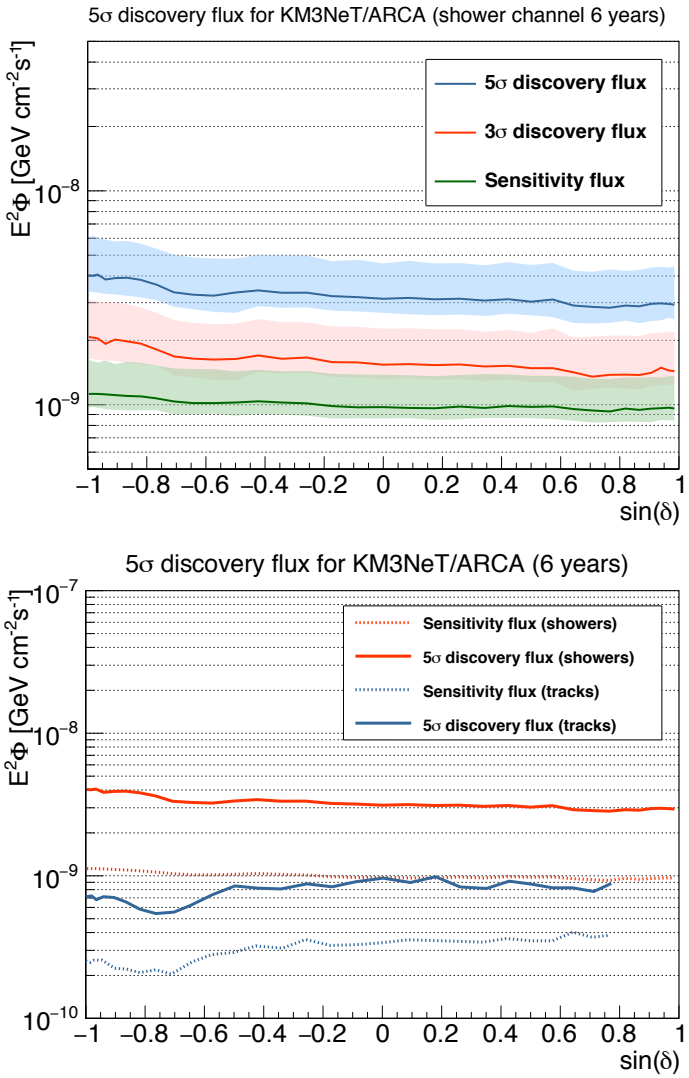

Fig. 6.31.: Top: estimated sensitivity (green), 5σ (red) and 3σ (blue) discovery fluxes after 6 years of operation of Phase 2 of KM3NeT/ARCA. The bands indicate the region with $\pm$ 50% background events. Bottom: comparison for the same period of the 5σ discovery and sensitivity fluxes between the track (blue) and shower (red) samples. The cascade sensitivity compared to the one obtained with tracks ranges between 15-30%.

The ratio of the 3σ discovery flux to the source flux ($\Phi_{3\sigma}/\Phi_{source}$ and the ratio of the sensitivity to the source flux ($\Phi_{90\%CL}/\Phi_{source}$) can be seen in Figure 6.33. The result for Vela X shows that after 2.5 years, a 3σ

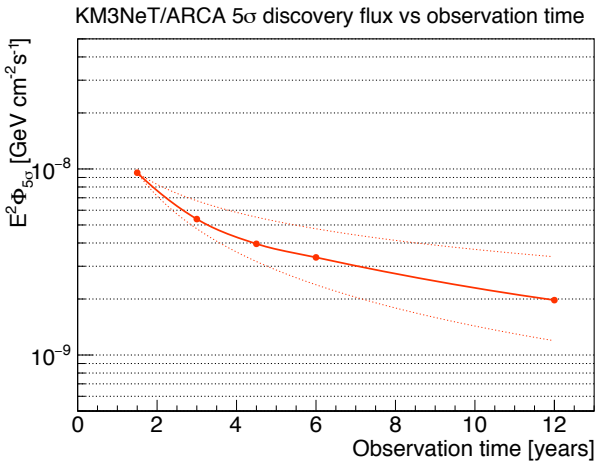

Fig. 6.32.: 5σ discovery flux for a point-source in the Galactic Centre using only shower-like events as a function of the KM3NeT/ARCA observation time. The dotted lines indicate a linear and a squared-root dependence, respectively.

pre-trial observation would be made by using only the shower channel. This case should be taken with a grain of salt, since the γ-ray energy spectrum observed by γ-ray experiments shows a spectrum compatible with a dominant leptonic scenario. In the case of RXJ 1713.7-3946, the assumed model would be discarded with 90% CL in 4.5 years if only background events are seen.

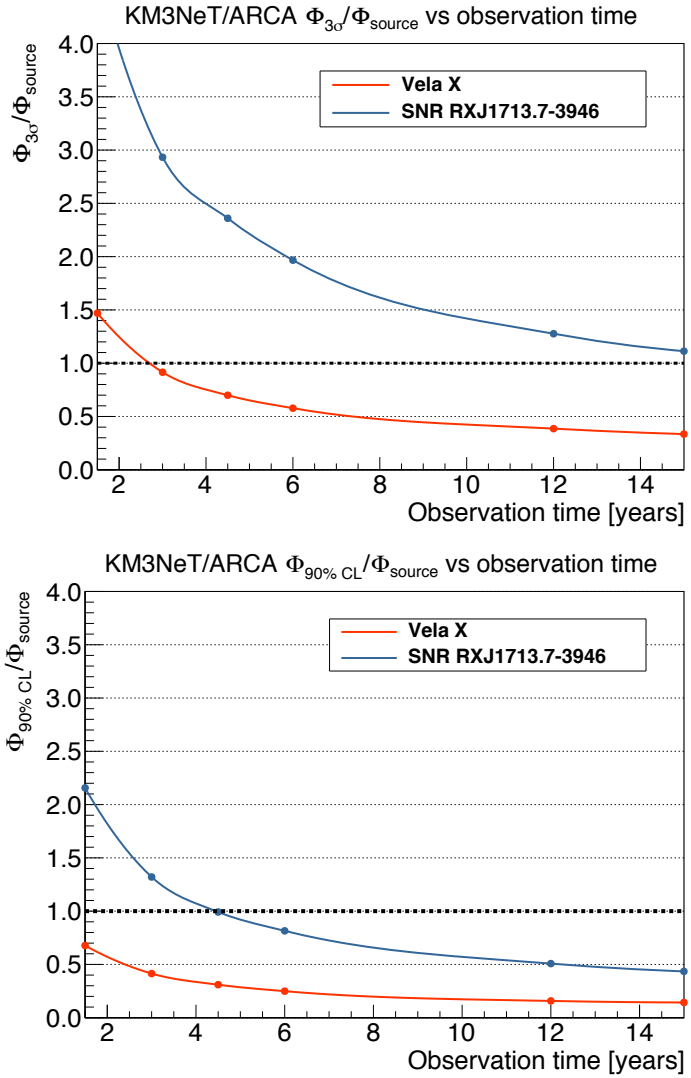

Fig. 6.33.: Top: ratio between the 3σ discovery flux and the considered source flux as a function of the observation time. Bottom: ratio between the sensitivity flux and the considered source flux as a function of the observation time.

Conclusions

> *Everything is awesome!*
>
> **— Philip Lord, Christopher Miller and Chris McKay**
> The Lego Movie (2014)

High energy neutrino astronomy is currently at an early yet intriguing stage. The first results observed by the IceCube Collaboration have shown the existence of a high energy neutrino flux of unknown origin with apparently no privileged direction. The ANTARES neutrino telescope has been able to exclude the possibility that some of their events had been produced due to a point-source at the Galactic Centre region. Furthermore, the last diffuse-flux ANTARES analysis has shown a result which is compatible with the flux observed by IceCube.

High energy neutrino astronomy has been traditionally linked with the origin of cosmic rays and $\gamma-$ray fluxes: the hadronic models imply that the sources where high energy protons are accelerated should be sources of $\gamma-$rays and neutrinos. The observation of a Pevatron at the Galactic Centre by HESS, the $\gamma-$ray flux of IC 443 and W44 and the last observations of the Auger observatory seem to imply that, indeed, the hadronic scenario occurs in a fraction of the astrophysical sources.

Currently, there are three high-energy neutrino telescopes in operation: ANTARES, IceCube and Baikal. Furthermore, the KM3NeT Collaboration is building the largest neutrino telescope network ever built. The analyses explained in the previous chapters mostly deal with data taken from ANTARES and IceCube, although prospects of the future KM3NeT are also given.

Two have been the main goals of the work presented in this Thesis. The first one has been to improve the current time calibration of the ANTARES neutrino telescope so to have the highest quality data possible. The second one has been to improve our knowledge about the existence of point and extended cosmic neutrino sources. No significant observations of these type of sources have been found in the analysis presented. Furthermore, an estimation of the sensitivity of particular point and extended source searches in the future KM3NeT telescope has been carried out.

6.4 Calibration of the ANTARES neutrino telescope

In ANTARES, a 1 ns accuracy level in the time measurements is needed in order to be able to reconstruct events with a median angular resolution of $\sim$0.3° for energies above $E_\nu > 10$ TeV. A new time calibration procedure has been performed for most of the data taking period of the ANTARES telescope. This calibration can be divided into three steps: the *inter-line* calibration, where the time offsets between different lines are obtained; the *inter-storey* calibration, for the determination of the time offsets between storeys; and the *intra-storey* calibration, for the time offset determination between ARSs in the same storey. The intra-storey calibration has been performed by using events coming from ^{40}K disintegrations, whereas the other two types requires the time residuals obtained after the reconstruction of down-going atmospheric muon events. This new calibration has shown to increase the number of well-reconstructed down going events ($\sim$10–20% improvement for down-going events with $\Lambda >$ -5.2), which indicates an improvement of the reconstruction.

6.5 Results of point and extended source analyses

The results of three different searches of point and extended neutrino sources have been presented. The first one corresponds to the first combined analysis between ANTARES and IceCube, which used ANTARES data taken

between 2007 and 2012, and IceCube data from the 40-, 59- and 79-strings configurations (2008 to 2011). The second one is the point and extended source search using ANTARES data between 2007 and 2015, which corresponds to the first published analysis that includes cascade events in this type of analysis in ANTARES, allowing an all neutrino flavour search. The last one corresponds to the performance estimation of the future KM3NeT telescope for these type of searches by using only the cascade channel.

First combined analysis with the ANTARES and IceCube neutrino telescopes

This is the first search made combining the data of the ANTARES and IceCube neutrino telescopes. In this analysis, only track events coming from the Southern Sky ($\delta < 0^\circ$) were considered. A better performance of the ANTARES telescope is observed for galactic point-sources in most of the Southern Sky. A very nice complementarity between both detectors is also observed for most of this region: IceCube presents a better sensitivity for high energy neutrinos due to its larger size, but a worse sensitivity for events with energies under 100 TeV because of the declination-dependent energy cut used to suppress the background of atmospheric muons.

Two types of searches are performed in this search. The first one corresponds to a search at the location of 40 candidate neutrino sources. The second one consists on a scan over the whole Southern Sky to search for significant event clusters. The most significant cluster in the candidate source list corresponds to the location of HESS J1741-302, with a post-trial probability of 11%. A higher post-trial probability is observed in the full Southern Sky search, with a 24% observed for the most significant cluster, located at $\alpha = 332.8^\circ$, $\delta = -46.1^\circ$.

Point and extended source searches with the ANTARES neutrino telescope

This search corresponds to the first published ANTARES analysis using shower events in a point source search analysis. A better median angular

resolution in shower-like events is observed in ANTARES compared to IceCube, leading to a value of 2–3° for the former. Even if the angular resolution for showers is worse compared to track-like events, a ∼20% improvement of the sensitivity is achieved with the addition of these events.

An update of the candidate source list is performed for this analysis. As a consequence, a total of 126 locations are searched for significant accumulations in the candidate list search. The location of 13 HESE events observed by IceCube are also checked. Furthermore, a scan around the Galactic Centre, with different assumptions on the source extensions is executed. Finally, a scan over the whole ANTARES visible sky is done.

No significant accumulation of events have been observed in these searches. The most significant location in the candidate-list search is HESSJ0632+057, with a 13% post-trial probability. A 60% post-trial probability is observed for the search around the 13 events observed by IceCube, being the most source-like location at $\alpha = 257.4°$, $\delta = -41.0°$. For the full ANTARES visible sky, a 5.9% post-trial probability is observed in the most significant location, at $\alpha = 343.8°$, $\delta = 23.5°$.

Point and extended source search estimations for KM3NeT/ARCA

The last of the performed analysis corresponds to the estimation of the KM3NeT/ARCA sensitivity for point and extended source searches using only shower-like events. A strong suppression of the atmospheric muon events is achieved after the training of a Random Forest Classifier.

This analysis shows the competitive status of the shower-like event channel compared to the track-like events one: Depending on the source declination, the point-source sensitivity for shower-like events is estimated to be between 15 and 30% of the KM3NeT/ARCA sensitivity using only tracks. Two specific cases are studied: SNR RXJ 1713.7-3946 and PWN Vela X. The most favourable results corresponds to Vela X, in which less that 2 years would be needed to observe a 3σ discovery by only using cascades within a purely hadronic scenario. However, for the case of Vela X, a purely hadronic scenario seems to be discarded.

T0 calibration tables

A

The validity periods of the previous and the new T0 tables are attached below.

A.1 Previous T0 tables

Table A.1 contains the list of the validity periods of the time offset tables which were previously official.

Start date (DD/MM/YY HH:MM)	**Reason**	**Start date** (DD/MM/YY HH:MM)	**Reason**
27/01/07 – 00:00	5 lines	09/10/13 – 22:01	T0 update
04/12/07 – 00:00	10 lines	19/11/13 – 22:01	HV tuning
17/05/08 – 00:00	12 lines	01/01/14 – 08:00	T0 update
13/08/09 – 14:00	HV tuning	15/02/14 – 08:01	T0 update
13/11/09 – 00:00	L10, L12 reconnection	15/03/14 – 05:00	T0 update
13/07/10 – 00:00	HV tuning	12/06/14 – 06:00	HV tuning
04/11/10 – 16:34	L6, L9 reconnection	24/07/14 – 18:00	T0 update
01/01/11 – 00:00	Older T0 table	11/10/14 – 08:00	T0 update
09/06/11 – 18:00	HV tuning	17/11/14 – 17:00	T0 update
12/12/11 – 15:00	HV tuning	18/12/14 – 07:00	HV tuning
14/01/12 – 00:00	Older T0 table	15/04/15 – 12:01	T0 update
24/02/12 – 13:42	T0 update	15/06/15 – 13:01	T0 update
02/08/12 – 00:00	T0 update	31/08/15 – 00:00	T0 update
28/11/12 – 00:00	HV tuning	15/10/15 – 04:01	T0 update
02/12/12 – 00:00	HV tuning	15/11/15 – 11:00	T0 update
17/12/12 – 13:26	HV tuning	29/02/16 – 20:01	HV tuning
03/03/13 – 10:01	T0 update	30/04/16 – 11:01	T0 update
27/04/13 – 00:00	T0 update	30/06/16 – 13:01	T0 update
26/05/13 – 09:00	T0 update	31/08/16 – 13:01	T0 update
02/07/13 – 12:01	T0 update	31/10/16 – 07:01	T0 update
10/08/13 – 19:01	T0 update	09/01/17 – 12:00	T0 update

Tab. A.1.: Validity periods of the previous time offsets calibration tables.

A.2 Current T0 tables

Tables A.2, A.3 and A.4 contain the list of the validity periods of the time offset tables which are currently official.

Start date (DD/MM/YY HH:MM)	**Label**	**Start date** (DD/MM/YY HH:MM)	**Label**	**Start date** (DD/MM/YY HH:MM)	**Label**
29/01/07 00:00	1	01/01/08 00:00	1	01/01/09 00:00	1
01/03/07 00:00	2	01/02/08 00:00	2	29/01/09 00:00	2
20/03/07 00:00	3	03/03/08 00:00	3	01/03/09 00:00	3
01/05/07 00:00	4	01/04/08 00:00	4	01/04/09 00:00	4
01/06/07 00:00	5	17/05/08 00:00	5	01/05/09 00:00	5
01/07/07 00:00	6	30/05/08 00:00	6	17/05/09 00:00	6
27/07/07 00:00	7	06/09/08 00:00	7	01/07/09 00:00	7
01/09/07 00:00	8	10/10/08 00:00	8	01/08/09 00:00	8
01/10/07 00:00	9	01/11/08 00:00	9	13/08/09 14:00	9
01/11/07 00:00	10	3/12/08 00:00	10	26/08/09 00:00	10
04/10/07 14:43	11	-	-	21/09/09 12:01	11
-	-	-	-	13/11/09 00:00	12

Tab. A.2.: Validity periods of the current time offsets calibration tables for 2007, 2008 and 2009.

Start date (DD/MM/YY HH:MM)	**Label**	**Start date** (DD/MM/YY HH:MM)	**Label**	**Start date** (DD/MM/YY HH:MM)	**Label**
02/01/10 15:01	1	01/01/11 00:00	1	14/01/12 00:00	1
01/02/10 00:00	2	31/01/11 02:31	2	01/02/12 00:00	2
01/03/10 00:00	3	01/03/11 01:01	3	24/02/12 00:00	3
20/03/10 00:00	4	01/04/11 14:01	4	01/04/12 00:00	4
02/05/10 17:30	5	04/05/11 07:01	5	22/04/12 00:00	5
01/06/10 01:00	6	09/06/11 18:00	6	12/06/12 00:00	6
13/07/10 14:16	7	01/07/11 03:01	7	10/07/12 00:00	7
07/08/10 12:01	8	01/08/11 00:00	8	02/08/12 00:00	8
01/09/10 00:01	9	19/08/11 01:00	9	01/09/12 00:00	9
30/09/10 16:01	10	22/09/11 01:01	10	01/10/12 00:00	10
04/11/10 16:35	11	19/10/11 01:30	11	30/10/12 00:00	11
-	-	20/11/11 02:00	12	02/12/12 11:30	12
-	-	12/12/12 15:00	13	17/12/12 13:26	13

Tab. A.3.: Validity periods of the current time offsets calibration tables for 2010-2012.

Start date (DD/MM/YY HH:MM)	**Label**	**Start date** (DD/MM/YY HH:MM)	**Label**	**Start date** (DD/MM/YY HH:MM)	**Label**
01/01/13 00:00	1	01/01/14 00:00	1	15/01/15 11:31	1
24/01/13 00:30	2	02/15/1408:01	2	15/02/15 03:01	2
03/03/13 10:01	3	15/03/14 05:00	3	15/03/15 05:00	3
01/04/13 00:00	4	15/04/14 00:00	4	15/04/15 12:01	4
01/05/13 00:00	5	15/05/14 00:00	5	15/05/15 12:01	5
26/05/13 09:00	6	12/06/14 00:00	6	15/06/15 13:01	6
02/07/13 12:01	7	24/07/14 18:00	7	15/07/15 12:01	7
10/08/13 19:01	8	08/08/14 00:00	8	15/08/15 12:01	8
10/09/13 16:01	9	09/09/14 00:00	9	15/09/15 05:01	9
09/10/13 22:01	10	11/10/14 00:00	10	15/10/15 04:00	10
19/11/13 11:01	11	17/11/14 00:00	11	15/11/15 11:00	11
19/12/13 10:01	12	18/12/14 00:00	12	15/12/15 08:00	12

Tab. A.4.: Validity periods of the current time offsets calibration tables for 2013, 2014 and 2015.

Start date (DD/MM/YY HH:MM)	**Label**
15/01/16 10:00	1
09/02/16 00:00	2
29/02/16 00:00	3
31/03/16 00:00	4
30/04/16 12:00	5
31/05/16 00:00	6
30/06/16 12:00	7
31/07/16 00:00	8
31/08/16 12:00	9
30/09/16 00:00	10
31/10/16 12:00	11
30/11/16 00:00	12

Tab. A.5.: Validity periods of the current time offsets calibration tables for 2016.

Resum

L'astronomia de neutrins és una disciplina naixent dins de l'astrofísica, la qual ha permès obrir una nova finestra per a observar l'Univers. Les primeres evidències per part de la col·laboració IceCube a 2013 [2] demostraren l'existència d'un fluix de neutrins còsmics d'altes energies. Aquest fluix ha continuat observant-se a anàlisis posteriors de la mateixa col·laboració [3, 4, 5]. Tanmateix, l'origen és encara desconegut. Degut a això, la cerca de fonts puntuals i extenses de neutrins còsmics és encara un tema d'apassionada actualitat a l'astronomia de neutrins. Aquest és precisament el tema principal del treball realitzat, a on s'ha procedit amb cerques de fonts puntuals i extenses de neutrins còsmics mitjançant les dades dels telescopis de neutrins ANTARES i IceCube. També s'hi ha efectuat una estimació de la sensibilitat del futur telescopi de neutrins KM3NeT per al mateix tipus de cerques fent servir únicament cascades. A més a més, s'hi ha realitzat una revisió completa del calibratge temporal del telescopi ANTARES.

L'astronomia de neutrins com a una nova finestra per a observar l'Univers

De la mateixa manera que al segle XX sorgiren noves maneres per a observar l'Univers amb fotons de l'espectre no visible (raigs γ, raigs X, microones, radi...), el final del segle XX i el principi del segle XXI ha marcat el començament de l'anomenada astronomia de neutrins.

L'astronomia de neutrins d'altes energies s'ha enllaçat tradicionalment amb la física darrere dels raigs còsmics. Coneixem l'existència dels raigs còsmics des de fa més d'un segle, quan científics com Victor Hess [6] o Kolhörster [7] feren les primeres observacions en les que detectaven una major descàrrega

d'un electroscopi a majors altituds. D'aquesta manera, es va determinar l'existència d'una radiació còsmica, la qual hui sabem que es compon majoritàriament per protons ($\sim$80%), nuclis d'heli ($\sim$15%), altres nuclis i electrons ($\sim$1%) [18, 19]. També coneixem l'espectre energètic dels raigs còsmics, que es pot descriure com una llei de potències,

$$\frac{dN}{dE} \propto E^{-\alpha}, \tag{A.1}$$

a on α indica l'índex espectral. Aquest índex no és el mateix, però, per a totes les energies, el qual indica un origen diferent de les partícules segons la seua energia. En conseqüència, els raigs còsmics de menys d'uns pocs GeV estan produïts al Sol o estan intensament afectats pel seu camp magnètic [19, 20, 21]. Els raigs còsmics d'energies entre uns pocs GeV fins al *genoll* ($\sim 10^6$ GeV) es sospita que inicialment s'acceleren als fronts de xoc de romanents de supernova [19, 20, 23], i posteriorment per camps magnètics de la galàxia [22]. L'índex espectral en aquest rang d'energies té un valor de α $\sim$2.6–2.7. Aquest índex varia a valors de $\sim$3.1 a energies entre 10^6 i 10^9 GeV (des del *genoll* fins al *turmell*), i torna a un valor de $\sim$2.6 per a energies per damunt de 10^9 GeV. Diferents fonts s'han proposat com a possibles acceleradors per a raigs còsmics per damunt del genoll. Tot i això, a mesura que augmenta l'energia, més improbable és que s'acceleren per fonts de tipus galàctic. Un criteri molt habitual per a determinar l'energia màxima a la que es pot accelerar un raig còsmic ve donada pel criteri de Hillas [26], el qual considera que el radi de Larmour ha de ser menor que la regió d'acceleració R a un cos astrofísic, de manera que

$$E_{max} \sim ZeRBU, \tag{A.2}$$

a on Z és la càrrega de la partícula, e és la càrrega de l'electró, B és la intensitat del camp magnétic a la regió d'acceleració, i U la velocitat dels centres de col·lisió magnètics. Per últim, per damunt dels 10^{20} eV es prodeix una forta baixada en el fluix de ràigs còsmics, degut a la interacció dels fotons del fons de microones amb els raigs còsmics, anomenat tall GZK [31, 32].

L'astronomia de neutrins d'altes energies també es sol lligar amb l'astronomia de raigs γ per damunt dels 100 TeV. Actualment, hi existeixen dos grans tipus de models per a explicar l'espectre energètic de les fonts astrofísiques de raigs γ. Per una banda, els models hadrònics proposen que la producció de raigs γ està produïda per l'anomenada producció piònica [19, 80], a on hadrons (majoritàriament protons) xocarien amb altres hadrons o amb fotons, tenint com a producte pions entre altres partícules:

$$p + nucli \rightarrow \pi + X \tag{A.3}$$

$$p + \gamma \rightarrow \Delta^{+} \rightarrow \begin{cases} \pi^{0} + p \\ \pi^{\pm} + n \end{cases} . \tag{A.4}$$

Els pions carregats decaurien produint neutrins ($\pi^{\pm} \rightarrow \mu^{\pm} + \overset{(-)}{\nu}$, $\mu^{+} \rightarrow e^{+} + \bar{\nu}_{\mu} + \nu_{e}$, $\mu^{-} \rightarrow e^{-} + \nu_{\mu} + \bar{\nu}_{e}$), mentres que els pions neutres es desintegrarien en un parell de fotons ($\pi^{0} \rightarrow 2\gamma$). Al capdavall, aquest model lligaria l'astronomia de neutrins amb l'astronomia de raigs γ i la dels raigs còsmics.

Per altra banda, els models leptònics proposen que els raigs γ s'hi produeixen per la interacció d'electrons i positrons amb camps electromagnètics [33, 34]. Els raigs γ de baixes energies s'hi poden produir per la radiació sincrotró deguda al moviment dels electrons i positrons al voltant d'un camp magnètic, mentres que la part d'energies més altes s'hi pot explicar pel mecanisme de compton invers, a on els fotons de més baixes energies augmenten la seua energia degut a xocs amb els electrons ($e^{-} + \gamma \rightarrow e^{-} + \gamma$).

La majoria de fonts semblen més compatibles amb els models leptònics, tot i que se n'han trobat casos on el model leptònic és desfavorit. Són els casos de les romanents IC443 i W44, observades per l'experiment Fermi [85] i el Pevatró al centre galàctic observat per HESS [92]. També l'experiment AUGER té forts indicis d'observar acceleració hadrònica a fonts extragalàctiques [30]. Altres fonts, com la remanent de Tycho o Cassiopea A semblen igualment compatibles amb els dos tipus de models [86, 87, 88, 89, 90, 91].

La física que acabem de descriure és el fonament de l'astronomia de neutrins d'altes energies. Tot i això, els primers resultats no vingueren per aquesta part, sinó amb l'observació de neutrins de més baixes energies: els neutrins produïts a les reaccions nuclears al nucli del Sol [56], el fons còsmic de neutrins (observat indirectament pels seus efectes sota el fons còsmic de microones)[75] i la detecció per part de Kamiokande II, Baksan i IMB de neutrins procedents de la supernova SN1987A [67, 68, 69, 70, 71]. Dins de l'astronomia d'altes energies, les primeres observacions s'han donat per l'experiment IceCube, el qual ha observat un fluix de neutrins còsmics d'altes energies sense una aparent predilecció en direccions [2, 3, 4, 5]. L'experiment ANTARES no ha fet cap descobriment en este sentit. Malgrat això, amb les dades d'ANTARES es descartà, amb un nivell de confiança superior al 90%, la possibilitat de que una acumulació sospitosa observada després de les primeres evidències d'IceCube fora deguda a una fons puntual en el centre de la Galàxia [130]. A més a més, els últims resultat de l'anàlisi d'ANTARES de fluixos difusos comencen a ser sensibles al fluix observat per IceCube [253].

Telescopis de neutrins

Els telescopis de neutrins consisteixen en una matriu de fotomultiplicadors col·locats a grans profunditats, ja siga al fons de la Mediterrània (ANTARES [143], KM3NeT [106]), al del llac Baikal de Rússia (Baikal-GVD [140, 173]), o al de l'Antàrtida (IceCube [142, 165]).

ANTARES està situat al fons de la mar Mediterrània (2500 m de profunditat), prop de la costa de Toulon (França). Està format per un total de 885 fotomultiplicadors disposats en 12 línies de 25 plantes (o *storeys*) cadascuna, formant un volum aproximat de 0.01 km^3. Cada fotomultiplicador i la seua electrònica associada està ficat dins d'una esfera de borosilicat, formant els anomenats mòduls òptics o OMs (Optical Modules, en anglés). Estes esferes de borosilicat són capaces de suportar les altes pressions del fons marí.

IceCube, situat a 2500 m de profunditat al gel antàrtic, és actualment el telescopi de neutrins més voluminós construït fins ara, amb 5160 fotomultiplicadors disposats en 86 línies de 60 plantes cadascuna: és a dir, formant un volum total aproximat de 1 km^3. A l'igual que ANTARES, cadascun dels

fotomultiplicadors estan ficats dins d'una esfera de borosilicat (també amb l'electrònica associada), formant els anomenats mòduls òptics digitals o DOMs (Digital Optical Modules, en anglés).

La col·laboració KM3NeT ha començat a construir la propera xarxa de telescopis de neutrins a la Mediterrània, la qual serà, a l'anomenada fase 2, d'un volum semblant al d'IceCube, però amb una major precisió a la reconstrucció de la direcció dels esdeveniments detectats. L'element més bàsic de KM3NeT són també els mòduls òptics digitals o DOMs. No obstant això, a KM3NeT els DOMs estan formats per un total de 31 fotomultiplicadors, els quals permeten una millor discriminació del fons ambiental comparat amb ANTARES. La fase 2 de KM3NeT estarà formada per dos detectors: KM3NeT/ARCA, situat prop de Sicília a 3500 m de profunditat, i KM3NeT/ORCA, prop de la localització d'ANTARES. KM3NeT/ARCA estarà format per dos blocs de construcció (*building blocks*) de 115 línies amb 18 DOMs cadascuna, formant un volum per bloc aproximat de 0.5 km^3. Donat que KM3NeT/ORCA està orientat a la determinació de la jerarquia de masses dels neutrins, estarà format per un únic bloc de construcció de menor volum, però de mateix nombre de línies.

El principi d'operació d'aquests telescopis es fonamenta en la detecció de la radiació Cherenkov produïda per les partícules secundàries carregades produïdes a la interacció d'un neutrí als voltants o a l'interior del detector. Segons siga el tipus (flavour o sabor) de neutrí, s'hi produiran diferents tipus de senyals. D'aquesta manera, la interacció d'un neutrí muònic hi produeix un muó, el qual deixa una traça rectilínia que pot creuar tot el detector. Aquest tipus d'esdeveniment és el que s'ha emprat tradicionalment per a les cerques de fonts puntuals, ja que presenten una millor resolució angular. Per altra banda, els neutrins electrònics produeixen hi una cascada de partícules localitzada, però degut a la seua pitjor reconstrucció angular, no s'han utilitzat tradicionalment en cerques de fonts puntuals. No obstant això, degut a que el fons per a aquests esdeveniments és considerablement menor, s'han inclòs amb l'objectiu d'augmentar la probabilitat de detectar una font còsmica a les anàlisis d'ANTARES i KM3NeT. Els neutrins de tipus tau també hi poden produir una cascada de partícules, pel que la reconstrucció d'aquest tipus d'esdeveniments obren la porta a l'anomenada *all-flavour neutrino astronomy* (astronomia de neutrins per a tots els tipus de neutrins).

Els possibles fons que s'hi observen es poden dividir entre els fons deguts a les condicions ambientals o del propi detector, i els fons físics. La presència d'isòtops radioactius de ^{40}K i d'éssers vius capaços de produir resplendors de llum de baixa intensitat constitueixen la major contribució del fons ambiental als telescopis de neutrins marins. Aquest fons no hi és al gel, pel que el fons degut a la pròpia electrònica del detector és major que qualsevol efecte ambiental a IceCube. Tot i aquest menor fons ambiental, la longitud d'absorció de la llum al gel antàrtic és molt variable degut a la presència de diferents concentracions d'impureses [170]. En aquest efecte s'ha d'afegir una menor longitud de dispersió de la llum al gel, el qual provoca una pitjor determinació de la direcció dels esdeveniments detectats.

Els fons físics es divideixen en dos tipus. Per una banda, els muons atmosfèrics produïts per la interacció de raigs còsmics amb nuclis de l'atmosfera són capaços d'arribar a les grans profunditats dels telescopis de neutrins. Aquest tipus d'esdeveniments tradicionalment s'han evitat a les cerques de neutrins còsmics utilitzant-ne únicament els que han creuat la Terra, ja que sols els neutrins són capaços de creuar-la sense interactuar. El segon tipus de fons físic correspon als neutrins produïts pel mateix tipus de reaccions que produeixen els muons atmosfèrics. Aquest fons de neutrins atmosfèrics n'és un que no es pot suprimir esdeveniment a esdeveniment, ja que són idèntics als neutrins còsmics.

Simulacions montecarlo i mètodes de reconstrucció d'esdeveniments

Per a poder estudiar la resposta dels telescopis de neutrins davant els fluixos de neutrins i als fons físics i ambientals, es requereixen simulacions. Més específicament, aquestes simulacions es fan servir per a obtenir la eficiència dels mètodes de reconstrucció dels esdeveniments, les distribucions de densitat de probabilitat de paràmetres de rellevància, i les magnituds necessàries per a conèixer la sensibilitat del telescopi davant qualsevol fluix. Les simulacions es fan tan semblants a la realitat com siga possible, de manera que els resultats dels mètodes de reconstrucció aplicats sobre els esdeveniments observat amb les dades dels telescopis siguen idèntics als simulats.

Les simulacions es poden dividir en tres passos:

El primer pas consisteix en la generació dels esdeveniments i en la propagació de la llum Cherenkov al medi a on està el telescopi (aigua o gel). Per a això, s'hi defineixen tres volums [175]: el primer és el volum instrumental, que es defineix com el cilindre que envolta el volum del detector. El segon és el volum *llauna* (de l'anglés, *can*), definit com el volum a on l'emissió Cherenkov pot arribar al telescopi. El tercer, correspon a la resta de l'espai. Així, la simulació completa es fa únicament dins del volum *llauna*, mentres que sols les pèrdues energètiques de les partícules se'n consideren fora. Els esdeveniments es simulen amb programes diferents segons les col·laboracions, i segons el tipus de partícula involucrada, muons atmosfèrics o neutrins. En el cas de la simulació dels neutrins, es tenen en compte les distribucions CTEQ6-D [144] per a calcular les seccions eficaces de xocs profundament inelàstics, i l'absorció dels neutrins deguts al creuament per la Terra. La generació dels neutrins es fa de normal amb un espectre energètic fixe. Per a poder estimar la quantitat de neutrins esperada per a un altre espectre energètic s'hi fan servir els anomenats pesos.

El segon pas correspon a la propagació de la llum i de les partícules dins del volum *llauna*. En aquest pas se n'han de considerar les pèrdues energètiques, interaccions hadròniques, emissions de llum i xocs múltiples. També en este pas es simula el fons ambiental i el fons degut a l'electrònica. En el cas d'ANTARES i KM3NeT, el fons ambiental està donat per la llum que apareix després dels decaïments dels nuclis de ^{40}K i per éssers vius bioluminescents. A IceCube no es dona el fons ambiental, pel que sols es requereix la simulació de l'electrònica.

El tercer pas consisteix en la reconstrucció dels esdeveniments, la qual cosa es fa de manera idèntica a les dades obtingudes. Els mecanismes de reconstrucció descrits en aquest treball es poden dividir en dos grans tipus: els de traces i els de cascades. Aquests mecanismes es solen basar en general en una sèrie de selecció de *hits* per a després aplicar-hi una o vàries maximitzacions de funcions de versemblança o d'estimadors M, els quals donen una sèrie de paràmetres òptims de l'esdeveniment (en general, energia reconstruïda i direcció). A més a més, en solen produir una sèrie de paràmetres de qualitat, els quals ens permeten distingir entre tipus

d'esdeveniments. L'excel·lent reconstrucció angular dels esdeveniments de neutrins és la que permet fer anàlisis de fonts puntuals. Així, a ANTARES s'obté una resolució angular mediana de 0,4° amb el mecanisme `AAFit` per a neutrins muonics que produeixen una traça de muons, i una mediana de 2–4° per als neutrins electrònics que produeixen una cascada a través de la interacció de corrent carregada amb el mecanisme `TANTRA`. Millors valors s'obtenen a KM3NeT, amb uns excel·lentísim 0.1° per a neutrins muónics per damunt dels 10 TeV (mecanisme `JGandalf`), i menys de 2° per a neutrins electrònics de més de 100 TeV (mecanisme *AAshowerFit*). A IceCube, malgrat el seu volum, la resolució angular mediana per a traces és lleugerament pitjor que la d'ANTARES, degut a la menor longitud de dispersió de la llum al gel.

Calibratge temporal del telescopi ANTARES

El calibratge temporal als telescopis de neutrins és necessari per al seu correcte funcionament, ja que el temps al que es detecta cadascun dels fotons procedents d'un esdeveniment s'han de mesurar amb precisió per a poder procedir-ne amb una bona reconstrucció. A anteriors anàlisis, s'ha estimat que es necessita una precisió temporal de 1 ns als fotons detectats (anomenats com *hits*) per a una correcta reconstrucció [158].

Un dels paràmetres a determinar al calibratge temporal és el desplaçament temporal o *time offset* que es posa a cadascun dels fotomultiplicadors del telescopi per a corregir els retards deguts a l'electrònica. Per a obtenir els *time offsets*, al telescopi ANTARES tradicionalment s'han emprat unes balises òptiques (en anglés, *Optical Beacons*) que inclouen una sèrie de LEDs capaços d'emetre pols de llum breus (4 ns en FWHM) de fins a 160 pJ d'intensitat. Cadascuna de les línies d'ANTARES conté quatre LED Optical Beacons. D'aquesta manera, els *time offsets* es poden determinar coneixent el moment i el lloc de l'emissió dels pols de llum, i coneixent el temps d'arribada a cada detecció. Damunt, també hi existeixen les balises òptiques amb làsers (Laser Optical Beacon en anglés), situats al fons de dues de les dotze línies. Cadascuna d'estes balises contenen un làser de llum verda capaç d'emetre pols de menys de 1 ns i d'energies de fins a 1 μJ d'intensitat. Degut a la seua alta intensitat, aquestes balises s'han fet servir predominantment per al càlcul dels *time offsets* entre les línies del detector.

En aquesta tesi es mostra un nou calibratge del telescopi mitjançant l'ús de traces de muons i amb la informació obtinguda pel calibratge mitjançant els fotons observats a partir de la desintegració dels isòtops de ^{40}K. Este calibratge s'ha efectuat després d'haver-se'n observat una lleugera desviació dels time-offsets respecte dels valors esperats. Aquest nou calibratge conté la major part del període de presa de les dades del telescopi ANTARES (des del començament de 2007 fins el final de 2016). En aquest nou calibratge, es distingeixen tres passos: el calibratge temporal entre línies (calibratge *inter-line*), entre plantes (calibratge *inter-storey*) i calibratge entre ARSs (calibratge *intra-storey*). Els calibratges inter-line i inter-storey es fan amb l'ús de muons atmosfèrics reconstruïts, mentres que el intra-storey utilitza els esdeveniments procedents de desintegracions de ^{40}K.

El calibratge amb traces de muons fa servir els anomenats temps residuals (*time-residuals* en anglés) obtinguts després de la reconstrucció amb el mètode *AAFit*. Els temps residuals es defineixen com la diferència entre el temps de detecció d'un fotó en un fotomultiplicador, i el temps en el que hauria d'arribar si aquest procedeix de la traça reconstruïda. Per a evitar biaixos, la informació del *storey* (planta) o de la línia per calibrar no s'inclou a la reconstrucció de la traça. També, per a evitar traces malament reconstruïdes, se'n prenen únicament les que es consideren ben reconstruïdes (valors de tall en el paràmetre de reconstrucció Λ major de –6.5 pel calibratge intra-storey, i –6.0 per al inter-line) sense que això limite l'estadística necessària.

El calibratge amb els esdeveniments deguts a la desintegració d'isòtops de ^{40}K s'empra solament per a obtenir els *time offsets* dels fotomultiplicadors d'una mateixa planta. En aquest calibratge, s'adopta que, de mitjana, el temps de detecció dels fotons deguts a este procés ha de ser idèntic pels pars de fotomultiplicadors d'una mateixa planta.

Com a resultat del nou calibratge, s'hi observa un augment del nombre d'esdeveniments ben reconstruïts. Per als esdeveniments que venen en direcció cap avall i per a un tall en el paràmetre $\Lambda > -5.2$, aquest pot variar entre un $\sim$10–20% segons el període avaluat. Aquest increment és menor als esdeveniments que hi van cap amunt, el qual és més difícil d'estimar per la manca d'estadística.

Mètodes estadístics per les cerques de fonts puntuals extenses de neutrins còsmics

Les cerques de fonts puntuals i extenses de neutrins còsmics es basen en la distribució espacial dels neutrins detectats. Així com els neutrins atmosfèrics es distribueixen sense que hi hagen direccions preferents, els neutrins còsmics procedents d'una font s'haurien d'acumular al voltant de la direcció de la font. Per a determinar si s'ha observat una font d'aquest tipus, s'ha desenvolupat un mètode estadístic que indica la significació d'una acumulació d'esdeveniments.

El mètode estadístic es basa en una funció de versemblança (*likelihood* en anglés). Per a cada conjunt de dades, aquesta funció es maximitza ajustant un paràmetre lliure que, al cas de l'anàlisi de fonts puntuals, és el nombre d'esdeveniments de senyal detectats, n_s, el qual es desconeix a priori. Posteriorment es calcula el test estadístic, definit com el quocient entre la funció de versemblança maximitzada i la mateixa funció de versemblança per a la hipòtesi nul·la de sols fons ($n_s = 0$). Per últim, es calcula la significació comparant el valor obtingut per a aquest test estadístic a partir de les dades reals amb la distribució dels valors del test estadístic esperat.

Aquestes distribucions es calculen mitjançant la realització de pseudoexperiments, als quals es simulen mostres semblants a la que s'ha d'analitzar. Per a la generació dels esdeveniments de fons d'aquestes simulacions, es fa servir la informació energètica, la declinació i/o l'estimador de l'error angular dels esdeveniments de la mostra de dades reals. L'ascensió recta es genera aleatòriament considerant que s'hi distribueix uniformement. Amb la finalitat de no introduir-ne cap biaix, únicament es pot accedir al valor real de les coordenades dels esdeveniments una vegada la mostra estiga definida amb els criteris de selecció de l'anàlisi (política d'*unblinding*). A més a més, donat que el test estadístic s'obté per a moltes direccions, s'hi aplica una correcció deguda als intents repetits per a cada direcció observada (*trial factor*).

Per a cada cerca, es construeix una mostra final de dades. Aquesta mostra s'obté realitzant diversos talls en paràmetres que ajuden a la reducció del nombre de muons i neutrins d'origen atmosfèric, de mode que es correspon

amb la que minimitza el fluix d'una font necessari per a un descobriment amb una significació de 5σ al 50% dels casos. Alguns d'aquests paràmetres de tall s'obtenen a partir de variables procedents de la reconstrucció dels esdeveniments. En altres casos, ha sigut necessari l'entrenament d'un bosc de classificació aleatòria (*Random Forest Classifier*, en anglés) que depén de variables diverses que ajuden a la discriminació entre els esdeveniments de tipus fons i tipus senyal.

La classificació mitjançant boscos aleatoris és un dels mètodes d'aprenentatge automàtic (*machine learning* en anglés) més utilitzats. Aquest mètode es basa en l'entrenament de N arbres de decisió mitjançant el mètode de *bootstrapping*. Més concretament, cadascun dels N arbres de decisió s'entrena fent servir una submostra escollida de manera aleatòria. A més, per a la realització de l'entrenament de cada arbre, es fa servir sols una part dels paràmetres disponibles per a la classificació, els quals es trien també aleatòriament. Per a determinar la classificació final d'un esdeveniment, es fa una votació amb el resultat de cadascun dels arbres entrenats.

Resultats

A la duració d'esta tesi s'han realitzat quatre cerques diferents de fonts còsmiques de neutrins puntuals i/o extenses. La primera correspon amb l'anàlisi que emprava esdeveniments de tipus traça de les dades recollides amb el telescopi de neutrins ANTARES al període 2007-2012 [130]. Posteriorment, es feren servir aquestes dades i les d'IceCube obtingudes amb les configuració de 40, 59 i 79 línies al primer anàlisi combinat entre ambdós detectors [235]. Els resultats del primer anàlisi d'ANTARES s'actualitzaren posteriorment afegint les dades de 2013 a 2015. A més a més, s'hi afegiren per primera vegada esdeveniments de tipus de cascada per a un anàlisi de fonts puntuals [111]. Per últim, es realitzà un anàlisi per a estimar la sensibilitat per a aquest tipus de fonts del futur telescopi de neutrins KM3NeT/ARCA fent servir únicament el canal de cascades, de la qual s'inclogueren uns resultats preliminars (actualitzats i ampliats en aquesta tesi) a la Letter of Intent de KM3NeT [106].

Cerca de fonts puntuals amb les dades d'ANTARES i IceCube

Aquesta fou la primera cerca a la que es combinaren les dades dels dos majors telescopis de neutrins construïts fins a la data, ANTARES i IceCube. Sols es van considerar els esdeveniments procedents del cel de l'hemisferi sud i reconstruïts com a traces. Al cas d'ANTARES, es feren servir les dades registrades des de 2007 fins a 2012, mentres que a IceCube el període comprenia des de 2008 fins a 2011. En aquest anàlisi, es mostrava la superioritat d'ANTARES a l'hora d'estudiar fonts puntuals de tipus galàctic per a la major part del cel de l'hemisferi sud. També es mostrava la complementarietat d'ambdós telescopis per a observar aquesta regió de l'espai: IceCube, degut a la seua gran mida, presenta una millor sensibilitat per als esdeveniments d'energies més altes. Tot i això, degut a que els esdeveniments procedents del cel de l'hemisferi sud no han creuat la Terra fins a arribar a IceCube, la forta reducció del fons de muons atmosfèrics provoca que la seua sensibilitat a energies dels neutrins menors de 100 TeV siga menor que en el cas d'ANTARES.

Es van realitzar dos tipus de cerques. A la primera, es buscà a la direcció de aproximadament 40 fonts candidates a ser emissores de neutrins. A la segona, es va fer un rastreig per tot el cel de l'hemisferi sud. En cap de les dues cerques s'obtingueren resultats estadísticament significatius. L'acumulació d'esdeveniments més significativa de la cerca de fonts candidates correspon a la localització de la font HESS J1741-302, amb una probabilitat després de biaixos (*post-trial* del 11% de ser-ne produïda pel fons. Per alta banda, la localització més significativa del rastreig de tot el cel s'observà a les coordenades equatorials $\alpha = 332.8°$, $\delta = –46.1°$, amb una probabilitat del 24% d'haver-se'n produït pel fons.

Cerca de fonts puntuals i extenses mitjançant les dades d'ANTARES entre 2007 y 2015

Aquesta cerca incloguí per primera vegada l'ús d'esdeveniments de tipus cascada en una cerca de fonts puntuals d'ANTARES. A ANTARES, els esdeveniments de tipus cascada presenten una resolució angular mediana al voltant de 2–3°, la qual és significativament millor que la d'IceCube (més de

10°). Tot i que els esdeveniments d'aquest tipus tenen una resolució angular pitjor que els de tipus traça, en aquesta cerca es demostra que poden arribar a millorar al voltant d'un 20% la sensibilitat d'aquest tipus de cerques.

En aquesta cerca s'actualitzà la llista de fonts candidates, de manera que es buscà en 126 direccions del cel. També es realitzà una cerca en la direcció de 13 dels neutrins d'altes energies reconstruïdes per IceCube. A més d'això, es procedí amb un rastreig per una regió propera al centre galàctic, degut a la major presència de neutrins d'alta energia reconstruïts per IceCube en aquesta regió. En aquest rastreig, també es buscaren fonts de fins a 4° d'extensió. Per últim, es buscà a totes les direccions del cel observable d'ANTARES.

D'igual mode que a la resta de cerques de fonts puntuals còsmiques de neutrins, no s'ha observat cap acumulació de neutrins estadísticament significativa. El lloc més significatiu de la cerca de fonts candidates correspon a HESSJ0632+057, amb una probabilitat després de biaixos del 13%. En la cerca al voltant de les direccions dels 13 esdeveniments observats per IceCube, la més significativa correspon a les coordenades equatorials $\alpha = 257.4°$, $\delta = -41.0°$, amb una probabilitat del 60% d'haver-se'n produït per una fluctuació estadística del fons. Per últim, la cerca de tot el cel trobà l'acumulació més significativa a $\alpha = 343.8°$, $\delta = 23.5°$, amb una probabilitat post-trial del 5.9%.

Estimacions per a fonts còsmiques de neutrins puntuals amb esdeveniments de tipus cascada mitjançant el telescopi KM3NeT

L'última de les anàlisis realitzades correspon amb l'estimació de la sensibilitat per a fonts còsmiques puntuals i extenses de neutrins mitjançant el telescopi KM3NeT fent servir únicament els esdeveniments de tipus cascada. Gran part de l'esforç d'aquesta anàlisi gravita al voltant de la reducció del fons de muons atmosfèrics, la qual es realitzà mitjançant un classificador de boscos aleatoris.

L'anàlisi realitzada hi mostra la competitivitat del canal de cascades front al de traces, suposant d'entre un 15 a un 30% de la sensibilitat de KM3NeT/ARCA emprant únicament traces. També s'estudià el cas concret de dues fonts

extenses galàctiques: la romanent de supernova SNR RXJ 1713.7-3946 i el plerió Vela X. Els resultats més optimistes s'han obtingut per a aquest últim, podent-se observar amb una significació de 3σ en menys de dos anys segons els models purament hadrònics (és a dir, que el fluix de raigs γ observat per Vela X es produïsca únicament degut a l'acceleració d'hadrons en aquesta font). Tot i això, aquests models hi són especialment optimistes, ja que actualment sembla més probable que la major part de la contribució del fluix de raigs γ siga per acceleració de leptons.

Bibliography

[1] B. P. Abbott et al. 'Observation of Gravitational Waves from a Binary Black Hole Merger'. In: *Phys. Rev. Lett.* 116.6 (2016), p. 061102. arXiv: 1602.03837 [gr-qc] (cit. on p. 3).

[2] M. G. Aartsen et al. 'Evidence for High-Energy Extraterrestrial Neutrinos at the IceCube Detector'. In: *Science* 342 (2013), p. 1242856. arXiv: 1311.5238 [astro-ph.HE] (cit. on pp. 3, 28, 29, 39, 150, 203, 206).

[3] M. G. Aartsen et al. 'Observation of High-Energy Astrophysical Neutrinos in Three Years of IceCube Data'. In: *Phys. Rev. Lett.* 113 (2014), p. 101101. arXiv: 1405.5303 [astro-ph.HE] (cit. on pp. 3, 29, 150, 170, 203, 206).

[4] Claudio Kopper, William Giang, and Naoko Kurahashi. 'Observation of Astrophysical Neutrinos in Four Years of IceCube Data'. In: *PoS* ICRC2015 (2016), p. 1081 (cit. on pp. 3, 29, 150, 170, 175, 177, 203, 206).

[5] Kopper C. 'Observation of Astrophysical Neutrinos in Six Years of IceCube Data'. In: *Proceedings, 35th International Cosmic Ray Conference (ICRC2017)*. 2017 (cit. on pp. 3, 29–31, 150, 203, 206).

[6] V.F. Hess. 'Über Beobachtungen der durchdringenden Strahlung bei sieben Freiballonfahrten'. In: *Physikalische Zeitschrift* 13 (1912), p. 1084 (cit. on pp. 4, 203).

[7] W. Kolhörster. 'Messungen der Durchdringenden Strahlung im Freiballon in Grösseren Höhen'. In: *Physikalische Zeitschrift* 14 (1913), p. 1153 (cit. on pp. 4, 203).

[8] C. D. Anderson. 'The Positive Electron'. In: *Phys. Rev.* 43 (1933), pp. 491–494 (cit. on p. 4).

[9] S. H. Neddermeyer and C. D. Anderson. 'Note on the Nature of Cosmic Ray Particles'. In: *Phys. Rev.* 51 (1937), pp. 884–886 (cit. on p. 4).

[10]Hideki Yukawa. 'On the Interaction of Elementary Particles I'. In: *Proc. Phys. Math. Soc. Jap.* 17 (1935). [Prog. Theor. Phys. Suppl.1,1(1935)], pp. 48–57 (cit. on p. 4).

[11]M. Conversi, E. Pancini, and O. Piccioni. 'Sull'assorbimento e sulla disintegrazione dei mesoni alla fine del loro percorso'. In: *Il Nuovo Cimento (1943-1954)* 3.1 (2008), p. 372 (cit. on p. 4).

[12]G. D. Rochester and C. C. Butler. 'Evidence for the Existence of New Unstable Elementary Particles'. In: *Nature* 160 (1947), pp. 855–857 (cit. on p. 4).

[13]C. M. G. Lattes, H. Muirhead, G. P. S. Occhialini, and C. F. Powell. 'Evidence for the Existence of New Unstable Elementary Particles'. In: *Nature* 160 (1947), pp. 855–857 (cit. on p. 4).

[14]B. Rossi. 'On the Magnetic Deflection of Cosmic Rays'. In: *Phys. Rev.* 36 (1930), p. 606 (cit. on p. 5).

[15]T.H. Johnson. 'The Azimuthal Asymmetry of the Cosmic Radiation'. In: *Phys. Rev.* 43 (1933), p. 834 (cit. on p. 5).

[16]Luis Alvarez and Arthur H. Compton. 'A Positively Charged Component of Cosmic Rays'. In: *Phys. Rev.* 43 (1933), pp. 835–836 (cit. on p. 5).

[17]Bruno Rossi. 'Directional Measurements on the Cosmic Rays Near the Geomagnetic Equator'. In: *Phys. Rev.* 45 (1934), pp. 212–214 (cit. on p. 5).

[18]C. Patrignani et al. 'Review of Particle Physics'. In: *Chin. Phys.* C40.10 (2016), p. 100001 (cit. on pp. 5–7, 11, 16–18, 204).

[19]M. Spurio, ed. *Particles and Astrophysics: A Multi-Messenger Approach*. Springer, 2015 (cit. on pp. 5, 6, 8, 9, 11, 20, 204, 205).

[20]M. S. Longair, ed. *High Energy Astrophysics*. 3rd ed. Cambridge University Press, 2011 (cit. on pp. 5, 6, 8–11, 204).

[21]J. A. Simpson. 'The Cosmic Ray Nucleonic Component: The Invention and Scientific Uses of the Neutron Monitor – (Keynote Lecture)'. In: *Space Science Reviews* 93.1 (2000), p. 11 (cit. on pp. 6, 204).

[22]V. L. Ginzburg, Ya. M. Khazan, and V. S. Ptuskin. 'Origin of cosmic rays: Galactic models with halo'. In: *Astrophysics and Space Science* 68.2 (1980), p. 295 (cit. on pp. 7, 204).

[23]M. Kachelriess. 'Lecture notes on high energy cosmic rays'. In: (2008). arXiv: `0801.4376 [astro-ph]` (cit. on pp. 8, 28, 204).

[24]M. Garcia-Munoz, J. A. Simpson, T. G. Guzik, J. P. Wefel, and S. H. Margolis. 'Cosmic-ray propagation in the Galaxy and in the heliosphere - The path-length distribution at low energy'. In: *Astrophysical Journal Supplement Series* 64 (1987), p. 269 (cit. on p. 8).

[25]A. Obermeier, P. Boyle, J. Horandel, and D. Muller. 'The boron-to-carbon abundance ratio and Galactic propagation of cosmic radiation'. In: *Astrophys. J.* 752 (2012), p. 69. arXiv: 1204.6188 [astro-ph.HE] (cit. on p. 8).

[26]A. M. Hillas. 'The Origin of Ultrahigh-Energy Cosmic Rays'. In: *Ann. Rev. Astron. Astrophys.* 22 (1984), pp. 425–444 (cit. on pp. 9, 204).

[27]Johannes Blumer, Ralph Engel, and Jorg R. Horandel. 'Cosmic Rays from the Knee to the Highest Energies'. In: *Prog. Part. Nucl. Phys.* 63 (2009), pp. 293–338. arXiv: 0904.0725 [astro-ph.HE] (cit. on p. 10).

[28]H. J. Volk, E. G. Berezhko, and Leonid T. Ksenofontov. 'Magnetic field amplification in Tycho and other shell-type supernova remnants'. In: *Astron. Astrophys.* 433 (2005), p. 229. arXiv: astro-ph/0409453 [astro-ph] (cit. on p. 10).

[29]A. AAb et al. 'Observation of a large-scale anisotropy in the arrival directions of cosmic rays above 8×10^{18} eV'. In: *Science* 357 (2017), p. 1266 (cit. on p. 10).

[30]Alexander Aab et al. 'An Indication of anisotropy in arrival directions of ultra-high-energy cosmic rays through comparison to the flux pattern of extragalactic gamma-ray sources'. In: *Astrophys. J.* 853 (2018), p. L29. arXiv: 1801.06160 [astro-ph.HE] (cit. on pp. 10, 205).

[31]Kenneth Greisen. 'End to the cosmic ray spectrum?' In: *Phys. Rev. Lett.* 16 (1966), pp. 748–750 (cit. on pp. 11, 204).

[32]G. T. Zatsepin and V. A. Kuzmin. 'Upper limit of the spectrum of cosmic rays'. In: *JETP Lett.* 4 (1966). [Pisma Zh. Eksp. Teor. Fiz.4,114(1966)], pp. 78–80 (cit. on pp. 11, 204).

[33]Degrange, Bernard and Fontaine, Gerard. 'Introduction to high-energy gamma-ray astronomy'. In: *Comptes Rendus Physique* 16 (2016), pp. 587–599. arXiv: 1604.05488 [astro-ph.HE] (cit. on pp. 11, 12, 22, 205).

[34]Stefan Funk. 'Ground- and Space-Based Gamma-Ray Astronomy'. In: *Ann. Rev. Nucl. Part. Sci.* 65 (2015), pp. 245–277. arXiv: 1508.05190 [astro-ph.HE] (cit. on pp. 11, 22, 205).

[35]W. L. Kraushaar, G. W. Clark, G. P. Garmire, et al. 'High-Energy Cosmic Gamma-Ray Observations from the OSO-3 Satellite'. In: *Astrophys. J.* 177 (Nov. 1972), p. 341 (cit. on p. 11).

[36]Ray W. Klebesadel, Ian B. Strong, and Roy A. Olson. 'Observations of Gamma-Ray Bursts of Cosmic Origin'. In: *Astrophys. J.* 182 (1973), pp. L85–L88 (cit. on p. 11).

[37]B. N. Swanenburg, K. Bennett, G. F. Bignami, et al. 'Second COS B catalog of high-energy gamma-ray sources'. In: *Astrphys. J. Lett.* 243 (1981), p. L69 (cit. on p. 12).

[38]R. C. Hartman et al. 'The Third EGRET catalog of high-energy gamma-ray sources'. In: *Astrophys. J. Suppl.* 123 (1999), p. 79 (cit. on p. 12).

[39]F. Acero et al. 'Fermi Large Area Telescope Third Source Catalog'. In: *Astrophys. J. Suppl.* 218.2 (2015), p. 23. arXiv: 1501.02003 [astro-ph.HE] (cit. on p. 12).

[40]M. Su, T. R. Slatyer, and D. P. Finkbeiner. 'Giant Gamma-ray Bubbles from Fermi-LAT: Active Galactic Nucleus Activity or Bipolar Galactic Wind?' In: *Aastrophys. J.* 724 (2010), p. 1044. eprint: 1005.5480 (astro-ph.HE) (cit. on p. 12).

[41]H. Y. K. Yang, M. Ruszkowski, and E. Zweibel. 'Unveiling the Origin of the Fermi Bubbles'. In: (2018). arXiv: 1802.03890 [astro-ph.HE] (cit. on p. 12).

[42]W. B. Atwood et al. 'The Large Area Telescope on the Fermi Gamma-ray Space Telescope Mission'. In: *Astrophys. J.* 697 (2009), pp. 1071–1102. arXiv: 0902.1089 [astro-ph.IM] (cit. on p. 12).

[43]F. Aharonian et al. 'Observations of the Crab Nebula with H.E.S.S'. In: *Astron. Astrophys.* 457 (2006), pp. 899–915. arXiv: astro-ph/0607333 [astro-ph] (cit. on p. 13).

[44]E. Lorenz. 'Status of the 17-m MAGIC telescope'. In: *New Astron. Rev.* 48 (2004), pp. 339–344 (cit. on p. 13).

[45]T. C. Weekes et al. 'VERITAS: The Very energetic radiation imaging telescope array system'. In: *Astropart. Phys.* 17 (2002), pp. 221–243. arXiv: astro-ph/0108478 [astro-ph] (cit. on p. 13).

[46]CTA Consortium Ong R.A. 'Cherenkov Telescope Array: The Next Generation Gamma-ray Observatory'. In: *Proceedings, 35th International Cosmic Ray Conference (ICRC2017)*. 2017 (cit. on p. 13).

[47]A. U. Abeysekara et al. 'The 2HWC HAWC Observatory Gamma Ray Catalog'. In: *Astrophys. J.* 843.1 (2017), p. 40. arXiv: 1702.02992 [astro-ph.HE] (cit. on p. 14).

[48]S. P. Wakely and D. Horan. 'TeVCat: An online catalog for Very High Energy Gamma-Ray Astronomy'. In: *International Cosmic Ray Conference* 3 (2008), pp. 1341–1344 (cit. on p. 14).

[49]W. Pauli. 'Dear radioactive ladies and gentlemen'. In: *Phys. Today* 31N9 (1978). Translation from the original letter in 1930, p. 27 (cit. on p. 14).

[50]E. Fermi. 'Versuch einer Theorie der β-Strahlen. I'. In: *Zeitschrift fur Physik* 88 (Mar. 1934), pp. 161–177 (cit. on p. 14).

[51]C. L. Cowan, F. Reines, F. B. Harrison, H. W. Kruse, and A. D. McGuire. 'Detection of the free neutrino: A Confirmation'. In: *Science* 124 (1956), p. 103 (cit. on p. 14).

[52]G. Danby, J. M. Gaillard, Konstantin A. Goulianos, et al. 'Observation of High-Energy Neutrino Reactions and the Existence of Two Kinds of Neutrinos'. In: *Phys. Rev. Lett.* 9 (1962), pp. 36–44 (cit. on p. 15).

[53]K. Kodama et al. 'Observation of tau neutrino interactions'. In: *Phys. Lett.* B504 (2001), pp. 218–224. arXiv: `hep-ex/0012035 [hep-ex]` (cit. on p. 15).

[54]A. S. Eddington. 'The internal constitution of the stars'. In: *The Observatory* 43 (1920), p. 341 (cit. on p. 15).

[55]H. A. Bethe. 'Energy Production in Stars'. In: *Phys. Rev.* 55 (5 1939), pp. 434–456 (cit. on p. 15).

[56]R. Davis. 'Solar neutrinos. II: Experimental'. In: *Phys. Rev. Lett.* 12 (1964), p. 303 (cit. on pp. 16, 206).

[57]B. Pontecorvo. 'Mesoniums and anti-mesoniums'. In: *Zh. Eksp. Teor. Fiz.* 33 (1957), p. 549 (cit. on p. 17).

[58]V. N. Gribov and B. Pontecorvo. 'Neutrino astronomy and lepton charge'. In: *Phys. Lett.* 28B (1969), p. 493 (cit. on p. 17).

[59]Ziro Maki, Masami Nakagawa, and Shoichi Sakata. 'Remarks on the unified model of elementary particles'. In: *Prog. Theor. Phys.* 28 (1962), pp. 870–880 (cit. on p. 17).

[60]Y. Fukuda et al. 'Evidence for oscillation of atmospheric neutrinos'. In: *Phys. Rev. Lett.* 81 (1998), pp. 1562–1567. arXiv: `hep-ex/9807003 [hep-ex]` (cit. on p. 17).

[61]S. Fukuda et al. 'Solar B-8 and hep neutrino measurements from 1258 days of Super-Kamiokande data'. In: *Phys. Rev. Lett.* 86 (2001), p. 5651. arXiv: `hep-ex/0103032 [hep-ex]` (cit. on p. 17).

[62] Q. R. Ahmad et al. 'Measurement of the rate of $\nu_e + d \rightarrow p + p + e^-$ interactions produced by ^8B solar neutrinos at the Sudbury Neutrino Observatory'. In: *Phys. Rev. Lett.* 87 (2001), p. 071301. arXiv: nucl-ex/0106015 [nucl-ex] (cit. on p. 17).

[63] Q. R. Ahmad et al. 'Direct evidence for neutrino flavor transformation from neutral current interactions in the Sudbury Neutrino Observatory'. In: *Phys. Rev. Lett.* 89 (2002), p. 011301. arXiv: nucl-ex/0204008 [nucl-ex] (cit. on p. 17).

[64] W. D. Arnett, J. N. Bahcall, R. P. Kirshner, and S. E. Woosley. 'Supernova 1987A'. In: *Annual review of astronomy and astrophysics* 27 (1989), pp. 629–700 (cit. on p. 18).

[65] B. W. Carroll and D.A. Ostlie, eds. *An introduction to Modern Astrophysics*. Second Edition. Pearson, 2014 (cit. on pp. 18, 19, 26, 27).

[66] F. Vissani, M. L. Costantini, W. Fulgione, A. Ianni, and G. Pagliaroli. 'What is the issue with SN1987A neutrinos?' In: *Vulcano Workshop 2010: Frontier Objects in Astrophysics and Particle Physics Vulcano, Italy, May 24-29, 2010*. 2010. arXiv: 1008.4726 [hep-ph] (cit. on p. 18).

[67] K. Hirata et al. 'Observation of a Neutrino Burst from the Supernova SN 1987a'. In: *Phys. Rev. Lett.* 58 (1987). [,727(1987)], pp. 1490–1493 (cit. on pp. 18, 206).

[68] K. S. Hirata et al. 'Observation in the Kamiokande-II Detector of the Neutrino Burst from Supernova SN 1987a'. In: *Phys. Rev.* D38 (1988), pp. 448–458 (cit. on pp. 18, 206).

[69] R. M. Bionta et al. 'Observation of a Neutrino Burst in Coincidence with Supernova SN 1987a in the Large Magellanic Cloud'. In: *Phys. Rev. Lett.* 58 (1987), p. 1494 (cit. on pp. 18, 206).

[70] C. B. Bratton et al. 'Angular Distribution of Events From Sn1987a'. In: *Phys. Rev.* D37 (1988), p. 3361 (cit. on pp. 18, 206).

[71] E. N. Alekseev, L. N. Alekseeva, I. V. Krivosheina, and V. I. Volchenko. 'Detection of the Neutrino Signal From SN1987A in the LMC Using the Inr Baksan Underground Scintillation Telescope'. In: *Phys. Lett.* B205 (1988), pp. 209–214 (cit. on pp. 18, 206).

[72] Stan Woosley and Thomas Janka. 'The physics of core-collapse supernovae'. In: *Nature Phys.* 1 (2005), p. 147. arXiv: astro-ph/0601261 [astro-ph] (cit. on p. 19).

[73] H. Th. Janka. 'Neutrino Emission from Supernovae'. In: (2017). arXiv: 1702.08713 [astro-ph.HE] (cit. on p. 19).

[74] Yu-Feng Li. 'Detection Prospects of the Cosmic Neutrino Background'. In: *Int. J. Mod. Phys.* A30.12 (2015). [Adv. Ser. Direct. High Energy Phys.25,233(2015)], p. 1530031. arXiv: 1504.03966 [hep-ph] (cit. on p. 19).

[75] Brent Follin, Lloyd Knox, Marius Millea, and Zhen Pan. 'First Detection of the Acoustic Oscillation Phase Shift Expected from the Cosmic Neutrino Background'. In: *Phys. Rev. Lett.* 115.9 (2015), p. 091301. arXiv: 1503.07863 [astro-ph.CO] (cit. on pp. 19, 206).

[76] Gary Steigman. 'Neutrinos And Big Bang Nucleosynthesis'. In: *Adv. High Energy Phys.* 2012 (2012), p. 268321. arXiv: 1208.0032 [hep-ph] (cit. on p. 19).

[77] P. A. R. Ade et al. 'Planck 2015 results. XIII. Cosmological parameters'. In: *Astron. Astrophys.* 594 (2016), A13. arXiv: 1502.01589 [astro-ph.CO] (cit. on p. 19).

[78] S. Betts et al. 'Development of a Relic Neutrino Detection Experiment at PTOLEMY: Princeton Tritium Observatory for Light, Early-Universe, Massive-Neutrino Yield'. In: *Proceedings, 2013 Community Summer Study on the Future of U.S. Particle Physics: Snowmass on the Mississippi (CSS2013): Minneapolis, MN, USA, July 29-August 6, 2013*. 2013. arXiv: 1307.4738 [astro-ph.IM] (cit. on p. 19).

[79] Kara Dion Hoffman. 'High Energy Neutrino Telescopes'. In: *New J. Phys.* 11 (2009), p. 055006. arXiv: 0812.3809 [astro-ph] (cit. on p. 21).

[80] U. F. Katz and Ch. Spiering. 'High-Energy Neutrino Astrophysics: Status and Perspectives'. In: *Prog. Part. Nucl. Phys.* 67 (2012), pp. 651–704. arXiv: 1111.0507 [astro-ph.HE] (cit. on pp. 20, 21, 205).

[81] S. R. Kelner and F. A. Aharonian. 'Energy spectra of gamma-rays, electrons and neutrinos produced at interactions of relativistic protons with low energy radiation'. In: *Phys. Rev.* D78 (2008). [Erratum: Phys. Rev.D82,099901(2010)], p. 034013. arXiv: 0803.0688 [astro-ph] (cit. on p. 22).

[82] John G. Learned and Sandip Pakvasa. 'Detecting tau-neutrino oscillations at PeV energies'. In: *Astropart. Phys.* 3 (1995), pp. 267–274. arXiv: hep-ph/9405296 [hep-ph] (cit. on p. 22).

[83] H. Athar, C. S. Kim, and Jake Lee. 'The Intrinsic and oscillated astrophysical neutrino flavor ratios'. In: *Mod. Phys. Lett.* A21 (2006), pp. 1049–1066. arXiv: hep-ph/0505017 [hep-ph] (cit. on p. 22).

[84] Paolo Lipari, Maurizio Lusignoli, and Davide Meloni. 'Flavor Composition and Energy Spectrum of Astrophysical Neutrinos'. In: *Phys. Rev.* D75 (2007), p. 123005. arXiv: 0704.0718 [astro-ph] (cit. on p. 22).

[85]M. Ackermann et al. 'Detection of the Characteristic Pion-Decay Signature in Supernova Remnants'. In: *Science* 339 (2013), p. 807. arXiv: 1302.3307 [astro-ph.HE] (cit. on pp. 23, 205).

[86]G. Morlino and D. Caprioli. 'Strong evidences of hadron acceleration in Tycho's Supernova Remnant'. In: *Astron. Astrophys.* 538 (2012), A81. arXiv: 1105.6342 [astro-ph.HE] (cit. on pp. 23, 205).

[87]P. Slane, S. H. Lee, D. C. Ellison, et al. 'A CR-hydro-NEI Model of the Structure and Broadband Emission from Tycho's Supernova Remnant'. In: *Astrophys. J.* 783.1 (2014). [Astrophys. J.799,238(2015)], p. 33. arXiv: 1401.2556 [astro-ph.HE] (cit. on pp. 23, 205).

[88]L. Saha, T. Ergin, P. Majumdar, M. Bozkurt, and E. N. Ercan. 'Origin of gamma-ray emission in the shell of Cassiopeia A'. In: *Astron. Astrophys.* 563 (2014), A88. arXiv: 1401.5626 [astro-ph.HE] (cit. on pp. 23, 205).

[89]Yajie Yuan, Stefan Funk, Gülauger Jóhannesson, et al. 'Fermi-LAT Detection of a Break in the Gamma-Ray Spectrum of the Supernova Remnant Cassiopeia A'. In: *Astrophys. J.* 779 (2013), p. 117. arXiv: 1310.8287 [astro-ph.HE] (cit. on pp. 23, 205).

[90]A. Atoyan and C. D. Dermer. 'Gamma Rays from the Tycho Supernova Remnant: Multi-zone versus Single-zone Modeling'. In: *Astrophys. J. Lett.* 749, L26 (Apr. 2012), p. L26. arXiv: 1111.4175 [astro-ph.HE] (cit. on pp. 23, 205).

[91]Augusto Ghiotto. 'A Deep Observation of Gamma-ray Emission from Cassiopeia A using VERITAS'. In: (2015). arXiv: 1511.00309 [astro-ph.HE] (cit. on pp. 23, 205).

[92]A. Abramowski et al. 'Acceleration of petaelectronvolt protons in the Galactic Centre'. In: *Nature* 531 (2016), p. 476. arXiv: 1603.07730 [astro-ph.HE] (cit. on pp. 23, 170, 205).

[93]Alessandro De Angelis and Mário João Martins Pimenta. *Introduction to particle and astroparticle physics: questions to the Universe*. Undergraduate lecture notes in physics. Milan: Springer, 2013 (cit. on pp. 24, 25).

[94]G. Morlino, E. Amato, and P. Blasi. 'Gamma ray emission from SNR RX J1713.7-3946 and the origin of galactic cosmic rays'. In: *Mon. Not. Roy. Astron. Soc.* 392 (2009), pp. 240–250. arXiv: 0810.0094 [astro-ph] (cit. on p. 24).

[95]Alexander Kappes, Jim Hinton, Christian Stegmann, and Felix A. Aharonian. 'Potential Neutrino Signals from Galactic Gamma-Ray Sources'. In: *Astrophys. J.* 656 (2007). [Erratum: Astrophys. J.661,1348(2007)], pp. 870–896. arXiv: astro-ph/0607286 [astro-ph] (cit. on pp. 24, 150).

[96] Francesco Vissani. 'Neutrinos from galactic sources of cosmic rays with known γ-ray spectra'. In: *Astropart. Phys.* 26 (2006), pp. 310–313. arXiv: astro-ph/0607249 [astro-ph] (cit. on pp. 24, 25, 190).

[97] Robert Brose, Simone Federici, Martin Pohl, et al. 'Analysis of GeV-band gamma-ray emission from SNR RX J1713.7-3946'. In: *PoS* ICRC2015 (2016), p. 900 (cit. on p. 24).

[98] F. L. Villante and F. Vissani. 'How precisely neutrino emission from supernova remnants can be constrained by gamma ray observations?' In: *Phys. Rev.* D78 (2008), p. 103007. arXiv: 0807.4151 [astro-ph] (cit. on pp. 25, 190).

[99] Francesco Vissani and Francesco Lorenzo Villante. 'Cosmic rays and neutrinos from supernova remnants (or: the time when H.E.S.S. met Ginzburg and Syrovatskii)'. In: *Nucl. Instrum. Meth.* A588 (2008), pp. 123–129 (cit. on pp. 25, 190).

[100] H. Abdalla et al. 'H.E.S.S. observations of RX J1713.7-3946 with improved angular and spectral resolution; evidence for gamma-ray emission extending beyond the X-ray emitting shell'. In: (2016). arXiv: 1609.08671 [astro-ph.HE] (cit. on p. 25).

[101] A. Trovato et al. 'Expectations for detection of neutrinos from point-like sources with KM3NeT/ARCA'. In: *Proceedings, 35th International Cosmic Ray Conference (ICRC2017)*. 2017 (cit. on pp. 25, 190).

[102] S. Gillessen, F. Eisenhauer, S. Trippe, et al. 'Monitoring stellar orbits around the Massive Black Hole in the Galactic Center'. In: *Astrophys. J.* 692 (2009), pp. 1075–1109. arXiv: 0810.4674 [astro-ph] (cit. on p. 25).

[103] Elena Amato. 'Particle acceleration and radiation in Pulsar Wind Nebulae'. In: *Proceedings, 14th International Symposium Frontiers of Fundamental Physics (FFP14): Marseille, France, July 15-18, 2014*. Vol. FFP14. 2016, p. 043. arXiv: 1503.02402 [astro-ph.HE] (cit. on p. 25).

[104] Dieter Horns and F. A. Aharonian. 'The Crab nebula. Linking MeV synchrotron and 50 TeV inverse Compton photons'. In: (2004). [ESA Spec. Publ.552,439(2004)]. arXiv: astro-ph/0407119 [astro-ph] (cit. on p. 25).

[105] L. Tibaldo, F. Aharonian, P. Bordas, et al. 'The Vela X pulsar wind nebula through the eyes of H.E.S.S. and Suzaku'. In: *PoS* ICRC2017 (2017), p. 719. arXiv: 1708.00388 [astro-ph.HE] (cit. on p. 25).

[106] S. Adrián-Martínez, M. Ageron, F. Aharonian, et al. 'Letter of Intent for KM3NeT2.0'. In: *JPhG* 43 (2016), p. 4001 (cit. on pp. 26, 33, 39, 56, 57, 59, 60, 66, 145, 181, 184, 188, 206, 213).

[107]V. Bosch-Ramon. 'Multifrequency Behavior of Microquasars in the GeV–TeV era: A review'. In: *Mem. Soc. Ast. It.* 83 (2012), p. 194. arXiv: 1106.2059 [astro-ph.HE] (cit. on p. 26).

[108]A. Neronov and M. Ribordy. 'Neutrino signal from gamma-ray loud binaries powered by high energy protons'. In: *Phys. Rev.* D79 (2009), p. 043013. arXiv: 0812.0306 [astro-ph] (cit. on p. 26).

[109]Tova M. Yoast-Hull, John S. Gallagher, Francis Halzen, Ali Kheirandish, and Ellen G. Zweibel. 'Gamma-ray puzzle in Cygnus X: Implications for high-energy neutrinos'. In: *Phys. Rev.* D96.4 (2017), p. 043011. arXiv: 1703.02590 [astro-ph.HE] (cit. on p. 26).

[110]A. Albert et al. 'Time-dependent search for neutrino emission from x-ray binaries with the ANTARES telescope'. In: *JCAP* 1704.04 (2017), p. 019. arXiv: 1609.07372 [astro-ph.HE] (cit. on p. 26).

[111]A. Albert et al. 'First all-flavor neutrino pointlike source search with the ANTARES neutrino telescope'. In: *Phys. Rev.* D96.8 (2017), p. 082001. arXiv: 1706.01857 [astro-ph.HE] (cit. on pp. 26, 145, 213).

[112]M. G. Aartsen et al. 'Searches for Time Dependent Neutrino Sources with IceCube Data from 2008 to 2012'. In: *Astrophys. J.* 807.1 (2015), p. 46. arXiv: 1503.00598 [astro-ph.HE] (cit. on p. 26).

[113]M. G. Aartsen et al. 'All-sky Search for Time-integrated Neutrino Emission from Astrophysical Sources with 7 yr of IceCube Data'. In: *Astrophys. J.* 835.2 (2017), p. 151. arXiv: 1609.04981 [astro-ph.HE] (cit. on pp. 26, 174).

[114]Daniele Gaggero, Alfredo Urbano, Mauro Valli, and Piero Ullio. 'Gamma-ray sky points to radial gradients in cosmic-ray transport'. In: *Phys. Rev.* D91.8 (2015), p. 083012. arXiv: 1411.7623 [astro-ph.HE] (cit. on p. 26).

[115]Daniele Gaggero, Dario Grasso, Antonio Marinelli, Alfredo Urbano, and Mauro Valli. 'The gamma-ray and neutrino sky: A consistent picture of Fermi-LAT, Milagro, and IceCube results'. In: *Astrophys. J.* 815.2 (2015), p. L25. arXiv: 1504.00227 [astro-ph.HE] (cit. on p. 26).

[116]D. Gaggero, D. Grasso, A. Marinelli, M. Taoso, and A. Urbano. 'Diffuse cosmic rays shining in the Galactic center: A novel interpretation of H.E.S.S. and Fermi-LAT γ-ray data'. In: *Phys. Rev. Lett.* 119.3 (2017), p. 031101. arXiv: 1702.01124 [astro-ph.HE] (cit. on p. 26).

[117]A. Albert et al. 'New constraints on all flavor Galactic diffuse neutrino emission with the ANTARES telescope'. In: *Phys. Rev.* D96.6 (2017), p. 062001. arXiv: 1705.00497 [astro-ph.HE] (cit. on p. 26).

[118]M. G. Aartsen et al. 'Constraints on Galactic Neutrino Emission with Seven Years of IceCube Data'. In: (2017). arXiv: 1707.03416 [astro-ph.HE] (cit. on p. 26).

[119]Piron, Frédéric. 'Gamma-Ray Bursts at high and very high energies'. In: *Comptes Rendus Physique* 17 (2016), pp. 617–631. arXiv: 1512.04241 [astro-ph.HE] (cit. on p. 27).

[120]B.P. Abbott et al. 'GW170817: Observation of Gravitational Waves from a Binary Neutron Star Inspiral'. In: *Phys. Rev. Lett.* 119.16 (2017), p. 161101. arXiv: 1710.05832 [gr-qc] (cit. on p. 27).

[121]Eli Waxman and John N. Bahcall. 'High-energy neutrinos from cosmological gamma-ray burst fireballs'. In: *Phys. Rev. Lett.* 78 (1997), pp. 2292–2295. arXiv: astro-ph/9701231 [astro-ph] (cit. on p. 27).

[122]M. G. Aartsen et al. 'Search for Prompt Neutrino Emission from Gamma-Ray Bursts with IceCube'. In: *Astrophys. J.* 805.1 (2015), p. L5. arXiv: 1412.6510 [astro-ph.HE] (cit. on pp. 27, 31).

[123]A. Albert et al. 'Search for High-energy Neutrinos from Binary Neutron Star Merger GW170817 with ANTARES, IceCube, and the Pierre Auger Observatory'. In: *Astrophys. J.* 850.2 (2017), p. L35. arXiv: 1710.05839 [astro-ph.HE] (cit. on p. 27).

[124]Hagai Netzer. 'Revisiting the Unified Model of Active Galactic Nuclei'. In: *Ann. Rev. Astron. Astrophys.* 53 (2015), pp. 365–408. arXiv: 1505.00811 [astro-ph.GA] (cit. on p. 27).

[125]C. Megan Urry and Paolo Padovani. 'Unified schemes for radio-loud active galactic nuclei'. In: *Publ. Astron. Soc. Pac.* 107 (1995), p. 803. arXiv: astro-ph/9506063 [astro-ph] (cit. on p. 27).

[126]A. A. Abdo et al. 'The Spectral Energy Distribution of Fermi bright blazars'. In: *Astrophys. J.* 716 (2010), pp. 30–70. arXiv: 0912.2040 [astro-ph.CO] (cit. on p. 28).

[127]J. H. Fan, J. H. Yang, Y. Liu, et al. 'The Spectral Energy Distributions of Fermi Blazars'. In: *Astrophys. J. Suppl.* 226.2 (2016), p. 20. arXiv: 1608.03958 [astro-ph.HE] (cit. on p. 28).

[128]M. Boettcher, A. Reimer, K. Sweeney, and A. Prakash. 'Leptonic and Hadronic Modeling of Fermi-Detected Blazars'. In: *Astrophys. J.* 768 (2013), p. 54. arXiv: 1304.0605 [astro-ph.HE] (cit. on p. 28).

[129]M. C. Gonzalez-Garcia, F. Halzen, and V. Niro. 'Reevaluation of the Prospect of Observing Neutrinos from Galactic Sources in the Light of Recent Results in Gamma Ray and Neutrino Astronomy'. In: *Astropart. Phys.* 57-58 (2014), pp. 39–48. arXiv: 1310.7194 [astro-ph.HE] (cit. on pp. 29, 30).

[130]S. Adrian-Martinez et al. 'Searches for Point-like and extended neutrino sources close to the Galactic Centre using the ANTARES neutrino Telescope'. In: *Astrophys. J.* 786 (2014), p. L5. arXiv: 1402.6182 [hep-ex] (cit. on pp. 29, 30, 145–148, 160, 171, 206, 213).

[131]C. Haack and C. Wiebusch. 'A measurement of the diffuse astrophysical muon neutrino flux using eight years of IceCube data.' In: *Proceedings, 35th International Cosmic Ray Conference (ICRC2017)*. 2017 (cit. on pp. 31, 39).

[132]H.M. Niederhausen and Y. Xu. 'High Energy Astrophysical Neutrino Flux Measurement Using Neutrino-induced Cascades Observed in 4 Years of IceCube Data'. In: *Proceedings, 35th International Cosmic Ray Conference (ICRC2017)*. 2017 (cit. on p. 31).

[133]M. G. Aartsen et al. 'Atmospheric and astrophysical neutrinos above 1 TeV interacting in IceCube'. In: *Phys. Rev.* D91.2 (2015), p. 022001. arXiv: 1410.1749 [astro-ph.HE] (cit. on p. 31).

[134]M. G. Aartsen et al. 'The contribution of Fermi-2LAC blazars to the diffuse TeV-PeV neutrino flux'. In: *Astrophys. J.* 835.1 (2017), p. 45. arXiv: 1611.03874 [astro-ph.HE] (cit. on p. 31).

[135]Aaron C. Vincent, Sergio Palomares-Ruiz, and Olga Mena. 'Analysis of the 4-year IceCube high-energy starting events'. In: *Phys. Rev.* D94.2 (2016), p. 023009. arXiv: 1605.01556 [astro-ph.HE] (cit. on p. 32).

[136]M. G. Aartsen et al. 'Flavor Ratio of Astrophysical Neutrinos above 35 TeV in IceCube'. In: *Phys. Rev. Lett.* 114.17 (2015), p. 171102. arXiv: 1502.03376 [astro-ph.HE] (cit. on p. 32).

[137]M. G. Aartsen et al. 'A combined maximum-likelihood analysis of the high-energy astrophysical neutrino flux measured with IceCube'. In: *Astrophys. J.* 809.1 (2015), p. 98. arXiv: 1507.03991 [astro-ph.HE] (cit. on p. 32).

[138]M. A. Markov. 'On high energy neutrino physics'. In: *Proceedings, 10th International Conference on High-Energy Physics (ICHEP 60): Rochester, NY, USA, 25 Aug - 1 Sep 1960*. 1960, pp. 578–581 (cit. on p. 33).

[139]A. Roberts and Wilkins G. In: 1978 (cit. on p. 33).

[140]L.B. et al. Bezrukov. 'Progress report on Lake Baikal neutrino experiment: Site studies and stationary string'. In: 1984, p. 550 (cit. on pp. 33, 61, 206).

[141]E. Andres et al. 'The AMANDA neutrino telescope: Principle of operation and first results'. In: *Astropart. Phys.* 13 (2000), pp. 1–20. arXiv: astro-ph/9906203 [astro-ph] (cit. on p. 33).

[142]A. Achterberg et al. 'First Year Performance of The IceCube Neutrino Telescope'. In: *Astropart. Phys.* 26 (2006), pp. 155–173. arXiv: astro-ph/0604450 [astro-ph] (cit. on pp. 33, 53, 206).

[143]M. Ageron, J. A. Aguilar, I. Al Samarai, et al. 'ANTARES: the first undersea neutrino telescope'. In: *NIMPA* 656 (2011), pp. 11–38 (cit. on pp. 33, 39, 45, 49, 206).

[144]J. Pumplin, D. R. Stump, J. Huston, et al. 'New generation of parton distributions with uncertainties from global QCD analysis'. In: *JHEP* 07 (2002), p. 012. arXiv: hep-ph/0201195 [hep-ph] (cit. on pp. 34, 67, 209).

[145]A. Z. Gazizov and S. I. Yanush. 'Hard pomeron enhancement of ultrahigh-energy neutrino nucleon cross-sections'. In: *Phys. Rev.* D65 (2002), p. 093003. arXiv: astro-ph/0105368 [astro-ph] (cit. on p. 34).

[146]Askhat Gazizov and Marek P. Kowalski. 'ANIS: High energy neutrino generator for neutrino telescopes'. In: *Comput. Phys. Commun.* 172 (2005), pp. 203–213. arXiv: astro-ph/0406439 [astro-ph] (cit. on pp. 35, 67).

[147]T. Chiarusi and M. Spurio. 'High-Energy Astrophysics with Neutrino Telescopes'. In: *Eur. Phys. J.* C65 (2010), pp. 649–701. arXiv: 0906.2634 [astro-ph.HE] (cit. on pp. 34, 36).

[148]A. Sánchez-Losa. 'Search for high energy cosmic muon neutrinos from variable gamma-ray sources and time calibration of the optical modules of the ANTARES telescope'. PhD thesis. Universitat de València, Valencia, Spain, 2015 (cit. on pp. 36, 40, 46, 93, 95, 100, 101).

[149]Tyce DeYoung, S. Razzaque, and D. F. Cowen. 'Astrophysical tau neutrino detection in kilometer-scale Cherenkov detectors via muonic tau decay'. In: *Astropart. Phys.* 27 (2007), pp. 238–243. arXiv: astro-ph/0608486 [astro-ph] (cit. on p. 37).

[150]Claudio Bogazzi. 'Search for cosmic neutrinos with ANTARES'. PhD thesis. Leiden U., 2014 (cit. on p. 38).

[151]A. Albert et al. 'All-flavor search for a diffuse flux of cosmic neutrinos with 9 years of ANTARES data'. In: (2017). arXiv: 1711.07212 [astro-ph.HE] (cit. on p. 39).

[152]J. A. Aguilar et al. 'The data acquisition system for the ANTARES Neutrino Telescope'. In: *Nucl. Instrum. Meth.* A570 (2007), pp. 107–116. arXiv: astro-ph/0610029 [astro-ph] (cit. on pp. 40, 43).

[153]P. Amram et al. 'The ANTARES optical module'. In: *Nucl. Instrum. Meth.* A484 (2002), pp. 369–383. arXiv: astro-ph/0112172 [astro-ph] (cit. on p. 41).

[154]M. de Jong. *The ANTARES Trigger Software*. ANTARES internal note. ANTARES-Soft/2005-005. 2005 (cit. on p. 45).

[155]E. Wisser. 'Neutrinos from the Milky Way'. PhD thesis. University of Leiden, 2015 (cit. on p. 45).

[156]J. Carr, S. Escoffier, and D. Zaborov. *Proposition for an alternative trigger based on the T3 cluster trigger*. ANTARES internal note. ANTARES-Soft/2007-016. 2007 (cit. on p. 45).

[157]D. Zaborov. *The K-40 Calibration method*. ANTARES internal note. ANTARES-CALI-2011-001. 2011 (cit. on p. 47).

[158]J. A. Aguilar et al. 'Time Calibration of the ANTARES Neutrino Telescope'. In: *Astropart. Phys.* 34 (2011), pp. 539–549. arXiv: 1012.2204 [astro-ph.IM] (cit. on pp. 47, 91–93, 95, 96, 99, 100, 210).

[159]S. Adrian-Martinez et al. 'The Positioning System of the ANTARES Neutrino Telescope'. In: *JINST* 7 (2012), T08002. arXiv: 1202.3894 [astro-ph.IM] (cit. on p. 48).

[160]J. A. Aguilar et al. 'Transmission of light in deep sea water at the site of the ANTARES Neutrino Telescope'. In: *Astropart. Phys.* 23 (2005), pp. 131–155. arXiv: astro-ph/0412126 [astro-ph] (cit. on pp. 50, 51).

[161]H. Yepes Ramírez. 'Characterization of the optical properties at the ANTARES site using the Optical Beacon system. Influence on the detector performance'. PhD thesis. Universitat de València, Valencia, Spain, 2014 (cit. on p. 50).

[162]C. Bigongiari and S. Mangano and J. Ruiz Rivas and others. *Results of the optical properties of sea water in the Antares site with the Optical Beacon system*. ANTARES internal note. ANTARES-PHYS/2013-015. 2013 (cit. on pp. 50, 52).

[163]S. Adrian-Martinez et al. 'Measurement of the Group Velocity of Light in Sea Water at the ANTARES Site'. In: *Astropart. Phys.* 35 (2012), pp. 552–557. arXiv: 1110.5184 [hep-ex] (cit. on p. 50).

[164]Christian et al Tamburini and ANTARES Collaboration. 'Deep-Sea Bioluminescence Blooms after Dense Water Formation at the Ocean Surface'. In: *PLOS ONE* 8.7 (July 2013), pp. 1–10 (cit. on p. 52).

[165]Francis Halzen and Spencer R. Klein. 'IceCube: An Instrument for Neutrino Astronomy'. In: *Rev. Sci. Instrum.* 81 (2010), p. 081101. arXiv: 1007.1247 [astro-ph.HE] (cit. on pp. 53, 54, 206).

[166]M. G. Aartsen et al. 'The IceProd Framework: Distributed Data Processing for the IceCube Neutrino Observatory'. In: *J. Parallel Distrib. Comput.* 75 (2015), pp. 198–211. arXiv: 1311.5904 [cs.DC] (cit. on p. 53).

[167]R. Abbasi et al. 'The IceCube Data Acquisition System: Signal Capture, Digitization, and Timestamping'. In: *Nucl. Instrum. Meth.* A601 (2009), pp. 294–316. arXiv: 0810.4930 [physics.ins-det] (cit. on p. 54).

[168]J. Ahrens et al. *IceCube Preliminary Design Document* (cit. on p. 54).

[169]R. Abbasi et al. 'IceTop: The surface component of IceCube'. In: *Nucl. Instrum. Meth.* A700 (2013), pp. 188–220. arXiv: 1207.6326 [astro-ph.IM] (cit. on p. 55).

[170]M. G. Aartsen et al. 'Measurement of South Pole ice transparency with the IceCube LED calibration system'. In: *Nucl. Instrum. Meth.* A711 (2013), pp. 73–89. arXiv: 1301.5361 [astro-ph.IM] (cit. on pp. 55, 56, 208).

[171]M. Ackermann et al. 'Optical properties of deep glacial ice at the South Pole'. In: *J. Geophys. Res. Atmos.* 111.D13 (2006), p. D13203 (cit. on p. 56).

[172]V. Aynutdinov et al. 'The BAIKAL neutrino experiment: Physics results and perspectives'. In: *Nucl. Instrum. Meth.* A602 (2009), pp. 14–20. arXiv: 0811.1109 [astro-ph] (cit. on pp. 61, 62).

[173]A. D. Avrorin et al. 'Status and recent results of the BAIKAL-GVD project'. In: *Phys. Part. Nucl.* 46.2 (2015), pp. 211–221 (cit. on pp. 61, 206).

[174]V. et al Aynutdinov. 'Status of the Baikal-GVD experiment - 2017'. In: *Proceedings, 35th International Cosmic Ray Conference (ICRC2017)*. 2017 (cit. on pp. 62, 63).

[175]D. Bailey. 'Monte Carlo tools and analysis methods for understanding the ANTARES experiment and predicting its sensitivity to Dark Matter'. PhD thesis. Wolfson College, Oxford, 2002 (cit. on pp. 66, 67, 209).

[176]D. Heck, J. Knapp, J.N. Capdevielle, G. Schatz, and T. Thouw. 'CORSIKA: A Monte Carlo code to simulate extensive air showers'. In: *Forschungszentrum Karlsruhe Report*. 1998 (cit. on p. 66).

[177]D. Heck and J. Knapp. 'Upgrade of the Monte Carlo code COSRIKA to simulate extensive air showers with energies $> 10^{20}$ eV'. In: *Forschungszentrum Karlsruhe Report*. 1998 (cit. on p. 66).

[178]G. Carminati, A. Margiotta, M. Spurio, et al. 'Atmospheric MUons from PArametric formulas: A Fast GEnerator for neutrino telescopes (MUPAGE)'. In: *CoPhC* 179 (2008), pp. 915–923 (cit. on p. 66).

[179] G. Ingelman, A. Edin, and J. Rathsman. 'LEPTO 6.5: A Monte Carlo generator for deep inelastic lepton - nucleon scattering'. In: *Comput. Phys. Commun.* 101 (1997), pp. 108–134. arXiv: hep-ph/9605286 [hep-ph] (cit. on p. 67).

[180] A. J. Heijboer. 'Track Reconstruction and Point Source Searches with ANTARES'. PhD thesis. NIKHEF, Amsterdam, 2004 (cit. on pp. 68, 72).

[181] V. Agrawal, T. k. Gaisser, P. Lipari, et al. 'Atmospheric neutrino flux above 1 GeV'. In: *PhRvD* 53 (1996), pp. 1314–1323 (cit. on p. 68).

[182] Morihiro Honda, T. Kajita, K. Kasahara, S. Midorikawa, and T. Sanuki. 'Calculation of atmospheric neutrino flux using the interaction model calibrated with atmospheric muon data'. In: *Phys. Rev.* D75 (2007), p. 043006. arXiv: astro-ph/0611418 [astro-ph] (cit. on p. 68).

[183] Rikard Enberg, Mary Hall Reno, and Ina Sarcevic. 'Prompt neutrino fluxes from atmospheric charm'. In: *Phys. Rev.* D78 (2008), p. 043005. arXiv: 0806.0418 [hep-ph] (cit. on p. 68).

[184] M. G. Aartsen et al. 'Search for Time-independent Neutrino Emission from Astrophysical Sources with 3 yr of IceCube Data'. In: *Astrophys. J.* 779 (2013), p. 132. arXiv: 1307.6669 [astro-ph.HE] (cit. on pp. 68, 88, 146, 148, 149).

[185] J. Brunner. *Updated tag list for the new ANTARES event format*. ANTARES internal note. ANTARES-Soft/1993-003. 1999 (cit. on p. 68).

[186] Rickard Ström. 'Exploring the Universe Using Neutrinos. A Search of Point Sources in the Southern Hemisphere Using the IceCube Neutrino Observatory'. PhD thesis. Uppsala Universitet, Stockholm, 2015 (cit. on pp. 69, 71).

[187] S. Navas and L. Thompson. *KM3 User Guide and Reference Manual*. ANTARES internal note. ANTARES-Soft/1999-011. 1999 (cit. on p. 70).

[188] CERN. *GEANT program manual*. CERN program library long writeup W5013, 1993 (cit. on p. 70).

[189] P. Antonioli, C. Ghetti, V. Korolkova, E. V.A. Kudryavtsev, and G. Sartorelli. 'A Three-Dimensional Code for Muon Propagation through the Rock: MUSIC'. In: *ApP* 7 (1997), pp. 357–368 (cit. on p. 70).

[190] J.H. Koehne et al. 'PROPOSAL: A tool for propagation of charged leptons'. In: *Computer Physics Communications*. Vol. 184(9). 2013, p. 2070 (cit. on p. 70).

[191] Johan Lundberg, P. Miocinovic, T. Burgess, et al. 'Light tracking for glaciers and oceans: Scattering and absorption in heterogeneous media with Photonics'. In: *Nucl. Instrum. Meth.* A581 (2007), pp. 619–631. arXiv: astro-ph/0702108 [ASTRO-PH] (cit. on p. 70).

[192]M. de Jong. *The TriggerEfficiency program*. ANTARES internal note. ANTARES-Soft/2009-001. 2009 (cit. on p. 71).

[193]R. Bormuth. *Description of the two standard trigger algorithms in the JPP software package (release r2356 to trunk at 27-11-2015)*. KM3NeT Internal Note. KM3NeT_SOFT_2015_001. 2015 (cit. on p. 71).

[194]J. Brunner. *The BBfit reconstruction algorithm*. ANTARES internal note. ANTARES-SOFT-2009-012. 2009 (cit. on p. 72).

[195]E. Wisser. 'Neutrinos from the Milky Way'. PhD thesis. NIKHEF, Amsterdam, 2015 (cit. on p. 72).

[196]E. Carmona. 'Study of the event reconstruction and expected performances for point-like sources of the future Antares neutrino telescope'. PhD thesis. Universitat de València, Valencia, 2003 (cit. on p. 72).

[197]S. Adrián-Martínez et al. 'Time calibration with atmospheric muon tracks in the ANTARES neutrino telescope'. In: *Astropart. Phys.* 78 (2016), pp. 43–51. arXiv: 1507.04182 [physics.ins-det] (cit. on pp. 73, 106, 109).

[198]S. Adrián-Martínez, I. Al Samarai, A. Albert, et al. 'Measurement of the atmospheric ν_μ energy spectrum from 100 GeV to 200 TeV with the ANTARES telescope'. In: *EPJC 73:2606* (2013) (cit. on pp. 75, 164).

[199]F. Schüssler. 'Energy reconstruction in neutrino telescopes'. In: *Proceedings, 33rd International Cosmic Ray Conference (ICRC2013)*. 2013 (cit. on p. 75).

[200]K. Melis, M. de Jong, and A. Heijboer. 'KM3NeT/ARCA Event Reconstruction Algorithms'. In: *Proceedings, 35th International Cosmic Ray Conference (ICRC2017)*. 2017 (cit. on pp. 76, 78).

[201]A. Trovato. 'Development of reconstruction algorithms for large volume neutrino telescopes and their application to the KM3NeT detector'. PhD thesis. Universita degli Studi di Catania, Scuola Superiore di Catania, 2013 (cit. on p. 77).

[202]Tino Michael. 'Light at the End of the Shower'. PhD thesis. NIKHEF, 2016 (cit. on p. 79).

[203]A. Albert et al. 'An algorithm for the reconstruction of neutrino-induced showers in the ANTARES neutrino telescope'. In: *Astron. J.* 154.6 (2017), p. 275. arXiv: 1708.03649 [astro-ph.IM] (cit. on p. 79).

[204]A. Heijboer. *Shower Direction Reconstruction: aashowerfit*. KM3NeT internal note. KM3NeT_ASTRO_2014_001. 2014 (cit. on p. 81).

[205]A. Albert et al. 'An algorithm for the reconstruction of high-energy neutrino-induced particle showers and its application to the ANTARES neutrino telescope'. In: *Eur. Phys. J.* C77.6 (2017), p. 419. arXiv: 1703.02432 [astro-ph.HE] (cit. on p. 83).

[206]F. Folger. 'Search for a diffuse cosmic neutrino flux using shower events in the ANTARES neutrino telescope'. PhD thesis. ECAP, 2014 (cit. on p. 83).

[207]F. Folger. *The Dusj shower reconstruction project*. ANTARES internal note. ANTARES-PHYS-2013-003. 2013 (cit. on p. 83).

[208]Q. Dorosti Hasankiadeh. 'Reconstruction of neutrino-induced showers with ANTARES'. PhD thesis. University of Groningen, 2013 (cit. on p. 86).

[209]Q Dorosti Hasankiadeh and H. Lohner. *Search for Showers Induced by Di use Flux of Cosmic Neutrinos*. ANTARES internal note. ANTARES-PHYS-2012-011. 2012 (cit. on p. 86).

[210]J. Ahrens et al. 'Muon track reconstruction and data selection techniques in AMANDA'. In: *Nucl. Instrum. Meth.* A524 (2004), pp. 169–194. arXiv: astro-ph/0407044 [astro-ph] (cit. on p. 87).

[211]Till Neunhoffer. 'Estimating the angular resolution of tracks in neutrino telescopes based on a likelihood analysis'. In: *Astropart. Phys.* 25 (2006), pp. 220–225. arXiv: astro-ph/0403367 [astro-ph] (cit. on p. 88).

[212]R. Abbasi et al. 'Time-Integrated Searches for Point-like Sources of Neutrinos with the 40-String IceCube Detector'. In: *Astrophys. J.* 732 (2011), p. 18. arXiv: 1012.2137 [astro-ph.HE] (cit. on pp. 88, 149).

[213]R. Abbasi et al. 'An improved method for measuring muon energy using the truncated mean of dE/dx'. In: *Nucl. Instrum. Meth.* A703 (2013), pp. 190–198. arXiv: 1208.3430 [physics.data-an] (cit. on p. 89).

[214]M. Ageron et al. 'The ANTARES Optical Beacon System'. In: *Nucl. Instrum. Meth.* A578 (2007), pp. 498–509. arXiv: astro-ph/0703355 [ASTRO-PH] (cit. on pp. 94, 96).

[215]D. Zaborov. *The K-40 calibration method*. ANTARES internal note. ANTARES-CALI-2011-001. 2011 (cit. on p. 97).

[216]I. Salvadori. *K40 Calibration*. ANTARES internal note. ANTARES-CALI-2016-001. 2016 (cit. on pp. 97, 102).

[217]J.P. Gómez González. 'Time calibration and search for cosmic sources of high energy neutrinos with the ANTARES neutrino telescope'. PhD thesis. Universitat de València, Valencia, Spain, 2013 (cit. on pp. 98, 106, 109).

[218] M. Circella. 'Maintenance of the ANTARES deep-sea neutrino telescope'. (conference) VLVNT 2011. 2011 (cit. on p. 99).

[219] J. Barrios-Martí. 'Update on IFIC time calibration'. (conference) ANTARES Collaboration Meeting in Oujda. 2013 (cit. on p. 99).

[220] J. Barrios-Martí. 'Update on IFIC time calibration'. (conference) ANTARES Collaboration Meeting in Marseille. 2013 (cit. on p. 99).

[221] T. Nijbroek. 'Last news on nanobeacons study'. (conference) ANTARES Collaboration Meeting in Vilanova i la Geltrú. 2014 (cit. on p. 99).

[222] J.A. Aguilar-Sánchez. 'Analysis of the optical beacon system and search for point-like sources in the ANTARES neutrino telescope'. PhD thesis. Universitat de València, Valencia, Spain, 2007 (cit. on p. 102).

[223] Olaf Behnke, Kevin Kröninger, Thomas Schörner-Sadenius, and Gregory Schott, eds. *Data analysis in high energy physics*. Weinheim, Germany: Wiley-VCH, 2013 (cit. on p. 124).

[224] Roger J. Barlow. 'Extended maximum likelihood'. In: *Nucl. Instrum. Meth.* A297 (1990), pp. 496–506 (cit. on p. 126).

[225] S. S. Wilks. 'The Large-Sample Distribution of the Likelihood Ratio for Testing Composite Hypotheses'. In: *Annals Math. Statist.* 9.1 (1938), pp. 60–62 (cit. on p. 131).

[226] J. Neyman. 'Outline of a Theory of Statistical Estimation Based on the Classical Theory of Probability'. In: *Phil. Trans. Roy. Soc. Lond.* A236.767 (1937), pp. 333–380 (cit. on pp. 133, 147).

[227] Jonathan P. Dumm. 'Searches for Point-like Sources of Neutrinos with the 40-String IceCube Detector'. PhD thesis. U. Wisconsin, Madison (main), 2011 (cit. on p. 133).

[228] Gary J. Feldman and Robert D. Cousins. 'A Unified approach to the classical statistical analysis of small signals'. In: *Phys. Rev.* D57 (1998), pp. 3873–3889. arXiv: `physics/9711021 [physics.data-an]` (cit. on p. 133).

[229] Alexander L. Read. 'Presentation of search results: The CL(s) technique'. In: *J. Phys.* G28 (2002). [,11(2002)], pp. 2693–2704 (cit. on p. 133).

[230] Leo Breiman. 'Random Forests'. In: *Machine Learning* 45.1 (2001), pp. 5–32 (cit. on pp. 139, 141).

[231] Leo Breiman, Jerome Friedman, R. A. Olshen, and Charles J. Stone. *Classification and regression trees*. Chapman and Hall/CRC, 1984 (cit. on p. 139).

[232] Yoav Freund and Robert E. Schapire. 'A Decision-Theoretic Generalization of On-Line Learning and an Application to Boosting'. In: *J. Comput. Syst. Sci.* 55.1 (1997), pp. 119–139 (cit. on p. 141).

[233] Trevor Hastie, Robert Tibshirani, and Jerome Friedman. *The Elements of Statistical Learning*. Springer Series in Statistics. New York, NY, USA: Springer New York Inc., 2009 (cit. on p. 141).

[234] Fabian Pedregosa et al. 'Scikit-learn: Machine Learning in Python'. In: *J. Machine Learning Res.* 12 (2011), pp. 2825–2830. arXiv: 1201.0490 [cs.LG] (cit. on p. 141).

[235] S. Adrian-Martinez et al. 'The First Combined Search for Neutrino Point-sources in the Southern Hemisphere With the Antares and Icecube Neutrino Telescopes'. In: *Astrophys. J.* 823.1 (2016), p. 65. arXiv: 1511.02149 [hep-ex] (cit. on pp. 145, 213).

[236] M. G. Aartsen et al. 'Lowering IceCube's Energy Threshold for Point Source Searches in the Southern Sky'. In: *Astrophys. J.* 824.2 (2016), p. L28. arXiv: 1605.00163 [astro-ph.HE] (cit. on pp. 146, 174).

[237] M. G. Aartsen et al. 'Search for astrophysical sources of neutrinos using cascade events in IceCube'. In: *Astrophys. J.* 846.2 (2017), p. 136. arXiv: 1705.02383 [astro-ph.HE] (cit. on p. 146).

[238] M. G. Aartsen et al. 'Observation and Characterization of a Cosmic Muon Neutrino Flux from the Northern Hemisphere using six years of IceCube data'. In: *Astrophys. J.* 833.1 (2016), p. 3. arXiv: 1607.08006 [astro-ph.HE] (cit. on pp. 171, 172).

[239] Scott P. Wakely and Deirdre Horan. 'TeVCat: An online catalog for Very High Energy Gamma-Ray Astronomy'. In: 3 (2007), p. 1341 (cit. on p. 171).

[240] A. U. Abeysekara et al. 'The 2HWC HAWC Observatory Gamma Ray Catalog'. In: *Astrophys. J.* 843.1 (2017), p. 40. arXiv: 1702.02992 [astro-ph.HE] (cit. on p. 172).

[241] F. Krauß et al. 'TANAMI Blazars in the IceCube PeV Neutrino Fields'. In: *Astron. Astrophys.* 566 (2014), p. L7. arXiv: 1406.0645 [astro-ph.HE] (cit. on p. 172).

[242] M. Kadler et al. 'Coincidence of a high-fluence blazar outburst with a PeV-energy neutrino event'. In: *Nature Phys.* 12.8 (2016), p. 807. arXiv: 1602.02012 [astro-ph.HE] (cit. on p. 172).

[243] S. Adrian-Martinez et al. 'ANTARES Constrains a Blazar Origin of Two IceCube PeV Neutrino Events'. In: *Astron. Astrophys.* 576 (2015), p. L8. arXiv: 1501.07843 [astro-ph.HE] (cit. on p. 172).

[244]S. Adrian-Martinez et al. 'Constraining the neutrino emission of gravitationally lensed Flat-Spectrum Radio Quasars with ANTARES data'. In: *JCAP* 1411.11 (2014), p. 017. arXiv: 1407.8525 [astro-ph.HE] (cit. on p. 172).

[245]M. G. Aartsen et al. 'Observation of High-Energy Astrophysical Neutrinos in Three Years of IceCube Data'. In: *Phys. Rev. Lett.* 113 (2014), p. 101101. arXiv: 1405.5303 [astro-ph.HE] (cit. on pp. 175, 177).

[246]Y. Bai, A. J. Barger, V. Barger, et al. 'Neutrino Lighthouse at Sagittarius A*'. In: *Phys. Rev.* D90.6 (2014), p. 063012. arXiv: 1407.2243 [astro-ph.HE] (cit. on p. 178).

[247]S. Adrian-Martinez et al. 'The Positioning System of the ANTARES Neutrino Telescope'. In: *JINST* 7 (2012), T08002. arXiv: 1202.3894 [astro-ph.IM] (cit. on p. 179).

[248]S. Adrian-Martinez et al. 'Search for Cosmic Neutrino Point Sources with Four Year Data of the ANTARES Telescope'. In: *Astrophys. J.* 760 (2012), p. 53. arXiv: 1207.3105 [hep-ex] (cit. on p. 180).

[249]J. A. Aguilar et al. 'Performance of the front-end electronics of the ANTARES neutrino telescope'. In: *Nucl. Instrum. Meth.* A622 (2010), p. 59. arXiv: 1007.2549 [astro-ph.IM] (cit. on p. 180).

[250]T. Eberl and T. Heid. 'Sensitivity of KM3NeT/ARCA to the neutrino flavour composition'. In: *Proceedings, 35th International Cosmic Ray Conference (ICRC2017)*. 2017 (cit. on p. 184).

[251]Morihiro Honda, T. Kajita, K. Kasahara, S. Midorikawa, and T. Sanuki. 'Calculation of atmospheric neutrino flux using the interaction model calibrated with atmospheric muon data'. In: *Phys. Rev.* D75 (2007), p. 043006. arXiv: astro-ph/0611418 [astro-ph] (cit. on p. 188).

[252]Rikard Enberg, Mary Hall Reno, and Ina Sarcevic. 'Prompt neutrino fluxes from atmospheric charm'. In: *Phys. Rev.* D78 (2008), p. 043005. arXiv: 0806.0418 [hep-ph] (cit. on p. 188).

[253]A. Albert et al. 'All-flavor Search for a Diffuse Flux of Cosmic Neutrinos with Nine Years of ANTARES Data'. In: *Astrophys. J.* 853.1 (2018), p. L7. arXiv: 1711.07212 [astro-ph.HE] (cit. on p. 206).

Acronyms

CC Charged Current. 75, 78

CL Confidence Level. 29, 133, 148, 156, 157, 171, 175, 192

DOM Digital Optical Module. 54, 55, 57, 58, 61, 71, 82, 88

EAS Cherenkov Extensive Air Shower array. 13, 14

GRB Gamma-ray burst. 11, 27, 31

IACT Imaging array Cherenkov Telescope. 13

ISM Interstellar medium. 7

MEOC Main Electro Optical Cable. 59

OB Optical Beacon. 50, 96, 97, 99, 101–105, 108, 109

OM Optical Module. 40–42, 47, 48, 54, 61, 70, 72, 73, 79, 91, 92, 94, 96–99, 101–103, 105–108, 111, 115

PMT Photomultiplier. 33, 38–41, 43, 44, 46, 48, 50, 51, 53, 54, 57, 58, 60, 61, 71, 77, 80, 81, 83, 87, 88, 102

PSF Point Spread Function. 125, 188

RFC Random Forest Classifier. 85, 136, 139, 181, 183, 188

SgrA* Saggitarius A* (black hole at the Galactic Centre). 23, 25

SNR Supernova remnant. 7–9, 22, 24–26

ToT Time over Threshold. 60

TS Test Statistic. 127, 128, 130–137

TTS Transit Time Spread. 41, 54, 57, 71

Colophon

This thesis was typeset with LaTeX 2_ε. It uses the *Clean Thesis* style developed by Ricardo Langner. The design of the *Clean Thesis* style is inspired by user guide documents from Apple Inc.

Download the *Clean Thesis* style at `http://cleanthesis.der-ric.de/`.